# Investigation of Mn and Ti based self-forming barriers for future back-end-of-line interconnects

Venkateswaran Selvaraju M.Sc

Thesis submitted for the award of Doctor of Philosophy

Under the supervision of

Prof. Greg Hughes

School of Physical Sciences

January 2019

# Declaration

I hereby certify that this material, which I now submit for assessment on the programme of study leading to the award of Doctor of Philosophy (Ph.D) is entirely my own work, and that I have exercised reasonable care to ensure that the work is original, and does not to the best of my knowledge breach any law of copyright, and has not been taken from the work of others save and to the extent that such work has been cited and acknowledged within the text of my work.

Signed: _______________ ID No.:_________________ Date: ____________

# Acknowledgements

Firstly, I would like to thank my supervisor, Prof. Greg Hughes, for his support and guidance throughout my Ph.D. and thank him for selecting me as a viable candidate for a Ph.D. position under the barrier layer project.

I would like to thank all my teammates in the surface science research group in School of Physics, DCU, Dr Justin Bogan, Dr Rob O'Connor, Anita brady-Boyd, Dr Conor Byrne, Dr Anthony McCoy, Mathew Snelgrove, Niall Flannagan, Dr Pierre Giovanni Mani Gonzalez and Dr Lee Walsh for their constant support during my Ph.D. as well as help in acclimating to the conditions in Ireland.

I would also like to thank all the staff in School of Physics, in particular, Pat Wogan, Des Lavelle and Lisa Peyton for their availability and constant help when needed.

I would like to thank Science Foundation of Ireland (SFI) and Intel Ireland for funding and continued support of the barrier layer project.

I would also like to thank the collaborators Alan Blake, Dr Paul Hurley and Dr Scott Monaghan from Tyndall National Institute for their help and support during the deposition and electrical characterization of the samples.

I would also like to thank Beamline scientists Dr Zheshen Li from Astrid II beamline Aarhus university, Dr Jean Pascal and Dr Denis Ceolin from Synchrotron SOLEIL, Paris and Dr Christoph Schlueter from DESY Hamburg for the constant support during the experiments at the respective synchrotron facilities.

Lastly, I would like to thank my parents and my family who allowed me to carry on with my higher studies faraway from India and always encouraging me to achieve more than I thought possible.

# Table of Contents


Declaration ..... i

Acknowledgements ..... ii

List of figures ..... vii

List of tables ..... xii

List of Publications arising from this work: ..... xiii

Abstract ..... xv

1. Introduction ..... 1

1.1 Various components of ICs and Issues in scaling: ..... 2

1.2 Requirement of Diffusion barrier for copper interconnects ..... 5

1.3 RC Time Delay ..... 6

1.4 Requirement for alternate diffusion barrier layers ..... 7

1.4.1 Manganese nitride-based copper diffusion barriers ..... 7

1.4.2 Self-forming barriers ..... 9

1.5 Requirement for an alternate interconnect metal ..... 12

1.6 Alternate Substrate dielectric materials ..... 13

1.7 Thesis Overview ..... 17

References ..... 18

2 Experimental Techniques and Principles ..... 26

2.1 Principles of Photoelectron Spectroscopy: ..... 26

2.1.1 X-Ray Photoelectron Spectroscopy ..... 26

2.1.2 Hard X-ray Photoelectron Spectroscopy ..... 40

2.2 X-ray Absorption Spectroscopy (XAS): ..... 43

2.2.1 Principles of XAS: ..... 43

2.3 Atomic Force Microscopy: ..... 47

2.3.1 Modes of Operation ..... 48

2.4 Electrical Characterization ..... 50

2.4.1 Four Point Probe measurements ........ 51

2.4.2 CV Measurements of MOS devices ........ 52

2.5 Adhesion Testing: ........ 55

References: ........ 57

3. Investigation of nitrogen incorporation into manganese-based copper diffusion barrier layers for future interconnect applications ........ 61

3.1 Introduction ........ 61

3.2 Experimental Details ........ 62

3.3 Results and Discussion ........ 64

3.4 Conclusion: ........ 84

References: ........ 85

4. Material and Electrical Characterization of Titanium and Manganese based Copper alloys as self-forming barrier layers for future copper interconnects ........ 89

4.1 Introduction ........ 89

4.2 Experimental Work: ........ 90

4.3 Results and Discussions ........ 91

4.2.1 SIMS Analysis ........ 104

4.2.2 Electrical characterization ........ 105

References: ........ 110

5.1 Introduction ........ 113

5.2 A synchrotron radiation photoemission study of metallic titanium deposited on $SiO_2$ based dielectric substrates ........ 114

5.2.1 Experimental work ........ 114

5.3 HAXPES and XANES studies of 20% CoTi Alloy: ........ 125

5.3.1 XPS and HAXPES Analysis: ........ 125

5.4 Conclusion ........ 136

References ........ 137

6. Conclusions and Future work ........ 136

**6.1 Conclusions** 136

**6.1.1 Nitrogen based Mn barrier layer for Cu interconnects** 136

**6.1.2 Self-forming Mn/Ti based copper alloy systems** 137

**6.1.3 Synchrotron radiation study of metallic Titanium deposited on low-κ dielectrics:** 139

**6.1.4 HAXPES and XAS studies of CoTi self-forming alloy:** 139

**6.2 Future Work:** 140

**References** 141

# List of figures

Figure 1.1: Moore's law applied to Intel microprocessors[2] ........ 1

Figure 1.2: Schematic of modern ICs showing various components and Cu interconnects connecting them [4] ........ 3

Figure 1.3: Comparison of response time delay due to gate oxide and interconnects [6] ........ 4

Figure 1.4: (a) electro migration of the metal creating a Void in metal lattice[8] (b) SEM image of the voids in ULSI Cu interconnect system [9] ........ 5

Figure 1.5: Resistance in copper interconnect lines ........ 6

Figure 1.6: Self-forming barrier process overview ........ 10

Figure 1.7: Changes in copper line resistance with decrease in line-width of IC node[40] ........ 13

Figure 1.8: Basic structure of a capacitor ........ 14

Figure 1.9: graph of change in elasticity with dielectric constant (κ) in carbon doped glasses ........ 15

Figure 1.10: Chemical structure of a CDO based dielectric[47] ........ 16

Figure 1.11: Structure of a porous CDO substrate ........ 17

Figure 2.1: principle of photoemission spectroscopy [2] ........ 26

Figure 2.2: Illustration of sample work function and spectrometer work function ........ 27

Figure 2.3: dependence of mean free path for various elements with change in the kinetic energy[3] ........ 29

Figure 2.4: Typical XPS survey spectrum for gold standard sample showing different elements present[6] ........ 30

Figure 2.5: Graph showing XPS of Si 2p spectrum for 4.5 nm SiO2 on bulk Si with signals from both substrate (99.1 eV) and overlying oxide (103.9 eV) ........ 32

Figure 2.6: Example of Ti metallic peak showing asymmetry ........ 34

Figure 2.7: schematic showing the decreased sampling depth with change in the angle of photoemission ........ 35

Figure 2.8: dependency of intensity of photoelectrons on sampling depth with change in angle of emission ........ 36

Figure 2.9: Twin anode setup for modern XPS systems [10] ........ 37

Figure 2.10: Basic hemispherical analyser ........ 38

Figure 2.11: Schematic of a modern day XPS system ........ 40

Figure 2.12: generation of x-ray beam at synchrotron sources[11] ........ 42

Figure 2.13: Experimental HAXPES setup[12] ........ 42

Figure 2.14: A typical XAS spectrum showing pre-edge, rising edge and extended absorption edge[17] .... 44
Figure 2.15: Overview of XAS setup .... 45
Figure 2.16: Principle of SIMS[18] .... 46
Figure 2.17: Block diagram of a sims system showing the basic elements including a sputter gun, mass analyser and flood gun [21] .... 47
Figure 2.18: Operating principle of a typical AFM[24] .... 49
Figure 2.19: working of an AFM in tapping mode .... 50
Figure 2.20: Structure of a general four-point probe instrument [18] .... 51
Figure 2.21: MOS capacitor (a) without barrier layer showing cu diffusion (b) with barrier layer .... 53
Figure 2.22: CV Profile of n-type MOS capacitor showing accumulation, depletion and inversion with respect to gate voltage sweep .... 54
Figure 2.23: scratch test .... 56
Figure 2.24: Peel test[33] .... 56
Figure 2.25: Blister test .... 57
Figure 2.26: Silicon Shadow mask used for copper deposition through hot filament evaporation .... 57
Figure 3.1: Initial ion implantation attempts of nitrogen into manganese films using in-situ ion gun implantation techniques .... 65
Figure 3.2: XPS survey spectrum of metallic manganese and nitrogen incorporated on TEOS showing the presence of N 1s in manganese nitride films while absence of N 1s in Mn metal films .... 66
Figure 3.3: XPS survey spectrum of metallic manganese and nitrogen incorporated on TEOS after 400°C anneal .... 69
Figure 3.4: Manganese 2p spectra for the Mn and Nitrogen containing Mn film with fitted components (for Nitrogen containing Mn) before and after thermal anneal .... 70
Figure 3.5: Mn 3s spectra from the Nitrogen containing Mn film showing the change of oxidation state from +3 to +2 on anneal .... 71
Figure 3.6: N 1s spectrum of nitrogen incorporated before and after anneals .... 72
Figure 3.7: C 1s of Nitrogen containing Mn on TEOS XPS spectrum before and after 400°C anneal .... 74
Figure 3.8: Si 2p and O 1s spectra showing the presence of manganese silicate following Mn deposition and the improved signal to noise upon anneal due to film thinning .... 75
Figure 3.9: Si 2p spectra of as received substrates of (i) dryox (ii) TEOS (iii) Silane .... 76
Figure 3.10: Si 2p spectra of as received nitrogen containing Mn films on (i) dryox (ii) TEOS (iii) Silane .... 77

Figure 3.11: Si 2p spectra of 400°C annealed nitrogen containing Mn films on (i) dryox (ii) TEOS (iii) Silane ........ 78
Figure 3.12: Si 2p spectra of as received nitrogen containing Mn films on (i) TEOS with degas substrate (ii) TEOS with no degas substrate both showing the presence of Mn silicate barrier upon deposition ........ 79
Figure 3.13: Si 2p spectra of 400°C annealed nitrogen containing Mn films on (a) TEOS with degas showing minimal changes to barrier signal (b) TEOS with no degas showing evolved Mn silicate signal ........ 80
Figure 3.14: Mn 2p spectra of TaN capped N containing Mn film before and after 400°C showing no significant changes on anneal ........ 81
Figure 3.15: AFM images of (a) Manganese metal film after 400°C anneal (b) nitrogen incorporated after 400°C anneal ........ 82
Figure 3.16: Profilometry measurements of thickness of Cu structures on (a) TEOS substrate (b) Mn thin film on TEOS (c) Nitrogen containing Mn thin film on TEOS ........ 83
Figure 3.17: Optical Microscopy images of (a) Cu on TEOS before tape test (b) Cu on Mn metal film before tape test (c) Cu on Nitrogen containing Mn film before tape test (d) Cu on TEOS after tape test (e) Cu on Mn metal after tape test (f) Cu on Nitrogen containing ........ 84
Figure 4.1: Delamination of (a) 5% CuMn (b) Cu and (c) CuTi on $SiO_2$ upon 400°C anneal ........ 90
Figure 4.2: XPS Survey spectra of as received (i) 20% CuMn sample and (ii) 20% CuTi sample specifying the elements present in the sample ........ 92
Figure 4.3: Annealed 20% CuMn and 20% CuTi XPS spectra showing metal segregation and surface copper oxide reduction to metallic copper on 400ºC anneal ........ 93
Figure 4.4: HAXPES Survey spectra of (i) 20% CuMn sample as received (ii) 20% CuMn sample after 400°C anneal ........ 95
Figure 4.5: Cu 2p spectra of (a) reference Cu and CuMn alloy on $SiO_2$ before and after 400°C anneal indicate absence of Cu oxide (b) reference Cu and CuTi alloy on $SiO_2$ before and after 400°C anneal96
Figure 4.6: Mn 2p spectra of Thick Mn and CuMn alloy on $SiO_2$ before and after 400°C anneal showing the presence of shake-up feature after the anneal while Mn metallic signal is observed on before and after anneal samples ........ 97
Figure 4.7: O 1s spectra of Thick Mn and CuMn alloy on $SiO_2$ before and after 400°C anneal showing the presence of Mn silicate barrier in the after anneal sample ........ 98
Figure 4.8: Si 1s spectra of CuMn alloy on $SiO_2$ before and after 400°C anneal showing clear indication of the growth of Mn silicate barrier upon anneal ........ 99

Figure 4.9: Ti 1s spectra of CuTi alloy on $SiO_2$ (a)before anneal indicate single state $TiO_2$ and residual metal at the surface and (b) after 400°C anneal showing formation of Ti silicate along with Ti sub-oxides while Ti metal is consumed ........ 100
Figure 4.10: O 1s spectra of CuTi alloy on $SiO_2$ (a) before anneal and (b) after 400°C anneal showing multiple peak components corresponding to $SiO_2$, $TiO_2$ and possibility of Ti silicate after the anneal ........ 101
Figure 4.11: HAXPES Si 1s spectra of (a) as received and (b) 400°C annealed 20% CuTi sample ....... 102
Figure 4.12: C 1s spectra of (a) thick Ti on SiO2 showing the presence of Ti carbide (b) CuTi alloy on SiO2 before anneal and (c) CuTi on SiO2 after 400°C anneal showing no peak components corresponding to Ti carbide indicating absence of free Ti metal ........ 103
Figure 4.13: SIMS profile of (i) 20% CuMn as received sample and (ii) 20% CuMn sample after 400°C anneal indicating the segregation of Mn metal at the interface as well as formation of Mn silicate barrier upon annealing ........ 104
Figure 4.14: SIMS profile of (i) 20% CuTi as received sample and (ii) 20% CuTi sample after 400°C anneal showing incomplete segregation of Ti with no clear indication of Ti-SiO2 interface barrier layer ........ 105
Figure 4.15: Four-point probe measurements of (i) 20% CuMn (ii) 20% CuTi (iii) pure Cu and (iv) reference bulk Cu resistivities before and after various annealing steps........ 106
Figure 4.16: CV analysis of as received 20% CuMn MOS structures showing large hysteresis corresponding to trapped and mobile charges upon deposition conditions ........ 107
Figure 4.17: CV analysis of 20% CuMn MOS structures after 400°C anneal show improved capacitance as well as the hysteresis is reduced ........ 108
Figure 4.18: CV analysis of as received 20% CuTi MOS structures indicating the presence of trapped and mobile charges upon deposition ........ 109
Figure 4.19: CV analysis of 20% CuTi MOS structures after 400°C anneal show removal of hysteresis as well as flat-band voltage approaching zero........ 109
Figure 5.1: Si 2p spectra of 5nm $SiO_2$ upon Ti deposition and anneals showing clear indication of formation of Ti silicide and upon Ti deposition ........ 116
Figure 5.2: Ti 3p spectra upon Ti deposition 5nm $SiO_2$ and various anneals........ 118
Figure 5.3: Si 2p spectra of native $SiO_2$ upon Ti deposition and anneals........ 119
Figure 5.4: Ti 3p spectra upon Ti deposition on native $SiO_2$, anneals and atmospheric exposure..... 120
Figure 5.5: Si 2p spectra of SoG upon Ti deposition and anneals........ 122
Figure 5.6: Figure 4: Ti 3p spectra upon Ti deposition on SoG substrate and anneals........ 123
Figure 5.7: C 1s spectra of SoG substrate upon Ti deposition and anneals........ 124

Figure 5.8: XPS spectra of CoTi alloy film on 20 nm thermal $SiO_2$ as loaded and 400°C anneal showing decrease in peak intensity of O 1s while increase in Ti 2p as a result of metal segregation............. 126
Figure 5.9: HAXPES survey spectra of CoTi on 20nm $SiO_2$ as received and annealed ........................ 128
Figure 5.10: HAXPES Co 2p spectra of CoTi on 20nm $SiO_2$ as received and annealed........................ 129
Figure 5.11: HAXPES Ti 1s spectra of CoTi on 20nm $SiO_2$ (a)as received with Single sate $TiO_2$ and metallic Ti (b) 300ºC anneal show decrease in metallic Ti signal and (c) 500ºC annealed showing formation of Ti silicate at high temperature ..................................................................................... 130
Figure 5.12: HAXPES Si 1s spectra of CoTi on 20 nm $SiO_2$ (a)as received showing $SiO_2$ and bulk Si along with sub-oxide(b) 300ºC anneal show formation of Ti silicate and (c) 500ºC annealed showing evolution of Ti silicate on high temperature anneals ....................................................................... 131
Figure 5.13: HAXPES O 1s spectra of CoTi on 20 nm $SiO_2$ (a)as received showing large surface contamination(b) 300ºC anneal show formation of Ti silicate and (c) 500ºC annealed showing evolution of Ti silicate on high temperature anneals ....................................................................... 132
Figure 5.14: HAXPES C 1s spectra of CoTi on 20 nm $SiO_2$ (a)as received sample showing evidence of metal carbonate (b) 300ºC anneal and (c)500ºC show no metal carbonate signal while a large carbon content is present ............................................................................................................. 133
Figure 5.15: XAS spectra of CoTi (a) normalised Co K-edge before and after annealing (b) first derivative of Co K-edge before and after annealing......................................................................... 135
Figure 5.16: XAS spectra of CoTi (a) normalised Ti K-edge before and after annealing (b) first derivative of Ti K-edge before and after annealing .......................................................................... 135

# List of tables

Table 3.1: Chemical composition of (i) nitrogen incorporated film - as loaded (Normal emission and 60$^o$ off normal) and annealed to 400 °C (ii) Chemical composition of manganese metal film - as loaded (Normal emission and 60$^o$ off normal) and annealed to 400°C ..... 67
Table 3.2: Curve fitting parameters for Mn 2p spectra ..... 70
Table 3.3: curve fitting parameters for N 1s spectra ..... 73
Table 3.4: Curve fitting parameters for C 1s spectra ..... 74
Table 3.5: Curve fitting parameters for Si 2p spectra ..... 76
Table 3.6: curve fitting parameters for Si 2p on all 3 substrates ..... 77
Table 3.7: curve fitting parameters for Si 2p on all 3 substrates after anneal ..... 78
Table 3.8: curve fitting parameters for Si 2p before anneal on sample with and without degas ..... 79
Table 4.1: XPS chemical composition of (i) CuTi as received and annealed (ii) CuMn as received and annealed ..... 93
Table 4.2: XPS based calculations of Cu and metal ratios of CuMn and CuTi alloy samples before and after annealing ..... 94
Table 4.3: Curve fitting parameters for O 1s spectra of CuMn sample before and after annealing ..... 98
Table 4.4: Curve fitting parameters for Si 1s spectra of CuMn sample before and after annealing ..... 99
Table 4.5: Curve fitting parameters for Ti 1s of CuTi sample spectra before and after annealing ..... 100
Table 4.6: Curve fitting parameters for O 1s spectra of CuTi sample before and after annealing ..... 101
Table 4.7: Curve fitting parameters for Si 1s spectra of CuTi sample before and after annealing ..... 102
Table 4.8: Curve fitting parameters for C 1s spectra of CuTi sample ..... 104
Table 5.1: Fitting parameters utilized for Si 2p of 5nm $SiO_2$ sample after Ti deposition ..... 116
Table 5.2: Fitting parameter used for curve fitting Si 2p of native oxide sample ..... 119
Table 5.3: Fitting parameters used in Si 2p spectra of SoG sample curve fitting ..... 121
Table 5.4: Ratio of Co and Ti in CoTi sample before and after annealing ..... 127
Table 5.5: XPS Chemical composition of CoTi sample before and after various anneals ..... 127
Table 5.6: Curve fitting parameters of Ti 1s for $TiO_2$ and Ti silicate peak component ..... 130
Table 5.7: Curve fitting parameters of Si 1s spectra of CoTi sample ..... 131
Table 5.8: O 1s fitting parameters of CoTi alloy sample before and after anneal ..... 132
Table 5.9:Curve fit parameters for C 1s spectra of CoTi sample ..... 133

# List of Publications arising from this work:

1. On the use of (3-trimethoxysilylpropyl) diethylenetriamine self-assembled monolayers as seed layers for the growth of Mn based copper diffusion barrier layers; A Brady-Boyd, R O'Connor, S Armini, **V Selvaraju**, G Hughes, J Bogan; Applied Surface Science 427, 260-266

2. Investigation of nitrogen incorporation into manganese based copper diffusion barrier layers for future interconnect applications
   **V.Selvaraju**, A.Brady-Boyd, R.O'Connor, G.Hughes, J.Bogan, Surfaces and Interfaces Volume 13, December 2018, Pages 133-138

3. Synchrotron radiation study of metallic titanium deposited on dielectric subtrates
   Justin Bogan*,* **Venkateswaran Selvaraju***,* Anita Brady-Boyd*,* Greg Hughes*, and* Robert O'Connor
   Journal of Vacuum Science & Technology B **36**, 040602 (2018)

4. Title: "Nucleation and Adhesion of ultra-thin Copper films on amino-terminated Self-Assembled Monolayers"
   J.Bogan, A.Brady-Boyd, S.Armini, R.Lundy, **V.Selvaraju**, R.O'Connor
   Applied Surface Science Volume 462 (2018), Pages 38-47

**Conference Papers**

1. Investigation of nitrogen incorporation into manganese based copper diffusion barrier layers for future interconnect applications
   **V.Selvaraju**, A.Brady-Boyd, R.O'Connor, G.Hughes, J.Bogan
   **Best Poster** award at **Materials for Advanced Metallization (MAM) 2017** held at Dresden during March 27- 29, 2017.

2. Synchrotron radiation study of titanium deposited on dielectric substrates
   Justin Bogan*,* **Venkateswaran Selvaraju***,* Anita Brady-Boyd*,* Greg Hughes*, and* Robert O'Connor
   Poster presentation at IOP Ireland spring conference 2018 held at Limerick, Ireland.

3. Characterisation of Electroless Deposited Cobalt by Hard and Soft X-ray Photoemission Spectroscopy
   A. Brady-Boyd, R. O'Connor, S. Armini, **V. Selvaraju**, G. Hughes and J.Bogan
   IEEE nano 2018 held Tyndall National Institute, Cork, Ireland

# Abstract

This thesis focusses on the investigation of the suitability of Mn and Ti based self-forming barriers for future generation of interconnects on both thermally grown $SiO_2$ and low-k dielectrics. The self-forming barriers chemically interact with the insulating substrate forming diffusion barriers upon annealing and this fabrication approach has potential application in future generations of interconnect technologies as the resultant barriers can be significantly thinner than the conventional deposited barrier layers. The principle in situ characterisation techniques used to study the interface chemistry resulting from the interaction of deposited films with the insulating substrates were soft and hard x-ray photoelectron spectroscopy (XPS and HAXPES). Secondary Ion Mass Spectroscopy (SIMS) measurements provided information on the structure of the barrier layers which could be correlated with the XPS results while the electrical measurements (four-point probe and CV measurements) helps in studying the feasibility of the self-forming barriers. Comparison of Mn based diffusion barriers with and without the incorporation of nitrogen in the film showed that the introduction of nitrogen improved the adhesion of the copper to the dielectric while chemically both had similar interfaces. Cu based alloy films of Mn and Ti were prepared and analysed and showed that both alloying elements improve the adhesion and electrical characteristics compared to pure copper films. However, while Mn forms a dielectric barrier of manganese silicate, ultra-thin films of Ti on $SiO_2$ based dielectrics showed the preferential formation of titanium silicide. Thick cobalt/titanium alloy films were also investigated as a potential interconnect and showed the possibility of using a cobalt based alloy as a replacement for copper and barrier stack for future generations of interconnects.

# 1.Introduction

Gordon Moore, co-founder of Fairchild Semiconductor and Intel, made one of the most famous and important technological observations in semiconductor history[1]. In 1965, he noted that the number of transistors in an integrated circuit (IC) doubles approximately every two years and he asserted this rate of growth would continue for at least another decade. Afterwards, the forecast period has been extended for future transistors and IC manufacturing and his statement is referred to as Moore's law and is shown in the figure 1.1 below.

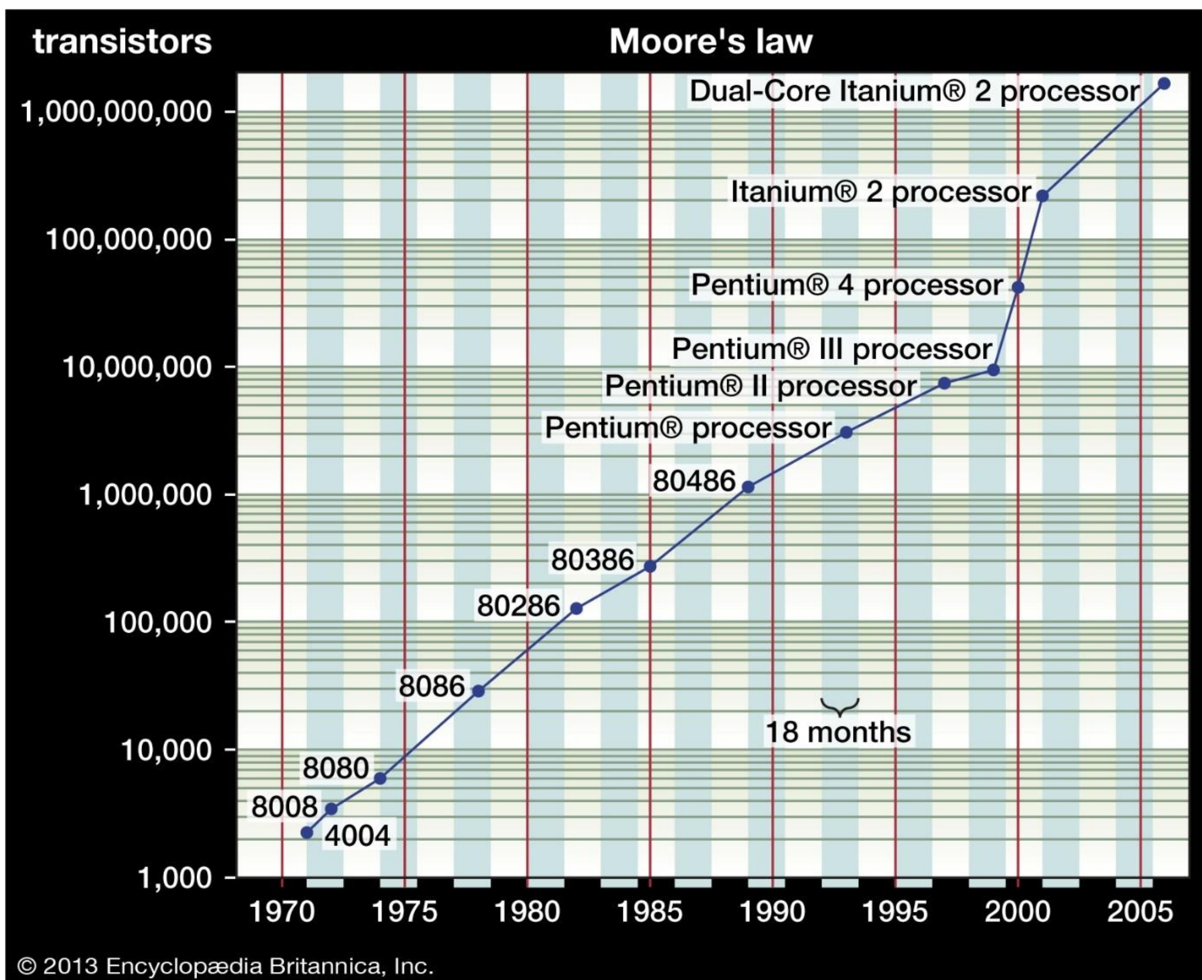


Figure 1.1: Moore's law applied to Intel microprocessors[2]

Moore's law has driven the semiconductor industry to produce integrated circuits (ICs) of smaller size down to transistor gate lengths of 22 nm and 14 nm[3] with a modern microprocessor containing several billion transistors. According to a recent report from the International Technology Roadmap for Semiconductors (ITRS), transistors could get to a point where they could shrink no further by as soon as 2021[4]. It will be no longer economically viable to make them smaller, finally putting an end to Moore's law. In theory, they will reach prohibitive costs and it will be impossible to continue on this path.

The other limitations in doubling the number of transistors include inevitable generation of heat that is unavoidably generated when more and more silicon circuitry is jammed into the same small area, high source to drain leakage current, limited gate material systems resulting in response time delay. So, for the projection of Moore's law to continue and also to have the transistor size further reduced, research is being undertaken on materials, their growth and the development of new fabrication techniques.

## 1.1 Various components of ICs and Issues in scaling:

A typical IC cross sectional image is shown in figure 1.2. It can be divided into three broad regions - Front-end-of-the-line (FEOL), Back-end-of-the-line (BEOL) and advanced packaging contacts.

FEOL is the part where the active individual transistors components are present while Back-end-of-the-line starts from the first layer of metal deposited to connect various active components together. It extends up to several levels including insulating layers, bonding sites and ends at contacts for packaging.

One of the main issues with scaling is response time delay[5]. As the size of the transistor node goes down, time delay increases and in sub 20nm nodes, the time delay due to the BEOL components dominates than the FEOL components as graphically shown in fig 1.3.

Figure 1.2: Schematic of modern ICs showing various components and Cu interconnects connecting them [4]

The previous generation of interconnects used Al interconnect with $SiO_2$ dielectric (Indicated by blue line in plot). As the time delay due to interconnect dominated more than that of the gate oxide, Cu was introduced as the alternate interconnect metal. On further scaling, the barrier stack was ineffective in preventing copper diffusion on scaling below 5nm and hence the total resistivity of the barrier/interconnect stack increases. So, in less than 10nm nodes (indicated by red line in plot), the RC time delay due to the BEOL increases and a new barrier/interconnect stack as well as a low-κ dielectric was required to reduce the RC time delay.

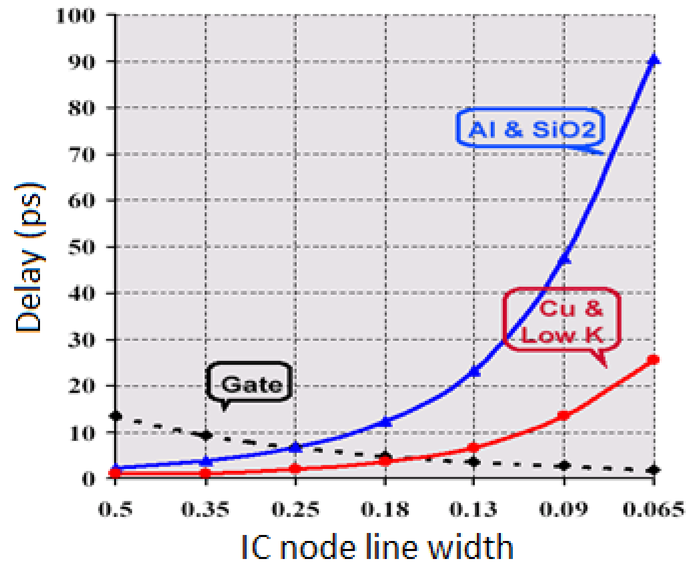


Figure 1.3: Comparison of response time delay due to gate oxide and interconnects [6]

Back-End-of-the-Line (BEOL) generally consists of metal interconnects, insulating layers and contacts for packaging sites. From the figure 1.2, it is observed that a high percentage of the BEOL of the IC is made up of interconnects and the surrounding inter layer dielectrics (ILDs). Hence suitable interconnect and ILD material systems are required for better functioning and reduced time delay of the IC.

The general requirements of a BEOL interconnect material is:

- Low resistivity
- Resistance to electro-migration
- Low capacitance
- Ease of fabrication
- Stability during manufacturing processes
- Good adhesion to insulator and other surrounding layers
- Good electrical contacts

Originally aluminium was used as the interconnect material of choice due to its relatively high conductivity and good adhesion properties to dielectric materials. But as the number of transistors increase in the microprocessor, the interconnect dimensions had to be shrunk so a metal with higher conductivity was required. The integration of copper into interconnect fabrication has been challenging due to the tendency of copper to diffuse into

the surrounding insulator layers, which are generally composed of mainly silicon dioxide based materials causing reliability issues and degradation of the electrical properties of the IC. Regardless of the disadvantages, introduction of copper as interconnect metal increased the performance of the devices in the front-end-of-line (FEOL).

## 1.2 Requirement of Diffusion barrier for copper interconnects

Electromigration is the phenomenon of momentum transfer between conduction electrons and metal ions which make up the structure of the interconnect material. In particular, when the current passes through a conductor, the electrons moving from one end to the other end, can collide and transfer some of their momentum to the metal atoms which can gradually move at high currents. Cu atoms exhibit high electromigration[6][7] causing a void within the metal lattice thereby leading to the failure of the interconnect. Hence there was a need for new methods of preventing diffusion of copper into the ILD materials. A typical electromigration of metal lattice at high current density and the corresponding void formation in the lattice is shown below.

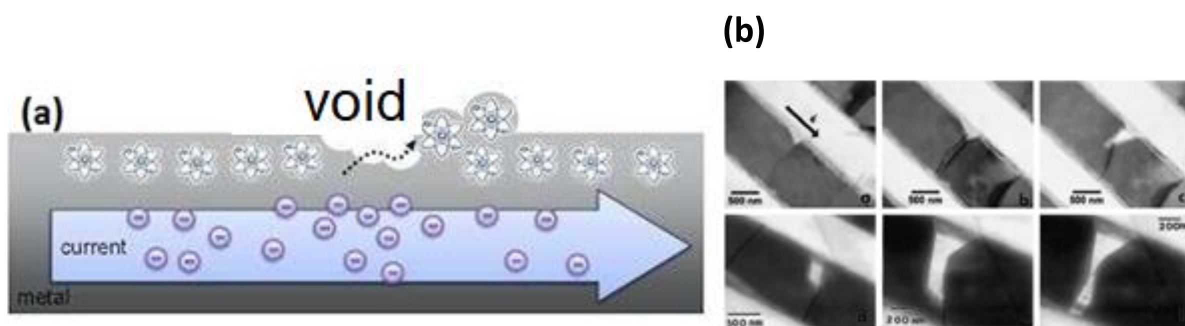


Figure 1.4: (a) electro migration of the metal creating a Void in metal lattice[8] (b) SEM image of the voids in ULSI Cu interconnect system [9]

Diffusion barriers are material systems used for the sole purpose of preventing copper diffusion at the copper/dielectric interface. Among the material systems used, tantalum has shown excellent properties as a diffusion barrier[10][11][12]. A typical diffusion barrier stack with a Cu interconnect layer is shown in figure 1.4. Although the diffusion issues were addressed, issues arose due to adhesion of interconnect metal and the barrier to the ILD

surface. Eventually a stack of Ta/TaN was introduced to solve both the diffusion and adhesion issues. TaN acts as a barrier while Ta metal provides a better adhesion for copper to the barrier layer.

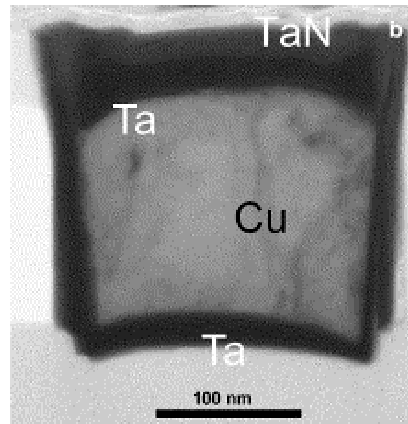


Figure 1.4: Current Ta/TaN copper diffusion barrier layer structure

## 1.3 RC Time Delay

The resistance-capacitance (RC) time delay is defined by the equation,

$$\tau = R.C \qquad (1.1)$$

Where τ is the response time, R is the resistance of the interconnect and C is the capacitance of the interlayer dielectric material. For a better response time, we should have a low resistance as well as low capacitance for the interconnect and ILD systems, respectively. As the size of the transistor shrinks so does the size of the interconnects. As the resistance of the interconnect is given by the equation,

$$R = \frac{\rho \, . \, L}{A} \qquad (1.2)$$

where A = w x h

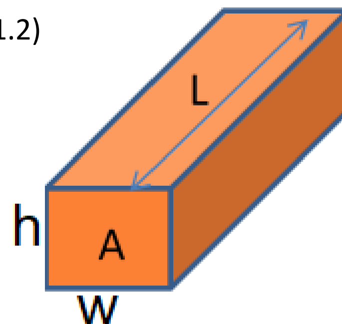


Figure 1.5: Resistance in copper interconnect lines

From equation 2, the smaller the cross-sectional area (A) of interconnect, the greater the resistance which in turn increases the power consumption in the line. As the size of the transistors decrease, so do the volume of the interconnects and consequently requires a decrease in thickness of the diffusion barrier stack for better efficiency of transistors.

## 1.4 Requirement for alternate diffusion barrier layers

As the size of the interconnect decreases an additional requirement is that the size of the required barrier layers also reduces to maintain dimensional scaling. Below 5 nm line width of the IC nodes, the effectiveness of the Ta/TaN barrier/adhesion stack decreases in preventing copper diffusion. So, a different barrier layer has to be introduced to replace Ta/TaN at very low thickness in the range of less than 2-3 nm as the interconnect thickness will be reduced further in future technology nodes. The barrier layer must be uniform as well as conformal and preferably can be deposited by currently available techniques for ease of fabrication. Ideally the metal-barrier resistivity should be less than that of aluminium (2.8μΩ cm). Therefore, there is a need to develop new scalable barrier layer solutions for future interconnects geometries

### 1.4.1 Manganese nitride-based copper diffusion barriers

From equation 2 it can be stated that by having a larger cross section area of the copper interconnect, the resistance of the interconnect line can be reduced resulting in reduced time delay. One of the methods is to reduce the thickness of the barrier stack by having a single layer acting as both a diffusion barrier as well as an adhesion liner for copper.

Traditionally, metal nitrides have been used as an adhesion buffer layer for interconnects on the barrier metal (TiN/ Ti stack for Al interconnect and TaN/ Ta stack for Cu interconnect). While the buffer layer helps in the adhesion, with its presence, the area available for the copper interconnect consequently reduces.

Among the alternative barrier layer materials currently under investigation are manganese based barrier layer systems[13][14][15]. Fabrication approaches involving manganese based barrier layers have shown that upon thermal annealing, the manganese forms manganese silicate at the dielectric interface which has been shown to be a good copper diffusion barrier[16][17]. One of the main challenges with the integration of the copper-manganese system is the adhesion of the copper to the barrier layer/ dielectric stack. As mentioned above, in previous technology nodes, the incorporation of nitrogen into metallic barrier layers has been shown to improve adhesion[18][19]. Following this trend of metal-nitrides as the buffer layer for adhesion of the metal, manganese nitride has gained some interest as a potential buffer layer for manganese-based barriers.

Early work on the formation of manganese nitride involved the use of bulk powders prepared by treating pure manganese in an ammonia atmosphere at high temperatures (>1000°C)[20]. This approach to forming manganese nitride was aimed at forming thick films, and the temperatures involved are beyond the thermal budget for BEOL processing. Some efforts to form and characterise manganese nitride thin films involve ion implantation using an ion gun[21]. Liu et al. in their work introduced nitrogen ions to a Cu lattice and deposited manganese which then forms manganese nitride on further treatment[22]. X-ray diffraction (XRD) studies confirm the various phases on thermal treatments but the amount of nitrogen that can be incorporated into the metal lattice was not studied in detail. In any case, the use of an ion gun is largely incompatible with CMOS processing. For incorporation into Ultra Large Scale Integration (ULSI) processes, the deposition of MnN by methods such as Chemical Vapour Deposition (CVD) or Atomic Layer Deposition (ALD) would be desirable.

In this work, we have undertaken a detailed X-ray photoelectron spectroscopy (XPS) analysis of CVD deposited manganese nitride layers to understand the chemical composition and chemical state of manganese and nitrogen (oxidation state, single or multi-phase, etc.). Previous studies on the electrical characteristics of the manganese nitride films showed promising results [23]. Furthermore, we characterised metallic manganese films on the same dielectric substrate in order to better understand the impact of nitrogen from the ion gun on

the chemical interactions within the material system. The surface morphology of the films was studied using atomic force microscopy (AFM) to gauge surface roughness and in particular the impact of nitrogen incorporation on the surface topography. As adhesion is one of the key drivers for nitrogen incorporation, we also qualitatively test whether adhesion is indeed improved by nitrogen by the deposition of a copper layer on top of the Mn and MnN films and subsequent tape test using scotch tape. The strength of adhesion can be determined by the delamination of the films after the tape test. Since numerical values cannot be obtained through this method, this technique is referred to qualitative analysis of adhesion.

### 1.4.2 Self-forming barriers

An alternative solution to achieving a reduced thickness of diffusion barrier layer thickness is by using the so called self-forming barrier technique. The main advantage of self-forming barrier over nitride barriers is, it is useful in addressing some of the issues regarding the conformal barrier layers, scalability and low thickness range of the diffusion barriers. Various methods of self-forming barriers have been explored but the main principle is that a thermal anneal results in the expulsion of an alloying element from a deposited Cu/metal alloy resulting in the element reacting with the dielectric surface to form a stable barrier layer which is few atomic layers thick [24] as shown in figure 1.3 below. This in turn reduces the volume of the barrier layer being deposited directly as the barrier layer forms in the first few atomic layers of the dielectric. As the volume of the interconnect channel occupied by the diffusion barrier is now reduced, there is a greater residual volume available for copper resulting in a decreased resistance and consequently in the related time delay [25][26].

#### *1.4.2.1 Copper based Alloy self-forming barriers*

One of the most widely-explored methods of self-forming barriers is depositing a copper-based alloy with high conductivity element (eg. Mn[27], Ti[28], Ru[29] etc.) and on thermal anneals, the alloying element would segregate to all interfaces due to difference in the diffusivities between the Cu and the alloy metal, forming a metal silicate diffusion barrier

with the dielectric while excess metal at the surface forms a metal oxide which can be later removed with further fabrication processes.

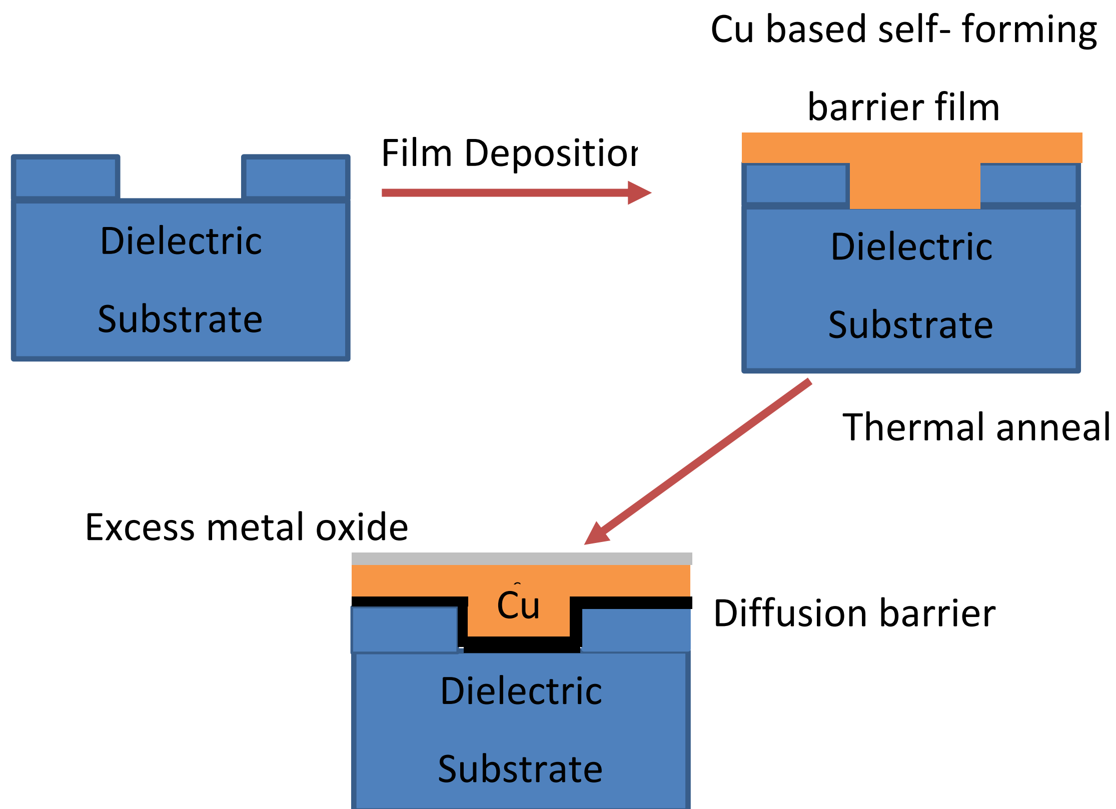


Figure 1.6: Self-forming barrier process overview

At room temperature, the deposited alloy is stable and a thermal anneal causes the segregation of the alloying material from the bulk interconnect line towards all surrounding surfaces of the conducting wire, including the interface between the metal and the inter-layer dielectric. Ideally, as the alloying metal reaches the interface with the ILD, it chemically reacts with the ILD surface to form a stable metal oxide or metal silicate barrier which should act to prevent Cu diffusion into the dielectric layer.

Generally, an alloying material is a suitable candidate to create a self-forming barrier if it has following characteristics:

- prevents any Cu diffusion from the metal line into any surrounding ILD materials;
- promote adhesion between the Cu line and the inter-layer dielectric since the copper has a poor adhesion to any Si based ILD material;

- can form barrier layer thin enough and capable of further scaling in future generations of interconnects [15].

As the alloy is being deposited in a single step instead of sequentially, the stringent thickness constraints for the deposition of sub 10 nm level interconnects can be achieved. Also, there is no need for a separate adhesion buffer layer as the diffusion barrier itself enhances the copper adhesion. As the alloying element segregates, the total resistivity of the self-forming barrier films are found to approach the resistivity of the copper metal thin film[13].

The Cu-Al metal alloy system has been investigated as a potential barrier layer [17]. It has proven to be effective in preventing electromigration Also, aluminium forms aluminium oxide with commonly used $SiO_2$ based dielectrics in IC manufacturing, thereby forming a highly insulating diffusion barrier. As the desirable factor in future interconnects is reducing the resistivity of the barrier stack, Al as an alloy metal with copper is not suitable for future diffusion barrier applications.

The recent studies have focused on the manganese based diffusion barrier system which has potential as a self-forming barrier composed of manganese silicate [24][30] which has proven to be a good copper diffusion barrier. Although, manganese silicate tends to be insulating ($\kappa$=5.4), the barrier is scalable to the required thickness by adjusting the temperature of the segregation anneals.

Another candidate for the alloying metal is titanium [31][32][28]. Titanium, upon deposition on $SiO_2$, preferentially forms titanium silicide and does not prevent copper diffusion as copper forms copper silicide [33] at industrial processing conditions. But alloy properties of titanium with copper completely differs to that of pure Ti deposition. Also, previous generations of interconnects using titanium in the diffusion barrier stack helped in integration with well-established IC fabrication processes.

In the current work, ultra-thin (10nm – 20nm) alloys of Cu with Mn and with Ti (20 atomic %) were sputter deposited onto 20 nm thermal $SiO_2$ which was grown on a silicon substrate. The chemical interactions between the deposited films and the $SiO_2$ surface were investigated by a range of spectroscopic techniques as a function of thermal anneal. Thicker alloy layers of Cu/Mn and Cu/Ti were deposited under identical conditions to fabricate MOS capacitors which were characterized by electrical measurements. A standard reference of pure Cu was deposited under similar conditions and the alloys films were compared with the Cu reference for effectiveness of the barrier layer as a function of thermal anneal.

## 1.5 Requirement for an alternate interconnect metal

The resistance of the Cu interconnect rapidly increases with the decrease in size of IC nodes and approaches unacceptably high values for sub-10 nm nodes as shown in the figure 1.6 below. Despite bulk resistivity being low, resistance of the Cu interconnect line rises rapidly on scaling as a result of increased electron scattering from small Cu grains and diffusive surfaces [34]. The need for a thick, and often highly resistive Cu barrier layer further reduces the volume available for Cu metal and increases Cu line resistance. Thinner alternative Cu barrier materials and their effect on Cu are being explored to extend Cu for BEOL[27] [35]. However, at future nodes Cu interconnects will become increasingly difficult to meet both line and via resistance technology targets with reliability. Thus, increased efforts in exploring Cu replacements [36] such as graphene [37] and cobalt (Co) for vias [38] as well as interconnects [39] continue to rise.

Although, Co is a possible candidate for both vias as well as BEOL interconnect, the resistivity of the Co line is reported to be around 30 μΩcm [41] for a 5 nm thick film which is much higher than the comparable value for copper (1.7E-8 Ωm). However, as Co does not require a discrete barrier layer its elimination results in a larger fill volume for the Co which helps in compensating for the increase in the resistivity of the Co interconnect lines. A decrease in resistivity of 30% has been reported for Co contact nodes and vias for future technology nodes [42][43].

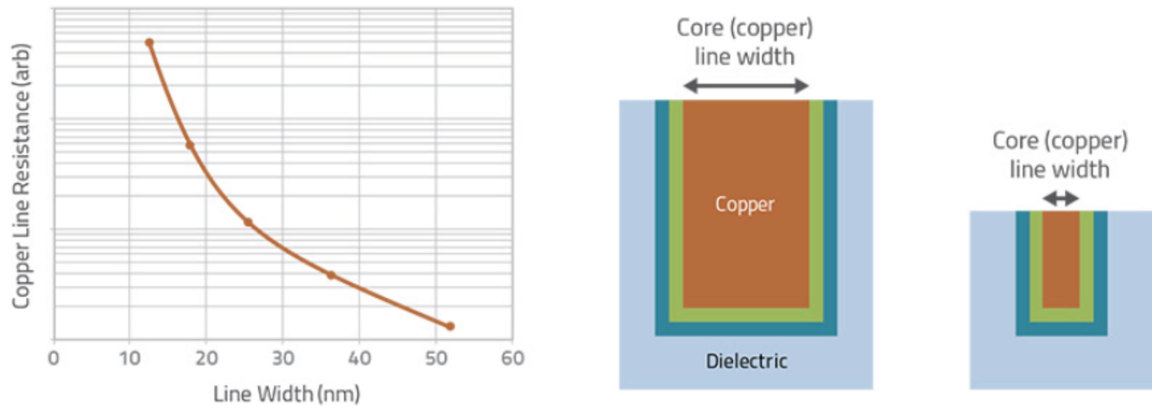


Figure 1.7: Changes in copper line resistance with decrease in line-width of IC node[40]

Another issue with using Co is that it needs an adhesion liner material. One of the potential candidates for this is an alloy of Cobalt rich CoTi configured as a self-forming liner/barrier. CoTi is reported to have a good adhesion, low resistivity and good barrier properties[44] for Cu on $SiO_2$.

In this work, an ultrathin (10nm – 20 nm) alloy film of CoTi (20% Ti) is deposited upon $SiO_2$ films and spectroscopic techniques are used to determine the chemical interactions at the interface of the alloy and substrate and the effect of vacuum annealing is analysed. To compare the effect of alloy deposition to a pure metallic Ti deposition on $SiO_2$, a highly controlled e-beam deposition of ultra-thin Ti films was undertaken on a similar substrate and the interface chemical interactions were investigated as a function of deposition and anneal.

## 1.6 Alternate Substrate dielectric materials

As discussed earlier, the response time delay not only depends on the resistance of the interconnect line, but also on the capacitance of the ILDs. The most commonly used ILD material is silicon dioxide ($SiO_2$) which has a dielectric constant of 3.9. As the scaling of the IC devices continues, there is a need for low – κ dielectric in order to reduce the RC time delay by reducing the parasitic capacitance of the ILDs.

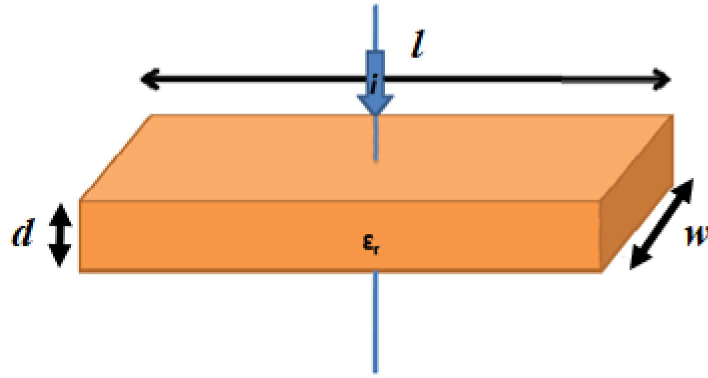


Figure 1.8: Basic structure of a capacitor

Capacitance of a dielectric can be defined as:

$$Capacitance\ C = \varepsilon_0\ \varepsilon_r\ \frac{A}{d} \quad (3)$$

where $\varepsilon_0$ is the permittivity of the free space and $\varepsilon_r$ is the relative permittivity of the dielectric, A and d, are the area and thickness of the dielectric, respectively. From the equation, we can see that A and d are constrained due to the desired size of the transistor node and the only parameter that can be adjusted to reduce the parasitic capacitance is the relative permittivity of the material. Relative permittivity of the dielectric, also known as the dielectric constant of the material can be defined as the ratio of total permittivity to the permittivity of the free space.

$$Dielectric\ constant\ \kappa = \frac{\varepsilon}{\varepsilon_0} \quad (4)$$

Here, $\varepsilon$ is the total permittivity, while $\varepsilon_0$ is the permittivity of free space. Dielectric constant is helpful in defining the polarizability of the given dielectric and also how fast the capacitive switching is possible.

One of the disadvantages of decreasing the substrate capacitance is the decrease in eleasticity of the material thereby producing integration challenge and as a result leads to reliability, stress, adhesion and packaging issues[45]. The following graph shows the possible

κ-values with introduction of carbon doped glasses which are widely researched as a replacement for existing $SiO_2$ substrate.

Fig 1.9 shows dielectric constants of various dielectrics including carbon doped glasses. The effectiveness of the dielectric reliability is usually tested using the technique time dependant dielectric breakdown (TDDB). The reliability testing, modelling and simulation carried out by semiconductor manufacturing industries using TDDB, shows that the dielectrics with dielectric constant of less 2.5 is required in 32nm nodes and below [3].

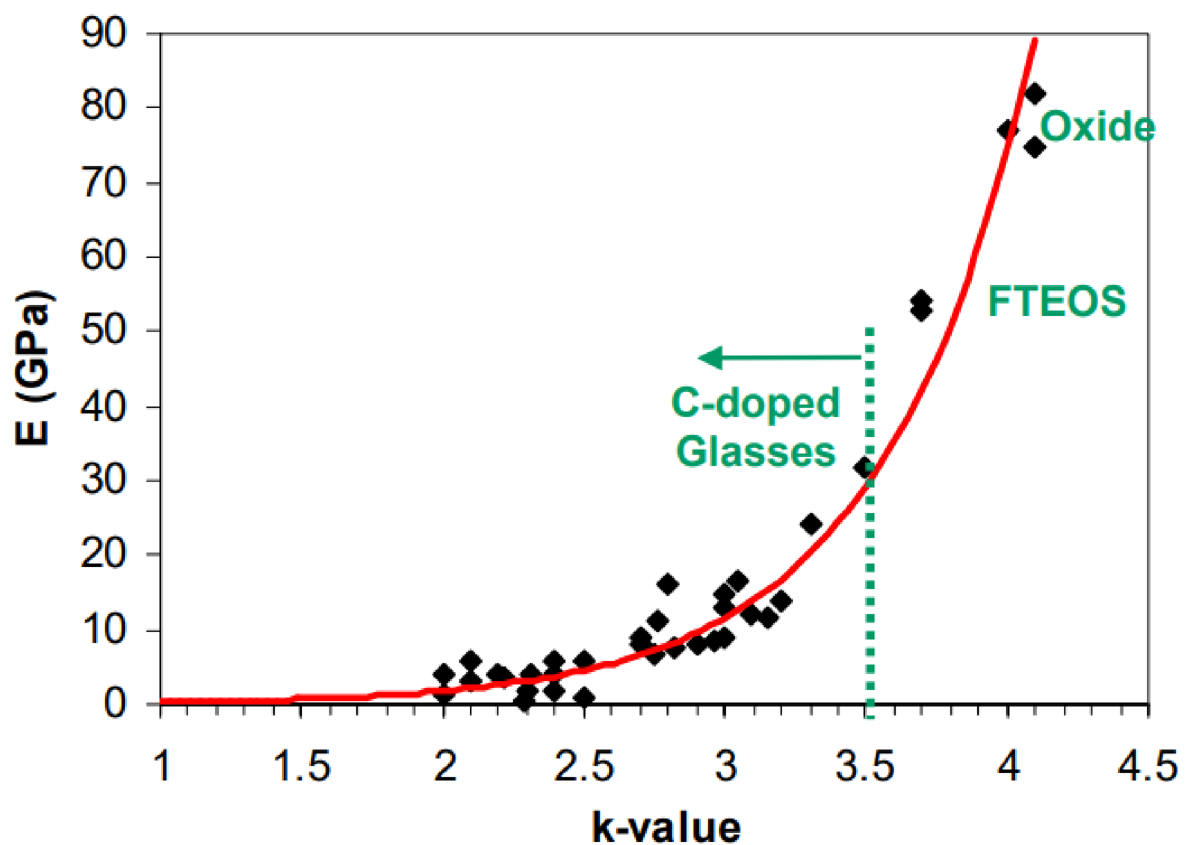


Figure 1.9: graph of change in elasticity with dielectric constant (κ) in carbon doped glasses

A common way to develop a low – κ dielectric is by introducing carbon into the lattice resulting in reducing the polarity of the Si – O bonds and consequently the dielectric constant [46]. The most commonly investigated low – κ dielectric materials are the carbon doped oxides (CDOs) where some of the Si – O bonds are replaced by Si – $CH_3$ bonds. The structure of a carbon doped oxide is shown below:

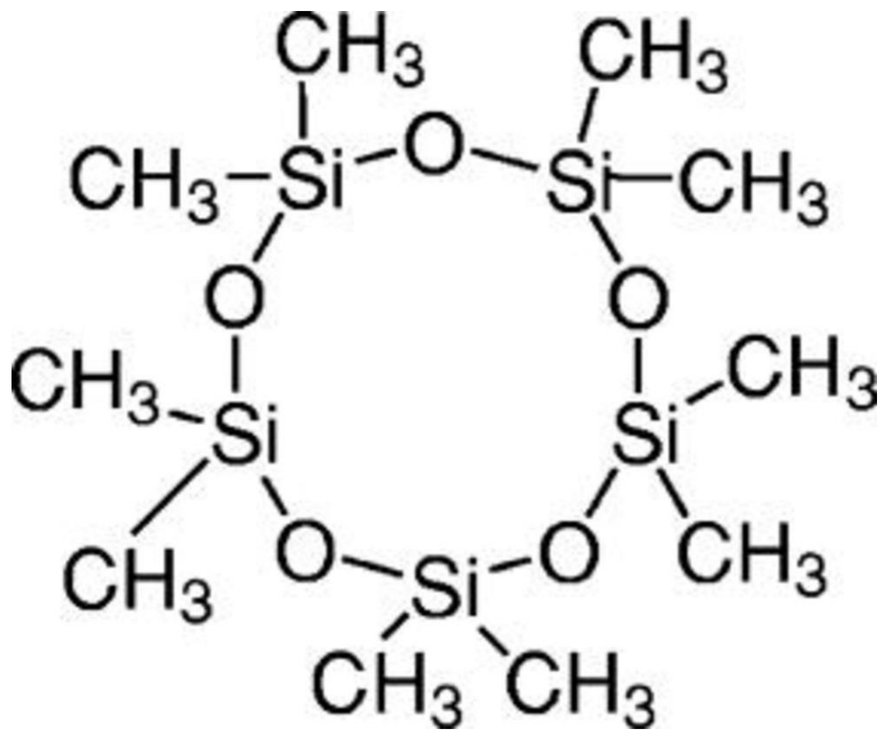


Figure 1.10: Chemical structure of a CDO based dielectric[47]

Another technique used to reduce the dielectric constant is by introducing porosity into the dielectric structure [48]. Figure 1.10 displays a schematic structure of a porous CDO substrate where the presence of voids reduces the dielectric constant of the material. One of the techniques generally used for depositing a porous substrate is through dip coating where the substrates were introduced into porogen solutions for few hours and then the substrates were baked to remove the solvent. Although, introducing porosity is efficient in reducing the dielectric constant, reliability issues arise due to the leakage at pores as well as diffusion of any barrier layer material and copper into this porous structure[49][50]. There are frequently manufacturing difficulties with these materials as the presence of voids reduce the Young's Modulus making these materials more susceptible to failure[51]. In order to effectively use the porosity further treatments like pore sealing has to be done before the fabrication process.

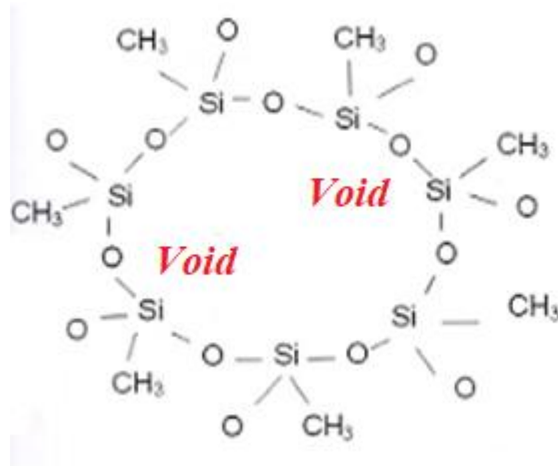


Figure 1.11: Structure of a porous CDO substrate

In this work, a prototype spin-on-glass (SOG) substrate manufactured by IMEC with a dielectric constant of ~2.2 and a carbon content of 24% was used in the analysis of ultra-thin Ti deposited films by chemical spectroscopic techniques.

## 1.7 Thesis Overview

Chapter 2 describes the theory and working principles of the experimental techniques used in this thesis. The main technique used is photoelectron spectroscopy (both conventional X-ray Photoelectron Spectroscopy (XPS) and the high-energy variant Hard X-ray Photoelectron Spectroscopy (HAXPES). Other techniques used in this work were Secondary Ion mass Spectrometry (SIMS) and X-ray Absorption Spectroscopy (XAS) for the material characterization while Atomic Force Microscopy (AFM) is used for analysing the surface morphology of the samples. Capacitance-Voltage (CV) analysis and four-point probe electrical measurements (FPP) were used to characterize the effectiveness of the diffusion barrier materials while tape test is used to test the adhesion of them to the substrate.

In chapter 3, the effectiveness of introducing nitrogen into metallic Mn films is analysed using XPS for the formation of manganese silicate diffusion barrier while tape testing is used on manganese nitride and metallic manganese to test the adhesion of the films on $SiO_2$ substrates.

Chapter 4 describes the possibility of using copper based alloys (Cu 80%:Mn20% and Cu80:Ti20%) as potential future interconnect solutions with the alloy chemical interactions with dielectric substrates being characterized using XPS, HAXPES and SIMS and also to observed the changes following high temperature anneal. Similar alloy targets are used to fabricate MOS capacitors in the $SiO_2$ substrates to study the electrical characteristics of these devices. A pure copper reference film is deposited using similar conditions and compared with the alloys to assess their effectiveness at preventing diffusion of copper into the dielectric for future interconnect applications.

In chapter 5, the possibility of using Co in future generations of BEOL interconnects is analysed and also the integration of low – κ dielectric as the ILD material. A photoemission study of the deposition of an ultra-thin Ti film on $SiO_2$ and a low – κ dielectric is presented in order to comparatively study the effects of the low-k on the chemical interactions at the interface. An alloy of CoTi (20% Ti) is deposited using sputtering and characterized using HAXPES and XAS as a possible adhesion liner for future Co interconnects.

Chapter 6 summarizes all of the studies undertaken in this thesis and draws overall conclusions based on the work. It also outlines possible future work that could be carried out based on these findings.

# References


[1] G.E. Moore, Cramming more components onto integrated circuits (Reprinted from Electronics, pg 114-117, April 19, 1965), Proc. Ieee. 86 (1965) 82–85. doi:10.1109/N-SSC.2006.4785860.

[2] E. Britannica, No Title, Br. Encycl. (n.d.). https://www.britannica.com/technology/Moores-law/media/705881/68188.

[3] ITRS, International Technology Roadmap for Semiconductors - Interconnect, 2011. http://www.itrs2.net/.

[4] International Technology Roadmap for Semiconductors (ITRS), Beyond CMOS, ITRS. (2015).

[5] Z. Tokei, How to solve the back-end-of-line RC delay problem ?, Semicond. Technol. Process. (2017) 1–8.

[6] J. Lienig, Electromigration and its Impact on Physical Design in Future Technologies, Int. Symp. Phys. Des. (2013) 33–40. doi:10.1145/2451916.2451925.

[7] B. Li, T.D. Sullivan, T.C. Lee, D. Badami, Reliability challenges for copper interconnects, Microelectron. Reliab. 44 (2004) 365–380. doi:10.1016/j.microrel.2003.11.004.

[8] G. Rangarajan, Addressing signal electromigration (EM) in today's complex digital designs, EE Times. (2013). https://www.eetimes.com/document.asp?doc_id=1280370.

[9] C.M. Tan, A. Roy, Electromigration in ULSI interconnects, Mater. Sci. Eng. R Reports. 58 (2007) 1–75. doi:10.1016/j.mser.2007.04.002.

[10] K. Holloway, P.M. Fryer, Tantalum as a diffusion barrier between copper and silicon Tantalum as a diffusion barrier between copper and sincon, Cit. Appl. Phys. Lett. Appl. Phys. Lett. Appl. Phys. Lett. Appl. Phys. Lett. 571 (1990). doi:10.1063/1.104051.

[11] S.I. Nakao, M. Numata, T. Ohmi, Thin and low-resistivity tantalum nitride diffusion barrier and giant-grain copper interconnects for advanced ULSI metallization, Japanese J. Appl. Physics, Part 1 Regul. Pap. Short Notes Rev. Pap. 38 (1999) 2401–2405.

[12] Y. Zhao, G. Lu, First-principles simulations of copper diffusion in tantalum and tantalum nitride, Phys. Rev. B - Condens. Matter Mater. Phys. 79 (2009). doi:10.1103/PhysRevB.79.214104.

[13] M. Franz, R. Ecke, C. Kaufmann, J. Kriz, S.E. Schulz, Investigation of barrier formation and stability of self-forming barriers with CuMn, CuTi and CuZr alloys, 2015 IEEE Int. Interconnect Technol. Conf. 2015 IEEE Mater. Adv. Met. Conf. IITC/MAM 2015. 156 (2015) 95–97. doi:10.1109/IITC-MAM.2015.7325640.

[14] S.-M. Chung, J. Koike, Analysis of dielectric constant of a self-forming barrier layer with Cu–Mn alloy on TEOS-SiO[sub 2], J. Vac. Sci. Technol. B Microelectron. Nanom.

Struct. 27 (2009) L28. doi:10.1116/1.3224884.

[15] J.G. Lozano, S. Lozano-Perez, J. Bogan, Y.C. Wang, B. Brennan, P.D. Nellist, G. Hughes, Interdiffusion and barrier layer formation in thermally evaporated Mn/Cu heterostructures on SiO2 substrates, Appl. Phys. Lett. 98 (2011) 1–4. doi:10.1063/1.3569146.

[16] C. Byrne, B. Brennan, A.P. McCoy, J. Bogan, A. Brady, G. Hughes, In Situ XPS Chemical Analysis of MnSiO3 Copper Diffusion Barrier Layer Formation and Simultaneous Fabrication of Metal Oxide Semiconductor Electrical Test MOS Structures, ACS Appl. Mater. Interfaces. 8 (2016) 2470–2477. doi:10.1021/acsami.5b08044.

[17] K. Matsumoto, K. Neishi, H. Itoh, H. Sato, S. Hosaka, J. Koike, Chemical vapor deposition of mn and mn oxide and their step coverage and diffusion barrier properties on patterned interconnect structures, Appl. Phys. Express. 2 (2009) 063503. doi:10.1143/APEX.2.036503.

[18] T.O. Hiroyuki Shimada, Ichiro Ohshima, Takeo Ushiki Shigetoshi Sugawa, Tantalum Nitride Metal Gate FD-SOI CMOS FETs, IEEE Trans. Electron Devices. 48 (2001) 1619–1626.

[19] K. Holloway, P.M. Fryer, C. Cabral, J.M.E. Harper, P.J. Bailey, K.H. Kelleher, Tantalum as a diffusion barrier between copper and silicon: Failure mechanism and effect of nitrogen additions, J. Appl. Phys. 71 (1992) 5433–5444. doi:10.1063/1.350566.

[20] M.D. Lyutaya, a. B. Goncharuk, Manganese nitrides, Sov. Powder Metall. Met. Ceram. 16 (1977) 208–212. doi:10.1007/BF00794089.

[21] Y. Au, Y. Lin, R.G. Gordon, Filling Narrow Trenches by Iodine-Catalyzed CVD of Copper and Manganese on Manganese Nitride Barrier/Adhesion Layers, J. Electrochem. Soc. 158 (2011) D248–D253. doi:10.1149/1.3556699.

[22] X. Liu, B. Lu, T. Iimori, K. Nakatsuji, F. Komori, Self-assembled MnN superstructure, Phys. Rev. Lett. 98 (2007) 1–4. doi:10.1103/PhysRevLett.98.066103.

[23] Y. Sun, C. Wang, Y. Wen, L. Chu, M. Nie, F. Liu, Negative Thermal Expansion and Correlated Magnetic and Electrical Properties of Si-Doped Mn 3 GaN Compounds, J. Am. Ceram. Soc. 93 (2010) 650–653. doi:10.1111/j.1551-2916.2009.03482.x.

[24] J. Koike, M. Wada, Self-forming diffusion barrier layer in Cu-Mn alloy metallization, Appl. Phys. Lett. 87 (2005) 1–3. doi:10.1063/1.1993759.

[25] J. Bogan, A.P. McCoy, R. O'Connor, P. Casey, C. Byrne, G. Hughes, Photoemission study of the identification of Mn silicate barrier formation on carbon containing low-κ dielectrics, Microelectron. Eng. 130 (2014) 46–51. doi:10.1016/j.mee.2014.09.012.

[26] P. Casey, J. Bogan, J.G. Lozano, P.D. Nellist, G. Hughes, Chemical and structural investigation of the role of both Mn and Mn oxide in the formation of manganese silicate barrier layers on SiO2, J. Appl. Phys. 110 (2011) 1–6. doi:10.1063/1.3630123.

[27] Y.K. Siew, N. Jourdan, I. Ciofi, K. Croes, C.J. Wilson, B.J. Tang, S. Demuynck, Z. Wu, H. Ai, D. Cellier, A. Cockburn, J. Bommels, Z. Tokei, Cu Wire resistance improvement using Mn-based Self-Formed Barriers, in: 2014 IEEE Int. Interconnect Technol. Conf. / Adv. Met. Conf. IITC/AMC 2014, 2014: pp. 311–314. doi:10.1109/IITC.2014.6831895.

[28] K. Kohama, K. Ito, Y. Sonobayashi, K. Ohmori, K. Mori, K. Maekawa, Y. Shirai, M. Murakami, Structure analyses of Ti-based self-formed barrier layers, Jpn. J. Appl. Phys. 50 (2011) 04DB03. doi:10.1143/JJAP.50.04DB03.

[29] A.P. McCoy, P. Casey, J. Bogan, J.G. Lozano, P.D. Nellist, G. Hughes, Chemical and structural investigations of the incorporation of metal manganese into ruthenium thin films for use as copper diffusion barrier layers, Appl. Phys. Lett. 101 (2012) 231603–231603. doi:10.1063/1.4769229.

[30] J. Bogan, Growth and chemical characterisation studies of Mn silicate barrier layers on SiO2 and CDO, Dublin City University, 2012.

[31] K. Ito, S. Tsukimoto, M. Murakami, Self-formation of Ti-rich interfacial layers in Cu(Ti) alloy films, Japanese J. Appl. Physics, Part 1 Regul. Pap. Short Notes Rev. Pap. 46 (2007) 1942–1946. doi:10.1143/JJAP.46.1942.

[32] S. Tsukimoto, T. Kabe, K. Ito, M. Murakami, Effect of annealing ambient on the self-formation mechanism of diffusion barrier layers used in Cu(Ti) interconnects, J. Electron. Mater. 36 (2007) 258–265. doi:10.1007/s11664-007-0094-8.

[33] C.A. Chang, C.K. Hu, Reaction between Cu and TiSi2 across different barrier layers, Appl. Phys. Lett. 57 (1990) 617–619. doi:10.1063/1.104249.

[34] J.M. Roberts, A.P. Kaushik, J.S. Clarke, Resistivity of sub-30 nm copper lines, in: 2015 IEEE Int. Interconnect Technol. Conf. 2015 IEEE Mater. Adv. Met. Conf. IITC/MAM 2015, 2015: pp. 341–343. doi:10.1109/IITC-MAM.2015.7325595.

[35] X. Zhang, L. Cao, V. Ryan, P.S. Ho, B. Taylor, C. Witt, C. Labelle, Co Liner Impact on Microstructure of Cu Interconnects, ECS J. Solid State Sci. Technol. 4 (2014) N3177–N3179. doi:10.1149/2.0141501jss.

[36] C. Adelmann, L.G. Wen, A.P. Peter, Y.K. Siew, K. Croes, J. Swerts, M. Popovici, K. Sankaran, G. Pourtois, S. Van Elshocht, J. Bommels, Z. Tokei, Alternative metals for advanced interconnects, in: 2014 IEEE Int. Interconnect Technol. Conf. / Adv. Met. Conf. IITC/AMC 2014, 2014: pp. 173–176. doi:10.1109/IITC.2014.6831863.

[37] I. Asselberghs, M. Politou, B. Soree, S. Sayan, D. Lin, P. Pashaei, C. Huyghebaert, P. Raghavan, I. Radu, Z. Tokei, Graphene wires as alternative interconnects, in: 2015 IEEE Int. Interconnect Technol. Conf. 2015 IEEE Mater. Adv. Met. Conf. IITC/MAM 2015, 2015: pp. 317–319. doi:10.1109/IITC-MAM.2015.7325590.

[38] M.H. Van Der Veen, K. Vandersmissen, D. Dictus, S. Demuynck, R. Liu, X. Bin, P. Nalla, A. Lesniewska, L. Hall, K. Croes, L. Zhao, J. Bömmels, A. Kolics, Z. Tökei, Cobalt bottom-up contact and via prefill enabling advanced logic and DRAM technologies, in: 2015 IEEE Int. Interconnect Technol. Conf. 2015 IEEE Mater. Adv. Met. Conf. IITC/MAM 2015, 2015: pp. 25–27. doi:10.1109/IITC-MAM.2015.7325605.

[39] J. Kelly, J.H.C. Chen, H. Huang, C.K. Hu, E. Liniger, R. Patlolla, B. Peethala, P. Adusumilli, H. Shobha, T. Nogami, T. Spooner, E. Huang, D. Edelstein, D. Canaperi, V. Kamineni, F. Mont, S. Siddiqui, Experimental study of nanoscale Co damascene BEOL interconnect structures, in: 2016 IEEE Int. Interconnect Technol. Conf. / Adv. Met. Conf. IITC/AMC 2016, 2016: pp. 40–42. doi:10.1109/IITC-AMC.2016.7507673.

[40] M. LAPEDUS, Dealing With Resistance In Chips, Semicond. Eng. (2018). https://semiengineering.com/dealing-with-resistance-in-chips/.

[41] M. Wislicenus, R. Liske, L. Gerlich, B. Vasilev, A. Preusse, Cobalt advanced barrier metallization: A resistivity composition analysis, Microelectron. Eng. 137 (2015) 11–15. doi:10.1016/j.mee.2014.09.017.

[42] J.F. Zheng, P. Chen, T.H. Baum, R.R. Lieten, W. Hunks, S. Lippy, A. Frye, W. Li, J. O'Neill, J. Xu, J. Zhu, J. Bao, V. Machkaoutsan, M. Badaroglu, G. Yeap, G. Murdoch, J. Bommels, Z. Tokei, Selective co growth on Cu for void-free via fill, in: 2015 IEEE Int. Interconnect Technol. Conf. 2015 IEEE Mater. Adv. Met. Conf. IITC/MAM 2015, 2015: pp. 265–267. doi:10.1109/IITC-MAM.2015.7325663.

[43] Y. Jiang, P. Nalla, Y. Matsushita, G. Harm, W. Jingyan, A. Kolics, L. Zhao, T. Mountsier, P. Besser, H.J. Wu, Development of electroless Co via-prefill to enable advanced BEOL metallization and via resistance reduction, in: 2016 IEEE Int. Interconnect Technol. Conf. / Adv. Met. Conf. IITC/AMC 2016, 2016: pp. 111–113. doi:10.1109/IITC-AMC.2016.7507700.

[44] M. Hosseini, J. Koike, Amorphous CoTix as a liner/diffusion barrier material for advanced copper metallization, J. Alloys Compd. 721 (2017) 134–142. doi:10.1016/j.jallcom.2017.05.335.

[45] P.R. Besser, Current challenges with copper interconnects, m (2007) 3–12. doi:10.1149/1.2408858.

[46] G. Dubois, W. Volksen, T. Magbitang, R.D. Miller, D.M. Gage, R.H. Dauskardt, Molecular network reinforcement of sol-gel glasses, Adv. Mater. 19 (2007) 3989–3994. doi:10.1002/adma.200701193.

[47] C. Ye, Z. Ning, T. Wang, X. Yu, Y. Wei, X. Qian, Effect of Doping on Structure and Dielectric Property of SiCOH Films Prepared by Decamethylcyclopentasiloxane, J. Electrochem. Soc. 154 (2007) G63. doi:10.1149/1.2430641.

[48] W. Volksen, T.P. Magbitang, R.D. Miller, S. Purushothaman, S. a. Cohen, H. Nakagawa, Y. Nobe, T. Kokubo, G.J.M. Dubois, A Manufacturing Grade, Porous Oxycarbosilane Spin-On Dielectric Candidate with K ≤ 2.0, J. Electrochem. Soc. 158 (2011) G155–G161. doi:10.1149/1.3591081.

[49] F. Lanckmans, K. Maex, Use of a capacitance voltage technique to study copper drift diffusion in (porous) inorganic low-k materials, in: Microelectron. Eng., 2002: pp. 125–132. doi:10.1016/S0167-9317(01)00588-3.

[50] P.-I. Wang, J.S. Juneja, Y. Ou, T.-M. Lu, G.S. Spencer, Instability of Metal Barrier with

Porous Methyl Silsesquioxane Films, J. Electrochem. Soc. . 155 (2008) H53–H58. doi:10.1149/1.2806030.

[51] G. Dubois, W. Volksen, T. Magbitang, M.H. Sherwood, R.D. Miller, D.M. Gage, R.H. Dauskardt, Superior mechanical properties of dense and porous organic/inorganic hybrid thin films, J. Sol-Gel Sci. Technol. 48 (2008) 187–193. doi:10.1007/s10971-008-1776-2.

# 2 Experimental Techniques and Principles

The principal material characterization technique used in this report is X-ray photoelectron spectroscopy (XPS) and its high energy variant Hard X-ray Photoelectron Spectroscopy (HAXPES). Electrical characterization was carried out using four-point probe (FPP) method and capacitance-voltage (CV) probe station at Tyndall National Institute. The surface morphology studies were carried out using the Atomic Force Microscopy (AFM).

## 2.1 Principles of Photoelectron Spectroscopy:

### 2.1.1 X-Ray Photoelectron Spectroscopy

The main technique used in the work is X-Ray Photoelectron Spectroscopy (XPS) and its high energy variant Hard X-ray photoelectron spectroscopy (HAXPES). XPS works on the principle of the photoelectric effect which states that when a photon is incident on a material with energy higher than its work function, photoelectrons are emitted. According to Einstein's photoelectric equation, the kinetic energy of the electron emitted is measured in order to deduce the binding energy of that particular electron using the following equation,

$$E_k = h\nu - E_b \qquad (2.1)$$

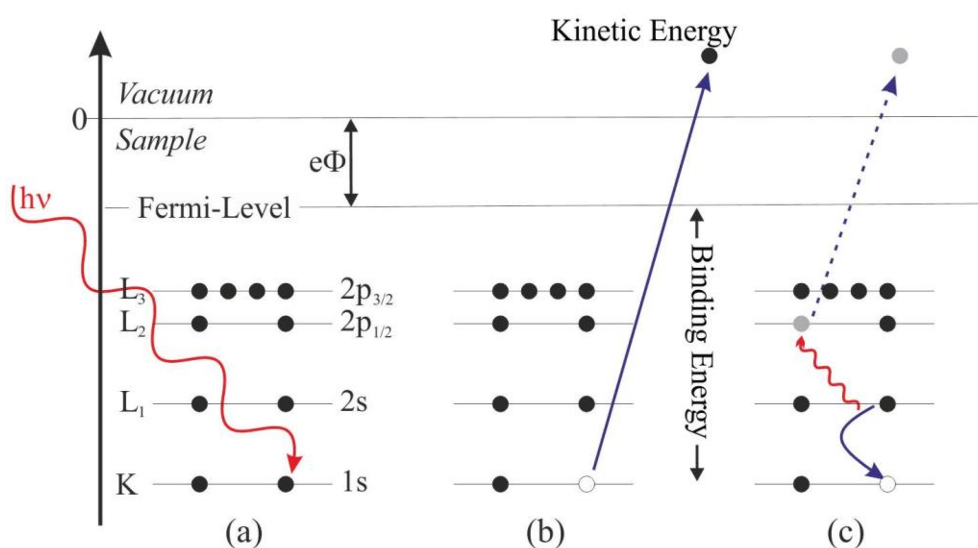


Figure 2.1: principle of photoemission spectroscopy [2]

Here $E_b$ is the binding energy and hv is the energy of the incident photon and KE is the observed kinetic energy of the photoemitted electron as schematically shown in Figure 2.1. The binding energy given by $E_b$ is unique for any energy level so by getting the binding energies from the XPS measurement, we can deduce the chemical composition of a material[1]. Therefore, by analysing the peaks in the XPS spectrum we can get a clear idea of all the elements present in the given material with the exception of hydrogen.

In conducting solids, there is an additional effect of work function is needed to remove the electron from sample surface. Hence the equation (2.1) can be rewritten as

$$E_k = h\nu - E_b - e_{\Phi} \qquad (2.2)$$

where $e_{\Phi}$ is the work function defined as the energy difference between the vacuum level and fermi level as shown in the figure 2.1. Although the work function indicates the energy required to remove the electron from fermi level, during the measurement of the kinetic energy by the spectrometer, the work function due to the spectrometer $\Phi_{sp}$ is significant compared to that of the work function of the sample. This can be illustrated in the figure below:

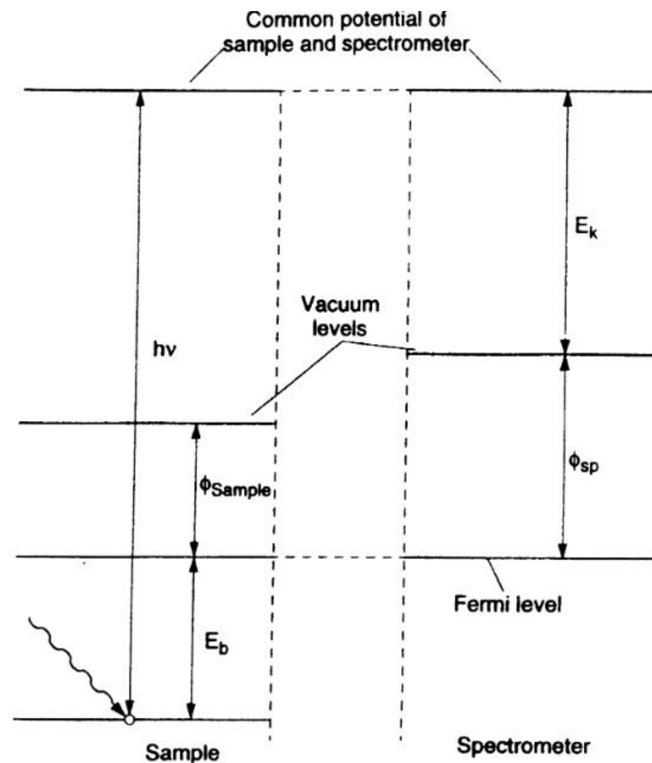


Figure 2.2: Illustration of sample work function and spectrometer work function

Hence final kinetic energy observed by the detector can be determined by the equation 2.2 which can be rewritten as

$$E_k = h\nu - E_b - \Phi_{sp} \qquad 2.3$$

where hν is the incident photon energy, $E_b$ is the binding energy,

With regards to the penetration of the x-ray beam, it is important to note that while the typical penetration depth of a 1 keV photon beam into solid matter is in the order of ~1µm, the escape depth of electrons at this energy is considerably smaller (approximately 10 nm). This difference is due to the fact that photoemitted electrons from deep within the sample interact strongly with matter and may lose kinetic energy via inelastic collisions with other atoms, which can occur within the solid before the photo-excited electrons emerge from the surface. All the photoelectrons emitted from a core level do not reach the analyser with the same kinetic energy. The depth from which majority of the photoelectrons with same kinetic energy, reaches the analyser is generally known as sampling depth of the XPS. Sampling depth typically depends on the mean free path of an electron emitted. Mean free path of an electron is the average distance an electron can travel before a collision losing significant kinetic energy and denoted by λ.

Mean free path depends on the density of the material as electron scattering can occur due to the collisions. Hence, mean free path varies from element to element. A typical mean free path curve of a traditional XPS measurements for various elements with change in the kinetic energy is shown below in fig 2.3.

From the figure above, it can be observed that the mean free path of the resulting photoelectron can be increased by increasing the initial photon energy. This principle forms the basis to the variation of the sampling depth in the traditional XPS and the high energy variant HAXPES.

It also shows that the photoemission measurements are highly surface sensitive meaning that surface contamination should be minimized if possible. Photoemitted electrons which lose energy due to inelastic collisions emerge with random kinetic energy and simply add to the background counts[2]. The XPS technique is sensitive to the presence of almost all elements above atomic concentrations of ~ 0.1 - 1%.

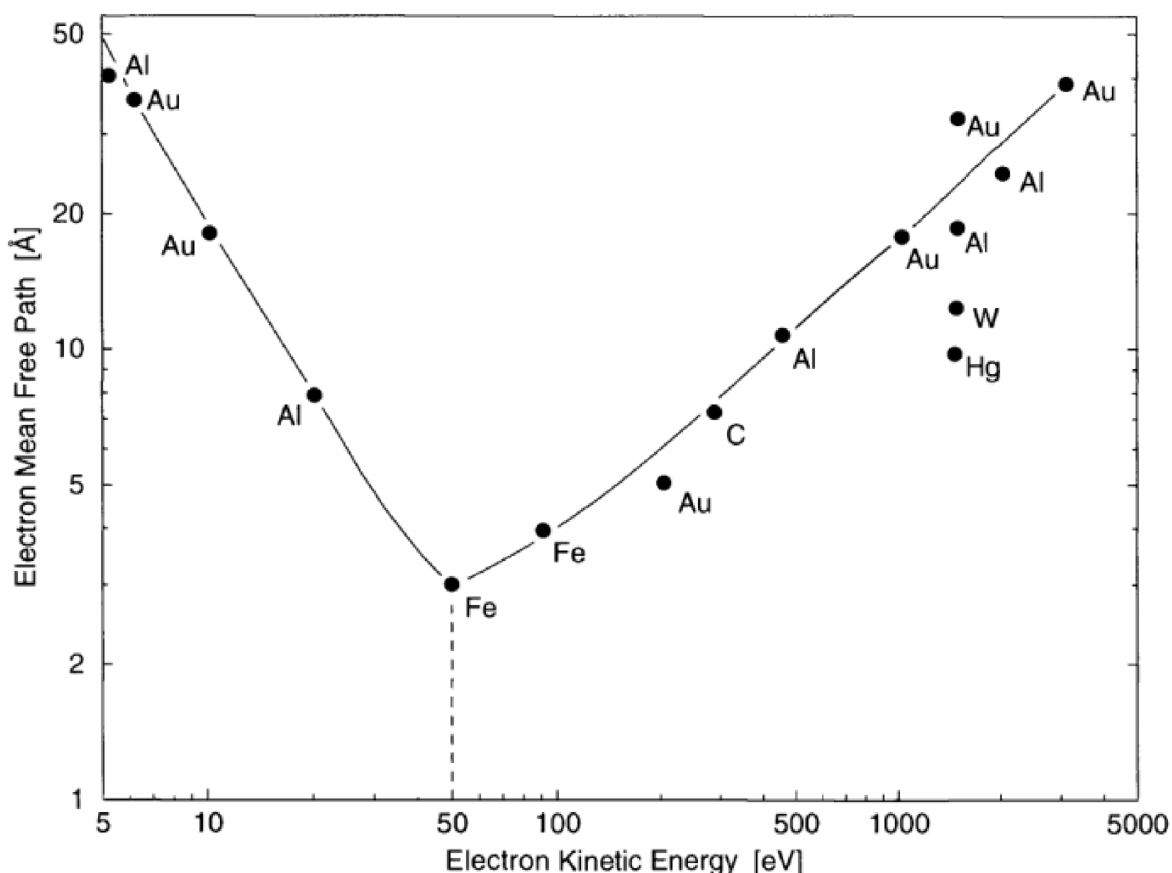


Figure 2.3: dependence of mean free path for various elements with change in the kinetic energy[3]

Upon escaping the sample surface electrons are focussed by a series of lenses, filtered according to kinetic energy using an energy analyser and finally counted by an electron detector. The spectrometer is setup to scan across the different electron energies in order to count and store the number of detected electrons for a given energy for a given detection time. This data is then outputted to an external computer system. The details are discussed later in the chapter.

### *2.1.1.1 Elemental identification:*

XPS is mainly used to identify elements present in the sample being analysed. Generally, a survey scan is carried on each sample and from the photoemission peaks in the spectrum, the elements can be identified by comparison with reference data. Multiple peaks can be attributed to a single element e.g. Ag has 3d, 3p and 3s core levels in the range of conventional XPS photon energy. The photoemission process will cause electrons with specific energies related to the atomic core level binding energies to be emitted. Any electrons that have lost energy increase the level of the background at binding energies higher

than the peak energy. The background is continuous because of the random nature of the loss processes. Any noise in the spectrum is due to the collection of single electrons randomly spaced in time. Similarly, multiple core levels of different elements may overlap in a given energy range and a number of reference texts are available for elemental identification through XPS[4][5]. A typical XPS survey spectrum for the standard gold sample is shown in Figure 2.4 identifying various elements present in on the surface under investigation. Rising above the background we can examine two distinct types of peaks. These are the photoemission peaks associated with core-level events and x-ray induced Auger lines. The most intense photoelectron lines are typically the narrowest lines observed in the spectra and are relatively symmetrical. However, metals exhibit considerable asymmetry due to coupling with conduction electrons. Auger lines are groups of lines caused by the transition of a core level electron to deeper underlying empty energy level which results in the transfer of energy to another bound electron giving it sufficient kinetic energy to be emitted from the surface. These lines can be readily distinguished by changing the energy of the x-ray source as the kinetic energy of the Auger lines will remain the same due to the interaction being dependant on the energy separation of the core levels while the photoemission lines will shift by the energy difference between the Mg and Al x-ray sources.

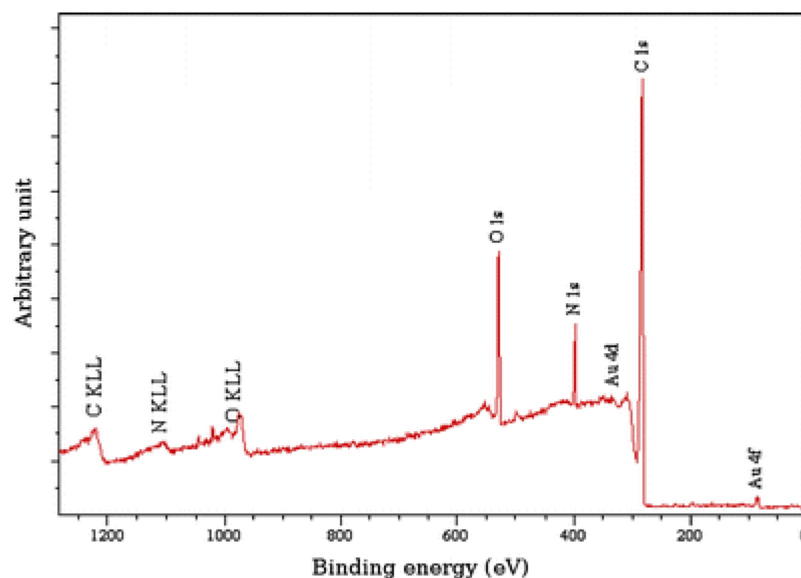


Figure 2.4: Typical XPS survey spectrum for gold standard sample showing different elements present[6]

### *2.1.1.2 Elemental Quantification:*

One of the main analysis that can be carried out from the survey spectrum of using the XPS technique is the relative stoichiometric chemical composition of the elements on surface of a sample by analysing the change in the peak area of core level peaks. In order to quantitatively determine the chemical composition of a surface, the composition needs to be homogenous within the XPS sampling depth. For example, to determine the composition of a thermal silicon dioxide layer on a silicon wafer, it is necessary to remove all the surface carbon contamination and the thickness of the layer has to be greater than the sampling depth. The relative sensitive factors for each element have also to be taken into account as the sensitivity for Si 2p and O 1s are different [7]. The relative binding energies of the two peaks (Si 2p and O 1s) must also be taken into account given that electron IMFP is strongly dependant on kinetic energy. As such, it can be said that electrons emerging from the Si 2p peak (E 99.6 eV) may emerge from a greater depth than O 1s electrons (BE 533 eV). Further factors include the photo-ionisation cross-section of that specific core-level which is the probability that an electron of that core-level will be excited. Finally the transmission function of the analyser which determines the relative sensitivity of the analyser to electrons of different kinetic energies. Based on the factors mentioned above, relative sensitivity factors (RSF) for each core level of an element can be calculated. Using these RSF values, chemical composition can be calculated as follows:

$$I_i = N_i \sigma_i \ \lambda_i \, \mathrm{K} \qquad 2.3$$

where: $I_i$ = intensity of photoelectron peak for element I, $N_i$ = average atomic concentration of element "i" in the surface under analysis $\sigma_i$ = photoelectron cross-section (Scofield factor) for element i, $\lambda_i$ = inelastic mean free path of a photoelectron from element i, K = all other factors related to quantitative detection of a signal (assumed to remain constant during experiment)

### *2.1.1.3 Chemical Shifts:*

In addition to knowing the elemental stoichiometry in any given sample, XPS spectra can provide information on the precise oxidation state of the elements present in the sample.

The charge transfer resulting from chemical bond formation can result in a shift in the binding energy of the elements in a material. This is apparent in an XPS spectrum by the related photoemission peak being located at a binding energy different from the unbonded element. This phenomenon is known as the chemical shift[8].

For example, for elemental silicon the $2p_{3/2}$ core level has the binding energy of 99.1 eV while for the silicon 2p peak in silicon dioxide the binding energy is approximately 103.9 eV as shown in figure 2.5. So, the binding energy shift in the peak position provides information on the oxidation state as the elemental silicon has the oxidation state of 0, whereas silicon in silicon dioxide has the oxidation state of +4. This chemical shift also shows that any silicon sub - oxides having an oxidation state between 0 and +4 will have a binding energy between 99.1 eV and 103.9 eV.

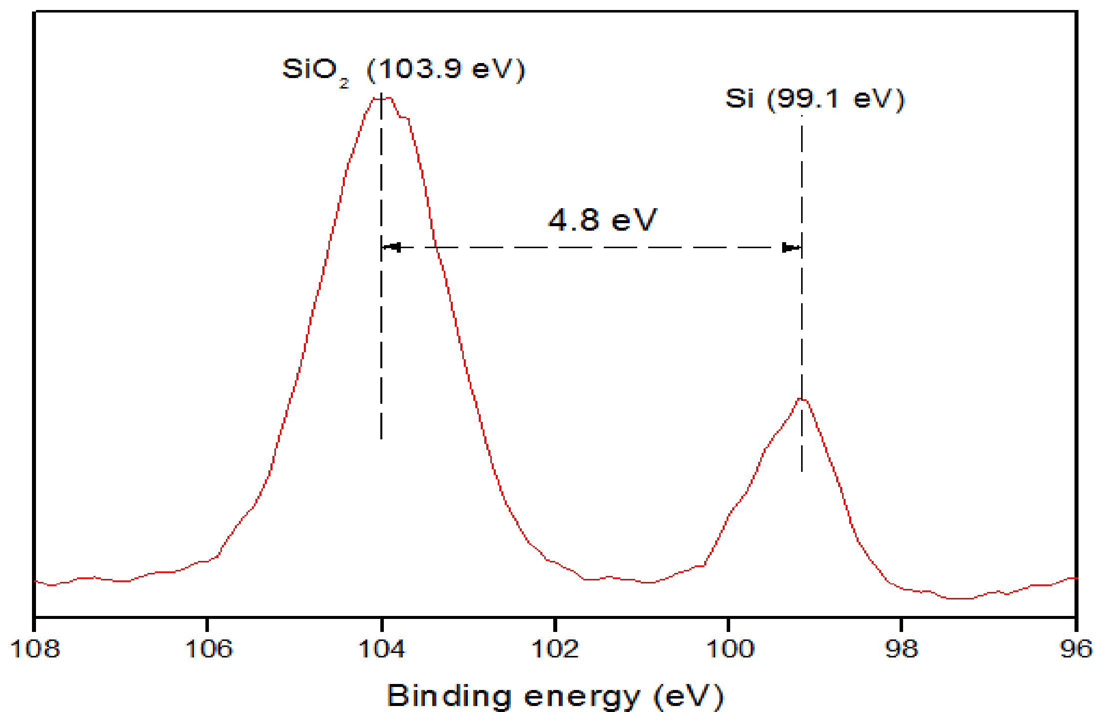


Figure 2.5: Graph showing XPS of Si 2p spectrum for 4.5 nm SiO2 on bulk Si with signals from both substrate (99.1 eV) and overlying oxide (103.9 eV)

Core levels in XPS use the nomenclature $nl_j$ where n is the principal quantum number, l is the angular momentum quantum number and j = l+s (where *s* is the spin angular momentum number and can be ±½). All orbital levels except the s levels (l = 0) give rise to a doublet with the two possible states having different binding energies. This is known as spin-orbit splitting (or j-j coupling). The peaks will also have specific area ratios based on the

degeneracy of each spin state, i.e. the number of different spin combinations that can give rise to the total j. For example, for the 2p spectra, where n is 2 and l is 1, j will be 1/2 and 3/2. The area ratio for the two spin orbit peaks ($2p_{1/2}$:$2p_{3/2}$) will be 1:2 (corresponding to 2 electrons in the $2p_{1/2}$ level and 4 electrons in the $2p_{3/2}$ level). These ratios must be taken into account when analysing spectra of the *p*, *d* and *f* core levels.

At higher binding energy, in some metal spectra like Al, strong satellite peaks might be observed and these satellite peaks can be misinterpreted as primary lines. These transitions can be attributed to the plasmon excitations. These plasmon peaks are associated with energy loss events for electron. In the case of Aluminium, the free electrons are constrained to move within energy bands that are characteristic of the material and these material properties influence the shape of the energy loss distribution, namely, scattering of the photoelectric electrons by free electrons with discrete energy bands produces energy loss distributions with relatively narrow structures. The convolution of an intense photoelectric peak with a relatively narrow energy loss distribution results in plasmon structures that could easily be mistaken for a primary line

#### *2.1.1.4 Peak Widths:*

Instrumental resolution contributes to the Gaussian line width of the peak. For XPS spectra in a narrow energy range (<20 eV) the instrumental resolution is assumed to be constant. The Lorentzian line width component of the peak originates from the core-hole lifetime in the photoemission process. Both the Lorentzian and Gaussian profiles contribute to the peak width and are assumed to be constant for the instrument and the particular element over the narrow energy range used to acquire individual peaks.

Other factors affecting the peak widths are broadening due to satellite peaks, phonon transitions and differential charging of the sample. All these factors might lead to asymmetric peak shape especially in the metallic samples.

For conductive samples, such as metals and graphite, there is a distribution of unfilled one-electron levels (conduction electrons) that are available for shake-up like events following core electron photoemission. When this occurs, instead of a discrete structure like

that seen for shake-up satellites, a tail on the higher binding energy side of the main peak – an asymmetric peak shape is evident. An example of this is shown in Figure 2.6. It is clear from this figure that the asymmetric tail of the metal peak shape will overlap with higher oxidation state species. As such it is important that the total photoelectron yield contribution from the metal is captured during curve-fitting analysis.

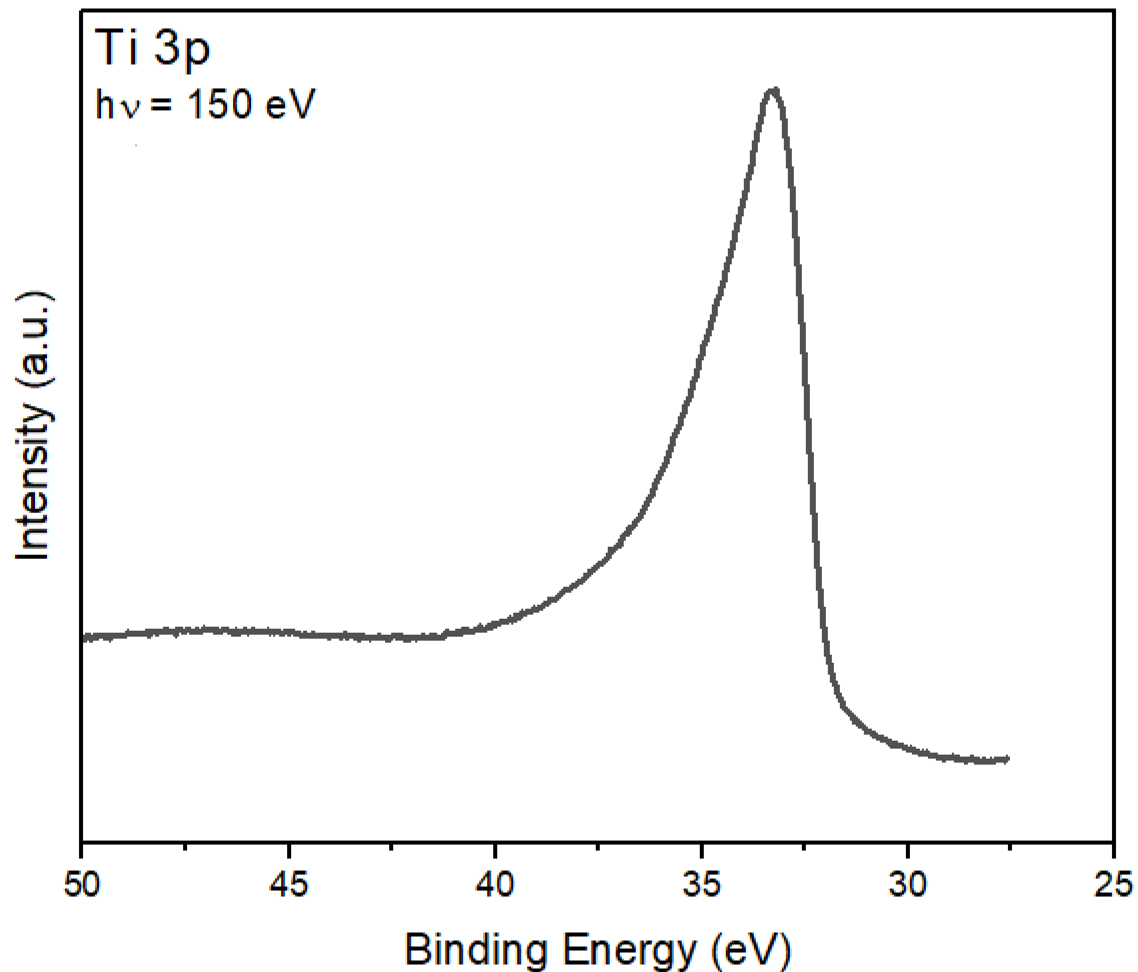


Figure 2.6: Example of Ti metallic peak showing asymmetry

### *2.1.1.5 Sampling Depth:*

Conventional XPS has a limited sampling depth of approximately 5-7 nm[9] depending on the material. Though X-rays can penetrate to distances in excess of a micron into the samples, the same cannot be said for electrons. As an electron travels through the material

there is a probability of interacting with the other electrons and atoms present in the material resulting in loss of energy. Hence the kinetic energy of these electrons reaching the analyser is lot less than the actual kinetic energy if unimpeded. Since XPS measurements rely on the KE of the electron reaching the analyser, the electrons losing kinetic energy will still be present but as a background signal rather contributing to the core level spectra.

The fraction of photoelectrons reaching the analyser unimpeded can be determined using the following equation;

$$I_k = I_0\,(1 - e^{\frac{-d}{\lambda \cos\theta}}) \qquad (2.4)$$

where $I_k$ is the intensity of the electrons exiting the material, $I_0$ is the intensity of incident photons, d is the depth from which the electrons are emitted and λ is the inelastic mean free path. In XPS, 95% of the signal comes from the depth d = 3λ, and this is known as the sampling depth.

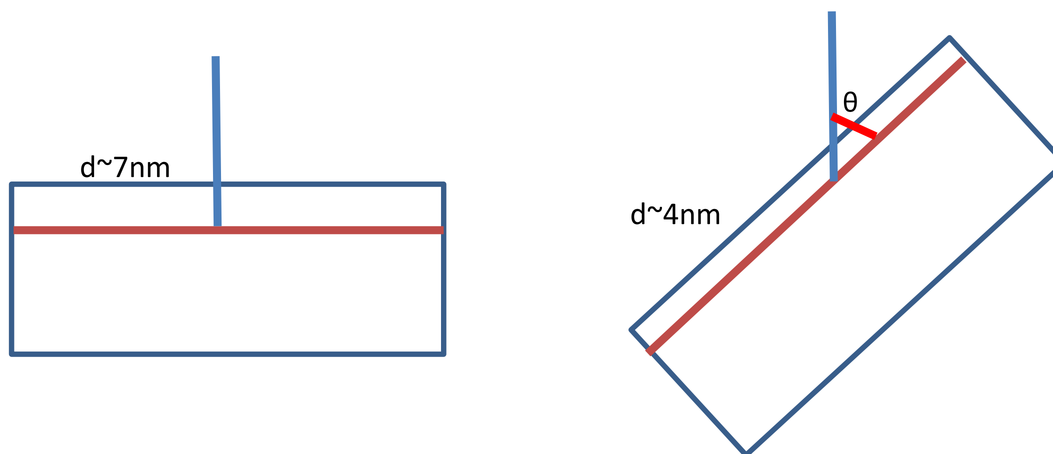


Figure 2.7: schematic showing the decreased sampling depth with change in the angle of photoemission

It can be seen from Figure 2.7 that electrons emerging perpendicular to the surface have the same sampling depth as those emerging at the glancing angles i.e. ~7 nm. However, the rotated samples the perpendicular depth from which the electrons escape from the surface is considerably less than for normal emission. As such, core level spectra taken at an increased angle are more surface sensitive than those taken at normal emission.

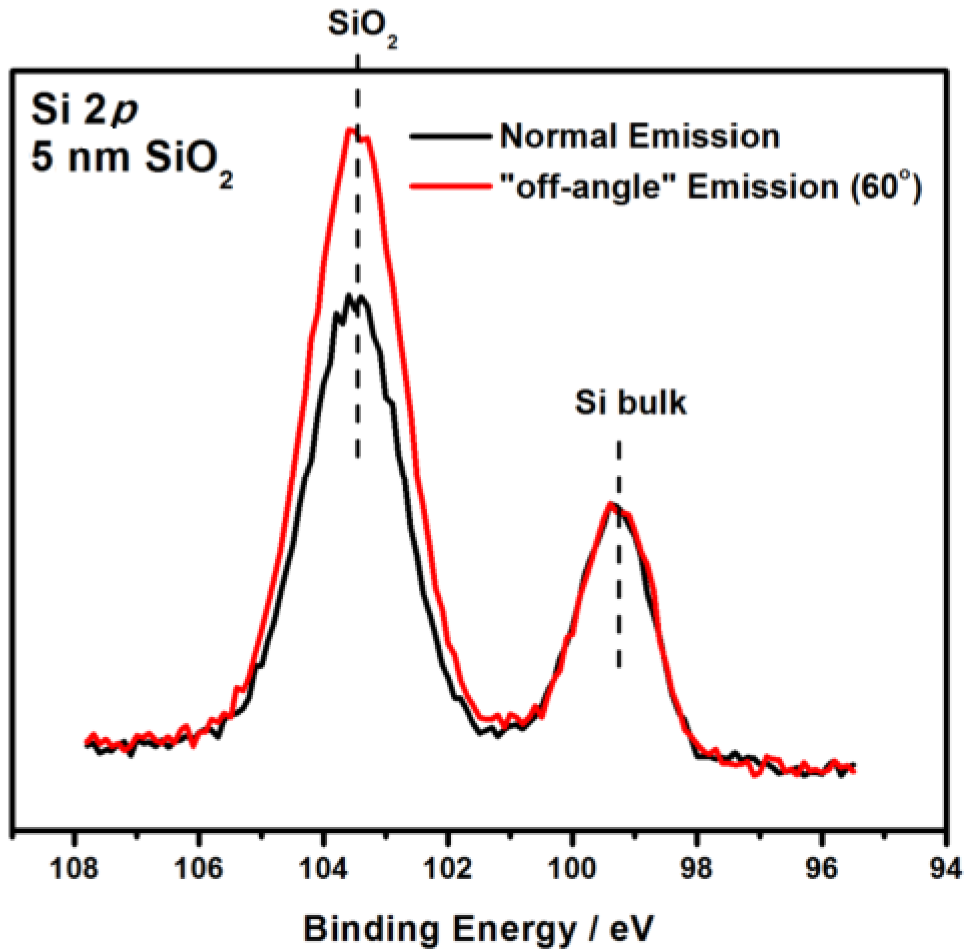


Figure 2.8: dependency of intensity of photoelectrons on sampling depth with change in angle of emission

For example, Si 2p spectra in Figure 2.8 which are taken from a $SiO_2$ surface (~ 5 nm) at emission angles equal to 0 ° (normal emission) and 60 ° shows that the spectrum taken at 60 ° has increased intensity from the Si oxide overlayer compared to normal emission spectra. This forms the basis for the concept of the angle resolved XPS. (ARXPS) which is a non-destructive depth profile analysis.

#### *2.1.1.6 XPS system used*

Most modern XPS systems use a twin X-ray anode source allowing the use of two different photon energies. The source consists of Cu anode coated with two metals. Commonly used are Al (photon energy 1486.6eV) on one side and Mg (photon energy 1253.6

eV) on the other. A high-energy acceleration voltage of 15 kV is supplied and the electrons bombards the anode surface generating the related Kα characteristic X-ray emission. The anode is water cooled to prevent any damage to anode through heating.

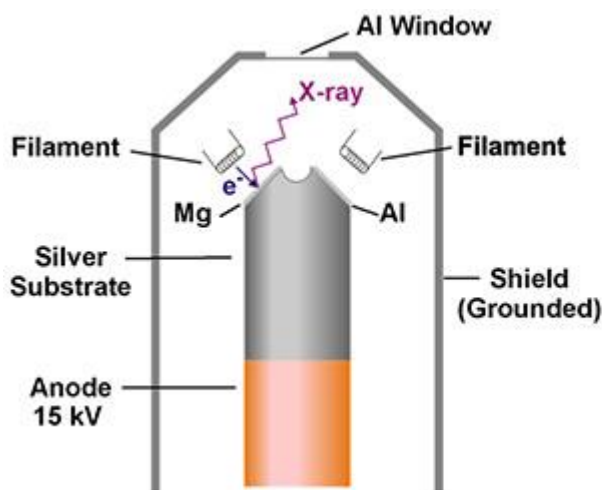


Figure 2.9: Twin anode setup for modern XPS systems [10]

The X-rays incident on the sample surface generate the photoemission signal which is emitted at all angles. To get an optimum signal, the analyser can have an electrostatic lens assembly as shown in Fig 2.9 to focus the photoelectrons towards the analyser. The focus of the lens assembly is generally limited to small area to get a good spatial resolution. The electron beam generates a continuous Bremsstrahlung energy distribution emission, with a maximum intensity at the Kα transition of an electrons from the unresolved Al or Mg 2p core level to 1s core level. For the aluminium target this results in a peak energy of 1486.7 eV with a line width of 0.85 eV and for the Mg target, the value is 1253.6 eV with width of 0.7 eV. The line width is a reflection of the doublet separation of the 2p peak and is a composite of the natural line widths of the 2p 3/2 and 2p 1/2 peaks. For Al 2p the doublet separation of the component peaks is 0.43 eV, making it difficult to resolve the individual peak components and so contributes to a broader overall line width. The doublet separation for the Mg 2p is significantly smaller than that of the Al 2p peak, producing the narrower overall line width.

The electrostatic lens focusses the photoelectrons emitted at various angles from the sample surface towards the hemispherical analyser. This is required especially in cases of

varying incident angles (angularly resolved XPS) as the electron spread is more while inelastic collisions are less. The photoelectrons are supplied a retardation voltage of $V_0$ while focussing towards the entrance of the analyser. The spread is further reduced by the slit assembly at the entrance of the analyser.

The hemispherical electron energy analyser as shown in figure 2.10 is essentially a dispersing element which allows the number of photoemitted electrons at a particular kinetic energy to be determined. The hemispherical analyser consists of two concentric plates with radius $R_1$ and $R_2$. The plates are supplied voltage $V_1$ and $V_2$ such that $V_1$ is positive with respect to $V_0$ while $V_2$ is negative with respect to $V_0$. The voltages at the plates allow only the photoelectrons with kinetic energy being analysed that can traverse through the analyser without hitting either hemispherical plates. The voltage range allowed between the plates are determined by the pass energy and the voltages supplied to the plates depend on the radius of the hemispherical plates:

$$V_1 = V_0\,(3 - 2\,\frac{R_0}{R_1}) \qquad (2.5)$$

$$V_2 = V_0\,(3 - 2\,\frac{R_0}{R_2}) \qquad (2.6)$$

where $R_0$ is the mean radius of $R_1$ and $R_2$. From the equations above the voltage supplied to the plates are determined as $V_1$ = 0.5 ($V_0$) and $V_2$ = -1.33 ($V_0$). The photoelectrons with large variations from these values collide with the hemispherical plates while the other photoelectrons reach the detector.

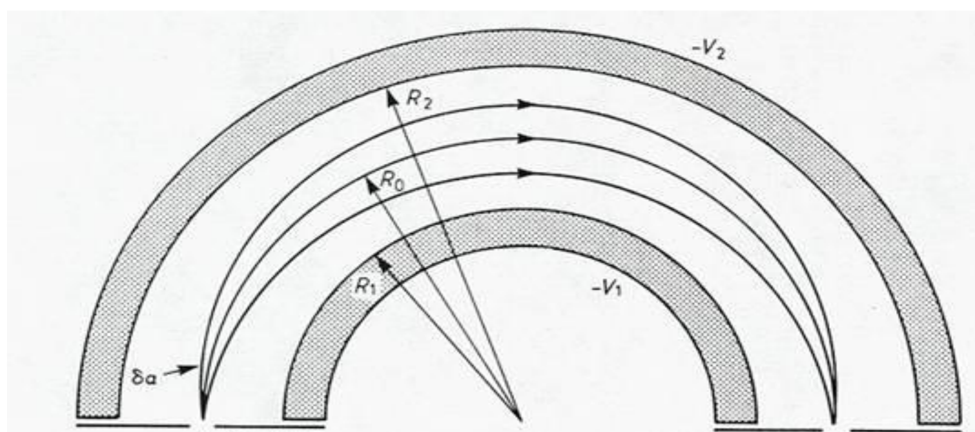


Figure 2.10: Basic hemispherical analyser

The FWHM of an XPS peak (ΔE) can be calculated using the equation:

$$\Delta E = \sqrt{\Delta E_{peak}^2 + \Delta E_{instrum}^2} \qquad (2.7)$$

where $\Delta E_{peak}$ is the natural line width of the XPS peak and $\Delta E_{instrum}$ is the instrumental resolution and is affected by the analyzer pass energy, slit widths and the line width of the incident X-rays. The instrumental line width of the incident X-rays depends on the line width of the x-ray source which 0.7 eV for Mg Kα source and 0.85 for Al Kα source. The use of a monochromator is likely to provide better instrumental resolution as it will reduce the broadening of the peak due to line width of the incident X-rays. In this work, a non-monochromatic source of Mg Kα is used.

Pass energy determines the number of photoelectrons entering the analyser by selectively allowing the photoelectrons in the acceptable range of the analyser. Pass energy depends on the ratio of R1 and R2 and helps in determining the resolution and sensitivity of the photoelectron peaks. From the equation 2.8, it can be seen that the higher the pass the pass energy, higher the sensitivity while the resolution decreases thereby increasing the peak width ΔE. the pass energy used in XPS measurements in this work are 50 eV for the survey spectra in order to increase the sensitivity to determine the elements present in the sample and 20 eV for narrow regions in order to get higher resolution peaks.

$$pass\ energy\ \ e\Delta V = E\ (\frac{R_2}{R_1} - \frac{R_1}{R_2}) \qquad (2.8)$$

The resolution of an analyser can be determined by the equation:

$$\frac{\Delta E_{analyzer}}{E} = \frac{W1+W2}{2R_0} + \ \delta\alpha^2 \qquad (2.9)$$

where E is the energy of the photoelectron peak, w1 is the entry slit width, w2 is the exit slit width and $R_0$ is the mean radius if the analyser plates.

The detector is typically a channeltron or channel plate made of array of detectors. The intensity of the photoemitted signal at different kinetic energies is then plotted to obtain a photoemission spectrum for the material under investigation. The schematic of the XPS system used is shown in figure 2.11.

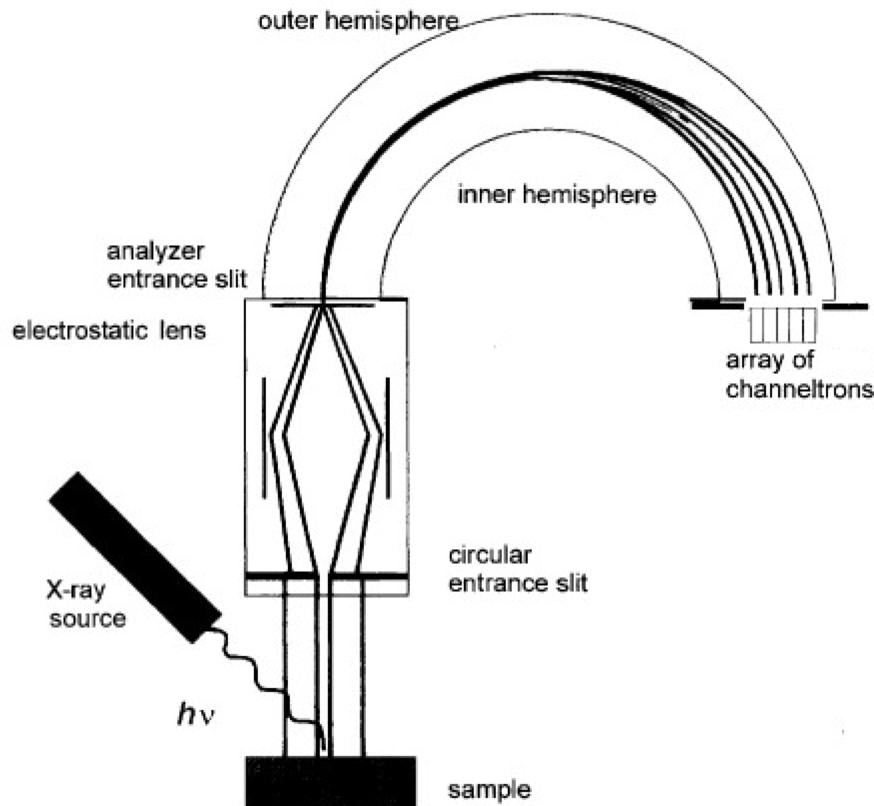


Figure 2.11: Schematic of a modern day XPS system

## 2.1.2 Hard X-ray Photoelectron Spectroscopy

HAXPES is a high photon energy variant of XPS. The main advantage of HAXPES over conventional XPS is the higher sampling depth. The higher energy of X-rays used in HAXPES enables the user to increase the sampling depth of 7 nm at 1.5keV to 20 to 30 nm at 10 keV as shown in the figure 2.3.

Another advantage of the HAXPES is the tuning the photon energy at the synchrotron radiation sources allowing to focus on the specific buried interface[10] of the sample. This can be used to complement the conventional angularly resolved XPS measurements.

#### *2.1.2.1 HAXPES at Synchrotron sources:*

Synchrotrons are generally composed of two connected evacuated rings: one accelerates the electron at near light speed and a storage ring in which the injected electrons are stored for experimental purposes. The storage ring is rather a many-sided polygon and the electron travelling at near light speed light emit broad band spectral radiation due to the momentum change at the corners of the storage ring as shown in fig 2.12. The broad band radiation is frequently coupled with a monochromator to select a particular photon energy for an experiment including HAXPES, XPS, XAS etc.

HAXPES measurements made at synchrotron are different from the conventional hard X-ray anode source like Cu due to following characteristics

- High Brilliance – with regards to synchrotron source brilliance is an important advantage compared to traditional XPS sources. It depends on number of photons produced, beam divergence and cross sectional area of the beam.

- High level of polarization and high collimation – advantageous in focussing on desirable surface even if the samples are patterned.

- Tuneable wavelength using monochromator – by adjusting the energy of the photon, the sampling depth can be changed thereby thick films can be analysed compared to the traditional XPS systems. While higher photon energy tuning requires crystal monochromator, sub-eV tuning utilizes grating monochromators for soft-rays from eV to 1000 eV for example European XFEL at DESY.

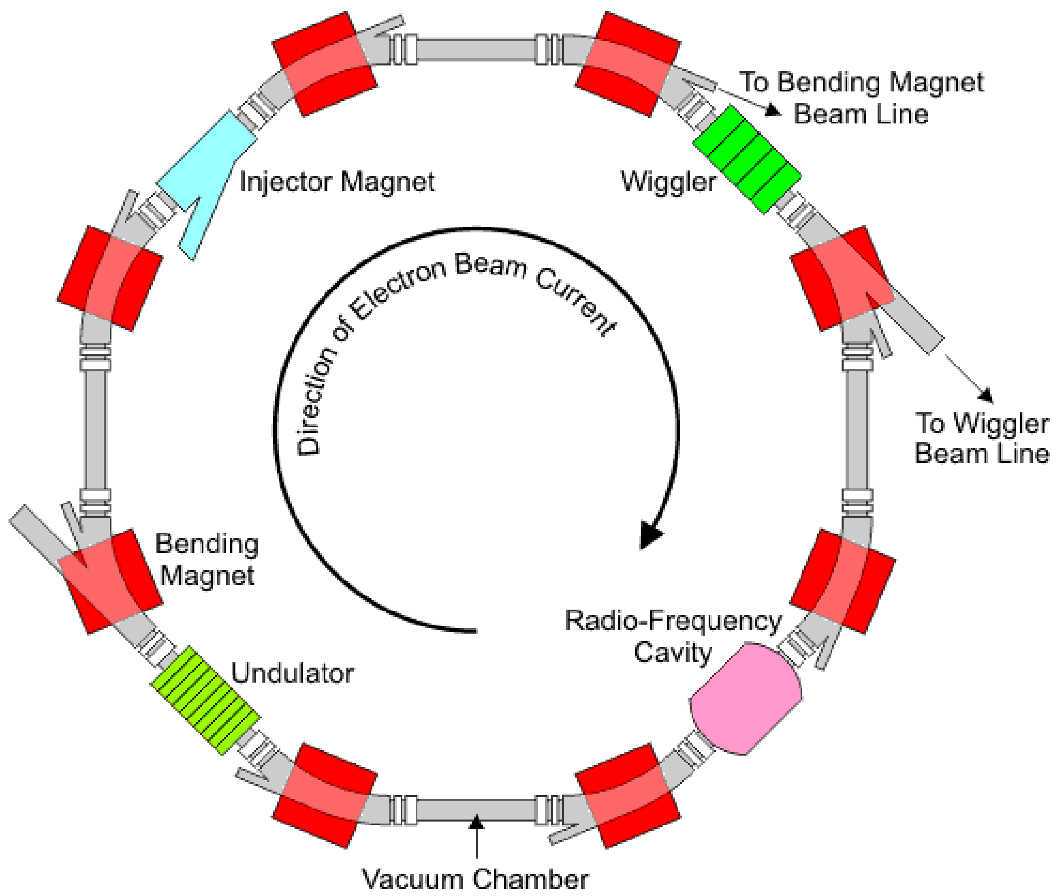


Figure 2.12: generation of x-ray beam at synchrotron sources[11]

The experimental HAXPES and XAS setup from Synchrotron SOLEIL (Galaxies beamline) used in this work is shown below:

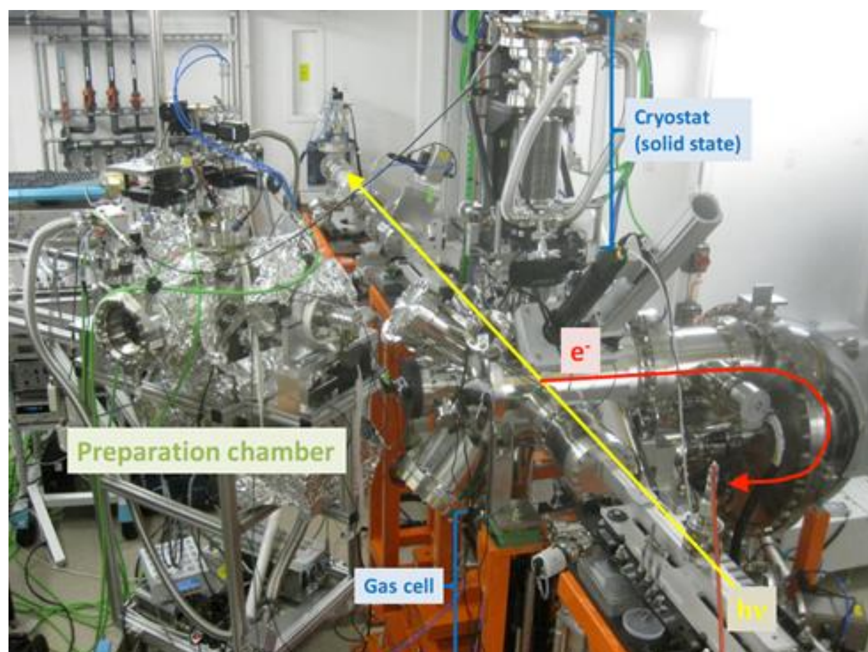


Figure 2.13: Experimental HAXPES setup[12]

## 2.2 X-ray Absorption Spectroscopy (XAS):

The X-ray Absorption Spectroscopy (XAS) technique has been used in identification of elements for a century[13] but the technique gained importance after the publication by Sayers, Stern and Lyle [14] by applying Fourier analysis to invert the experimental data collected in wave vector phase to energy distribution function. This resulted in the capacity to quantitatively determine structural parameters such as bond distance, coordination number, thermal and disorder parameters[15].

Although XAS has been in use from the early 1900s, from the experimental point of view the improvement in instrumentation was carried out in early 1960s when diffractometers for X-rays were modified by using monochromators of silicon crystal to allow step scaling. This enabled selection of the energy region for the desired absorption edge allowing calculation of the precise absorption coefficient. The first use of this type of experimental setup was performed by Van Nordstrand [16] to study the catalysis effect of transition metals and determine their chemical fingerprint fine structure.

### 2.2.1 Principles of XAS:

XAS measures the exponential decay of the photon beam focussed on the sample. It is based on Beer's law which states that absorbance of a material is directly proportional to the concentration on the attenuating species in the material sample. The equation for the Beer's law can be rewritten including the initial and final intensity as follows:

$$\log\frac{I_0}{I} = \varepsilon\, L\, C \tag{2.10}$$

where $I_0$ and I are the initial and final photon intensity, ε is absorption coefficient, L is the path length of the material, and C is the concentration of the material. The main XAS study includes the study of absorption edges. Each element has its own absorption edge and depending on the atomic number and absorption at these edges the probability of X-ray absorption increases. By studying a wide range of energies (several hundred eV) from the rising edge,

one could get information related to geometry, electronic structure and chemical make-up (spin-orbit coupling) of the material.

A normal XAS spectrum can be divided into four parts:

1. Pre-edge: Region up to 10 eV below absorption edge – caused due to one of the following reasons: the states at the Fermi energy in metals giving a "rising edge" with an arc tangent shape; the bound core excitons in insulators with a Lorentzian line-shape.
2. X-ray absorption near edge structure (XANES): ±40 eV from the absorption edge
   Also known as Near edge X-ray absorption fine structure (NEXAFS) - it is used in determining the density of states and chemical bonds present. As such, it is used in chemical fingerprint of the element present.
3. Extended X-ray absorption fine structure (EXAFS): 50 -1000 eV above absorption edge. Useful in determining the coordination number of the element being analysed.
4. Other features of the XAS spectra can be attributed to electric-dipole allowed transitions (i.e. $\Delta\ell = \pm 1$) to unoccupied final states

A typical XAS spectrum is shown in the figure below:

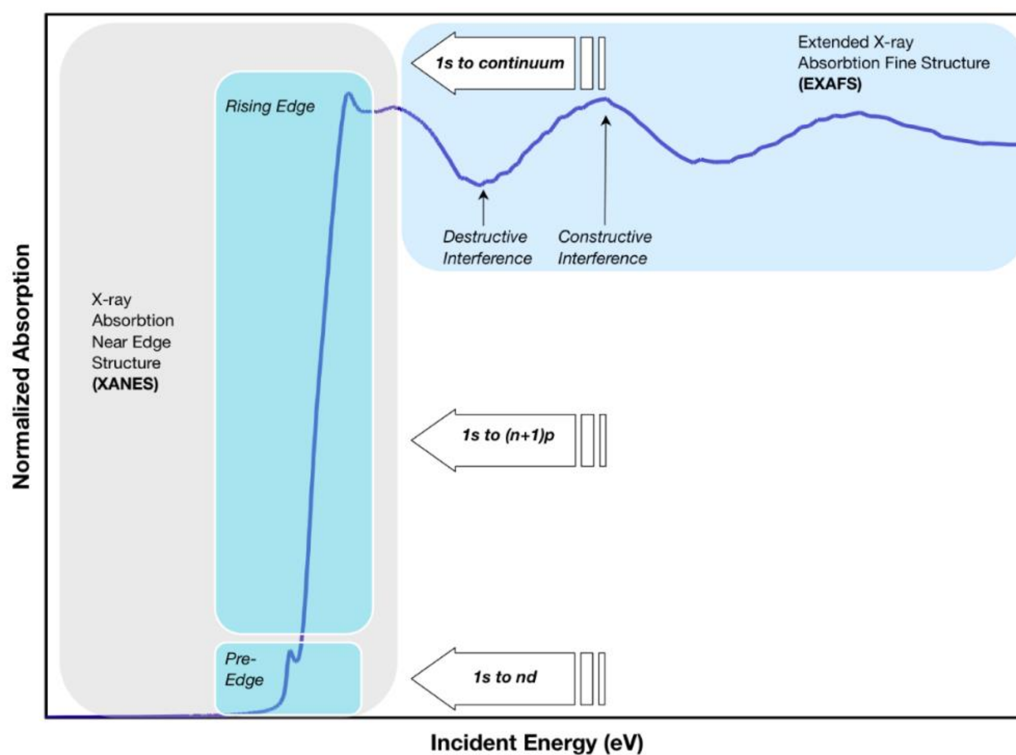


Figure 2.14: A typical XAS spectrum showing pre-edge, rising edge and extended absorption edge[17]

### *2.2.1.1 Apparatus used:*

XAS measurements are generally performed at synchrotron radiation sources as they provide the variable energy range required for measurement of various absorption edges. Also, synchrotron sources provide high flux and brightness required for the XAS measurements. Furthermore, beamline optics and focussing devices help in high spatial resolution of the data obtained. A general overview of the XAS instrumentation is shown in the figure 2.15 below.

The initial photon intensity is recorded and the resultant sample current from the sample is measured for each photon energy. The data acquired shows two profiles, one for the photon intensity and the other for the sample current. When an absorption edge occurs, there will be photoemission, resulting in the increase of sample current at the absorption edge. Since the sample current is obtained throughout the sample, this mode of XAS operation is bulk sensitive. The measurements in this work were carried out at Galaxies beamline at SOLEIL, France.

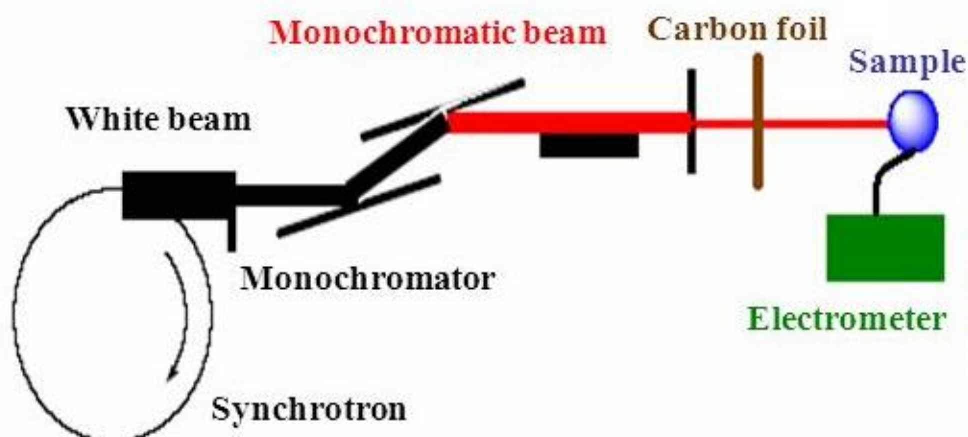


Figure 2.15: Overview of XAS setup

## 2.3 Secondary Ion Mass Spectrometry (SIMS):

Secondary Ion Mass Spectrometry, also known as SIMS, is used to determine the concentration of any elements in the surface of the thin film by sputtering the surface and analysing the mass of the ions sputtered as schematically shown in figure 2.16.

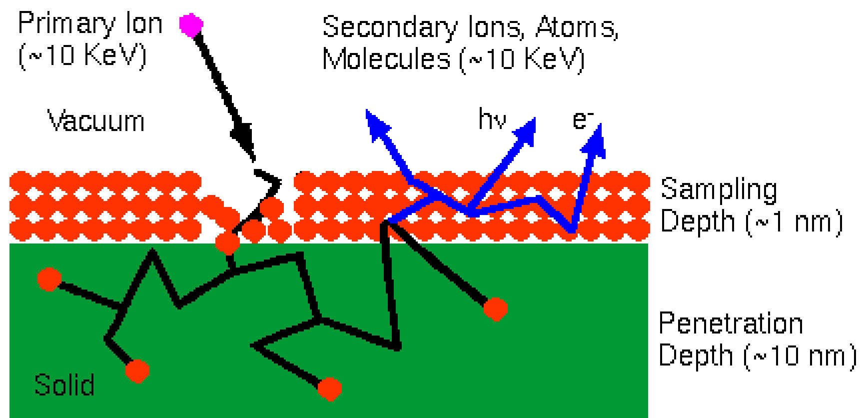


Figure 2.16: Principle of SIMS[18]

SIMS generates a primary ion beam with energy of the range of 1 to 50 keV (in our case 5 keV of Ar) and is focussed on the sample surface as shown in figure 2.16. The atomic and molecular species sputter from approximately 1 – 2 nm into the surface and can be in the form of ions or neutral species. The sputtered ions are then analysed in a mass spectrometer which provides information on the mass-to-charge ratio of the detected species[19]. The SIMS technique is destructive, but the damage can be limited by adjusting the mass and energy of the primary ions from the SIMS ion gun. In some non – conducting samples, sample charging might occur due to sputtering of top surface which can be reduced by grounding or supplying a flood of low energy electrons or ions from a charge compensation gun.

Sputter rates depend on primary beam intensity, sample material, and crystal orientation. Sputter rates in a typical SIMS experiments vary between 0.5 and 5 nm/s. The detection limit of SIMS generally depends on the sensitivity of the sample. The detailed sensitivity factors have been summarised for Cs primary ion bombardment[20]. The SIMS detection limits for most trace elements are between $10^{-12}$ and $10^{-16}$ atoms/cc.

Figure 2.17 shows a typical SIMS system. The Ion beam is focussed to a small spot size creating a crater during sputtering of the sample surface. The resulting secondary ions from the crater can be analysed from the centre of the crater to minimize the edge effects. By using a raster scan over a large sampling area, an elemental map can be obtained.

The use of SIMS analysis with XPS is a powerful combination of techniques for the identification of the surface distribution of elemental and molecular species in that it provides optimised compositional sensitivity coupled with chemical state information. Issues of surface and interface contaminants are often best addressed using both methods, providing faster and more comprehensive materials characterisation.

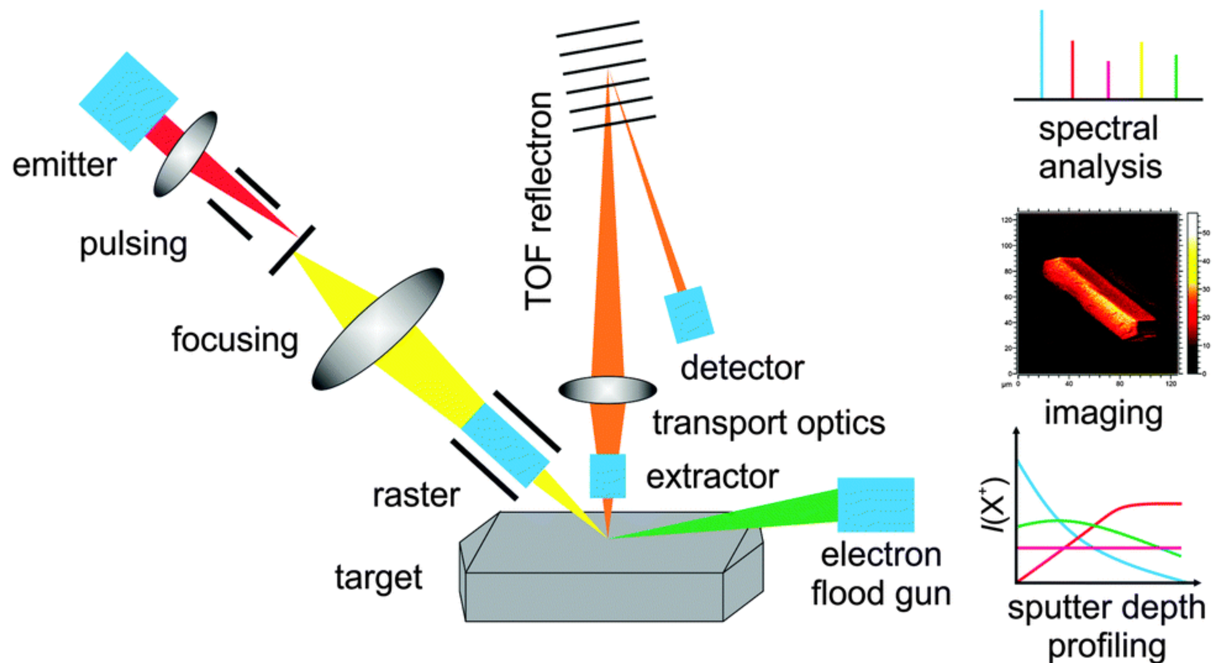


Figure 2.17: Block diagram of a sims system showing the basic elements including a sputter gun, mass analyser and flood gun [21]

## 2.3 Atomic Force Microscopy:

Atomic Force Microscopy (AFM) is one of the techniques used for analysing the surface morphology and roughness of a thin film. AFM is based on the use of an extremely sharp tip (ideally atomically sharp) to measure the physical interactions at short range to determine surface topography[22]. The operation of AFM involves bringing an atomically sharp tip within close proximity of a surface and measuring the force that the tip experiences as it scans across a defined area. The tip is attached to the end of a cantilever. The basis of operation emerged from the discovery that inter-atomic forces exist between two materials

that are in close proximity of each other. Such forces can include Van der Waals, electrostatic or magnetic, the magnitude of which the AFM is designed to determine[23].

$$F = -K\,x \qquad (2.11)$$

where K is the spring constant of the AFM tip. The distance between the tip and the surface of the sample determines the type and the magnitude of the force on the cantilever arm. General principle of an AFM is shown in the figure2.18 below.

The main principle of any AFM system is achieving high resonant frequency capable of vibrational stability to amplify the subatomic amplitudes using a low spring constant and ow mass for the cantilever. Since the deflection of the cantilever is dependent on the force at the sample surface which is small due to low magnitude of the forces such as $10^{-11}$ N for Van der Waal's force, the detector should be highly sensitive to the smallest deflection in the cantilever arm[22].

In modern AFM systems, the back of the cantilever is coated with metal such as gold (Au) or Aluminium (Al) for high reflectance. A laser is used to reduce the beam divergence and it has high intensity. The reflected laser light is measured using the photodiode. As the cantilever deflects, the position of the photodiode changes and the laser beam deflection is measured at each point to generate a topographic image of the surface.

## 2.3.1 Modes of Operation

Different AFM modes of operation are possible and are categorized according to the interaction of the cantilever tip with the sample surface. In contact mode, the tip is in contact with the sample surface. The cantilever measures the deflection due to repulsive force between the tip and the sample surface. Main disadvantage of the contact mode is that the

tip has the tendency to be dragged along the surface due to lateral forces acting at the surface.

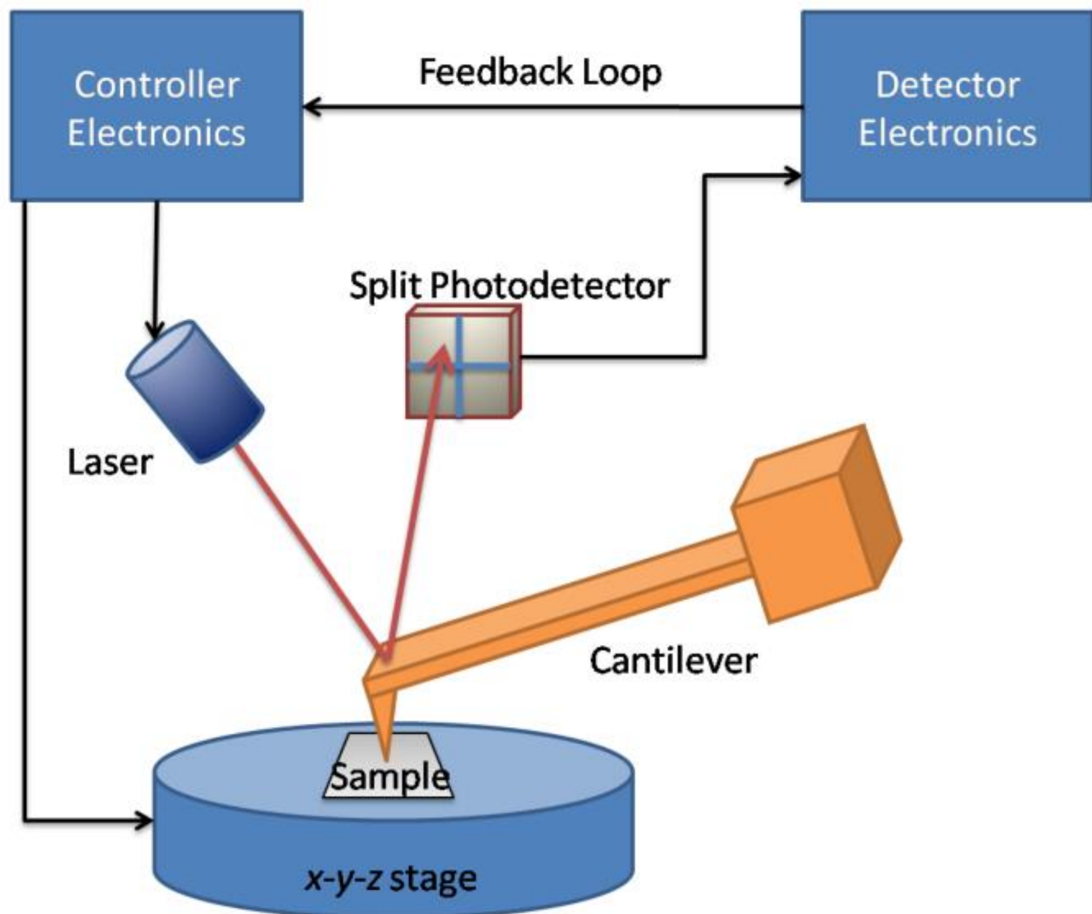


Figure 2.18: Operating principle of a typical AFM[24]

In non-contact mode, the tip is maintained at a distance from the surface so that it no longer feels a repulsive force rather an attractive force. Typical distance between the cantilever tip and the sample surface lie between 5 to 15 nm. As the magnitude of the forces measured are far weaker at this height than the ones obtained through contact mode, and hence the forces measured cannot be distinguished between the actual surface or the contaminants in the surface.

In tapping mode, the tip is in contact with the sample surface for a short time eliminating the possibility of the lateral force and being dragged along the surface. The probe

taps repeatedly, and the feedback loop adjusts the height of the tip to maintain the constant amplitude of oscillation. In this report tapping mode of AFM is used. the AFM system used in this work is shown in the figure 2.19 below:

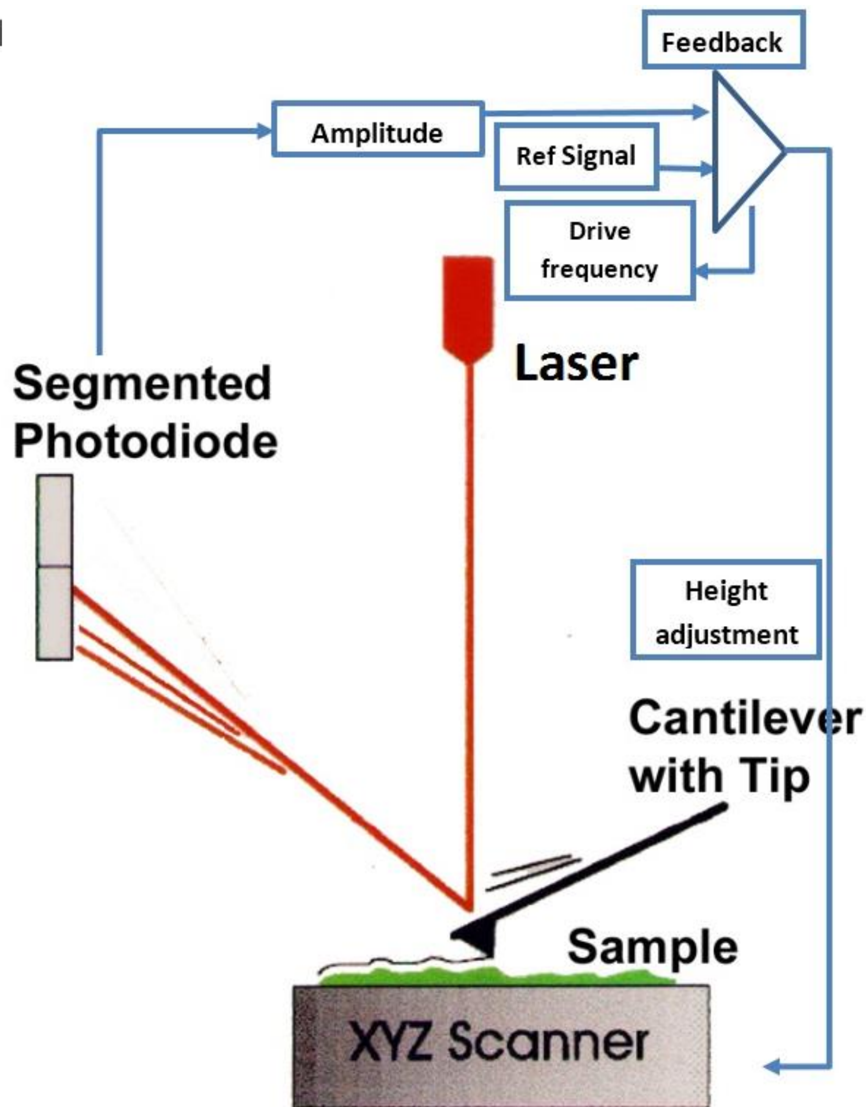


Figure 2.19: working of an AFM in tapping mode

## 2.4 Electrical Characterization

To test the effectiveness of the barrier, electrical characterization is carried out through four -point probe measurements and capacitance-voltage (CV) measurements. While the four-point probe measurements give the resistivity of the sample, CV measurements helps in determining dielectric thickness, doping concentration of the substrate, flat band voltage, interface states etc.

### 2.4.1 Four Point Probe measurements

Four-point probe measurements are useful in determining the conductivity of any semiconductor material or metals. The material can either be bulk or thin film. The experimental apparatus consists of four equally placed tips, normally tungsten tips, with finite thickness. The typical probe spacing is ~1mm.

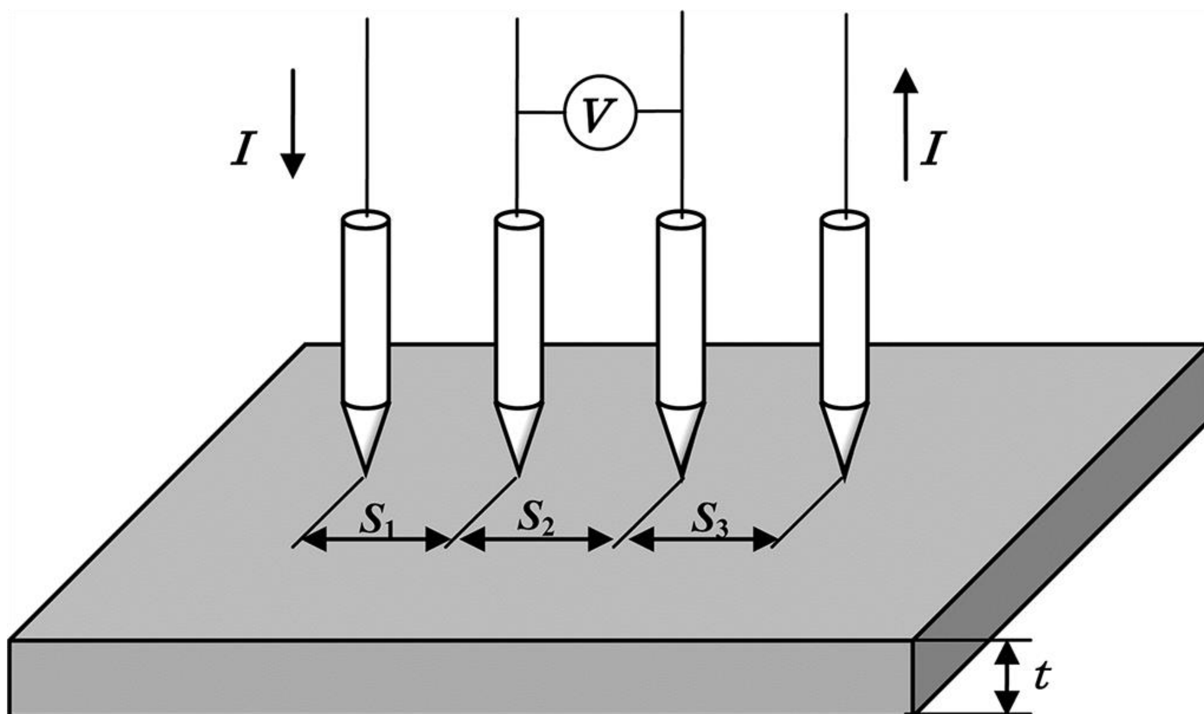


Figure 2.20: Structure of a general four-point probe instrument [18]

With the four tips in contact with the sample surface, a high impedance current source supplies current to outer tips while the inner two tips are connected to the voltmeter to measure voltage drop between them as shown in figure 2.19. From the supplied current and the resultant voltage, the sheet resistance of the sample can be measured. Using the standard values for the instrument used in this work, the equation for the sheet resistance can be modified as follows:

$$Sheet\ resistance\ R_s = 4.5324 * \frac{V}{I} \qquad (2.12)$$

Once the sheet resistance is measured, the resistivity of the material can be found using the equation,

$$Resitivity\ \rho = Sheet\ resistance\ (R_s) * Thickness\ (t) \quad (2.13)$$

### 2.4.2 CV Measurements of MOS devices

Since Cu has the tendency to diffuse through the ILD[25][26][27] as $Cu^+$, methods involving charge detection can be used to investigate Cu diffusion. Capacitance - Voltage sweep measurements of MOS structures is one of the principal techniques to observe Cu diffusion electrically. One of the other techniques possible is the measurement of leakage current through Current – Voltage (IV) characteristics of the MOS devices[28].

MOS devices are essentially a Cu gate structure on an $SiO_2$ film with p-type or n-type Si substrate as schematically shown in Figure 2.21. The MOS devices fabrication in this work are similar to the MOS fabrication process involved in the IC manufacturing. The barrier layer and copper are sequentially deposited on the substrate through a mask of required shape and size (normally multiples of 1micron square), then subjected to lithographic techniques.

As the $Cu^+$ ion diffuses through the dielectric, there will be charge accumulation at the interface of the dielectric and silicon substrate which impact on the CV measurements. While the MOS structure without a barrier layer shows diffusion, the MOS capacitor with barrier layer can be tested with CV measurements for its effectiveness in preventing copper diffusion through the dielectric.

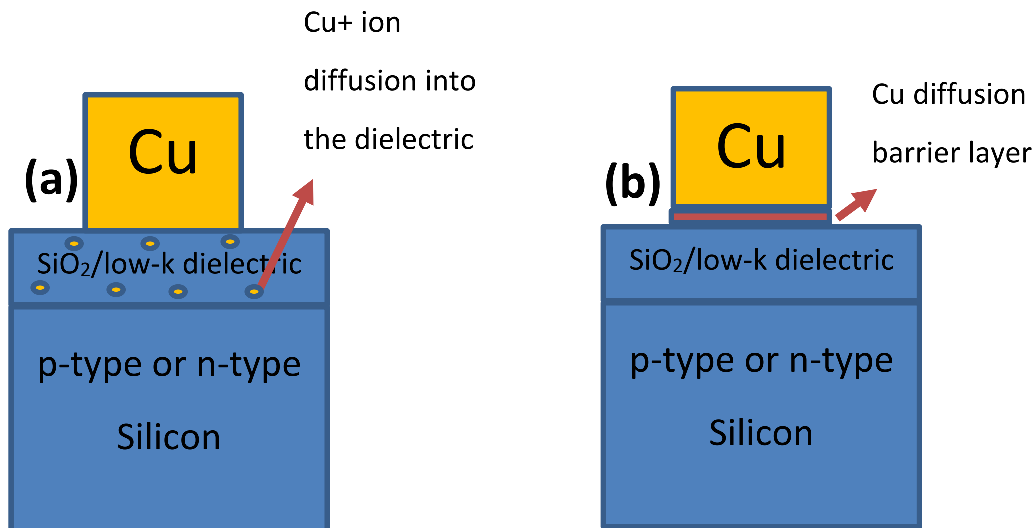


Figure 2.21: MOS capacitor (a) without barrier layer showing cu diffusion (b) with barrier layer

The MOS structure is effectively a capacitor with a semiconductor as one of the electrical contacts. Since the semiconductor is used as a contact, there will be variable capacitance while sweeping through a range of gate voltages. For an n-type semiconductor substrate as the gate voltage is reduced towards negative values a depletion layer is formed near the dielectric interface, and on decreasing the gate voltage, the depletion layer reaches an equilibrium. This voltage is known as flat band voltage ($V_{fb}$). The further decrease results in inversion and forms the basis of transistor switching. Fig 2.22 shows the various stages of a typical n-type MOS capacitor on gate voltage at 1MHz frequency sweep.

Modern MOS fabrication methods can produce near ideal MOS device behaviours like zero leakage current through the dielectric, similar work function for the metal as well as the doped Si substrate to get a perfect flat-band condition, absence of trapped charges or interface defects etc.[29]. If the insulator is not perfect, there will be resulting DC current flow on applied bias interrupting the CV measurements.

The difference in the work function of the metal and the substrate gives the value of the flat – band voltage of the MOS capacitor. Ideal MOS devices have zero difference in the work function there by obtaining the flat – band voltage at gate voltage of zero.

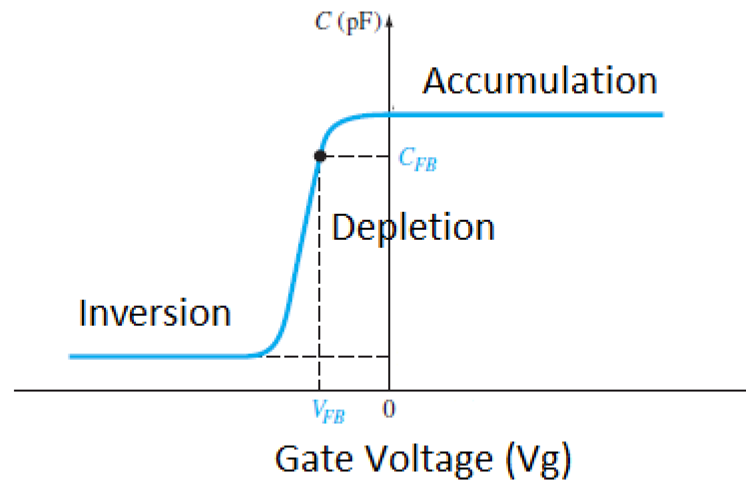


Figure 2.22: CV Profile of n-type MOS capacitor showing accumulation, depletion and inversion with respect to gate voltage sweep

The interface states and trapped charges occur through multiple causes:

- Oxygen vacancy during the deposition of the dielectric – can be removed through annealing.
- Fixed oxide charge – located deep in the valence band or high in conduction band and hence not noticeable in the CV measurements.
- Interface states occur at the interface of the dielectric and Si substrate – formed due to the distortion of the periodic Si lattice upon growth of the dielectric – directly affect the CV profile as these states are found throughout the energy band gap of the substrate.
- Elemental contamination during the fabrication – presence of mobile ions distorts the CV profile thus interpreting the data becomes difficult - can be avoided by fabricating at ultra - clean environments and stringent deposition techniques.

Thus, the flat – band voltage can be calculated by including all the charges and defects as:

$$V_{fb} = \varphi_{ms} - \frac{Q_{total}}{C_{dielectric}} \qquad (2.14*)$$

where $V_{fb}$ is the flat band voltage, $\phi_{ms}$ is the work function difference between the metal and the substrate, $Q_{total}$ is the total charge due to the defects in the dielectric and $C_{dielectric}$ is the capacitance of the dielectric. When copper ions diffuse into the dielectric, there will be increased charge concentration in the dielectric resulting in the shift of flat band voltage. Effectiveness of the barrier can be identified by comparing with the pure copper sample with no barrier at the same analysis conditions.

## 2.5 Adhesion Testing:

Adhesion is the ability of two materials surface to stick to each other. Copper generally needs an adhesion buffer layer to effectively bond to the silicon dioxide dielectric. Hence in the current generation of interconnects, TaN is used as an adhesion buffer layer. As there are multiple dielectric and interconnect interfaces present, having a separate adhesion buffer is a limiting factor to continued downward scaling and the efficiency of the ICs. For future generations of diffusion barriers, the barrier should also be a good adhesion buffer so as to reduce the thickness of the barrier stack thereby providing more volume for the interconnect metal.

Adhesion can be viewed thermodynamically in terms of the difference in the surface energies between two dissimilar materials. Most methods of testing adhesion include the removal of a film from the substrate surface. Although, quantitative adhesions methods include complicated calculations as film deformations frequently occur before delamination in most of the adhesion tests[30]. Hence, accurate measurements of surface energy calculations are difficult to carry out.

There are various methods for testing adhesion. Commonly used ones are:

***Scratch test*** – A finely tipped stylus is drawn across the surface of a film while an increasing load is applied. At the critical load, the film is completely removed and a measure of the adhesion can be obtained by comparing the critical loads on the different films[31].

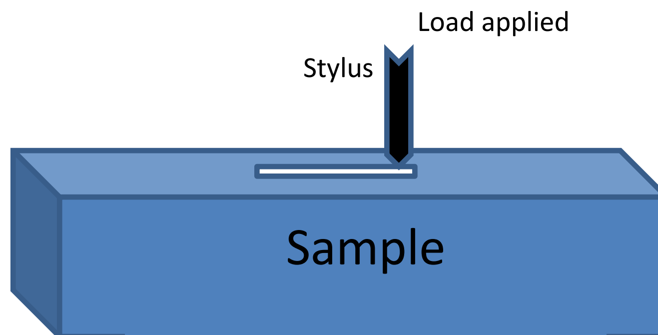


Figure 2.23: scratch test

***Peel test*** – A piece of adhesive tape is overlaid on the surface of the film to be tested and it is peeled from the surface by applying a force through a load cell. However, the measurements can be varying as sometimes films are only partially delaminated[32].

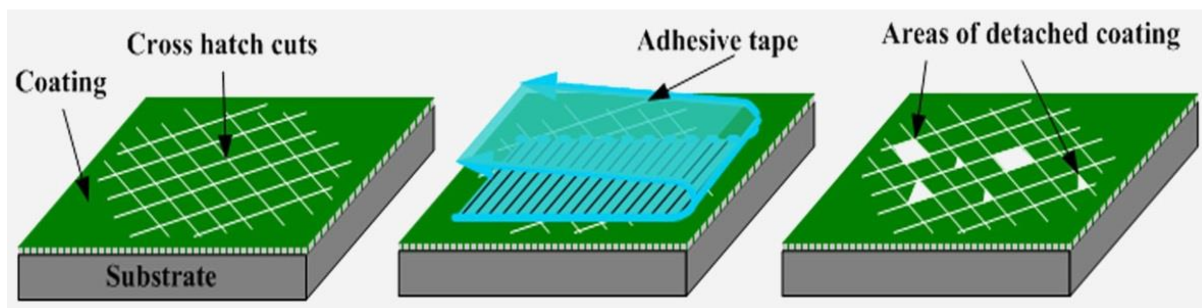


Figure 2.24: Peel test[33]

***Blister method*** – A small hole is drilled through the back of the substrate and compressed air is applied at increasing pressure to delaminate the film. By studying the propagation of the delamination, adhesion strength can be deduced. This method removes the disadvantages of deformations and strains induced into the film – substrate interface through other adhesion measurement techniques techniques[34]. A typical blister test for adhesion in the figure 2.25 below.

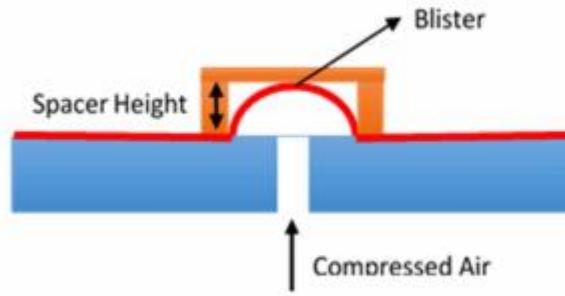


Figure 2.25: Blister test

In this work, a qualitative analysis of copper thin film adhesion was carried out using the peel test. A thick copper film is deposited by hot filament evaporation. Multiple copper structures are formed while using a silicon shadow mask during copper deposition. The silicon shadow mask used in our work is shown in the figure 2.26 below:

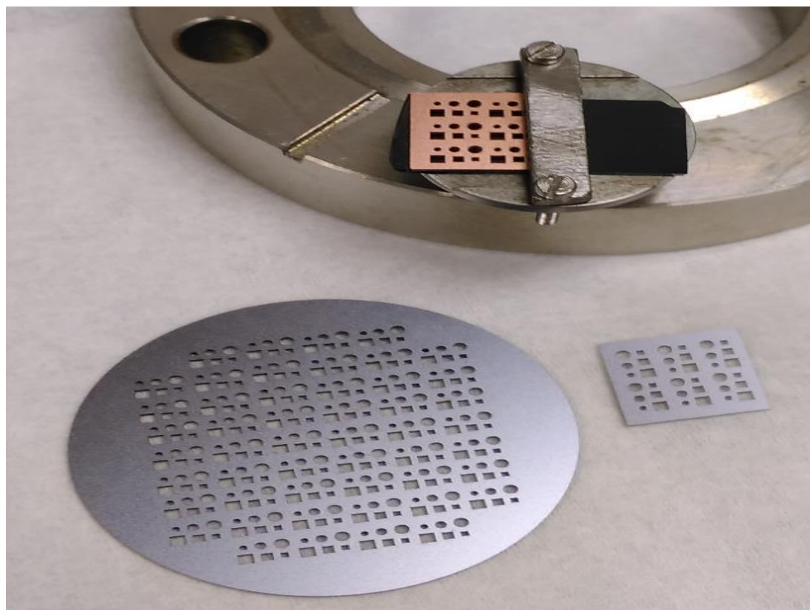

Figure 2.26: Silicon Shadow mask used for copper deposition through hot filament evaporation

Images are recorded before and after the peel test (tape test). Using the Keyence 3d microscope software, the copper structures were analysed and the percentage of area of copper removed from the surface after the tape test is calculated.

## References:

[1] X. Yin, J. Zhang, X. Wang, Sequential injection analysis system for the determination of arsenic by hydride generation atomic absorption spectrometry, Fenxi Huaxue. 32 (2004) 1365–1367.

doi:10.1017/CBO9781107415324.004.

[2] J.C. Vickerman, I.S. Gilmore, ***Surface Analysis - The Principal Techniques: Second Edition***, 2. ed, Wiley, Chichester, 2009. doi:10.1002/9780470721582.

[3] M. Kettner, ***Reactivity of transition metals – influence of the degree of oxidation of active substrate***, Charles University, Prague, 2017.

[4] K.D. Moulder, J. F., Stickle, W. F., Sobol, P. E. & Bomben, ***Handbook of X-ray Photoelectron Spectroscopy***, Perkin-Elmer Corporation (1995).

[5] H. Bubert, H. Jennet, Surface and thin film analysis, 2002. doi:10.1002/9783527636921.ch24.

[6] S. Thibault, H. Aubriet, C. Arnoult, D. Ruch, Gold nanoparticles and a glucose oxidase based biosensor: An attempt to follow-up aging by XPS, Microchim. Acta. 163 (2008) 211–217. doi:10.1007/s00604-008-0028-z.

[7] P.E.S. John F. Moulder, William F. Stickle, Handbook of x-ray photoelectron spectroscopy : a reference book of standard spectra for identification and interpretation of XPS data - Catalog - UW-Madison Libraries, Update, Perkin-Elmer Corporation, Eden Prairie, Minn, 1995. https://search.library.wisc.edu/catalog/999931119402121.

[8] D. Briggs, M.P. Seah, ***Practical surface analysis by Auger and X-ray photoelectron spectroscopy***, IM Publications, 1990. doi:10.1016/S0039-9140(97)80038-0.

[9] S. Tanuma, C.J. Powell, D.R. Penn, Calculations of electron inelastic mean free paths, Surf. Interface Anal. 37 (2005) 1–14. doi:10.1002/sia.1997.

[10] C. Dallera, F. Fracassi, L. Braicovich, G. Scarel, C. Wiemer, M. Fanciulli, G. Pavia, B.C.C. Cowie, Nondestructive diagnostics of high- κ dielectrics for advanced electronic devices, Appl. Phys. Lett. 89 (2006) 183521. doi:10.1063/1.2374843.

[11] P. Barnes, J.K. Cockcroft, S. Jacques, M. Vickers, How do Synchrotrons Work?, Univ. London. (1997). http://pd.chem.ucl.ac.uk/pdnn/inst2/work.htm.

[12] J.P. Rueff, J.M. Ablett, D. Céolin, D. Prieur, T. Moreno, V. Balédent, B. Lassalle-Kaiser, J.E. Rault, M. Simon, A. Shukla, The GALAXIES beamline at the SOLEIL synchrotron: Inelastic X-ray scattering and photoelectron spectroscopy in the hard X-ray range, J. Synchrotron Radiat. 22 (2015) 175–179. doi:10.1107/S160057751402102X.

[13] A. Mottana, A. Marcelli, The Historical Development of X-ray Absorption Fine Spectroscopy and of Its Applications to Materials Science, Hist. Mech. Mach. Sci. 27 (2015) 275–301. doi:10.1007/978-94-017-9645-3_15.

[14] D.E. Sayers, E.A. Stern, F.W. Lytle, New technique for investigating noncrystalline structures: Fourier analysis of the extended x-ray-absorption fine structure, Phys. Rev. Lett. 27 (1971) 1204–1207. doi:10.1103/PhysRevLett.27.1204.

[15] J.A. van Bokhoven, C. Lamberti, ***X-Ray Absorption and X-Ray Emission Spectroscopy: Theory and Applications***, John Wiley & sons 2015. doi:10.1002/9781118844243.

[16] R.A. Van Nordsthand, The Use of X-Ray K-Absorption Edges in the Study of Catalytically Active Solids, Adv. Catal. 12 (1960) 149–187. doi:10.1016/S0360-0564(08)60602-1.

[17] M. Zhang, XANES Theory, Libretexts. (2017). https://chem.libretexts.org/Textbook_Maps/Physical_and_Theoretical_Chemistry_Textbook_Maps/Supplemental_Modules_(Physical_and_Theoretical_Chemistry)/Spectroscopy/X-ray_Spectroscopy/XANES%3A_Theory.

[18] A.G. O'Donnell, I.M. Young, S.P. Rushton, M.D. Shirley, J.W. Crawford, Visualization, modelling and prediction in soil microbiology, Nat. Rev. Microbiol. 5 (2007) 689–699. doi:10.1038/nrmicro1714.

[19] J.B. Clegg, ***Secondary Ion Mass Spectrometry—a Practical Handbook for Depth Profiling and Bulk Impurity Analysis*** Wiley, New York, 1989, Surf. Interface Anal. 17 (1991) 221–221. doi:10.1002/sia.740170411.

[20] J. Pisonero, B. Fernández, D. Günther, Critical revision of GD-MS, LA-ICP-MS and SIMS as inorganic mass spectrometric techniques for direct solid analysis, J. Anal. At. Spectrom. 24 (2009) 1145–1160. doi:10.1039/b904698d.

[21] J.P. Hofmann, M. Rohnke, B.M. Weckhuysen, Recent advances in secondary ion mass spectrometry of solid acid catalysts: Large zeolite crystals under bombardment, Phys. Chem. Chem. Phys. (2014). doi:10.1039/c3cp54337d.

[22] G. Binnig, C.F. Quate, Atomic Force Microscope, Phys. Rev. Lett. 56 (1986) 930–933. doi:10.1103/PhysRevLett.56.930.

[23] A. McCoy, Chemical investigations of ruthenium based barrier layer systems for future interconnect technologies, 2014. http://doras.dcu.ie/20071/1/Thesis_pdf.pdf.

[24] J. Bogan, Growth and chemical characterisation studies of Mn silicate barrier layers on SiO2 and CDO, Dublin City University, 2012.

[25] I. Fisher, M. Eizenberg, Copper ion diffusion in porous and nonporous SiO2-based dielectrics using bias thermal stress and thermal stress tests, Thin Solid Films. 516 (2008) 4111–4121. doi:10.1016/j.tsf.2007.10.011.

[26] Y. Shacham-Diamand, A. Dedhia, D. Hoffstetter, W. Oldham, Copper Transport in Thermal SiO2, J. Electrochem. Soc. 140 (1993) 2427–2432. doi:10.1149/1.2220837.

[27] J.D. McBrayer, Diffusion of Metals in Silicon Dioxide, J. Electrochem. Soc. 133 (1986) 1242. doi:10.1149/1.2108827.

[28] J.C. Ranuárez, M.J. Deen, C.H. Chen, A review of gate tunneling current in MOS devices, Microelectron. Reliab. 46 (2006) 1939–1956. doi:10.1016/j.microrel.2005.12.006.

[29] H.H. Wieder, ***MOS (Metal Oxide Semiconductors) Physics and Technology***, J. Vac. Sci. Technol. 21 (1982) 1048–1049. doi:10.1116/1.571867.

[30] S.J. Bennett, K.L. Devries, M.L. Williams, ***Adhesive fracture mechanics***, Int. J. Fract. 10 (1974) 33–43. doi:10.1007/BF00955077.

[31] J.E. Lee, H.J. Kim, D.E. Kim, Assessment of adhesion between thin film and silicon based on a scratch test, J. Mech. Sci. Technol. 24 (2010) 97–101. doi:10.1007/s12206-009-1124-7.

[32] B.N. Chapman, ***Thin-film adhesion***, J. Vac. Sci. Technol. 11 (1974) 106–113. doi:10.1116/1.1318537.

[33] P. Testing instruments, Cross- hatch test, Presto Gr. (2018). http://www.prestogroup.com/articles/test-the-resistance-of-coating-to-separation-with-cross-hatch-tester/.

[34] J. Chen, S.J. Bull, Approaches to investigate delamination and interfacial toughness in coated systems: An overview, J. Phys. D. Appl. Phys. 44 (2011). doi:10.1088/0022-3727/44/3/034001.

# 3. Investigation of nitrogen incorporation into manganese-based copper diffusion barrier layers for future interconnect applications

## 3.1 Introduction

The ideal barrier layer for complementary metal-oxide-semiconductor (CMOS) interconnects should have as low as possible electrical resistance to improve the overall interconnect conductivity, good adhesion to both the dielectric and the copper interconnects, and good control over the thickness of the barrier. Among the materials currently under investigation are manganese based barrier layer systems [1][2][3]. Barrier formation approaches involving manganese have shown that, upon thermal annealing the manganese forms manganese silicate at the dielectric interface, a material which has been shown to be a good copper diffusion barrier [4][5]. One of the main challenges with the integration of the copper-manganese system is the adhesion of the copper to the barrier layer/ dielectric stack. In previous technology nodes, the incorporation of nitrogen to metallic barrier layers has been shown to improve adhesion [6][7]. Following this trend of metal-nitrides as the buffer layer for adhesion of the metal, manganese nitride has gained some interest as a potential buffer layer for manganese based barriers.

BEOL processing techniques are much different from the bulk processing techniques. Hence the deposition and characterization of thin film manganese nitride greatly varies from their bulk counterparts. Some efforts to form and characterise manganese nitride thin films involve ion implantation using an ion gun have been reported [8].

Herein, we present a detailed spectroscopic study of manganese nitride deposited by CVD by research collaborators in IMEC, Belgium, to understand the chemical composition of the manganese and nitrogen in the film and the chemical state of the manganese nitride films (oxidation state, single or multi-phase, etc.). Previous studies on the electrical characteristics of the manganese nitride films have shown promising results[9]. Furthermore, we

characterised metallic manganese films on the same dielectric substrate in order to better understand the impact of nitrogen on the chemical interactions within the material system. The surface morphology of the films is studied using atomic force microscopy (AFM) to gauge surface roughness and in particular the impact of nitrogen incorporation on the surface.

As adhesion is one of the key drivers for nitrogen incorporation, we also qualitatively test whether adhesion is indeed improved by the deposition of a copper layer on top of the Mn and MnN films and subsequent tape testing.

## 3.2 Experimental Details

Initial attempts at carrying out nitrogen ion implantation in Mn metal lattice, (deposited through in-situ e-beam deposition) through Ar ion gun using nitrogen gas with 1KV acceleration voltage was carried out the ion gun was operated at rough vacuum. The sample ion current was observed to be 1.2 µA and a retardation potential of 0.5KV was supplied to prevent sputtering at the sample surface. The results of ion implantation technique were found to be insufficient in depositing a stable single phase manganese nitride in formation of metal nitride along with multiple nitrogen states. Hence, the use CVD deposition technique was proposed

Thin manganese and manganese nitride films were deposited on Tetra Ethyl Ortho Silicate (TEOS) sol-gel $SiO_2$ using CVD in IMEC. As the films are targeted for industrial applications, they were deposited under conditions relevant to industrial manufacturing processes. Manganese was deposited from bis(tetramethylcyclopentadienyl)manganese(II) = $C_{18}H_{26}Mn$ with the sample heated to 150°C and nitrogen partial pressure of 10 mbar while manganese nitride was formed using bis(2,2,6,6-tetramethylpiperidido)manganese(II), $Mn(tmp)_2$ = $Mn(NC_9H_{18})_2$, with ammonia as a co-reactant. To study the effect of nitrogen incorporation, a similar deposition process was carried out for purely metallic manganese films. Both the manganese metal and the manganese nitride films were deposited ex-situ i.e., outside the analysis chamber and exposed to the atmosphere in transit before analysis in our laboratory.

X-ray photoelectron spectroscopy (XPS) analysis was carried out using a VG Microtech electron spectrometer at a base pressure of 5 X $10^{-9}$ mbar. The photoelectrons were excited with a conventional Mg Kα (hv = 1253.6 eV) x-ray source and an electron energy analyser operating at 20 eV pass energy, yielding an overall resolution of 1.2 eV. All XPS curve fitting analysis presented in this study was performed using AAnalyzer curve fitting software program version 1.20. Si 2p spectra were fitted with Voigt doublet profiles with a Lorentzian value of 0.39 eV. O 1s and N 1s spectra were fitted with Voigt profiles with Lorentzian values of 0.55 eV, and 0.5 eV, respectively. Mn 2p spectra are fitted with Voigt – asymmetric profiles. A Lorentzian value of 0.87 eV was used to fit all Mn 2p spectra.

In agreement with previous work, the Mn 2p peaks shown in this study are primarily used to identify the presence of oxidised Mn species on the sample surface, with the O 1s and Si 2p spectra used to conclusively identify the presence of differing oxidised Mn species such as Mn silicate and Mn oxide[10]. A Shirley-Sherwood type background was used for all core level spectra. The gaussian width of the components used in curve fitting of various spectra has been tabulated. Following initial analysis, the films were thermally annealed at 200 °C and 400 °C in UHV at a pressure of 1 × $10^{-9}$ mbar, with samples maintained at the target temperature for 60 minutes, in order promote the formation of chemically stable compounds at the barrier layer – substrate interface.

All AFM images and the root mean square (RMS) surface roughness values were obtained from tapping mode measurements acquired by a Veeco Dimension 3100 atomic force microscope. The AFM silicon cantilever probes used were supplied by Budget Sensors with dimensions of: L x W x T = 125 x 30 x 4 $\mu m^3$, nominal resonant frequency = 300 kHz, force constant = 40 N/m, tip radius of <10nm, with an Al reflective coating. All images were analysed using Gwyddion software version 2.39 [11].

In order to test the adhesion of copper, approximately 80 nm of copper was simultaneously deposited on a TEOS substrate, a Mn metal film and a MnN film using hot-filament thermal evaporation in a Leybold Univex chamber at a vacuum pressure of 2×$10^{-6}$

mbar. A laser diced Si shadow mask with square structures of side dimensions 500 microns was used to define the copper capacitor structures simultaneously on the three substrates with a single deposition for direct comparative purposes. The samples were then analysed using a Bruker Dektak XT stylus profiler to test for uniformity and thickness of the deposited copper structures. Following the Dektak measurements, the samples were subjected to a tape test as an initial test of adhesion. The tape test was carried out by securing the samples to a glass slide using double sided tape and then placing the scotch tape 5912 over the samples, fully covering the surface. The tape is then peeled off in a single motion and the sample is viewed under an optical microscope for signs of delamination. A Keyence VHX 2000E 3D digital microscope was used to image the Cu structures before and after the tape test to ascertain whether the deposition of Mn-metal and Mn-nitride impacts on the adhesion of copper.

## 3.3 Results and Discussion

Initial attempts at the deposition of manganese nitride were carried out at DCU. Multiple attempts were carried out to successfully implant nitrogen into the manganese thin films. XPS spectra of N 1s after the multiple ion implantation attempts is shown in fig 3.1. The first attempt showed a strong N-O bonds rather than the expected Mn-N bonds in the -3 oxidation state for metal nitride. This may be due to the impurities in the nitrogen supply line.

Further attempts were carried out after most of the oxygen was purged from the supply line. XPS characterization shows that the resultant films despite have a strong metal nitride peak also show multiple nitrogen states. The metal nitride formed was removed on further thermal anneals. Hence the metal nitride formed can be assumed to be surface localized and not stable at high temperature.

Although, the ion implantation technique shows great promise in depositing manganese nitride in ultra-high vacuum, the main disadvantage is that the use of an ion gun

is largely incompatible with CMOS processing. For incorporation to Ultra Large-Scale Integration (ULSI) processes, the deposition of MnN by methods such as Chemical Vapour Deposition (CVD) or Atomic Layer Deposition (ALD) would be desirable.

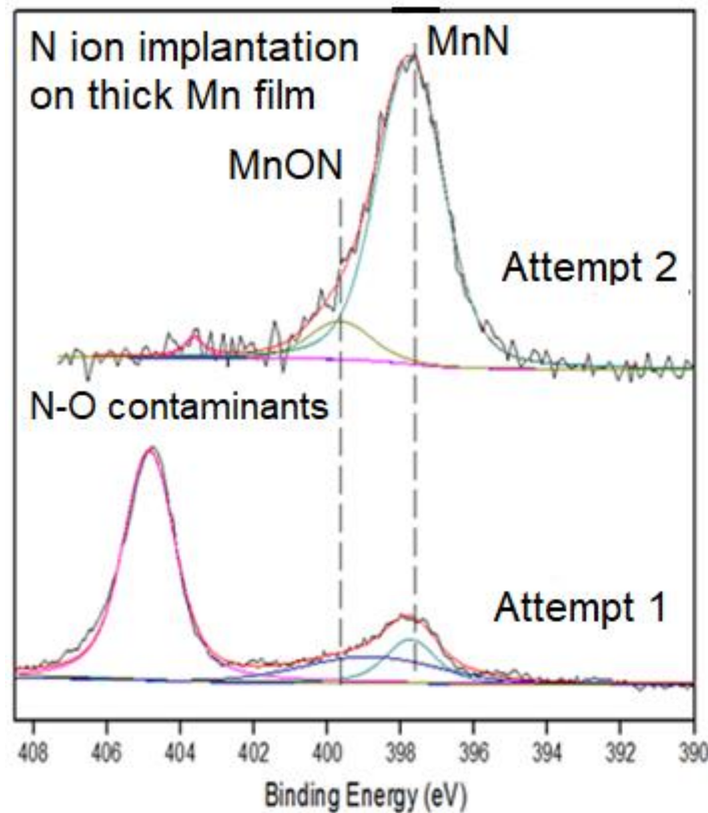


Figure 3.1: Initial ion implantation attempts of nitrogen into manganese films using in-situ ion gun implantation techniques

XPS survey spectra of the deposited manganese metal and nitrogen incorporated films are shown in figure 3.2. Similar peak profiles are acquired in both cases, however, the presence of a N 1s peak in the case of the nitrogen incorporated indicates that nitrogen was successfully incorporated during the CVD process. A Si 2p signal is detected during scanning of the nitrogen incorporated manganese film, indicating that the deposited film is sufficiently thin such that the TEOS is within the sampling depth of XPS.

The manganese metal and the nitride films show a significant oxygen signal indicating that both films are heavily oxidised by the time of measurement. Enthalpy data on bulk manganese

oxide and nitride have shown that manganese oxide has a larger enthalpy of formation than that of nitrogen incorporated[12] and so manganese oxide forms on both materials.

The presence of a silicon signal in the nitrogen incorporated films and not in the manganese metal films suggests that volume expansion of the manganese metal films upon ambient oxidation is more pronounced than that of the nitrogen incorporated films, despite being of the same nominal thickness during deposition. Overlayer thickness calculations carried out by observing the suppression of substrate peak area before and after nitrogen incorporated manganese films deposition, suggest that the thickness of the nitrogen incorporated films is 5 nm.

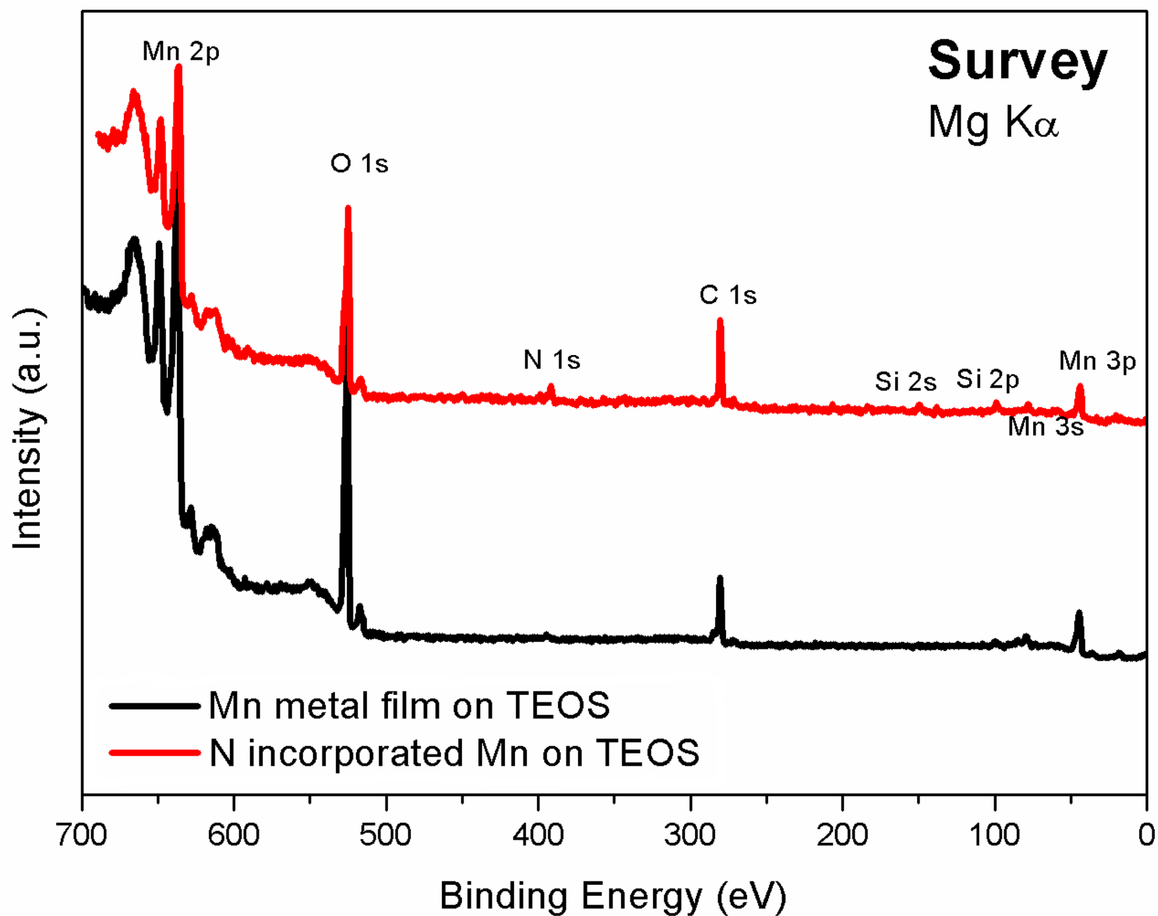


Figure 3.2: XPS survey spectrum of metallic manganese and nitrogen incorporated on TEOS showing the presence of N 1s in manganese nitride films while absence of N 1s in Mn metal films

In order to, determine the chemical composition of the sample, relative sensitivity factors need to be determined. The chemical composition of the nitrogen incorporated films,

displayed in Table 3.1, were calculated using the appropriate relative sensitivity factors and it was found that the films were predominantly comprised of manganese oxide, with a low concentration of nitrogen present (~ 5%).

| Nitrogen containing Mn on TEOS | Si (%) | O (%) | C (%) | Mn (%) | N (%) |
|---|---|---|---|---|---|
| Relative sensitivity factors | 0.15 | 0.66 | 0.25 | 0.22 | 0.42 |
| As received Normal emission | 3 | 41 | 25 | 25 | 6 |
| 60° Off Normal | 1 | 39 | 33 | 21 | 6 |
| 400°C Anneal Normal emission | 9 | 35 | 11 | 40 | 5 |
| Mn on TEOS | | | | | |
| As received Normal Emission | 1 | 51 | 23 | 25 | 0 |
| 60° Off Normal | 0 | 47 | 29 | 24 | 0 |
| 400°C Anneal Normal emission | 3 | 36 | 28 | 32 | 1 |

Table 3.1: Chemical composition of (i) nitrogen incorporated film - as loaded (Normal emission and 60° off normal) and annealed to 400 °C (ii) Chemical composition of manganese metal film - as loaded (Normal emission and 60° off normal) and annealed to 400°C

XPS measurements taken at an angle of 60° off normal emission which enhanced surface sensitivity indicate that the nitrogen, although only present in small concentrations, is homogeneously distributed through the film.

The carbon concentration increases at the higher take-off angle suggesting that the carbon present is from surface contamination. However, the carbon concentration of 25% at normal emission is higher than the typically recorded values for surface contamination and suggests that there may also be some carbon distributed throughout the film, possibly resulting from the CVD process.

Upon 400°C thermal anneal, as shown in fig 3.3, the nitrogen incorporated films show that the nitrogen concentration remains unchanged. However, with a reduction in carbon contamination we would expect an increase in both manganese and nitrogen signals if the

underlying substrate was unaffected by the anneal. We indeed see an increase in the Mn signal, but the nitrogen remains the same, and when compared with the manganese signal, is only approximately 50% of its original ratio. The oxygen concentration falls from 41% to 35% which, as discussed below, is ascribed to a reduction in the oxidation state of the manganese from +3 to +2. This reduction, in tandem with the removal of carbon from the surface (evidenced by the fall in carbon concentration from 25% to 11%) allows for the detection of a larger photoemission signal from the silicon substrate due to the thinner over layer. In contrast, the chemical composition calculations of manganese metal films shown in Table 3.1 (where no silicon signal was detected) display predominantly oxidised manganese and oxygen signals indicating the presence of high a percentage of manganese oxide rather than metallic manganese. The presence of a significant carbon signal further suggests the presence of unreacted chemical precursor from the CVD process as the nitrogen incorporated and manganese metal films undergo a similar deposition process. The increase in the C 1s signal in the Mn metal film after the anneal may be attributed to the presence of C contamination at the interface of the $SiO_2$ and the Mn metal film.

Upon the thermal anneal, the oxygen concentration falls from 51% to 36% in Mn thin films which is attributed to a reduction in the oxidation state of the manganese, which results in the thinning of the manganese oxide over layer. This thinning is confirmed by an increase in the Si 2p signal following anneal to 3% of the overall XPS signal, which suggests that more of the substrate now falls within the sampling depth of XPS owing to the thinner overlayer.

The manganese 2p spectra of both the as-received metallic manganese and Nitrogen containing Mn films shown in figure 3.4 both display peak profiles consistent with manganese oxide. As per previous studies, the metallic manganese is found to be in the mixed phase +3/+2 oxidation state[10].

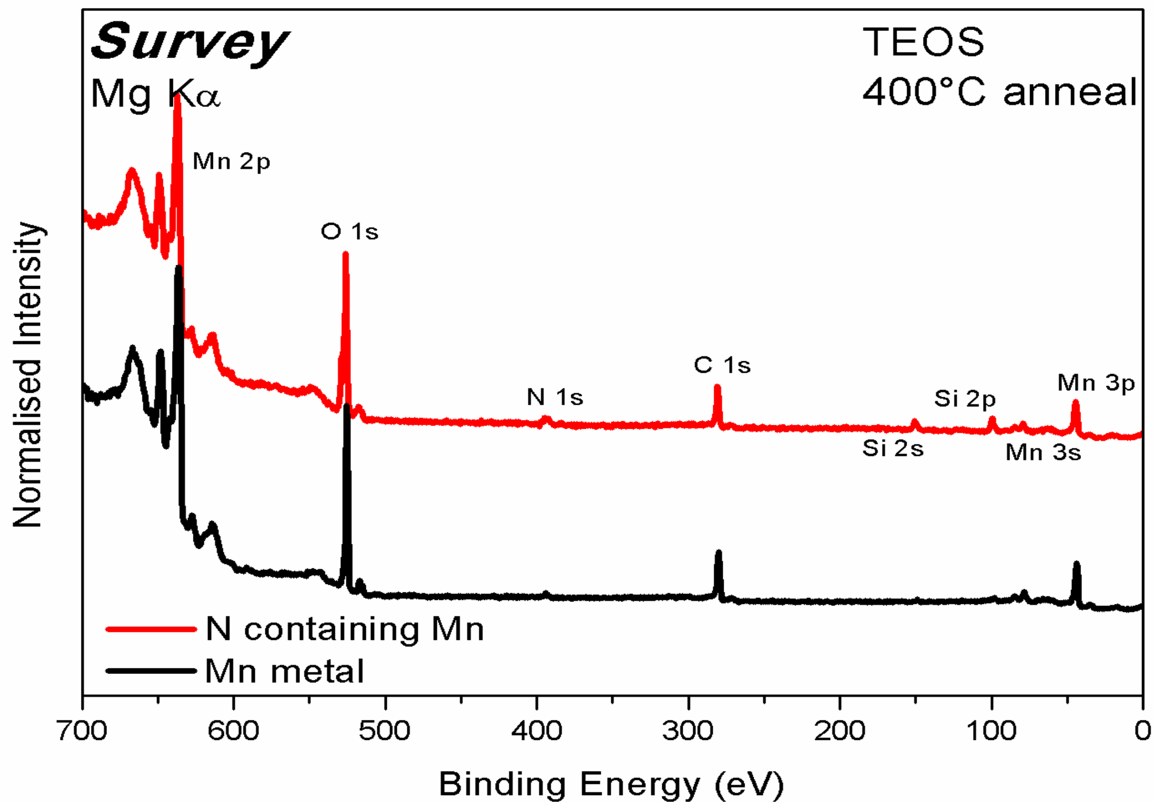


Figure 3.3: XPS survey spectrum of metallic manganese and nitrogen incorporated on TEOS after 400°C anneal

In order to better understand the chemical state of the manganese in Nitrogen containing Mn, peak fitting analysis was carried out following the parameters determined by Beisinger et al.,[13] to determine the oxidation state of the manganese in the film. From these parameters, the film is determined to be predominantly manganese (III) oxide. However, the peak at 638.8 eV binding energy indicates that there is a metallic Mn signal in the film. Despite the inclusion of six component peaks relating to the manganese (III) oxide and one peak relating to the residual metal, it is difficult to get an entirely accurate fit in the area ~642.5 - ~647.0 eV. This may be attributed to either small amounts of nitrogen incorporated dispersed throughout the film, or trace amounts of another Mn oxidation state beyond the manganese (III) oxide as previously discussed.

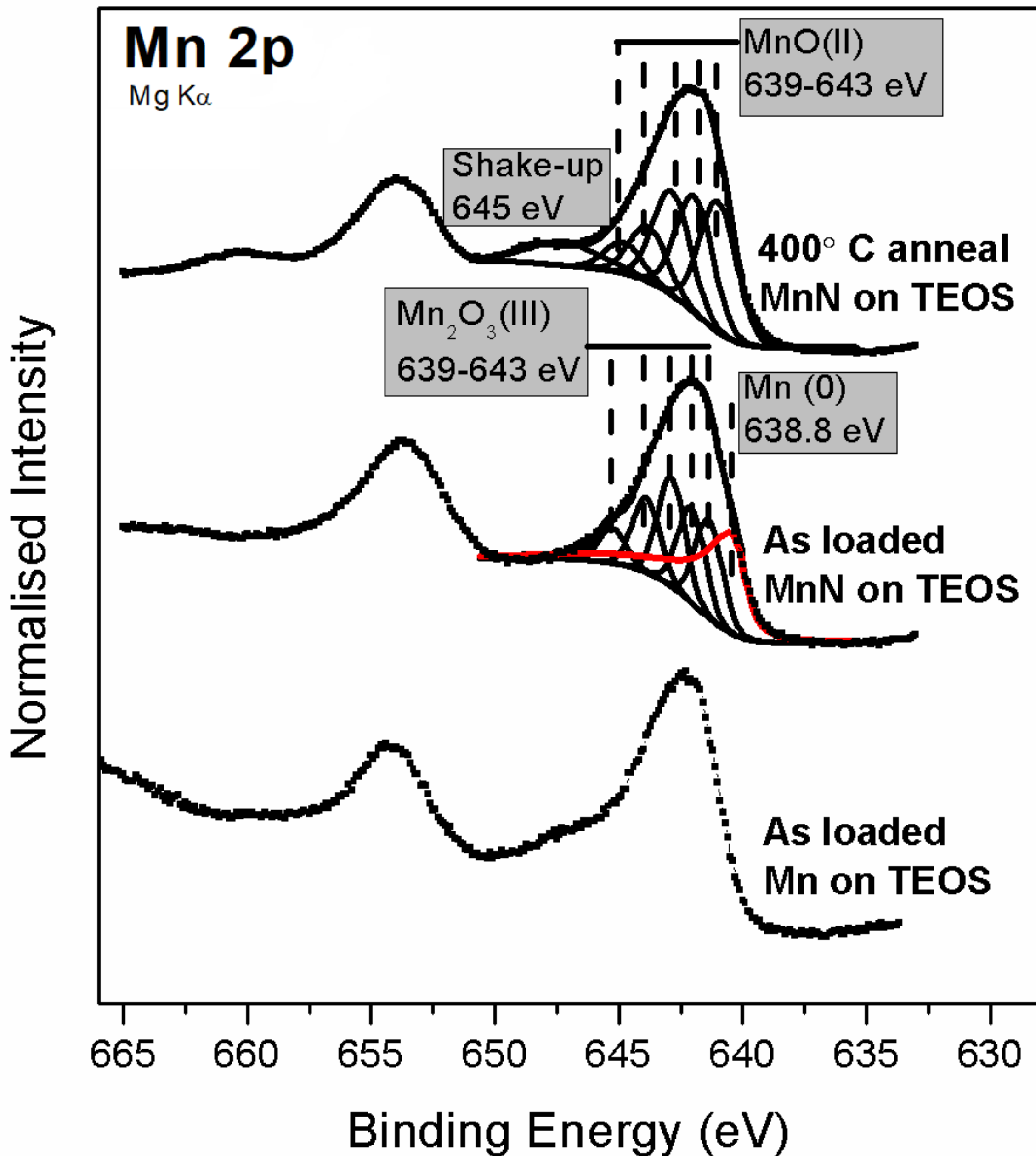


Figure 3.4: Manganese 2p spectra for the Mn and Nitrogen containing Mn film with fitted components (for Nitrogen containing Mn) before and after thermal anneal

The curve fitting parameters utilized are tabulated in table 3.2 below.

| Before anneal | | After anneal | |
|---|---|---|---|
| Peak position (eV) | Gaussian width (eV) | Peak position (eV) | Gaussian width (eV) |
| 641.3 | 1.25 | 640.3 | 1.7 |
| 643.5 | 1.30 | 641.5 | 1.7 |
| 644.3 | 1.30 | 642.3 | 1.7 |
| 645.3 | 1.30 | 643.2 | 1.7 |
| 646.4 | 1.25 | 645 | 3.5 |

Table 3.2: Curve fitting parameters for Mn 2p spectra

As it is difficult to unambiguously determine the precise oxidation state of the manganese in the nitrogen incorporated film from the Mn 2p spectrum, analysis of the Mn 3s spectrum, and in particular the splitting between the two constituent peaks could prove helpful in determining the oxidation of the manganese film. The Mn 3s spectrum of the as loaded film shown in figure 3.5 suggests that the manganese is present predominantly in the +3-oxidation state as evidenced by a peak separation of 5.5 eV[14]. Angle resolved spectra (not shown) which have an increased surface sensitivity display a reduction in the concentration of metallic manganese, indicating that the manganese metal is buried near the interface and protected by the overlying manganese oxide.

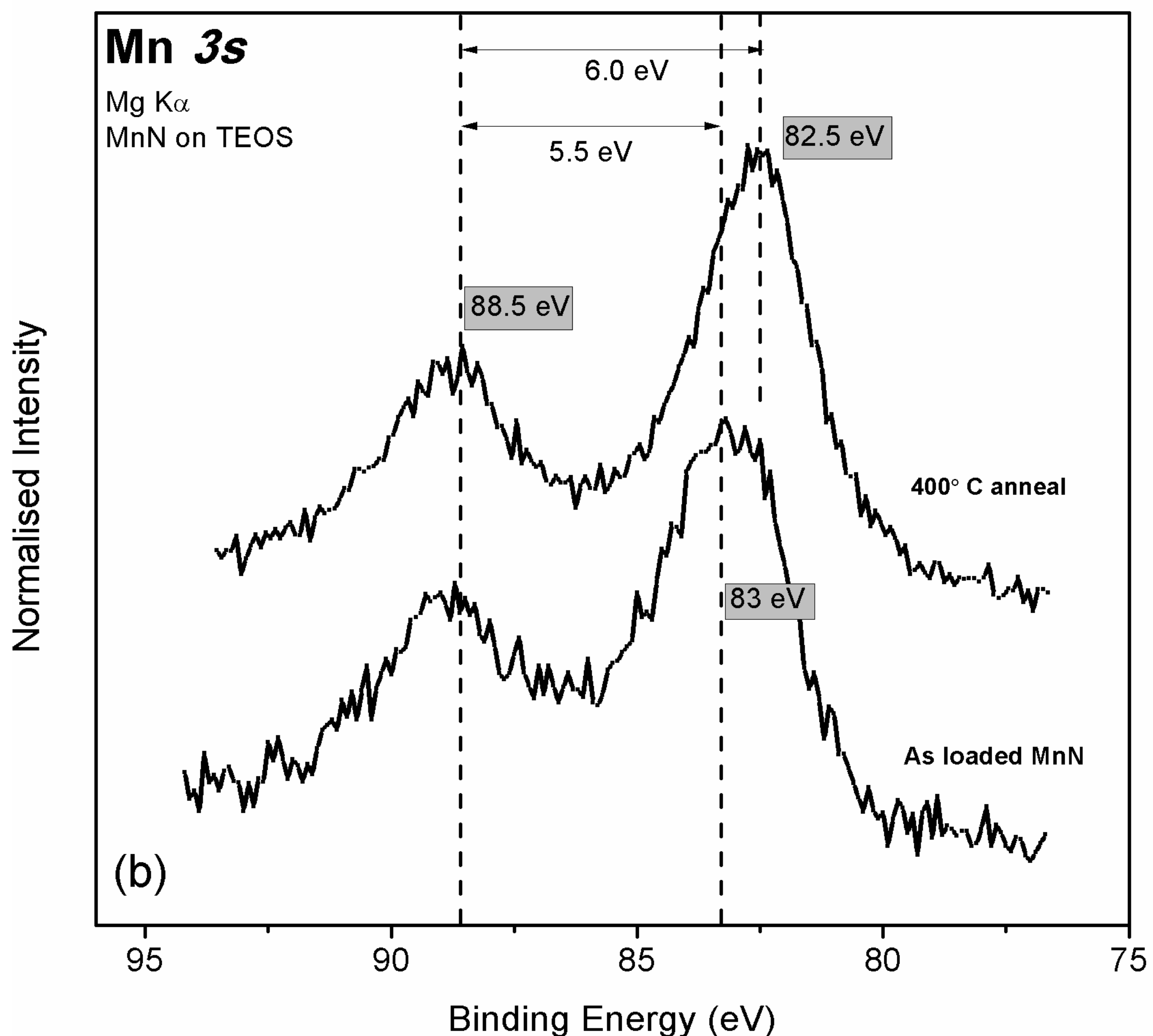


Figure 3.5: Mn 3s spectra from the Nitrogen containing Mn film showing the change of oxidation state from +3 to +2 on anneal

Upon 200°C thermal anneal, the Mn 2p peak profile changes significantly. This is attributed to the manganese (III) oxide being converted to manganese (II) oxide within the oxygen deficient environment of the UHV chamber. The presence of the distinctive shake-up feature at 645 eV is a strong indicator of Mn in a +2 oxidation state[13]. Fig 3.5 confirms this change in oxidation state of manganese on anneal. The Mn 3s spectrum splitting changes from 5.5 eV (+3 oxidation state) to 6 eV corresponding to +2 oxidation state [14].

Although, the Mn 2p and Mn 3s spectra are inconclusive in determining the presence of nitrogen incorporated as the film is predominantly oxidised, the N 1s spectra for a Nitrogen containing Mn sample is shown in figure 3.6 indicates the presence nitrogen in a single chemical state in the as loaded sample. Although the concentration of nitrogen is small as discussed above, the signal is strong enough to easily resolve the chemical state of the nitrogen. The nitrogen is in a single chemical state with a binding energy of 397 eV which is consistent with manganese-nitride in -3 oxidation state, as metal-nitrides have binding energies below 398 eV[15] in agreement with electronegativity values.

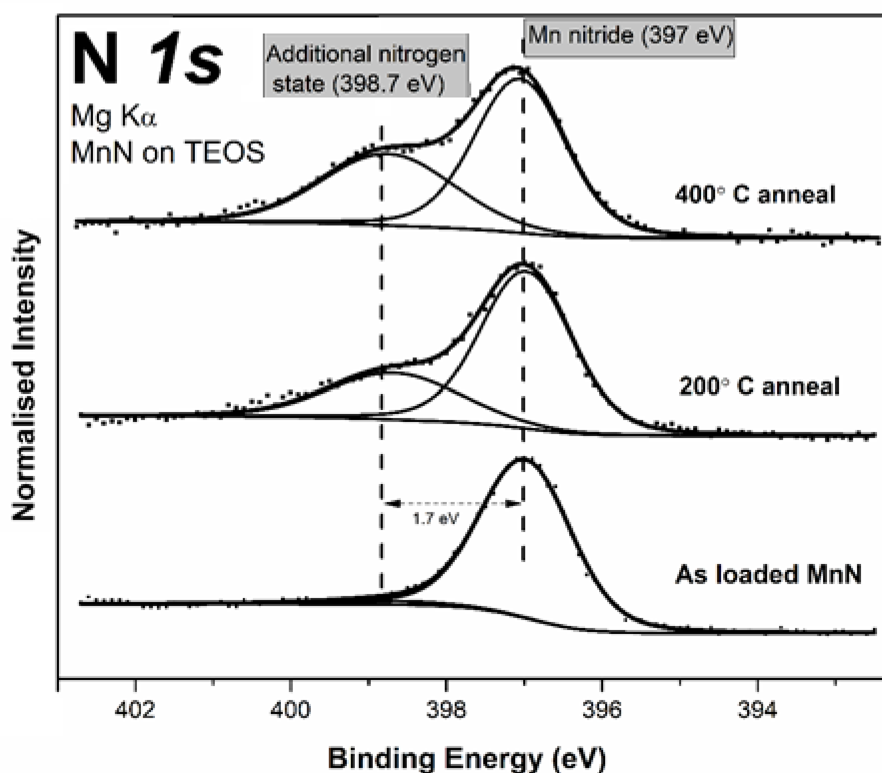


Figure 3.6: N 1s spectrum of nitrogen incorporated before and after anneals

Upon thermal annealing, we observe the growth of an additional component peak at 398.7 eV consistent with nitrogen in -2 oxidation state. As discussed above, thermal annealing causes the reduction of manganese from a +3 to a +2 oxidation state. This results in the expulsion of oxygen from the film, but the growth of the peak in the N 1s spectrum at a binding energy of 398.7 eV, is consistent with the partial decomposition of the Nitrogen containing Mn and a chemical interaction between the nitrogen in the film and the released oxygen resulting in the formation of a manganese oxynitride species. As the electronegativity of O is higher than that of N, adding O-N bonds to the Mn-N environment would result in the observed increase in the binding energy of the associated N atoms. The curve fitting parameters utilized were tabulated below.

| **Peak position (eV)** | **Gaussian width (eV)** |
|---|---|
| 397.0 | 1.4 |
| 398.7 | 1.7 |

Table 3.3: curve fitting parameters for N 1s spectra

The C 1s spectra shown in figure 3.7 shows three peaks at binding energies of 285 eV, 286.7 eV, and 288.6 eV corresponding to C-C, C-O, and C=O bonds respectively [16]. The chemical precursor for Nitrogen containing Mn deposition contains both manganese and nitrogen in the same molecule and as we deduced from composition calculations, there is evidence of the presence of some unreacted precursor in the deposited film. The C-C (285 eV) bond maybe attributed to the presence of both surface contamination and unreacted precursor while the C-N (286.7 eV) and C-O (288.6 eV) bonds are from the precursor. The thermal anneal reduces the amount of C-O and C=C bonds.

The enthalpy of formation of manganese carbide is low compared to that of manganese oxide[17]. If there is metallic manganese present in the film, it would be expected to readily form a metal carbide with the carbon present in the film [18]. The absence of carbide implies the absence of free metal present in the nitrogen incorporated film. However,

this conflicts with the fitting of the Mn 2p spectrum which requires a metallic component to arrive at an accurate fit. However, as mentioned the metallic component may correspond to manganese in a nitride state, which leaves no free metallic manganese to form Mn-carbide.

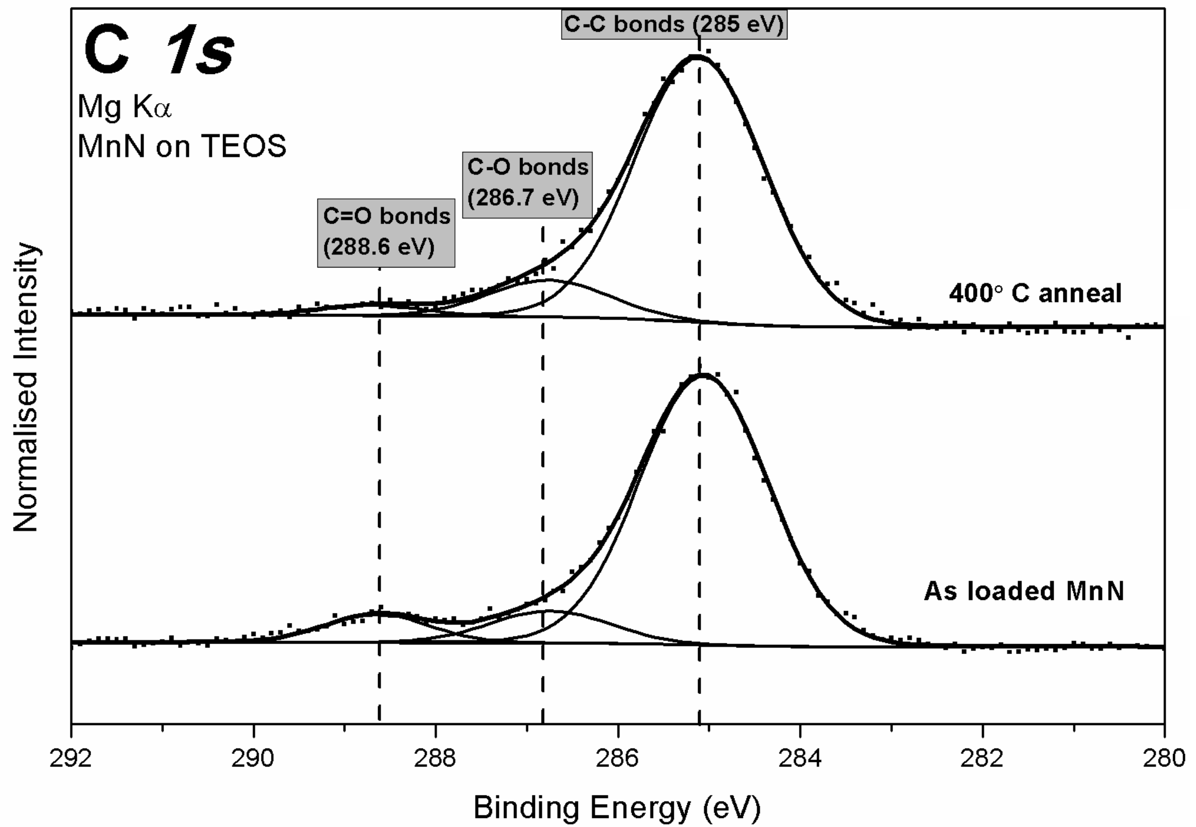


Figure 3.7: C 1s of Nitrogen containing Mn on TEOS XPS spectrum before and after 400°C anneal

The curve fitting parameters used for C 1s spectra are tabulated below:

| Peak position (eV) | Gaussian width (eV) |
|---|---|
| 285.1 | 1.5 |
| 286.7 | 1.3 |
| 288.3 | 1.1 |

Table 3.4: Curve fitting parameters for C 1s spectra

As well as being of interest for adhesion promotion, manganese based films have the potential to form $MnSiO_3$ at the interface with the ILD, which has been shown to be an effective copper diffusion barrier. The nitrogen incorporated films studied in this work show

manganese silicate formation as evidenced by analysis of the Si 2p displayed in Figure 3.8. The Si 2p spectrum shows a peak at 102.4 eV corresponding to manganese silicate as the $MnSiO_3$ binding energy position is 1.1 eV from the $SiO_2$ binding energy position (103.8 eV)[19]. The peak fitted profile of the O 1s spectra also suggests the presence of manganese silicate. Upon annealing, the surface concentration of the nitrogen incorporated films was removed and hence more of the substrate signal was detected. This can be evidenced by increase in peak area at 533.3eV and decrease in the signal to noise ratio of Si 2p spectra. In addition, the change in profile of the O 1s spectra confirms the conversion of Mn(III) oxide to Mn(II) oxide on vacuum anneal, as discussed above. The curve fitting parameters were also tabulated below.

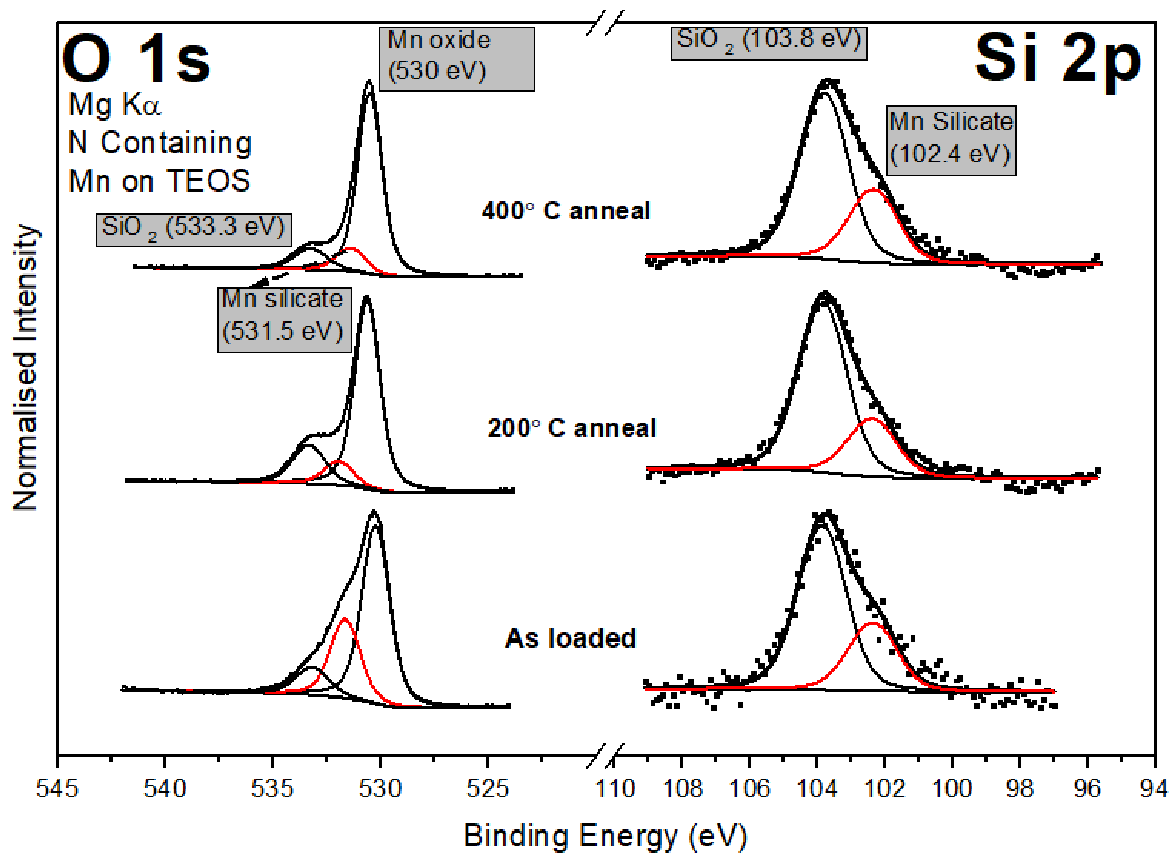


Figure 3.8: Si 2p and O 1s spectra showing the presence of manganese silicate following Mn deposition and the improved signal to noise upon anneal due to film thinning

| Peak position (eV) | Gaussian width (eV) |
| --- | --- |
| 103.8 | 1.39 |
| 102.4 | 1.70 |

Table 3.5: Curve fitting parameters for Si 2p spectra

One of the factors studied was whether the thickness and quality of $SiO_2$ substrate will affect the formation of Mn silicate barrier. For this study, three different substrates were used: thick thermally grown $SiO_2$ (dryox), sol-gel grown $SiO_2$ (TEOS) and native $SiO_2$ (Silane). As received substrate Si 2p spectra is shown in the figure 3.9. The dryox and TEOS substrates show single peak $SiO_2$ at 103.8 eV corresponding to +4 oxide and as there are no other peaks, there was no sub-oxides present after the deposition of $SiO_2$. While there is a small peak at 103.8 eV in the silane substrate, the bulk peak at 99.6 eV dominates which shows that the silane substrate is a native oxide as intended.

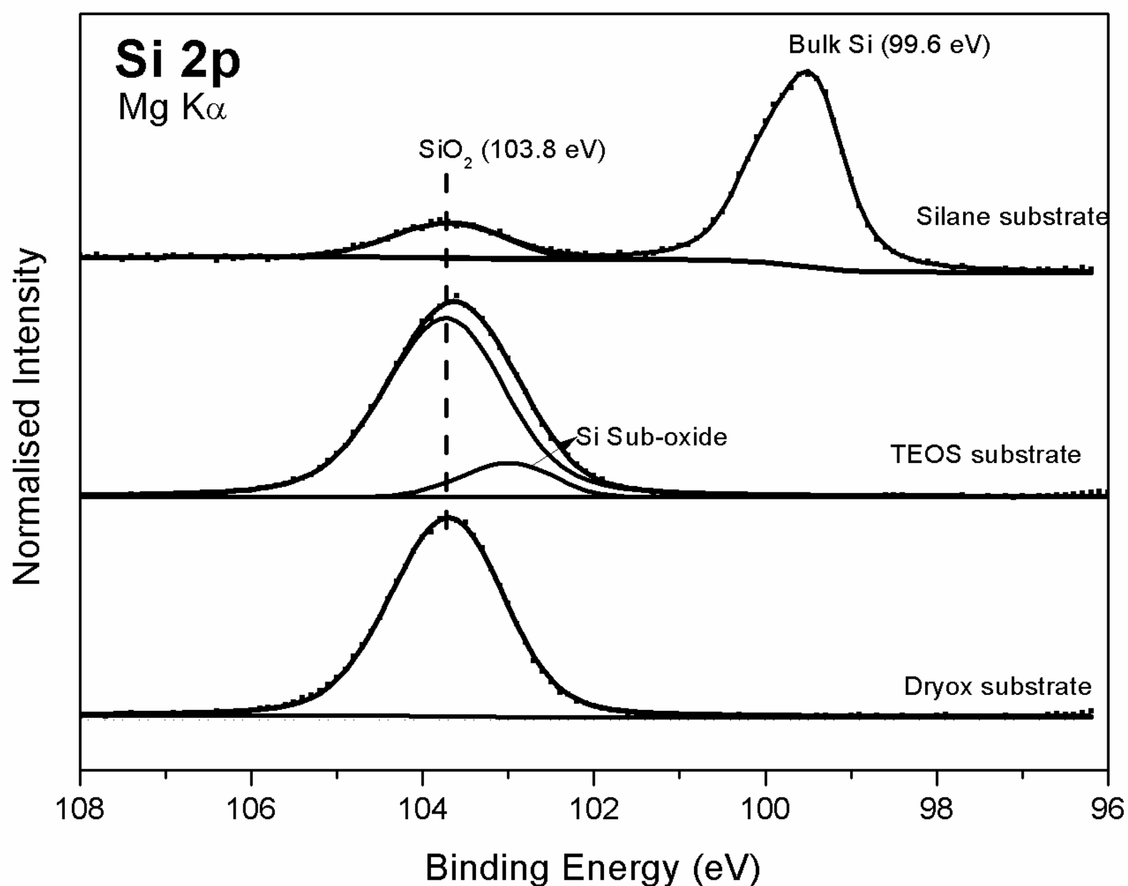


Figure 3.9: Si 2p spectra of as received substrates of (i) dryox (ii) TEOS (iii) Silane

The Si 2p spectra shown below in fig 3.10 indicate the presence of Mn silicate even at deposition process on all substrates. Even though the silane substrate is intended to be a thin $SiO_2$ as indicated in the fig 3.7, the deposition process involve the growth of more $SiO_2$ along with deposition of Mn film containing small amount of nitrogen and growth of Mn silicate similar to other $SiO_2$ based substrates. Although Mn silicate is formed on all substrates, the

ratio of peak heights of $SiO_2$: Mn silicate is more on the dryox substrate compared to TEOS and silane.

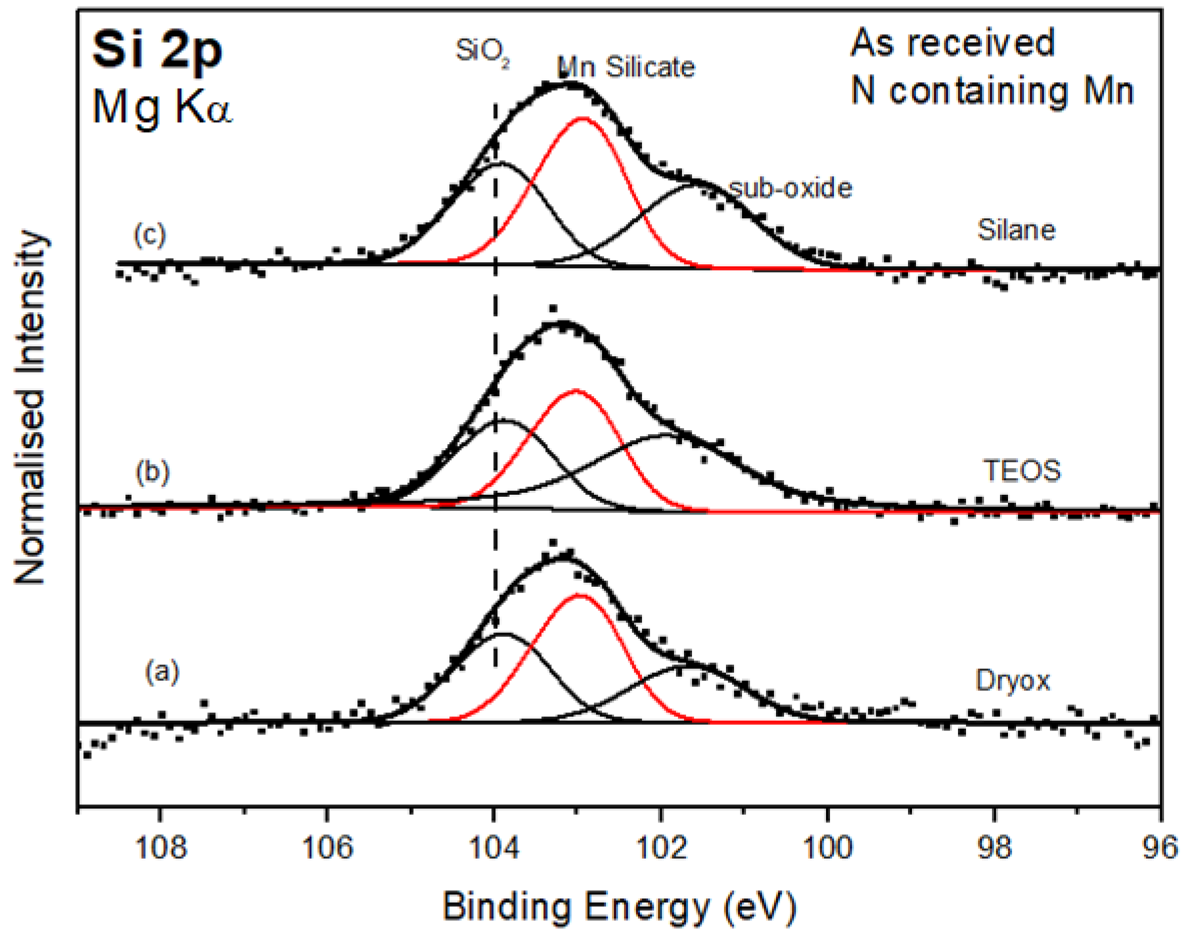


Figure 3.10: Si 2p spectra of as received nitrogen containing Mn films on (i) dryox (ii) TEOS (iii) Silane

| Peak position (eV) | Gaussian width (eV) |
| --- | --- |
| 103.8 | 1.1 |
| 102.5 | 1.0 |
| 101.3 | 1.4 |

Table 3.6: curve fitting parameters for Si 2p on all 3 substrates

Upon annealing, the growth of the manganese silicate is similar in all three substrates. Since the ratio of the manganese silicate to the $SiO_2$ peak area is more in dryox substrate than in the silane and TEOS substrate, the quality of the $SiO_2$ grown does affect minimally the growth of manganese silicate barrier at the interface before and after anneal.

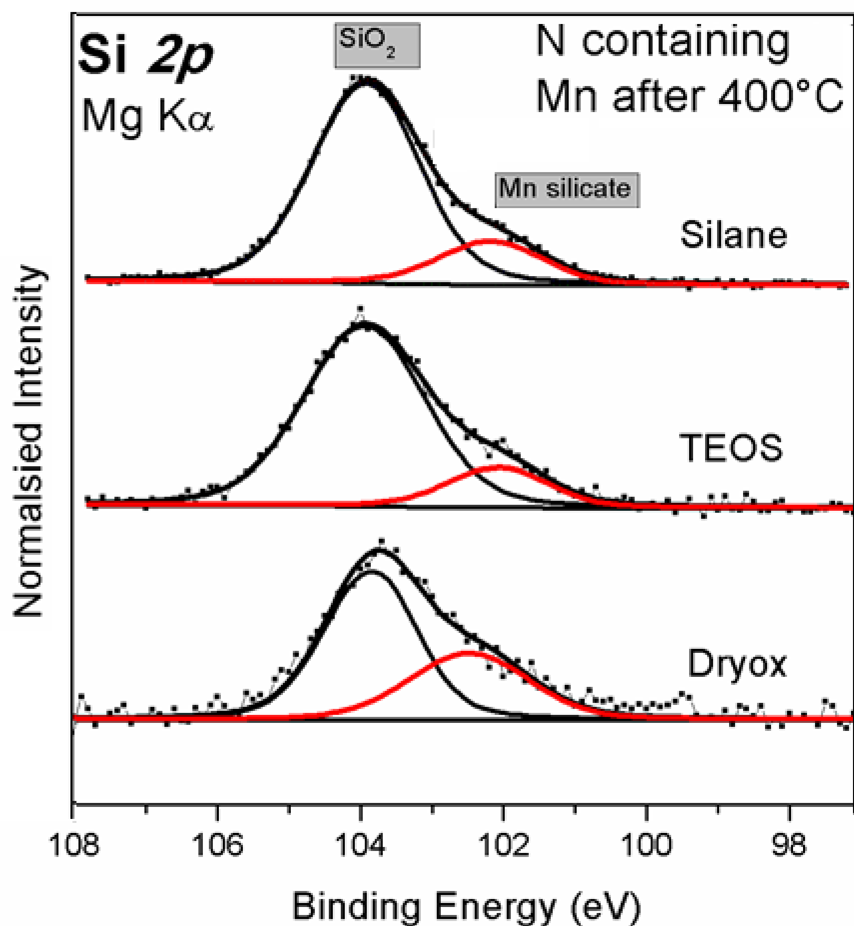


Figure 3.11: Si 2p spectra of 400°C annealed nitrogen containing Mn films on (i) dryox (ii) TEOS (iii) Silane

| Peak position (eV) | Gaussian |
|---|---|
| 103.8 | 1.1 |
| 102.5 | 1.0 |

Table 3.7: curve fitting parameters for Si 2p on all 3 substrates after anneal

Most of the manufacturing processes include surface treatments and one of the most used surface treatment process is degas of the substrate before and after the deposition process (pre and post bake treatments) to control the amount of surface moisture present during deposition. Herein we studied the effect of substrate degas on growth of manganese silicate. Fig 3.47 show the as deposited N containing Mn films on both degassed and non-

degassed TEOS substrates. Mn silicate grows equally on both substrates with and without degas during deposition conditions.

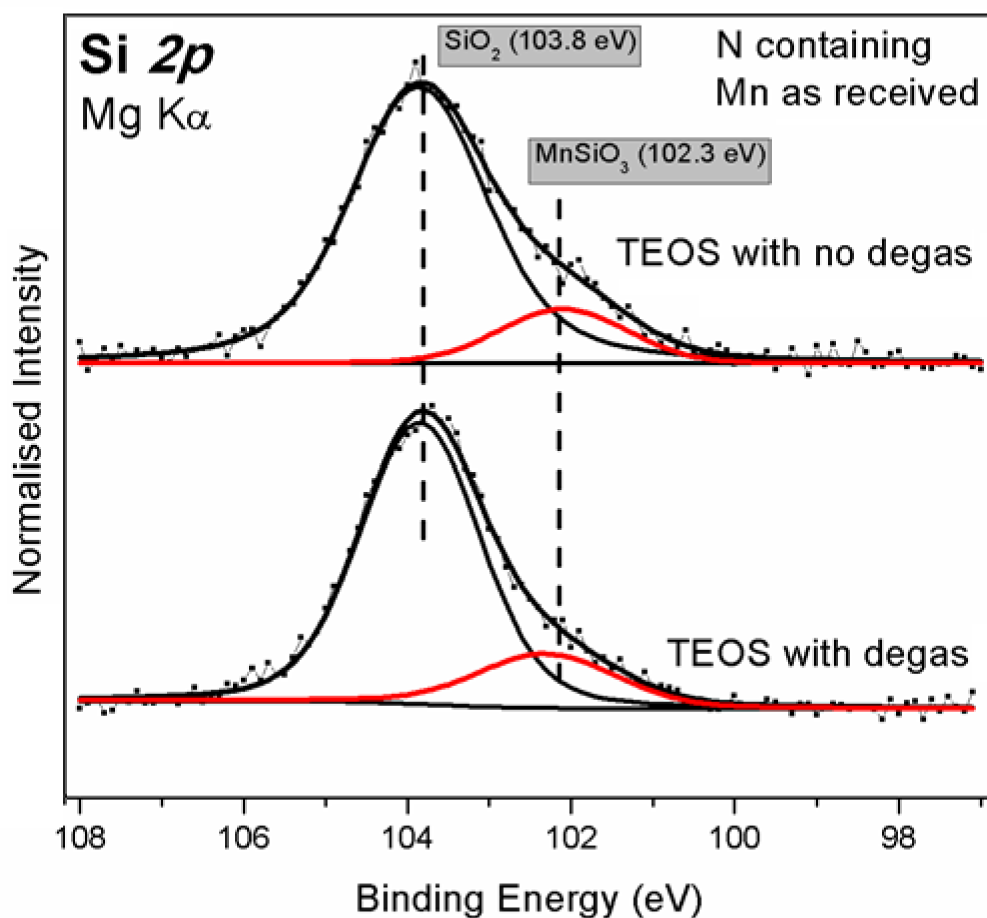


Figure 3.12: Si 2p spectra of as received nitrogen containing Mn films on (i) TEOS with degas substrate (ii) TEOS with no degas substrate both showing the presence of Mn silicate barrier upon deposition

| Peak position (eV) | Gaussian |
|---|---|
| 103.8 | 1.1 |
| 102.5 | 1 |

Table 3.8: curve fitting parameters for Si 2p before anneal on sample with and without degas

Upon annealing, there was a considerable growth of Mn silicate on TEOS with no degas substrates while a minimal growth on TEOS with degas substrate. This can be attributed to the presence of more moisture which serves as an oxygen promoter for the formation of more Mn silicate. In the degassed substrate, less moisture leads to minimal growth of Mn silicate. Hence, the surface treatment, especially substrate degas, affects the growth of the barrier layer. The fitting parameters were maintained the same as before annealing.

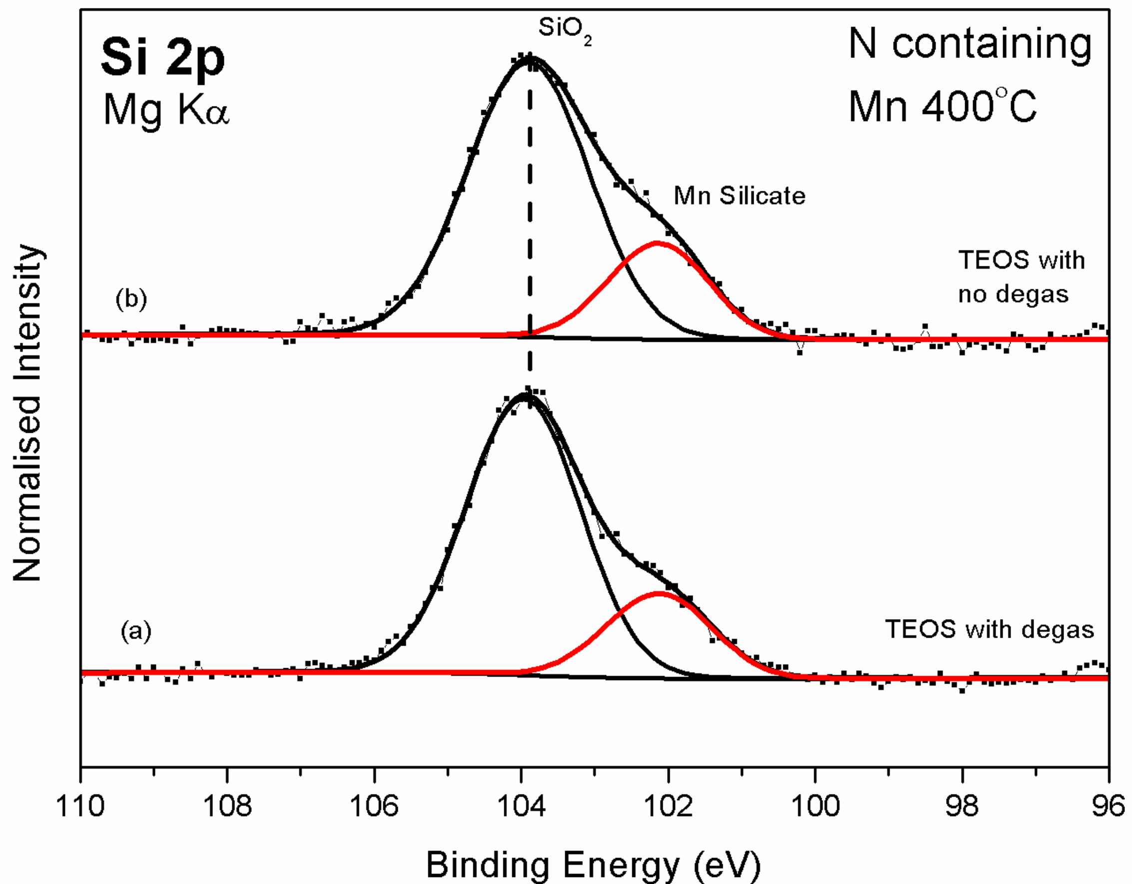


Figure 3.13: Si 2p spectra of 400°C annealed nitrogen containing Mn films on (a) TEOS with degas showing minimal changes to barrier signal (b) TEOS with no degas showing evolved Mn silicate signal

As most of the samples observed are ex-situ prepared, the manganese films are mostly oxidised compared to the intended manganese nitride. To study if the oxidation occurs during the deposition chamber or during transfer, a Ta capped sample was analysed. The Mn 2p spectra shown in the figure below, indicates the presence of broad peak at 641.6 eV indicate the presence of Mn oxide during deposition. Although the presence of oxide is less compared to the uncapped samples, the strong peak at 638.8 eV indicate most of the film unoxidized and the transfer process causes most of the oxidation of the thin films.

While the changes in the oxidation state of Mn 2p spectra were observed, the TaN capped nitrogen incorporated Mn sample does not show any significant change on high temperature anneals.

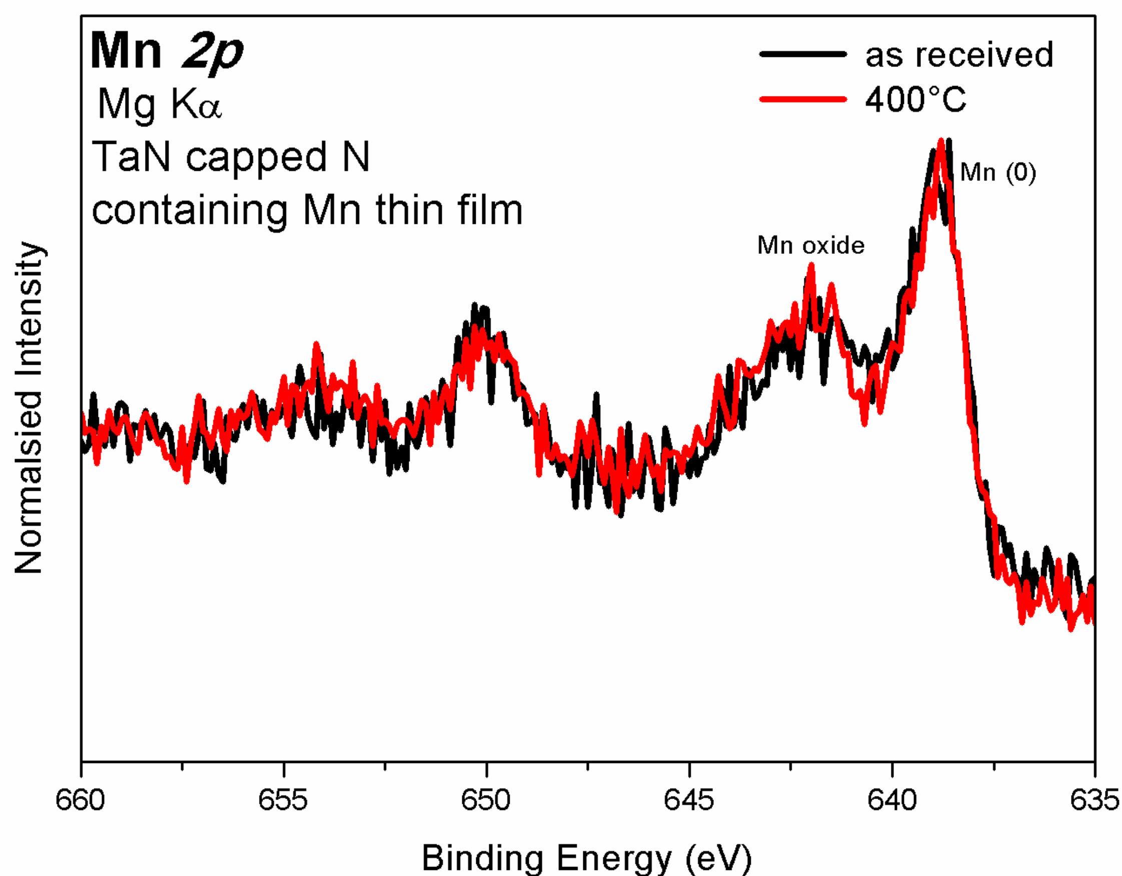


Figure 3.14: Mn 2p spectra of TaN capped N containing Mn film before and after 400°C showing no significant changes on anneal

N 1s and Ta 4p transitions were close to each other from the binding energy perspective. Hence it is difficult to discern the presence of metal nitrides whether they be manganese nitride or tantalum nitride. Hence an alternate metal cap required to study the presence of manganese nitride.

To investigate the impact of nitrogen on the surface morphology and roughness of the films, atomic force microscopy measurements were carried out on the samples. A 2D Fourier transform was used to remove the noise frequency during the scans. The images were then flattened to get an absolute zero point. Figure 3.50(a) shows the AFM image of the Mn metal film after annealing. The surface of the manganese metal films displayed an RMS roughness of ~5 nm. However, in the nitrogen incorporated films shown in figure 3.50(b), the surface was more the surface profile displayed an RMS roughness of <1 nm). It is clear from the images that even a small amount of nitrogen contributes significantly to lowering the roughness of the films. This may be due to more uniform oxidation of the Nitrogen containing

Mn film compared to the metallic Mn film, as both films are heavily oxidised upon air exposure.

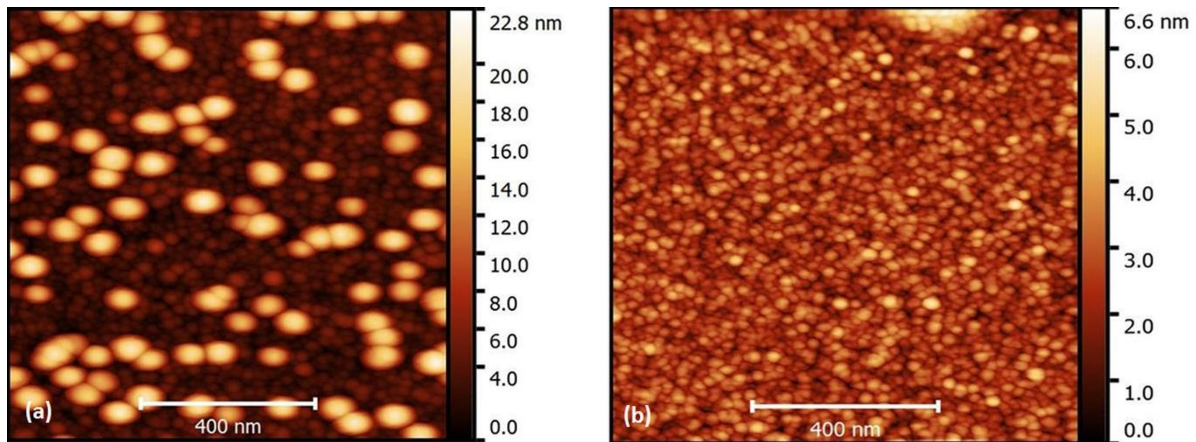


Figure 3.15: AFM images of (a) Manganese metal film after 400°C anneal (b) nitrogen incorporated after 400°C anneal

In order to examine the effect of Nitrogen containing Mn on adhesion, conventional tape testing[20] was applied as a qualitative indicator of adhesion strength. Copper with a nominal thickness of 80nm was deposited using thermal evaporation through a shadow mask to form discrete structures with edge length of approximately 500 µm. Dektak profilometry measurements which are shown in figure 3.51 indicate uniform copper structures with comparable thickness on each sample after analysing multiple structures. The shadowing effects were observed due to the presence of Si shadow masks to deposit multiple Cu structures and the angular alignment of the sample from the filament.

The samples were affixed to a glass slide and a tape test was carried out on all three samples simultaneously using Scotch tape 5912. Low magnification (x100) microscope images of the test structures before and after the tape test are shown in figure 3.52. Initial images before the test show clear copper deposition on all three samples in keeping with the Dektak profiles.

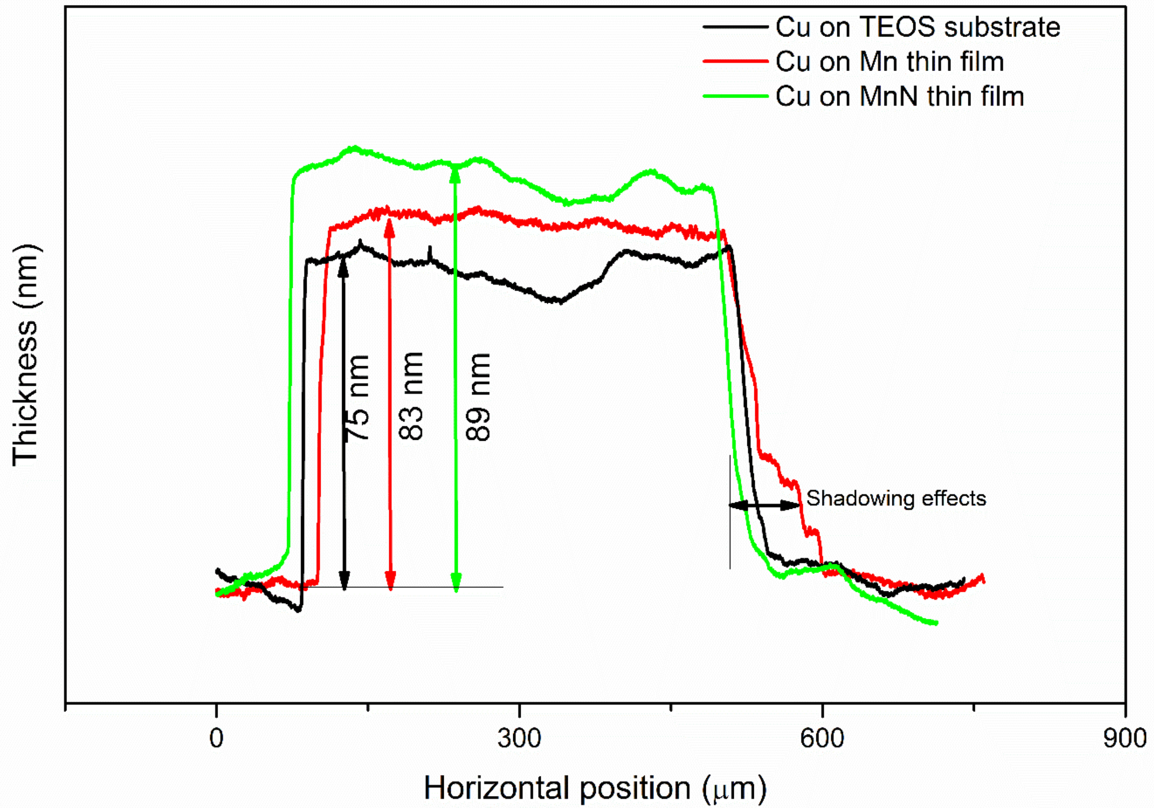


Figure 3.16: Profilometry measurements of thickness of Cu structures on (a) TEOS substrate (b) Mn thin film on TEOS (c) Nitrogen containing Mn thin film on TEOS

Following the tape test, the TEOS without any Mn based interlayer shows almost complete delamination of the deposited copper from two of the four structures that were tested. Samples with Mn metal show similar behaviour to the bare TEOS substrate, where again two of the structures show significant delamination. In the case of the Mn-nitride covered TEOS, there is almost no visible delamination, indicating that the adhesion of the copper to the underlying $SiO_2$ is indeed improved by Mn-nitride. It is noteworthy that despite having a nitrogen content of just 5% a noticeable improvement in adhesion is observed.

While it is evident that growth of stoichiometric Nitrogen containing Mn is extremely difficult given the propensity of manganese species to oxidation it appears that, at least in terms of improving adhesion, this parasitic oxidation doesn't degrade performance.

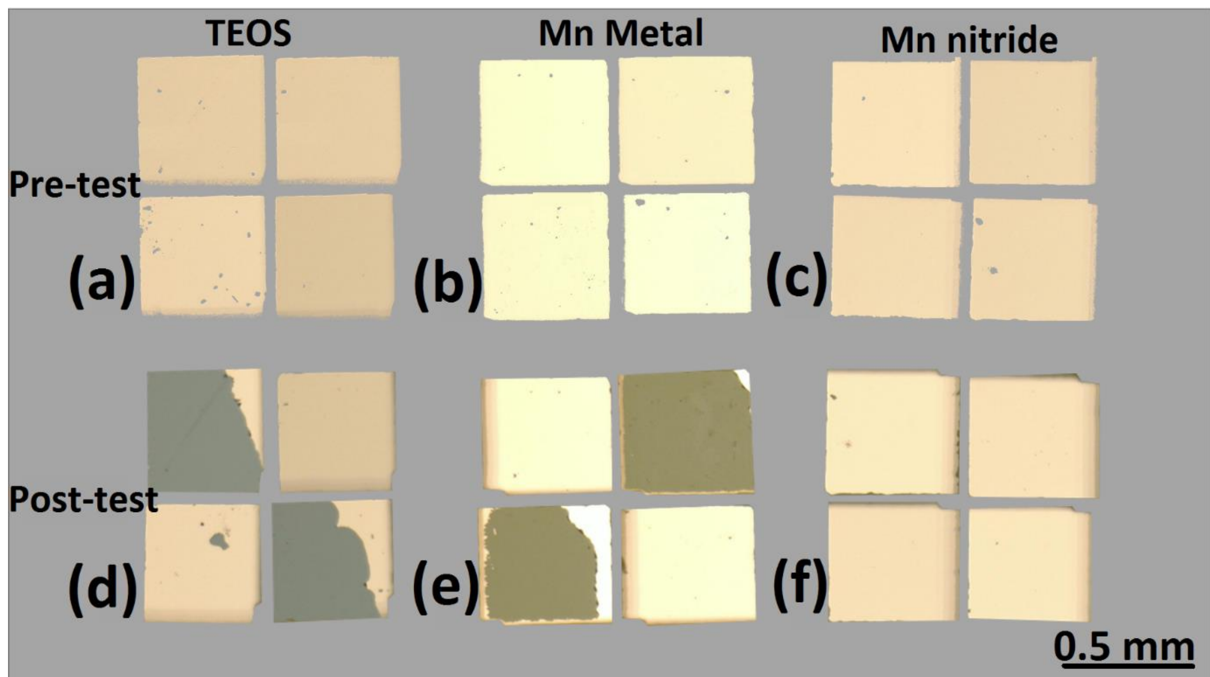


Figure 3.17: Optical Microscopy images of (a) Cu on TEOS before tape test (b) Cu on Mn metal film before tape test (c) Cu on Nitrogen containing Mn film before tape test (d) Cu on TEOS after tape test (e) Cu on Mn metal after tape test (f) Cu on Nitrogen containing

## 3.4 Conclusion:

In summary, the chemical composition of CVD Mn metal and Mn nitride thin films on TEOS $SiO_2$ substrates has been investigated by photoelectron spectroscopy. It has been shown that while both films are heavily oxidised by exposure to ambient conditions, the Mn nitride films contain ~5% nitrogen in the form of MnN homogenously distributed throughout the entire film. AFM indicates that the incorporation of the nitrogen improves the surface morphology of the overlayer compared to Mn metal films. Additionally, there is significant evidence of the formation of Mn silicate at the overlayer-substrate interface without the application of thermal anneal. In-vacuo thermal anneal up to 400 °C results in the reduction of the Mn oxide from +3 to +2 and the formation of trace amounts of Mn oxynitride within the nitride films. The adhesion studies using tape test shows that the copper structures MnN have better adhesion compared to that of the copper structures on the TEOS substrate or Mn metal film which helps in confirmation of improved adhesion in presence of 5% nitrogen in the film. Substrate degas affects the growth of the manganese silicate barrier layer as the

non-degassed substrate supports more manganese silicate growth than the degassed substrate after the high temperature anneal.

# References:


[1] M. Franz, R. Ecke, C. Kaufmann, J. Kriz, S.E. Schulz, Investigation of barrier formation and stability of self-forming barriers with CuMn, CuTi and CuZr alloys, 2015 IEEE Int. Interconnect Technol. Conf. 2015 IEEE Mater. Adv. Met. Conf. IITC/MAM 2015. 156 (2015) 95–97. doi:10.1109/IITC-MAM.2015.7325640.

[2] S.-M. Chung, J. Koike, Analysis of dielectric constant of a self-forming barrier layer with Cu–Mn alloy on TEOS-$SiO_2$, J. Vac. Sci. Technol. B Microelectron. Nanom. Struct. 27 (2009) L28. doi:10.1116/1.3224884.

[3] J.G. Lozano, S. Lozano-Perez, J. Bogan, Y.C. Wang, B. Brennan, P.D. Nellist, G. Hughes, Interdiffusion and barrier layer formation in thermally evaporated Mn/Cu heterostructures on $SiO_2$ substrates, Appl. Phys. Lett. 98 (2011) 1–4. doi:10.1063/1.3569146.

[4] C. Byrne, B. Brennan, A.P. McCoy, J. Bogan, A. Brady, G. Hughes, In Situ XPS Chemical Analysis of $MnSiO_3$ Copper Diffusion Barrier Layer Formation and Simultaneous Fabrication of Metal Oxide Semiconductor Electrical Test MOS Structures, ACS Appl. Mater. Interfaces. 8 (2016) 2470–2477. doi:10.1021/acsami.5b08044.

[5] K. Matsumoto, K. Neishi, H. Itoh, H. Sato, S. Hosaka, J. Koike, Chemical vapor deposition of mn and mn oxide and their step coverage and diffusion barrier properties on patterned interconnect structures, Appl. Phys. Express. 2 (2009) 063503. doi:10.1143/APEX.2.036503.

[6] T.O. Hiroyuki Shimada, Ichiro Ohshima, Takeo Ushiki Shigetoshi Sugawa, Tantalum Nitride Metal Gate FD-SOI CMOS FETs, IEEE Trans. Electron Devices. 48 (2001) 1619–1626.

[7] K. Holloway, P.M. Fryer, C. Cabral, J.M.E. Harper, P.J. Bailey, K.H. Kelleher, Tantalum as a diffusion barrier between copper and silicon: Failure mechanism and effect of nitrogen additions, J. Appl. Phys. 71 (1992) 5433–5444. doi:10.1063/1.350566.

[8] Y. Au, Y. Lin, R.G. Gordon, Filling Narrow Trenches by Iodine-Catalyzed CVD of Copper and Manganese on Manganese Nitride Barrier/Adhesion Layers, J. Electrochem. Soc.

158 (2011) D248–D253. doi:10.1149/1.3556699.

[9] Y. Sun, C. Wang, Y. Wen, L. Chu, M. Nie, F. Liu, Negative Thermal Expansion and Correlated Magnetic and Electrical Properties of Si-Doped $Mn_3GaN$ Compounds, J. Am. Ceram. Soc. 93 (2010) 650–653. doi:10.1111/j.1551-2916.2009.03482.x.

[10] M.C. Biesinger, B.P. Payne, A.P. Grosvenor, L.W.M. Lau, A.R. Gerson, R.S.C. Smart, Resolving surface chemical states in XPS analysis of first row transition metals, oxides and hydroxides: Cr, Mn, Fe, Co and Ni, Appl. Surf. Sci. 257 (2011) 2717–2730.

[11] D. Nečas, P. Klapetek, Gwyddion: An open-source software for SPM data analysis, Cent. Eur. J. Phys. 10 (2012) 181–188. doi:10.2478/s11534-011-0096-2.

[12] A.D. Mah, The Heats of Combustion and Formation of Two Manganese Nitrides, Mn5N2and Mn4N, J. Am. Chem. Soc. 80 (1958) 2954–2955. doi:10.1021/ja01545a012.

[13] J.C.V. I.S. Gilmore, Surface Analysis – The Principal Techniques 2nd Edition, Wiley 2009. doi:10.1002/9780470721582.

[14] V.R. Galakhov, M. Demeter, S. Bartkowski, M. Neumann, N.A. Ovechkina, E.Z. Kurmaev, N.I. Lobachevskaya, Y.M. Mukovskii, J. Mitchell, D.L. Ederer, Mn 3s exchange splitting in mixed-valence manganites, Phys. Rev. B. 65 (2002) 113102. doi:10.1103/PhysRevB.65.113102.

[15] J. Baltrusaitis, P.M. Jayaweera, V.H. Grassian, XPS study of nitrogen dioxide adsorption on metal oxide particle surfaces under different environmental conditions, Phys Chem Chem Phys. 11 (2009) 8295–8305. doi:10.1039/b907584d.

[16] K.D. Moulder, J. F., Stickle, W. F., Sobol, P. E. & Bomben, Handbook of X-ray Photoelectron Spectroscopy, (1995).

[17] K.K. Kelley, G.E. Moore, Specific Heats at Low Temperatures of Manganese Carbide and Manganese Dioxide 1, J. Am. Chem. Soc. 65 (1943) 782–785. doi:10.1021/ja01245a015.

[18] P. Casey, J. Bogan, G. Hughes, Photoemission study of carbon depletion from ultralow-carbon doped oxide surfaces during the growth of Mn silicate barrier layers, J. Appl. Phys. 110 (2011) 124512. doi:10.1063/1.3669998.

[19] P. Casey, J. Bogan, J.G. Lozano, P.D. Nellist, G. Hughes, Chemical and structural investigation of the role of both Mn and Mn oxide in the formation of manganese silicate barrier layers on SiO2, in: J. Appl. Phys., 2011. doi:10.1063/1.3630123.

[20] B.N. Chapman, ***Thin-film adhesion***, J. Vac. Sci. Technol. 11 (1974) 106–113. doi:10.1116/1.1318537.

# 4. Material and Electrical Characterization of Titanium and Manganese based Copper alloys as self-forming barrier layers for future copper interconnects

## 4.1 Introduction

As the chip size decreases with each generation of IC manufacturing, for better interconnect stack, the thickness of the barrier layer should be minimum, as the resistivity of barrier adds to the time delay of the entire device[1]. Also, the minimum thickness of the barrier adds more available area to the copper interconnect. The concept of self-forming barrier evolved with this aim and consequently research has been proposed on various metals/alloys replacing Ta/TaN stack as the self-forming barrier for copper interconnect[2]. One of the methods for depositing self-forming barriers and adaptable with current production technique is by deposition of copper based alloy and on anneal due to varying diffusivity of copper and the barrier metal, metal segregation occurs at all interfaces. The excess metal can then be removed from the copper surface while barrier is formed at the dielectric interface.

Various alloying metals have been proposed, like Mn[3], Ti[4], Zr[5] etc. Mn is found to be a good self-forming barrier metal forming manganese silicate[6] with dielectric on anneal while Ti is analysed in great deal[7] and has been used as the adhesion liner for previous generation of interconnects with Al. The alloying concentration of metal also plays an important role as the alloying metal might be more resistive compared to copper thus adding to the time delay.

The other advantage of the self-forming alloy barrier is the diffusion barrier itself acting as the adhesion liner, rather than a separate adhesion liner for copper metal. Initially a 5% Mn/Ti – Cu alloy was analysed. Although the resistivity was low, on anneal, both copper and copper alloys films delaminated indicating that the concentration of the alloying metal needs to be increased. The delaminated films after annealing are shown in the fig 4.1 below:

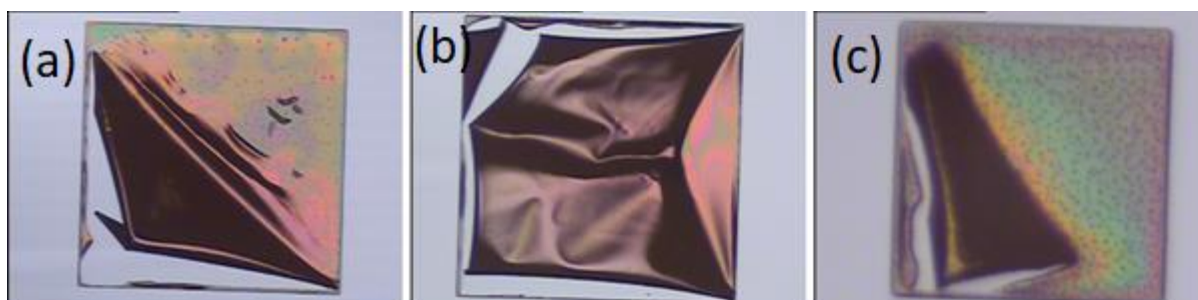


Figure 4.1: Delamination of (a) 5% CuMn (b) Cu and (c) CuTi on $SiO_2$ upon 400°C anneal

In this chapter, CuMn and CuTi alloys of 20% by wt were analysed for material composition as well as electrically to determinethe feasibility of the alloys as self-forming diffusion barrier. A pure copper film is deposited with similar deposition conditions and compared to the self-forming alloys.

## 4.2 Experimental Work:

Alloys of 20% CuMn and CuTi were deposited in the Tyndall National Laboratory using sputtering. Alloy targets are manufactured by Testbourne Ltd, UK. The blanket layers and the MOS structures are then analysed for material composition and electrical studies respectively.

Initial XPS characterization was carried out using conventional Mg Kα X-ray source (photon energy 1253.3 eV) and analyser parameters of 20 eV pass energy. The chamber pressure is maintained at $5 \times 10^{-9}$ mbar during the measurements. As the thickness of the alloy films were more than the sampling depth of conventional XPS, no substrate signal was detected. As a result, the study focusses more on the interface characterization using HAXPES measurements.

HAXPES measurements used in this work were carried out at the synchrotron source at DESY Hamburg, Germany. The photon energy used is 5900 eV while a 100 eV pass energy is used. The spot size of the X-ray beam was ~ 110 µm in diameter. Multiple spots were analysed to assess the uniformity of the deposited films while both CuTi and CuMn are loaded

on same sample holder to get identical annealing conditions. A pure Cu film was also analysed and compared with the alloy sample results.

Although the photoemission measurements determine the elemental characterization, cross sectional depth profile measurements were carried out using SIMS measurements of both as received and 400°C annealed samples. Combined measurements of HAXPES and SIMS allows for the characterization of the alloy – substrate interface of 20nm thick samples deposited under industrial manufacturing conditions.

Peak fits were performed for the photoelectron spectroscopy (both conventional XPS and HAXPES) using AAnalyzer curve fitting software program version 1.20. While Silicon (2p and 1s), O 1s and C 1s spectra were fitted using Voigt profile, metallic core level spectra are fitted using Voigt – asymmetric profiles. Shirley Sherwood type background fitting was used on peak profiles.

CV measurements were carried on the MOS structures of CuTi and CuMn 20% alloys using an Agilent 4156C Precision Semiconductor Parameter Analyzer with samples mounted on a Cascade Semiautomatic electrical probe station. As the sample holder itself acts as one of the electrical contacts (bottom contact with the substrate), only a single tip is used in the probe station as a top contact. Separate measurement runs for accumulation and inversion were carried out, each starting at V = 0. Similar split measurement runs starting at V = 0 were carried out for the IV characteristics as well.

## 4.3 Results and Discussions

Initial XPS measurements were taken on the 10 nm CuTi and CuMn samples. Fig 4.2 shows the as received Cu, CuTi and CuMn survey spectra. From the XPS survey spectrum, the presence of Cu, Ti, O and C in the CuTi alloy samples were observed while Cu, Mn, O and C are observed on CuMn samples. In both samples the substrate signal was absent as there is no peak corresponding to Si 2p at 100 eV and Si 2s at 150 eV[8] showing that the alloy film is thicker than the sampling depth of the conventional XPS system. Presence of multiple satellite

peaks ~945 indicate presence of copper oxide. A significant amount of oxygen is present in the spectra indicating the presence of Cu oxide and alloying metal oxides (MnO and $TiO_2$).

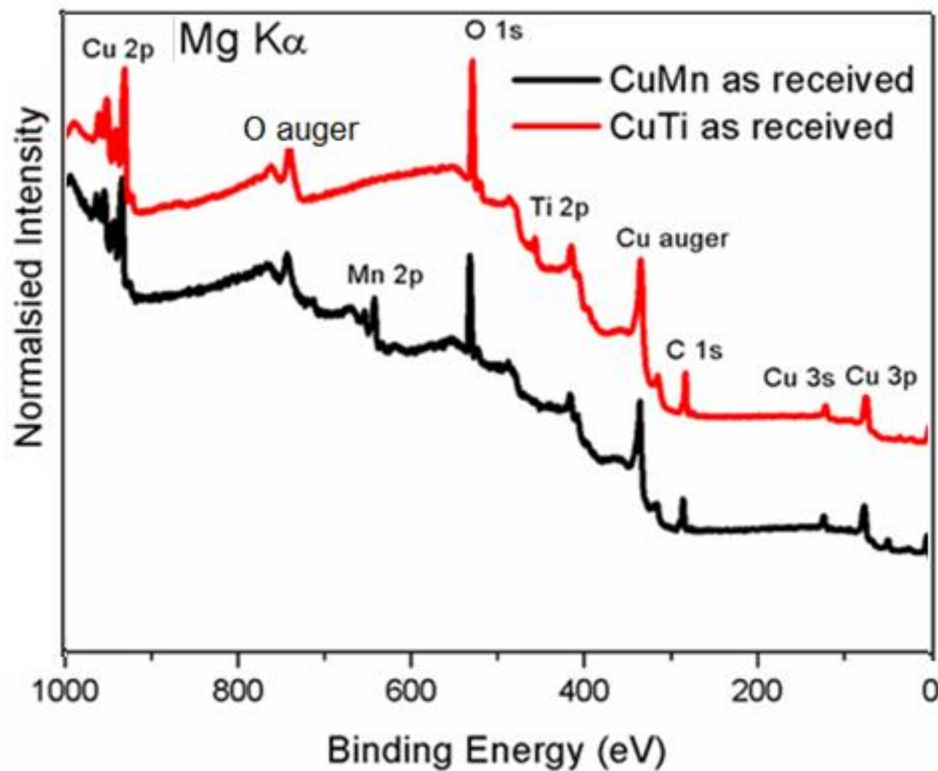


Figure 4.2: XPS Survey spectra of as received (i) 20% CuMn sample and (ii) 20% CuTi sample specifying the elements present in the sample

Fig 4.3 shows the annealed survey spectra indicating the increase in the alloying element (Ti/Mn) due to segregation of individual metals from the Cu alloys. It also shows decrease in the intensity of C 1s peak which can be attributed to the removal of carbon contamination at the surface of both CuMn and CuTi samples. The decrease in the O 1s peak intensity may be attributed to the reduction of copper oxide to metallic copper shown by the absence of satellite peak at ~945 eV after anneal and removal of surface contamination upon annealing. The detailed chemical compositions derived from the XPS measurements shown in table 4.1 indicate the decrease in oxygen concentration showing that the reduction of the metal after the anneal. The presence of high C 1s concentration after the anneal show that the C contamination is present throughout the film. The ratio of the Cu: alloy metal changes after the anneal indicating that the alloying segregate at the surface after the anneal.

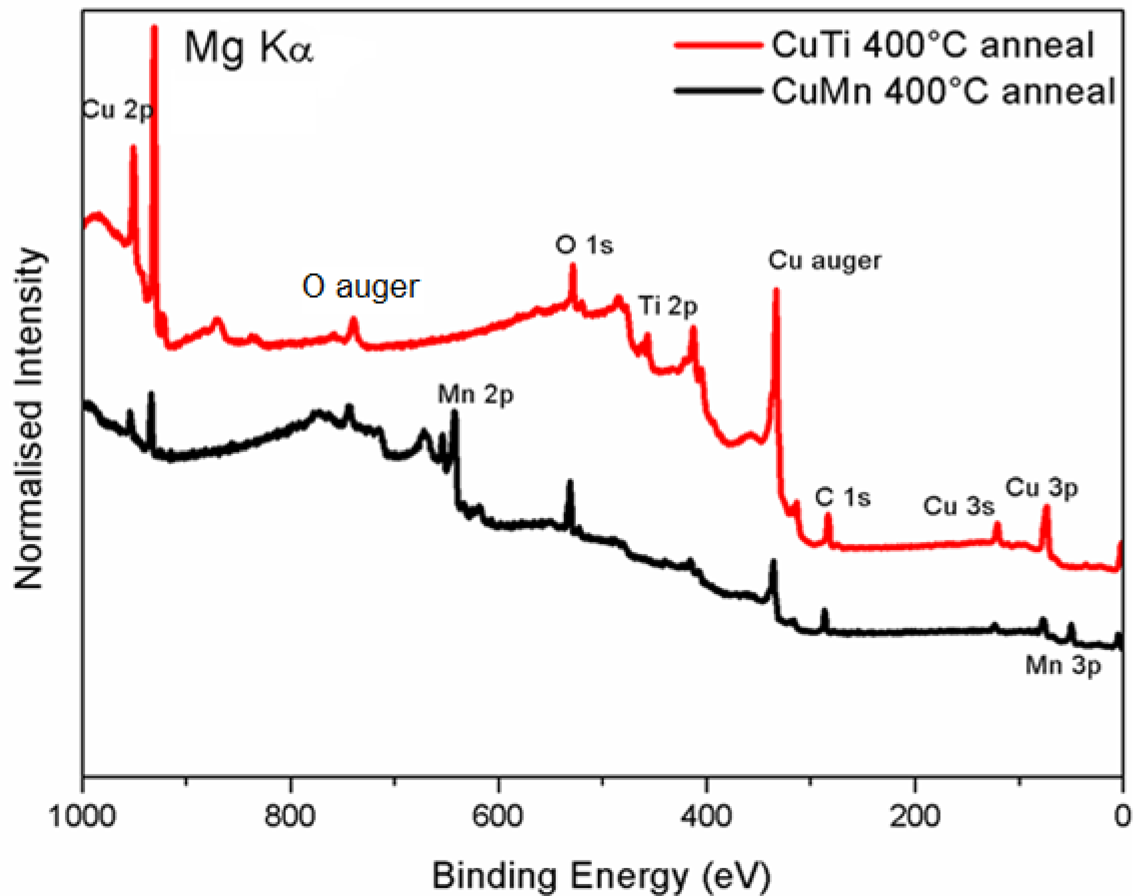


Figure 4.3: Annealed 20% CuMn and 20% CuTi XPS spectra showing metal segregation and surface copper oxide reduction to metallic copper on 400°C anneal

| | *O 1s (%)* | *C 1s (%)* | *Ti 2p (%)* | *Cu 2p (%)* |
|---|---|---|---|---|
| ***CuTi as received*** | 42 | 37 | 8 | 13 |
| ***CuTi 400°C anneal*** | 35 | 37 | 20 | 8 |
| | ***O 1s (%)*** | ***C 1s (%)*** | ***Mn 2p (%)*** | ***Cu 2p (%)*** |
| ***CuMn as received*** | 41 | 36 | 8 | 15 |

Table 4.1: XPS chemical composition of (i) CuTi as received and annealed (ii) CuMn as received and annealed

Although, both samples show segregation of alloying metal, there is more Mn segregation at the surface in CuMn sample after annealing compared to Ti in CuTi sample. The change in the ratios of Cu:Ti and Cu:Mn is shown in the table 4.2.

| | Cu | Mn |
|---|---|---|
| ***CuMn as received*** | 66 | 34 |
| ***CuMn 400C anneal*** | 8 | 92 |
| | ***Cu*** | ***Ti*** |
| ***CuTi as received*** | 78 | 22 |
| ***CuTi 400C anneal*** | 30 | 70 |

Table 4.2: XPS based calculations of Cu and metal ratios of CuMn and CuTi alloy samples before and after annealing

Table 4.2 shows the ratio of Cu and alloying metal in CuTi and CuMn alloy samples within the XPS sampling depth before and after the thermal anneals. Although, the initial alloy targets of CuMn were 80:20 ratio, the calculated chemical composition from the XPS measurements show the Cu/Mn ratio to be 66:34 which is the eutectic composition[9] for CuMn alloy. The CuTi ratio is calculated to be 78:22 which is similar to the specified elemental ratio in the sputter target (80:20). On anneal, as expected, the metal segregate at the surface. Cu:Mn ratio after anneal was found to be 8:92 while Cu:Ti ratio was 30:70.

The HAXPES survey spectra shown in fig 4.4 show the presence of the silicon substrate signal. The survey spectra also show presence of C 1s, O 1s and alloying metal (Mn 2p). Although the Cu 2p signal dominates the survey spectra, the narrow windows scans can easily detect the alloying elements. The 400°C anneal plot indicate the presence of more Mn 2p resulting from the metal segregation while the concentration of C 1s and O 1s peaks were reduced after the anneal through the reduction of the metal oxides and removal of surface contamination.

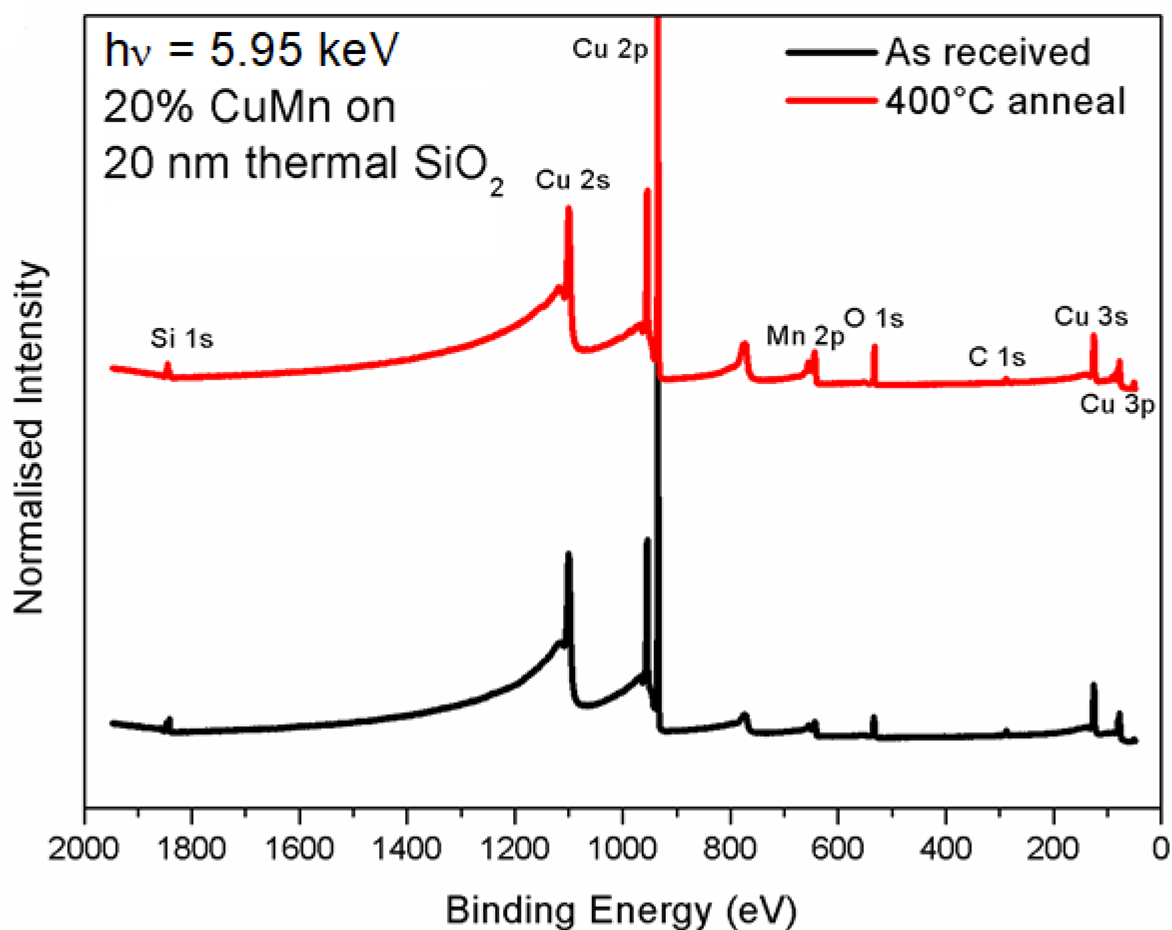


Figure 4.4: HAXPES Survey spectra of (i) 20% CuMn sample as received (ii) 20% CuMn sample after 400°C anneal

Cu 2p spectra before and after thermal anneal of CuTi sample shown in fig 4.5 indicate presence of CuO which is removed on anneal indicated by the narrow peaks and the absence of satellite feature at 945 eV binding energy. Although copper is reduced, the oxygen peak height remains the same. It indicates the possibility of the oxidation of alloy metal by the oxygen released by reducing the copper. While there are changes in the Cu 2p spectra of CuTi, there are minimal changes observed from Cu 2p spectra of CuMn before and after thermal anneals.

The HAXPES manganese 2p spectrum of the as loaded 20% CuMn sample (shown in fig 4.6) displays a peak profile consistent with manganese oxide. The manganese in CuMn alloy sample is found to be oxidised and in the mixed phase +3/+2 oxidation state (multiple

peak components between 639.5 eV and 643 eV) while the reference thick metallic Mn film forms Mn +4 oxide. However, the peak at 638.8 eV binding energy indicates that there is a metallic Mn signal in the film. Comparatively, the reference Mn film show definitive +4 Mn oxide as well as a strong Mn metallic peak[10].

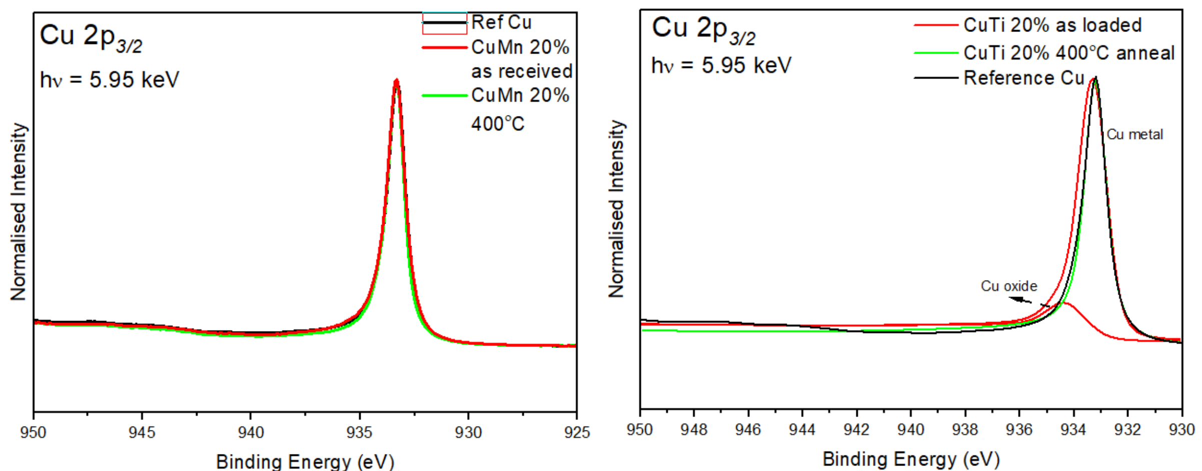


Figure 4.5: Cu 2p spectra of (a) reference Cu and CuMn alloy on $SiO_2$ before and after 400°C anneal indicate absence of Cu oxide (b) reference Cu and CuTi alloy on $SiO_2$ before and after 400°C anneal

Upon 400°C thermal anneal, the Mn 2p peak profile changes significantly. This is attributed to the manganese (III) oxide being converted to manganese (II) oxide within the oxygen deficient environment of the UHV chamber. The presence of the distinctive shake-up feature at 645 eV is a strong indicator of Mn in a +2 oxidation state [11]. Also, the metallic Mn peak at 638.8 eV decreases, showing that the oxygen released from reduction of +3 Mn oxide reacting with any residual metal present in the alloy film resulting in formation of more +2 Mn oxidation state (oxide/silicate).

O 1s spectra shown in fig 4.7 for the CuMn alloy, indicate the presence of multiple oxygen peak components in the as loaded sample. The $SiO_2$ substrate signal can be observed by the peak at 533.2 eV while the peak for metal oxide can be observed at 530.5 eV. The peak positions agree with the previous studies from our group[8]. As indicated in the XPS survey spectra shown in fig 4.2, there is a presence of copper oxide as well. As the sample is deposited by sputtering, presence of multiple sub-oxides as well as C-O bonds corresponding

to the peaks between 530 eV and 533 eV were observed in the as loaded sample. As the presence of multiple sub-oxides are present, the presence of manganese silicate cannot be determined with accuracy.

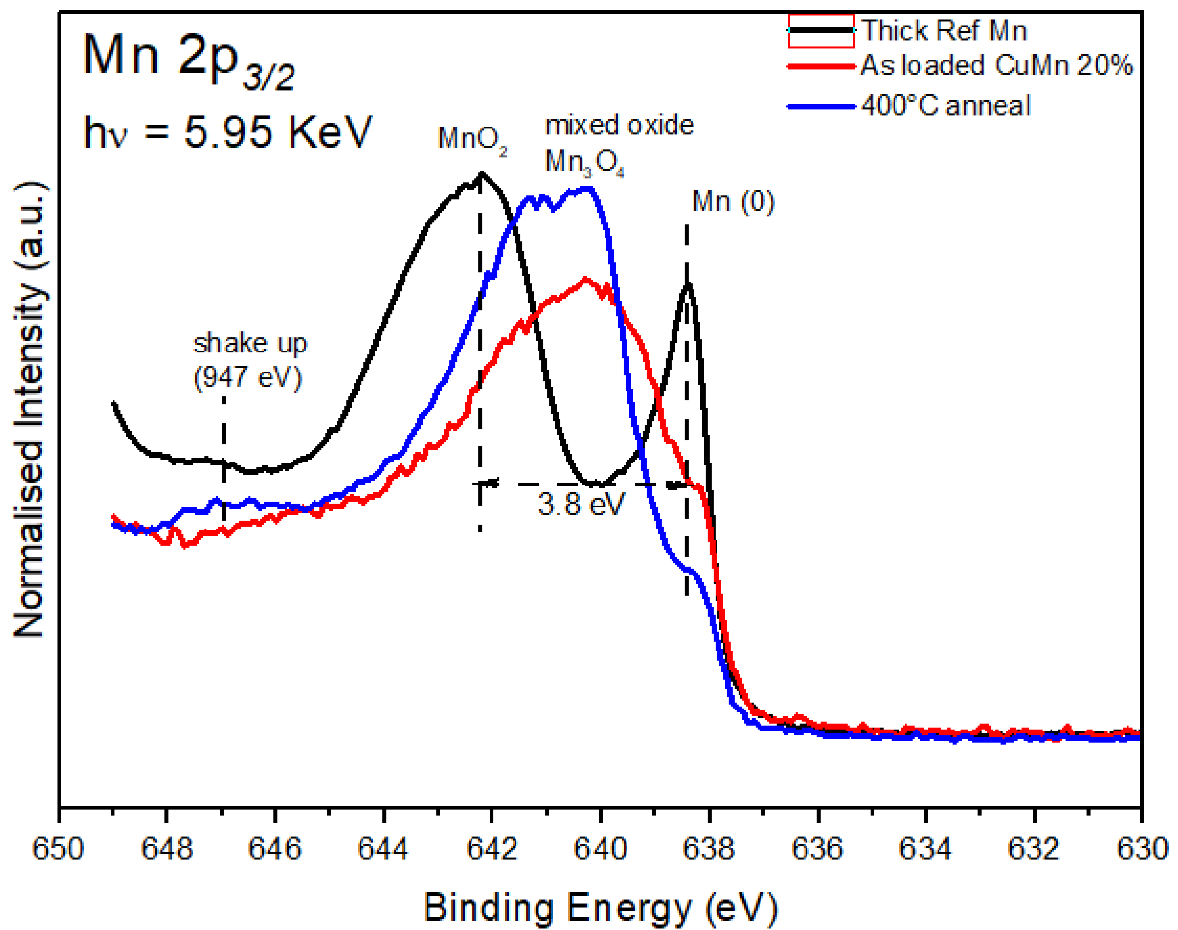


Figure 4.6: Mn 2p spectra of Thick Mn and CuMn alloy on $SiO_2$ before and after 400°C anneal showing the presence of shake-up feature after the anneal while Mn metallic signal is observed on before and after anneal samples

The anneal removes the multiple components due to sputter damage during the deposition (sputtering) as the process is considerably destructive at the interface and surface contamination. The 200°C annealed sample clearly shows the presence of manganese silicate at 532 eV which grows on further high temperature anneals. The peak positions are consistent

with the previous studies on manganese silicate. Annealed CuMn sample also shows the conversion of Mn +3 oxide to Mn +2 oxide.

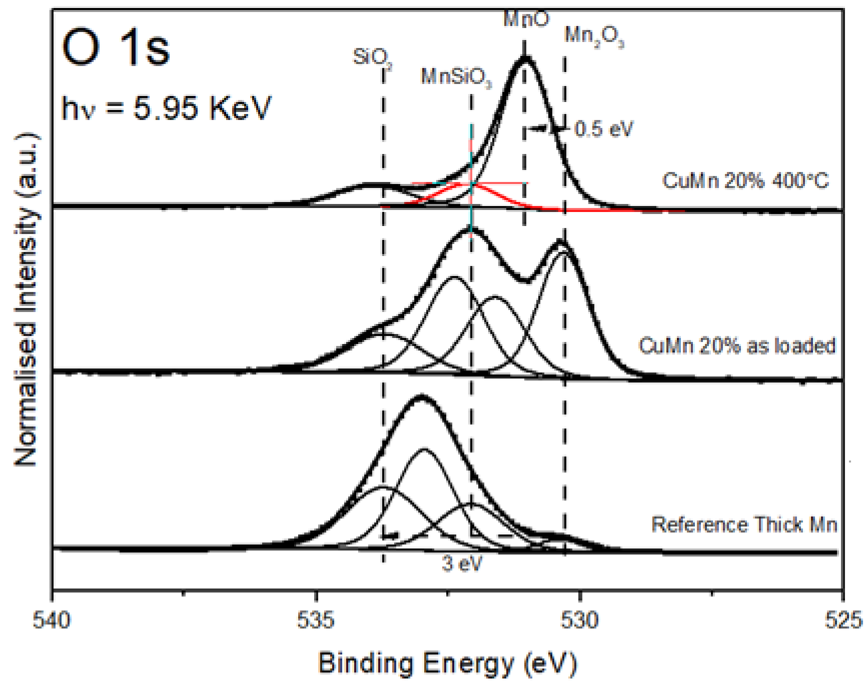


Figure 4.7: O 1s spectra of Thick Mn and CuMn alloy on $SiO_2$ before and after 400°C anneal showing the presence of Mn silicate barrier in the after anneal sample

| Before anneal | | After anneal | |
|---|---|---|---|
| **Peak poistion (eV)** | **Gaussian width (eV)** | **Peak position (eV)** | **Gaussian width (eV)** |
| 530.3 | 1.2 | 530.8 | 1.2 |
| 531.6 | 1.4 | 532.0 | 1.1 |
| 532.3 | 1.4 | 533.8 | 1.3 |
| 533.8 | 1.3 | | |

Table 4.3: Curve fitting parameters for O 1s spectra of CuMn sample before and after annealing

Si 1s spectra shown in fig 4.8 indicate that the signal is obtained from the Si substrate. This shows that the sampling depth is large enough to observe the signal from the complete alloy and $SiO_2$ film and the silicon substrate. The as received CuMn spectrum shows multiple transitions along with the ones corresponding to $SiO_2$ (1844.8 eV) and bulk Si (1839 eV)[12]. The peak at 1843 eV can be attributed to the silicate component while the peak at 1841 eV

can be attributed to the sub-oxides formed due to the sputter damage. the formation of manganese silicate indicate that the barrier is formed upon deposition.

The growth of the peak at 1843 eV after the 400ºC anneal corresponding to the manganese silicate peak attests to the facts obtained from the O 1s spectra. The peak at 1841 eV corresponding to the sub-oxides formed due to the sputter damage is also removed upon anneal.

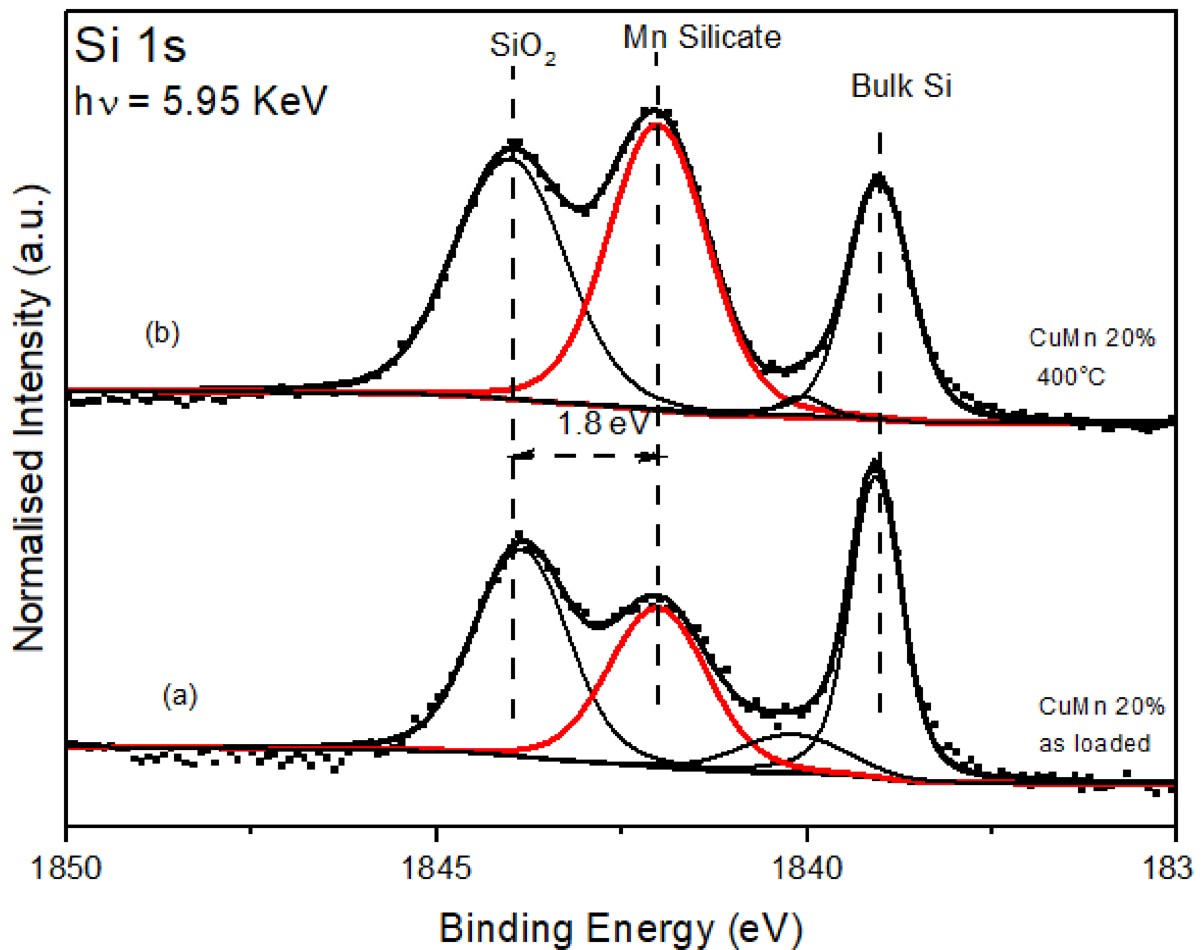


Figure 4.8: Si 1s spectra of CuMn alloy on $SiO_2$ before and after 400°C anneal showing clear indication of the growth of Mn silicate barrier upon anneal

| Peak position (eV) | Gaussian width (eV) |
|---|---|
| 1843.9 | 1.3 |
| 1842.1 | 1.4 |
| 1840.1 | 1.0 |
| 1839.0 | 1.0 |

Table 4.4: Curve fitting parameters for Si 1s spectra of CuMn sample before and after annealing

Ti 1s spectra shown in fig 4.9 indicate that the as received alloy sample has both metallic i.e., Ti (0) oxidation state peak at 4965 eV as well as titanium dioxide i.e., Ti (4+) peak at 4969 eV. Upon thermal anneal, the peak intensity at 4965 eV decreases while the $TiO_2$ peak becomes broader. The peak at 4970.5 eV may be attributed to the formation of titanium silicate at the interface of the alloy and $SiO_2$. Multiple sub-oxides were observed between 4965.8 eV and 4967.8 eV in the after anneal sample due to the interaction between the Ti and the $SiO_2$ dielectric at the alloy-dielectric interface.

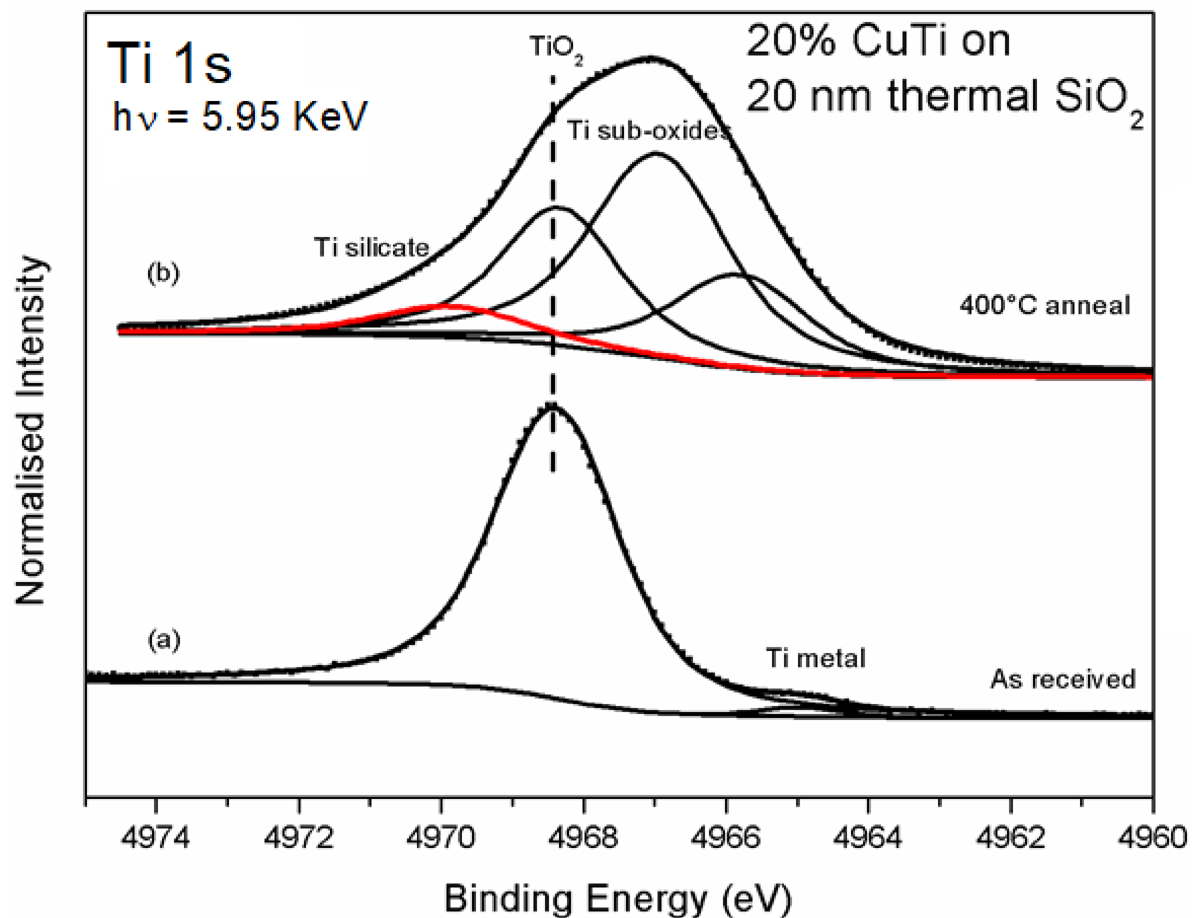


Figure 4.9: Ti 1s spectra of CuTi alloy on $SiO_2$ (a)before anneal indicate single state $TiO_2$ and residual metal at the surface and (b) after 400°C anneal showing formation of Ti silicate along with Ti sub-oxides while Ti metal is consumed

| Before anneal | | After anneal | |
|---|---|---|---|
| **Peak poistion (eV)** | **Gaussian width (eV)** | **Peak position (eV)** | **Gaussian width (eV)** |
| 4965.0 | 0.6 | 4966.0 | 1.0 |
| 4968.7 | 1.2 | 4967.0 | 1.0 |
| | | 4968.7 | 1.2 |
| | | 4970.0 | 1.0 |

Table 4.5: Curve fitting parameters for Ti 1s of CuTi sample spectra before and after annealing

Further investigation of the O 1s spectra shown in fig 4.10 show a high intensity peak at 530.6 eV indicate the presence of titanium dioxide[13]. There is a slight decrease in the peak intensity of titanium dioxide after the anneal and consequently can be attributed to the formation of titanium silicate. The other peaks in the as loaded sample can be attributed to the C – O (531 eV), sputter damage and sub-oxides at 532 eV and substrate $SiO_2$ peak at 533.3 eV. On anneal, multiple peaks are observed even though the sputter damage and carbon contamination are reduced. This may be attributed to the formation of titanium silicate[14] and various Ti oxides due to the interaction of Ti with the $SiO_2$ substrate.

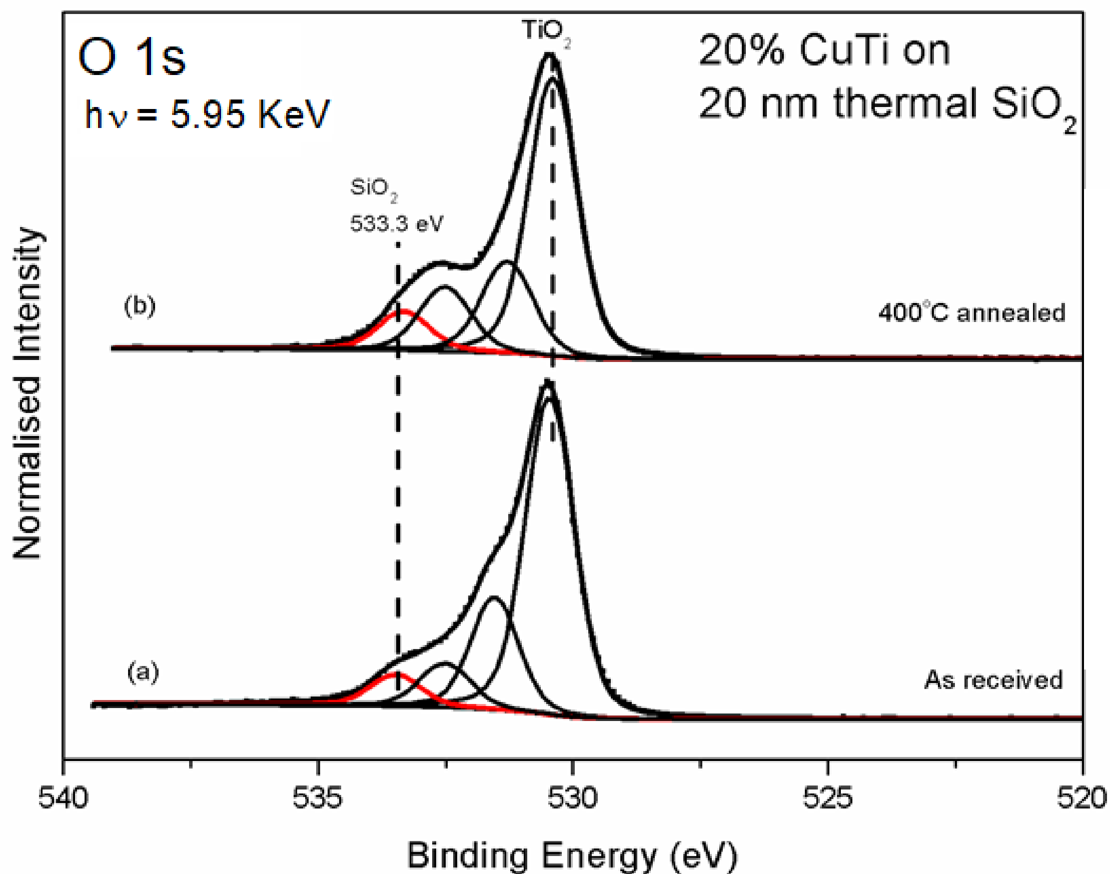


Figure 4.10: O 1s spectra of CuTi alloy on $SiO_2$ (a) before anneal and (b) after 400°C anneal showing multiple peak components corresponding to $SiO_2$, $TiO_2$ and possibility of Ti silicate after the anneal

| Before anneal | | After anneal | |
|---|---|---|---|
| Peak poistion (eV) | Gaussian width (eV) | Peak position (eV) | Gaussian width (eV) |
| 533.3 | 1.1 | 533.3 | 1.1 |
| 532.5 | 1.0 | 532.7 | 1.0 |
| 531.5 | 1.0 | 531.5 | 1.0 |
| 530.0 | 1.0 | 530.0 | 1.0 |

Table 4.6: Curve fitting parameters for O 1s spectra of CuTi sample before and after annealing

Multiple peak components were observed from the HAXPES Si 1s spectra of CuTi alloy shown in fig 4.11. The peak 1839 eV corresponds to the presence of bulk Si substrate signal while the peak at 1843.8 eV show the presence of strong $SiO_2$ signal. The presence of bulk Si peak indicates that the sampling depth of HAXPES spectra is more than 30 nm. The peaks between 1839 eV and 1843.8 eV show the presence of silicon sub-oxides. As the substrate is thermally deposited $SiO_2$ with no sub-oxides present, the sub-oxides must be formed during the deposition of CuTi alloy. As the sputtering process generally involves high powered ions impacting the surface of the substrate, there will be considerable defects at the substrate surface known as sputter damage. The sub-oxides peaks observed from the Si 1s spectra can be attributed to the sputter damage.

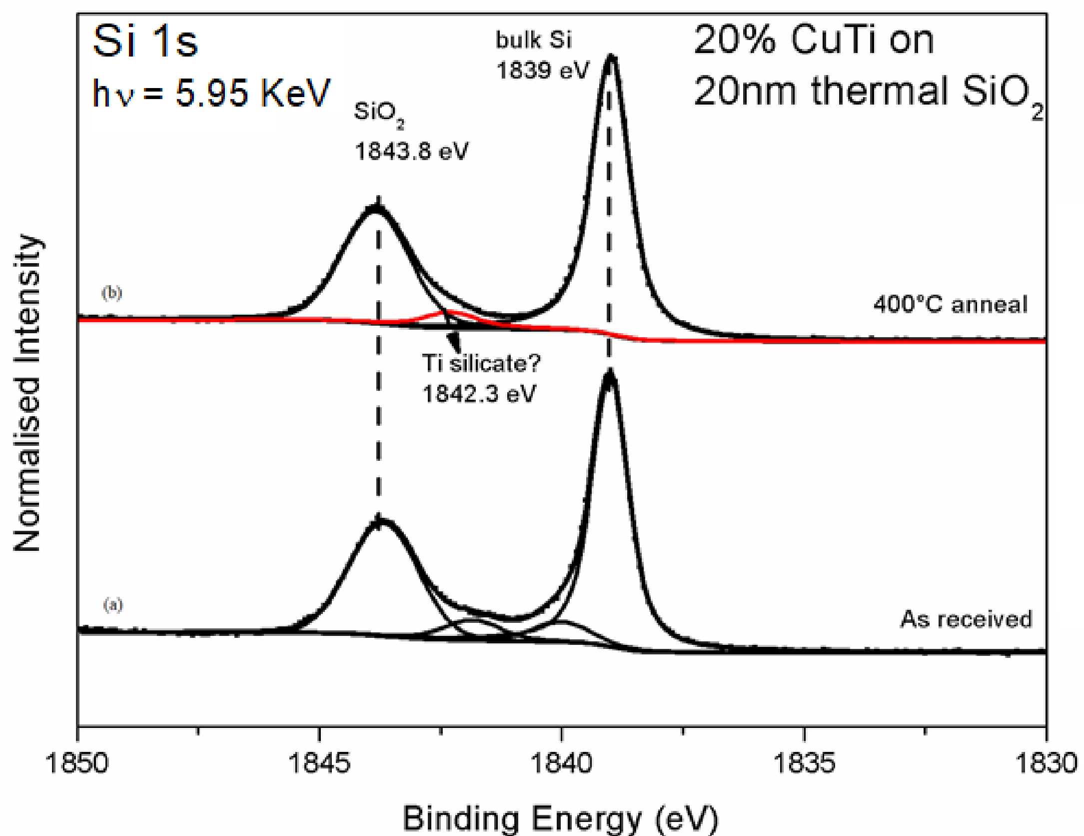


Figure 4.11: HAXPES Si 1s spectra of (a) as received and (b) 400°C annealed 20% CuTi sample

| Before anneal | | After anneal | |
|---|---|---|---|
| **Peak position (eV)** | **Gaussian width (eV)** | **Peak position (eV)** | **Gaussian width (eV)** |
| 1843.8 | 1.3 | 1843.8 | 1.3 |
| 1842.0 | 1.0 | 1842.2 | 1.0 |
| 1840.0 | 1.0 | 1839.0 | 1.0 |
| 1839.0 | 1.0 | | |

Table 4.7: Curve fitting parameters for Si 1s spectra of CuTi sample before and after annealing

After annealed plot show that the sub-oxide states formed due to the sputter damage were removed on anneal. The $SiO_2$ peak is asymmetric indicating the presence of multiple chemical states after the anneal. Although the peak position is in corresponding for the formation for titanium silicate, further investigation is required to study the presence of titanium silicate at the interface of CuTi alloy and dielectric.

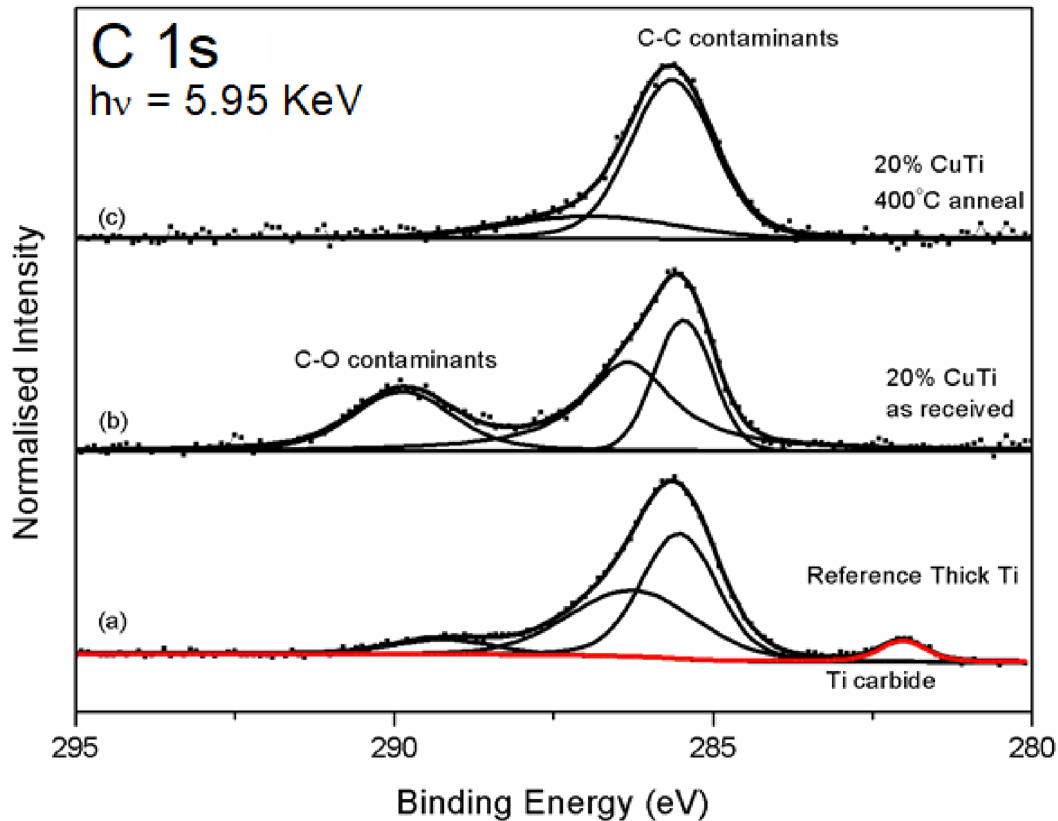


Figure 4.12: C 1s spectra of (a) thick Ti on SiO2 showing the presence of Ti carbide (b) CuTi alloy on SiO2 before anneal and (c) CuTi on SiO2 after 400°C anneal showing no peak components corresponding to Ti carbide indicating absence of free Ti metal

C 1s spectra are shown in fig 4.12. Due to high concentration of surface contamination in CuTi sample, a strong peak at 285.1 eV was observed even after annealing along with a peak at 286 eV and 288 eV corresponding to C-O and C=O contaminations[15]. In the spectrum of a reference Ti sample, there is a detectable Ti carbide peak at 282 eV[16]. Absence of the Ti carbide peak in the CuTi sample indicate the absence of Ti metal present at the surface. Even after the anneal, there is still a strong peak at 285.1 eV and the absence of Ti carbide indicate absence of free Ti metal segregation at the surface as confirmed by the Ti 1s peak profile.

| Peak position (eV) | Gaussian width (eV) |
|---|---|
| 282.0 | 1.0 |
| 285.3 | 1.1 |
| 286.7 | 1.7 |
| 289.0 | 1.2 |

Table 4.8: Curve fitting parameters for C 1s spectra of CuTi sample

### 4.2.1 SIMS Analysis

A SIMS depth profiles for the CuMn sample before and after anneal are shown in fig 4.65. The SIMS plot for the as received sample confirms the results obtained through HAXPES measurements. There is evidence of Cu and Mn homogenously distributed through the alloy film and there is no metal oxide signal observed in the sputter deposited metal film. There is a relatively abrupt interface between the $SiO_2$ substrate and the alloy film.

The after anneal profile clearly shows the segregation of the Mn to the surface of the Cu film where it becomes oxidised. There is also evidence for some of the Mn which has diffused to the bottom interface of the alloy that it has chemically interacted with the $SiO_2$, consistent with the formation of manganese silicate. It should also be noted that the Cu signal at this interface drops to zero further into the $SiO_2$ layer which is consistent with the manganese silicate acting as an effective Cu diffusion barrier layer.

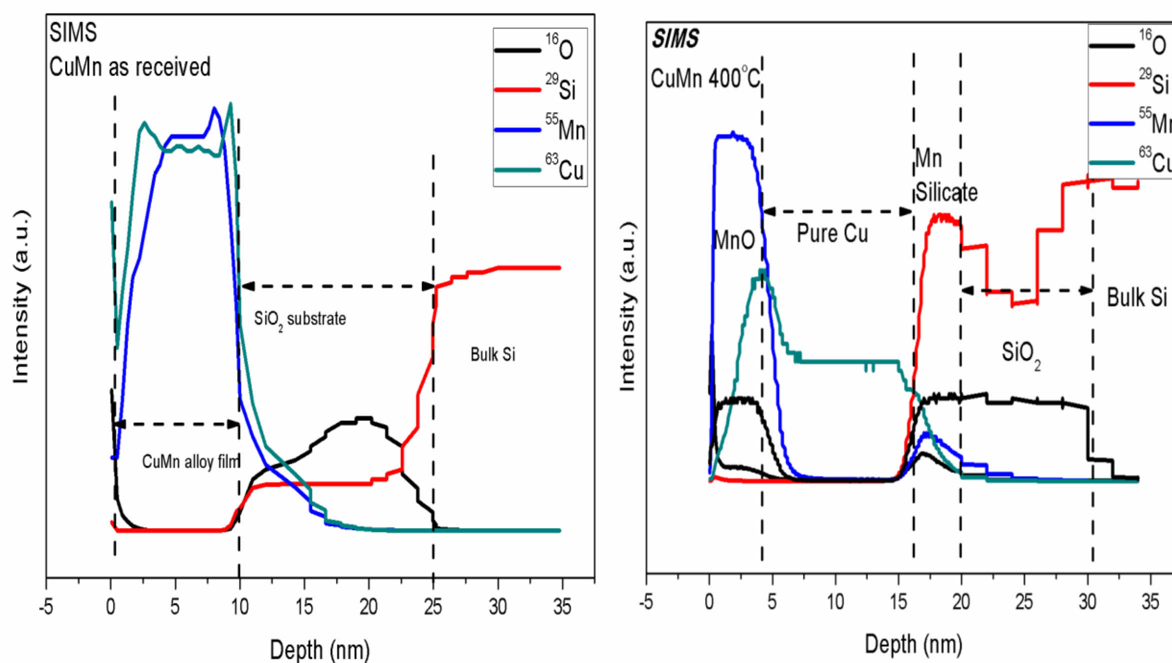


Figure 4.13: SIMS profile of (i) 20% CuMn as received sample and (ii) 20% CuMn sample after 400°C anneal indicating the segregation of Mn metal at the interface as well as formation of Mn silicate barrier upon annealing

The CuTi SIMS profiles before and after annealing are shown in fig 4.66. As was observed for the the CuMn alloy sample, in the as received CuTi sample, both elements are present at fairly uniform concentrations through the film and there is no metal oxide present in the bulk of the alloy film. SIMS plots of CuTi sample after annealing shows segregation of the metallic Ti to both upper and lower interfaces of the alloy. While there is a segregation process upon anneal, there is no clear distinction of the segregated metallic films as observed with the CuMn sample. Also, there is evidence of some diffusion of both Cu and Ti metals into the $SiO_2$ substrate. Also, at the interface of the alloy and substrate after anneal sample, there is a clear evidence for formation of titanium silicate further supporting the observations from the HAXPES data.

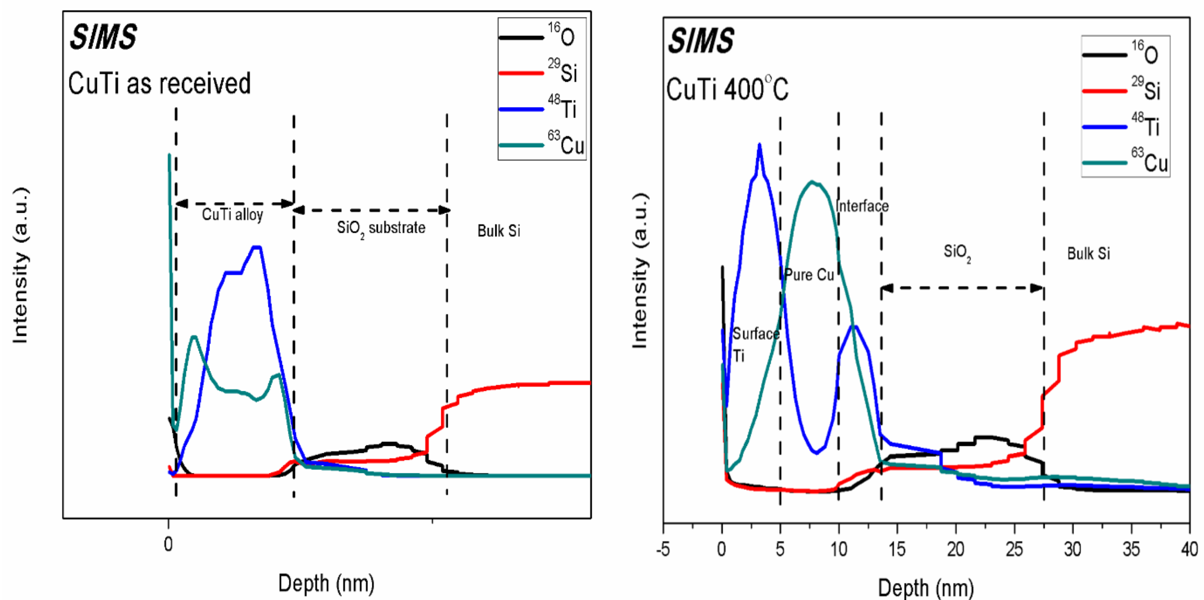


Figure 4.14: SIMS profile of (i) 20% CuTi as received sample and (ii) 20% CuTi sample after 400°C anneal showing incomplete segregation of Ti with no clear indication of Ti-SiO2 interface barrier layer

### 4.2.2 Electrical characterization

Four-point probe measurements on the CuMn and CuTi samples indicate high sheet resistance, $5.7 \times 10^{-7}$ Ω m and $7.5 \times 10^{-7}$ Ω m respectively, compared to that of the pure Cu thin film sample ($9.13 \times 10^{-8}$ Ω m) and the known value of the bulk resistivity of Cu (1.72 x 10-

[8] Ω m). Higher sheet resistance in CuTi alloy sample compared to the CuMn sample may be attributed to the presence of high concentration of $TiO_2$ at the sample surface.

Upon various anneals, the resistivity of the alloy films decreases as the individual metals segregate from the alloy films. CuMn films after 500°C anneal show lower resistivity compared to that of CuTi films. This is consistent with the SIMS data showing more effective expulsion of the alloying element for the CuMn film compared with the CuTi film. As the CuMn sample show a eutectic composition, after the first anneal, the change in resistivity is high while the further high temperature anneals doesn't show much difference. CuTi sample on the other hand the change in resistivity is significant at 400°C annealing step.

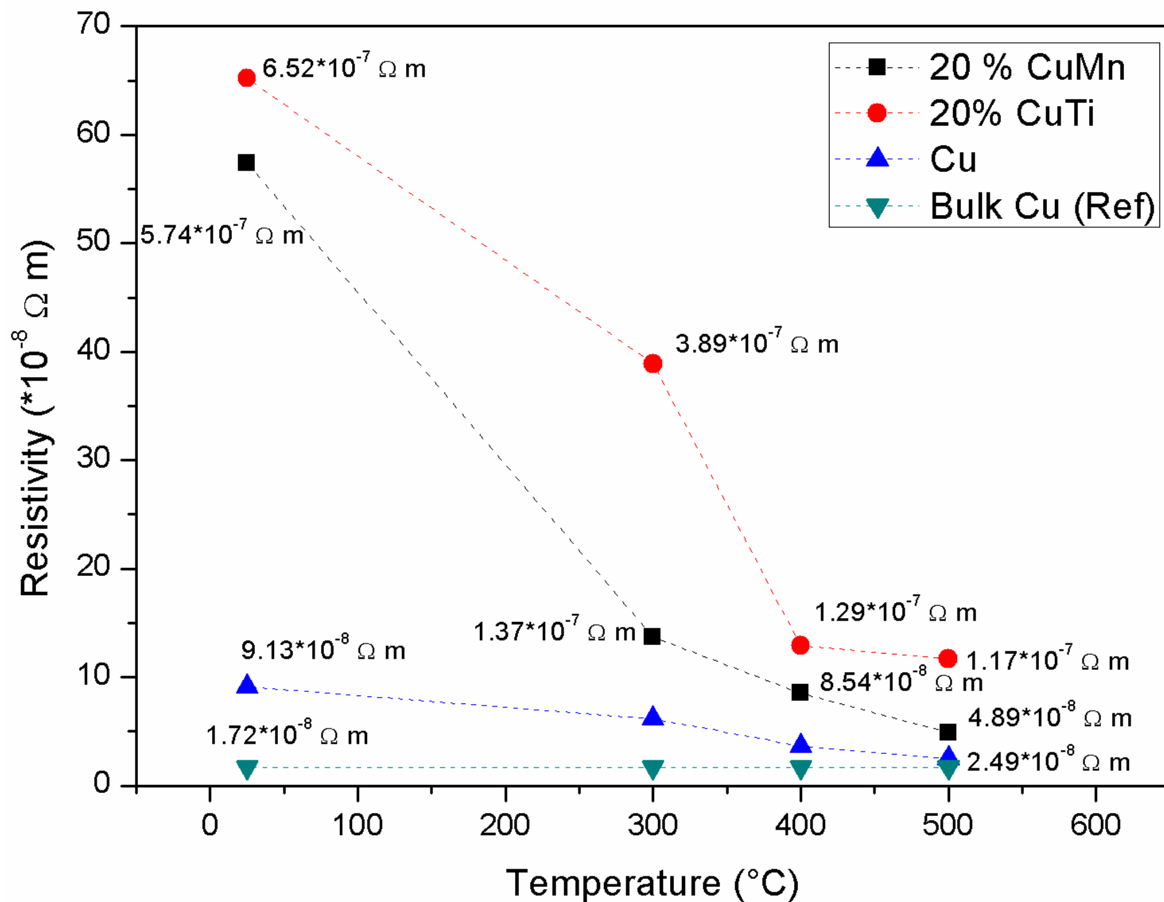


Figure 4.15: Four-point probe measurements of (i) 20% CuMn (ii) 20% CuTi (iii) pure Cu and (iv) reference bulk Cu resistivities before and after various annealing steps

CV measurements of the pre-anneal CuMn samples were analysed and shown in fig 4.68. Multiple MOS structures of area 200µm x 200µm were analysed at four different frequencies – 1KHz, 10KHz, 100KHz and 1MHz. No discernible variability was observed between various devices. Presence of large hysteresis confirms the presence of large charge accumulation due to interface states at the alloy-substrate interface due to sputter damage. The larger hysteresis at higher frequencies can be attributed to the high amount of trapped charges at higher frequencies. The trapped charges also cause shift in the flat-band voltage at various frequencies. The capacitance obtained is significantly higher than the ideal capacitance containing single insulating layer (in this case $SiO_2$) MOS structure. The increase in the observed capacitance can be attributed to the formation of multiple sub-oxide states and the substrate-alloy interactions.

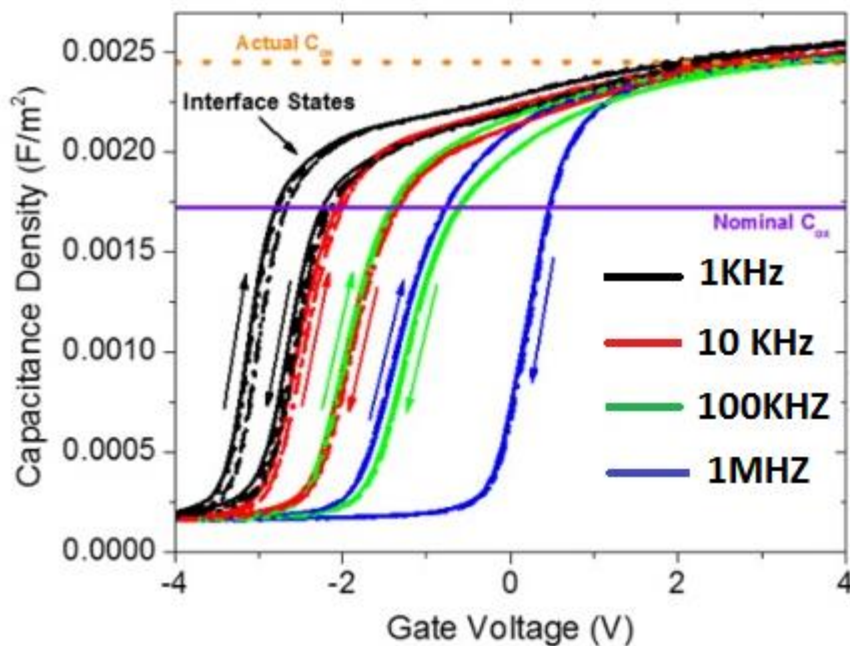


Figure 4.16: CV analysis of as received 20% CuMn MOS structures showing large hysteresis corresponding to trapped and mobile charges upon deposition conditions

Fig 4.17 show the post-anneal CuMn CV profile. Post-anneal CuMn show no variation between various MOS structures as well as a complete elimination of the hysteresis in the measurements. This confirms that the annealing significantly improves the electrical characteristics of these structures however, there is still evidence of the presence of

interfaces states., the actual capacitance is decreased significantly after the anneal closer to that of the ideal capacitance for the thickness of the $SiO_2$ film. This can be attributed to the complete segregation of Mn from alloy forming Cu strip as observed from the SIMS plot after annealing. Flat-band voltage is nearing 0 indicate minimal amount of interface states. This is also confirmed by the change in the flat-band voltage position upon multi-frequency CV analysis.

CV analysis of the pre-anneal CuTi sample shown in fig 4.70 indicates a small variability in multiple devices analysed. As before, sputter damage, consistent with the formation of sub-oxides states in the as received sample HAXPES Si 1s spectra, is the main cause of the non-ideal responses, providing many defect sites that allow the migration of Ti into $SiO_2$ to form a higher κ -value $TiSi_xO_y$ on high temperature anneals The change in the flat-band voltage shift although present, the shift at various frequencies are smaller compared to the CuMn MOS structures.

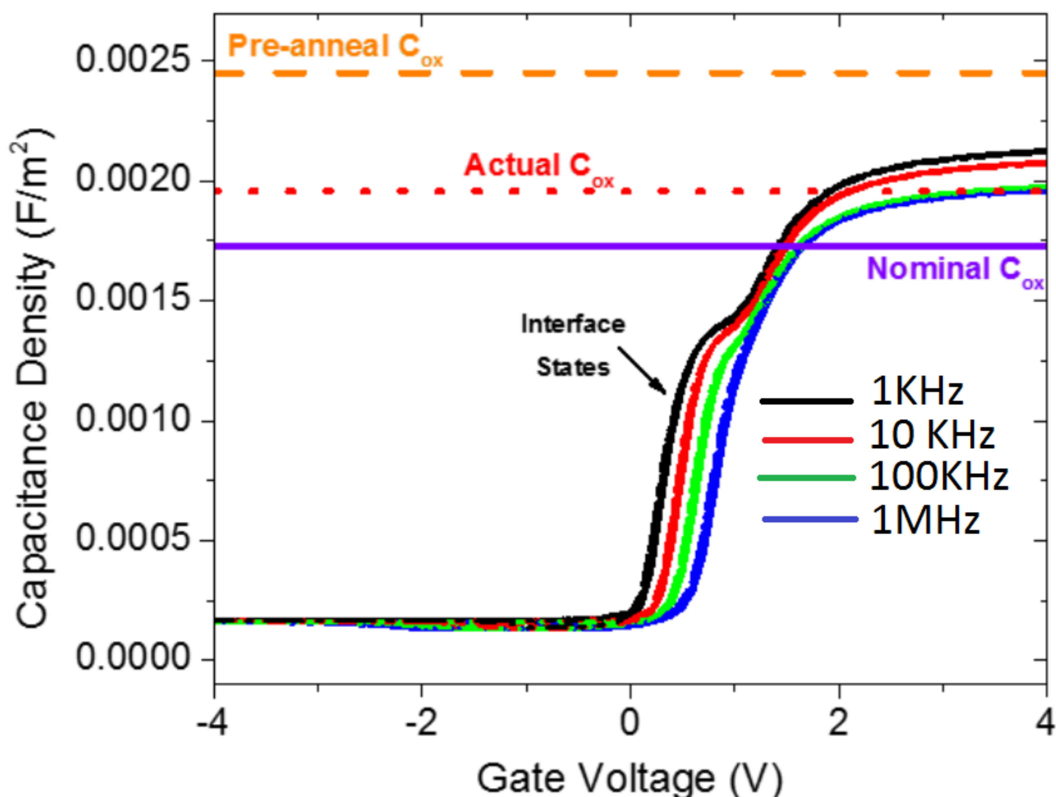


Figure 4.17: CV analysis of 20% CuMn MOS structures after 400°C anneal show improved capacitance as well as the hysteresis is reduced

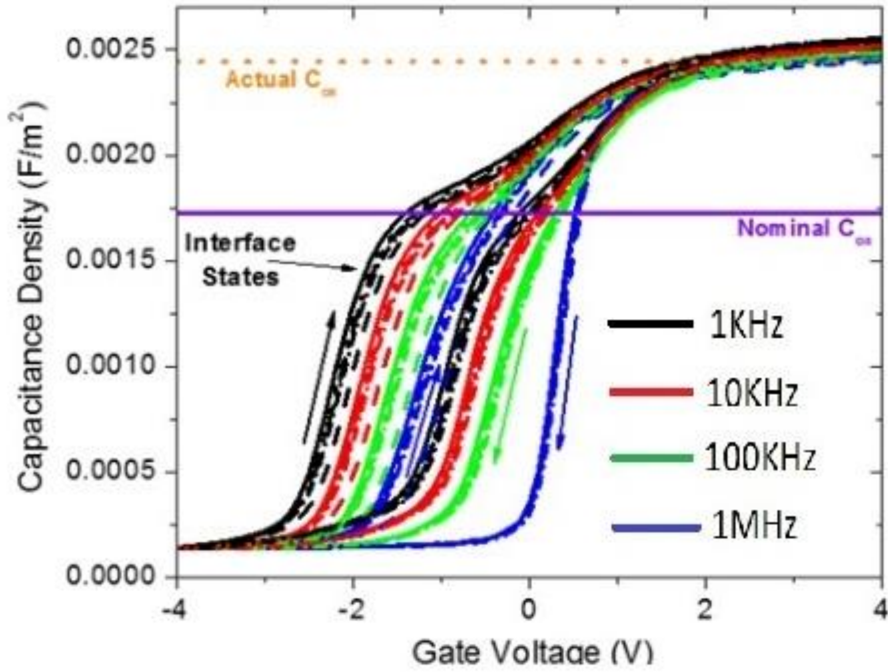


Figure 4.18: CV analysis of as received 20% CuTi MOS structures indicating the presence of trapped and mobile charges upon deposition

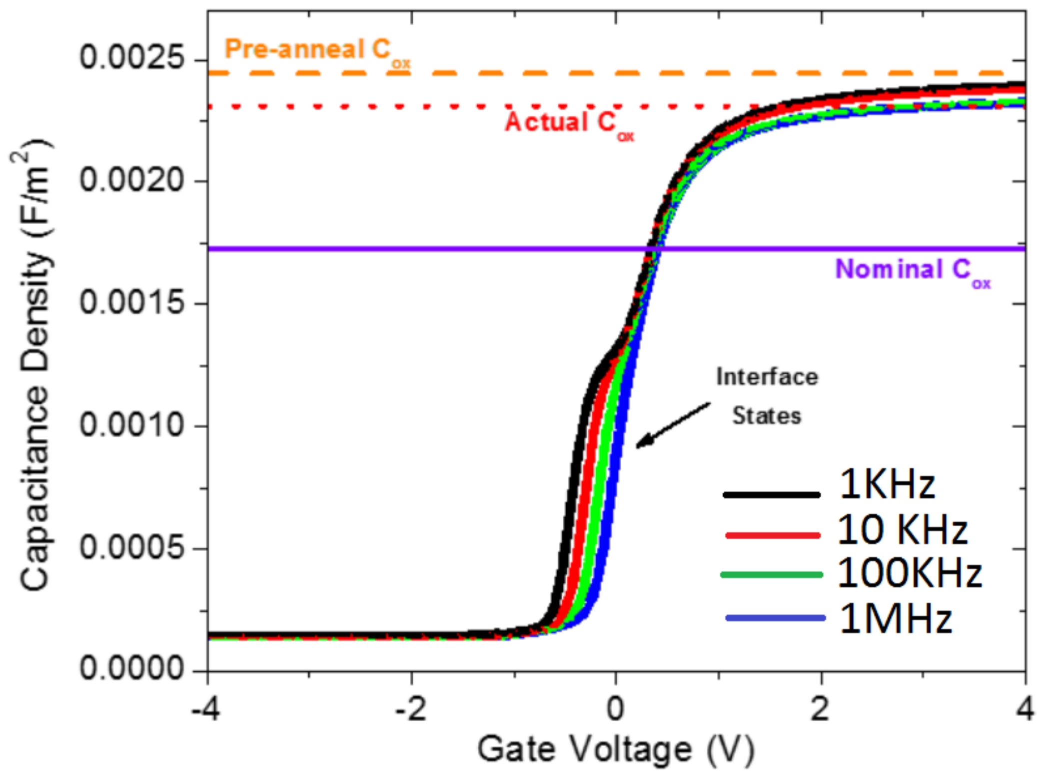


Figure 4.19: CV analysis of 20% CuTi MOS structures after 400°C anneal show removal of hysteresis as well as flat-band voltage approaching zero

Similar to the CuMn post-anneal sample, CuTi show no variation between various MOS structures as well as a complete elimination of the hysteresis in the measurements. Comparatively, in CuTi samples, although overall capacitance is decreased due to the removal of sputter damage, the actual capacitance is still higher compared to the ideal capacitance. Compared to CuMn sample, upon multi-frequency CV analysis the plots are close together and the flat-band voltage is almost 0. The increase in the actual capacitance may be attributed to a thick oxide at the surface and possibly a higher dielectric constant of titanium silicate[17], formed after the anneal at the interface between the $SiO_2$ and the alloy..

**4.4 Conclusions:**

XPS and HAXPES studies indicate that the 5% alloys the annealed samples show delamination of the alloy film. 20% alloys indicate the presence of both metal and Cu and upon annealing manganese/titanium silicate is formed. It is further confirmed by the SIMS analysis which shows clear evidence of segregation of the alloying elements to the surface where the metal becomes oxidised and to the interface with the SiO2 where silicates form. Four-point probe measurements show that the CuMn and CuTi 20% alloys have higher resistivity compared to copper and upon annealing, while CuMn show decrease in resistivity while CuTi sample show higher resistivity compared to CuMn sample. CV analysis shows that both CuMn and CuTi samples has sputter damage which is removed on annealing. CuMn has lower capacitance compared to CuTi samples but the interface states are higher than in CuTi sample. As the future generation of interconnects focusses on reducing the RC time delay, the lower resistivity and capacitance observed in CuMn samples show that CuMn is more favourable than the CuTi alloy system for the BEOL self-forming barrier - interconnect stack.

# References:


[1] M. Sun, M.G. Pecht, D. Barbe, Lifetime RC time delay of on-chip copper interconnect, in: IEEE Trans. Semicond. Manuf., 2002: pp. 253–259. doi:10.1109/66.999601.

[2] Z. Tokei, K. Croes, G.P. Beyer, Reliability of copper low-k interconnects, Microelectron. Eng. 87 (2010) 348–354. doi:10.1016/j.mee.2009.06.025.

[3] J.G. Lozano, S. Lozano-Perez, J. Bogan, Y.C. Wang, B. Brennan, P.D. Nellist, G. Hughes, Interdiffusion and barrier layer formation in thermally evaporated Mn/Cu heterostructures on SiO2 substrates, Appl. Phys. Lett. 98 (2011) 1–4. doi:10.1063/1.3569146.

[4] Y. Shacham-Diamand, A. Dedhia, D. Hoffstetter, W. Oldham, Copper Transport in Thermal $SiO_2$, J. Electrochem. Soc. 140 (1993) 2427–2432. doi:10.1149/1.2220837.

[5] M. Franz, R. Ecke, C. Kaufmann, J. Kriz, S.E. Schulz, Investigation of barrier formation and stability of self-forming barriers with CuMn, CuTi and CuZr alloys, 2015 IEEE Int. Interconnect Technol. Conf. 2015 IEEE Mater. Adv. Met. Conf. IITC/MAM 2015. 156 (2015) 95–97. doi:10.1109/IITC-MAM.2015.7325640.

[6] J. Bogan, Growth and chemical characterisation studies of Mn silicate barrier layers on SiO2 and CDO, PhD thesis Dublin City University, 2012.

[7] A.T.. Wee, A.C.. Huan, T. Osipowicz, K.. Lee, W.. Thian, K.. Tan, R. Hogan, Surface and interface studies of titanium silicide formation, Thin Solid Films. 283 (1996) 130–134. doi:10.1016/0040-6090(95)08504-1.

[8] K.D. Moulder, J. F., Stickle, W. F., Sobol, P. E. & Bomben, ***Handbook of X-ray Photoelectron Spectroscopy***, Perkin-Elmer Corporation (1995).

[9] Copper Binary Eutectic Alloys - Melting point, Eng. Toolbox. (2008). https://www.engineeringtoolbox.com/copper-alloys-melting-points-d_1435.html.

[10] M.C. Biesinger, B.P. Payne, A.P. Grosvenor, L.W.M. Lau, A.R. Gerson, R.S.C. Smart, Resolving surface chemical states in XPS analysis of first row transition metals, oxides and hydroxides: Cr, Mn, Fe, Co and Ni, Appl. Surf. Sci. 257 (2011) 2717–2730.

[11] J. Bogan, A.P. McCoy, R. O'Connor, P. Casey, C. Byrne, G. Hughes, Photoemission study of the identification of Mn silicate barrier formation on carbon containing low-κ dielectrics, Microelectron. Eng. 130 (2014) 46–51. doi:10.1016/j.mee.2014.09.012.

[12] K. Kobayashi, High-resolution hard X-ray photoelectron spectroscopy: Application of valence band and core-level spectroscopy to materials science, Nucl. Instruments Methods Phys. Res. Sect. A Accel. Spectrometers, Detect. Assoc. Equip. 547 (2005) 98–112. doi:10.1016/j.nima.2005.05.016.

[13] A.Y. Stakheev, E.S. Shpiro, J. Apijok, XPS and XAES study of titania-silica mixed oxide system, J. Phys. Chem. 97 (1993) 5668–5672. doi:10.1021/j100123a034.

[14] S.M. Mukhopadhayay, S.H. Garofalini, Surface studies of $TiO_2SiO_2$ glasses by X-ray

photoelectron spectroscopy, J. Non. Cryst. Solids. 126 (1990) 202–208. doi:10.1016/0022-3093(90)90820-C.

[15] S.K. Jerng, D.S. Yu, J.H. Lee, C. Kim, S. Yoon, S.H. Chun, Graphitic carbon growth on crystalline and amorphous oxide substrates using molecular beam epitaxy, Nanoscale Res. Lett. 6 (2011) 1–6. doi:10.1186/1556-276X-6-565.

[16] L. Zhang, R. V. Koka, A study on the oxidation and carbon diffusion of TiC in alumina-titanium carbide ceramics using XPS and Raman spectroscopy, Mater. Chem. Phys. 57 (1998) 23–32. doi:10.1016/S0254-0584(98)00187-4.

[17] D.K. Sarkar, E. Desbiens, M.A. El Khakani, High-k titanium silicate dielectric thin films grown by pulsed-laser deposition, Appl. Phys. Lett. 80 (2002) 294–296. doi:10.1063/1.1435072.

# 5. Cobalt and Titanium based interconnect and barrier stack for future interconnects

## 5.1 Introduction

The resistivity of the Cu interconnect rapidly increases on decrease in size of IC nodes and approaches unacceptably high values on sub-10 nm nodes. Despite bulk resistivity being low, resistivity of the Cu interconnect line rises rapidly on scaling as a result of increased electron scattering from small Cu grains and diffusive surfaces [1]. The need for a thick and often highly resistive Cu barrier further reduces the volume available for Cu metal and increases the total line resistance. Thinner alternative Cu-alloy barrier materials are being explored to extend Cu for BEOL applications[2]. However, at future nodes Cu interconnects will become increasingly difficult to meet both line and via resistance technology targets with reliability. Thus, increased efforts in exploring Cu replacements [3] such as graphene [4] and cobalt (Co) [5] for via as well as interconnects [6] continue to increase.

As a thin layer of Co upon deposition on $SiO_2$ surface forms islands[7], a metal seed layer is needed to form a uniform thin layer of Co on $SiO_2$ based substrates. Self-forming alloys have been proposed as one of the possible ways to deposit a cobalt based alloy, and on anneal, the alloying metal segregates at the interface forming a thin adhesion layer for cobalt which acts as seed layer for further deposition of cobalt. Several metals have been proposed as the liner material for Co and research has been carried out with metals like W[8], Ru[9] and Ti.

Among the metals considered as a potential adhesion layer for a cobalt interconnect, Ti metal has been studied in detail as an adhesion liner for Al interconnects[10]. The process of integration of Ti into the BEOL with the existing manufacturing process is also well established compared to other metals. Dielectric constant of Ti silicate barrier layer is tunable by changing the concentration of $TiO_2$ and hence more suitable in future scaling of the barrier layers. While the behavior of such metals on $SiO_2$ is well understood[11], there have been

very few fundamental surface chemistry studies of the interactions of these materials with carbon-containing low-k materials[12].

In this chapter, a detailed synchrotron radiation based photoemission study of the interaction of titanium deposited in-situ on both $SiO_2$ and carbon-containing low-k spin-on-glass (SoG) [13] (dielectric constant ~2.5) in order to evaluate how titanium interacts with carbon-containing ILDs has been carried out. Also, the results of Hard X-ray Photoelectron spectroscopy (HAXPES) and X-ray absorption spectroscopy (XAS) measurements of 20% CoTi alloy as a possible adhesion liner/Co seed layer for the BEOL Co interconnects are presented.

## 5.2 A synchrotron radiation photoemission study of metallic titanium deposited on $SiO_2$ based dielectric substrates

The continued scaling of CMOS technology requires the integration of low-κ materials into BEOL processes. If low-k materials and alternative interconnects are to have a future in advanced CMOS, a thorough understanding of the surface chemistry of potential liners and barriers with the $SiO_2$ based low-κ dielectrics is key. As such, there is a renewed interest in titanium and its interactions with other metals (cobalt in particular) and advanced low-κ dielectrics[14].

### 5.2.1 Experimental work

The three silicon oxide based substrates used in this study (all grown on (100) p-type Si) were native silicon oxide, 5 nm thermally grown $SiO_2$ grown using dry oxidation at 850°C at Tyndall National Institute Cork, and carbon-containing spin-on-glass (SoG) with 16% carbon incorporated into the film. SoG films were deposited from a sol-based organo-silica precursor featuring both terminal and linking carbon groups resulting in 16% carbon incorporation and a dielectric constant of 2.5[15]) at IMEC Belgium. The sol was spin-coated on top of 300 mm Si wafers with 1 nm of thermally grown $SiO_2$ and soft-baked at 150 °C for 2 minutes followed by a hard-bake for 2 hours at 400 °C in an $N_2$ atmosphere.

The surfaces were prepared using thermal degas at 200°C for 2 h, with the ultra-high vacuum chamber reaching a maximum pressure of $1\times10^{-9}$ mbar during degassing. The photoemission experiments were carried out on the SX700 beamline at the ASTRID II synchrotron in the University of Aarhus. The core level spectra of Si 2p / Ti 3p were obtained using photon energy of 150 eV, while C 1s spectra was obtained using 325 eV photon energy. Metallic titanium thin film deposition was performed at room temperature using an Oxford Applied Research EGC04 mini electron-beam evaporator, at a chamber pressure of $5\times10^{-9}$ mbar. Identical deposition conditions (vacuum base pressures, times, and electron-beam settings) were used for titanium depositions on all three substrates. Based on effective attenuation length (EAL) calculations carried out by comparing the peak area of the substrate before and after Ti deposition, the titanium over layers were all 1 nm in thickness. In this work the calculations are made by monitoring the attenuation of the Si 2p peak area before and after deposition of the over layer. The degree to which the substrate signal is suppressed can be related to the thickness of the deposited films if the density is known. The calculated thickness is accurate for homogenous films that display uniform coverage. In the case of very thin films such as those used in this work, uniform coverage may not be achieved and so the thickness should be taken as nominal. High temperature vacuum annealing was performed at pressures $5\times10^{-9}$ mbar, with samples being held at the target temperature for 60 min. Annealing temperatures between 150 and 500 °C were measured using a thermocouple attached directly to the sample. All curve fitting analysis presented in this study were performed using AAnalyser curve fitting software program version 1.20.

### 5.2.2 Results and Discussion

Figure 5.1 shows the Si 2p spectra for the 5 nm thermally grown $SiO_2$ substrate throughout the experimental sequence. Before Ti deposition, the primary component peak within the as-loaded Si 2p spectrum at 104.4 eV is attributed to $SiO_2$. No bulk silicon is observed indicating that the sampling depth of the photoemission spectra acquired at a photon energy of 150 eV is less than the 5nm thickness of the thermal $SiO_2$. The peak is comprised of 3 sub-oxides which, as shown by the fit in figure 5.72 contribute little to the overall signal.

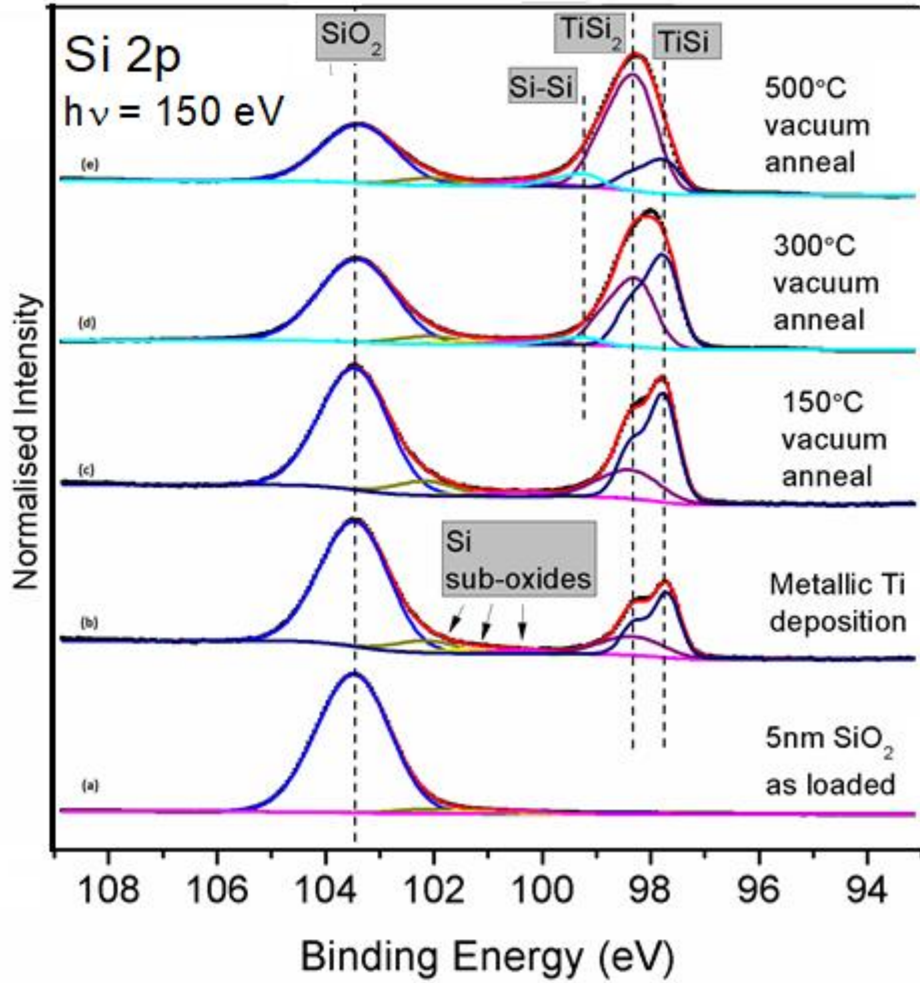


Figure 5.1: Si 2p spectra of 5nm $SiO_2$ upon Ti deposition and anneals showing clear indication of formation of Ti silicide and upon Ti deposition

| Peak position (eV) | Gaussian width (eV) |
|---|---|
| 104.0 | 1.40 |
| 102.8 | 1.10 |
| 101.9 | 1.00 |
| 101.0 | 1.00 |
| 99.0 | 0.73 |
| 98.5 | 0.67 |

Table 5.1: Fitting parameters utilized for Si 2p of 5nm $SiO_2$ sample after Ti deposition

Upon deposition, the titanium overlayer is predominantly metallic as evidenced by the Ti 3p spectrum shown in figure 5.2. However, the peak profiles of metallic titanium and

titanium silicide are indistinguishable in the Ti 3p spectrum. Further information on the chemical state of the Ti following deposition can be obtained from observing the notable change in the Si 2p peak (fig 5.1), where a new feature is observed at approximately 97.8 eV. This is indicative of the formation of Ti-silicide. The reason that this feature is attributed to Ti-silicide rather than Ti-silicate or the release of free silicon is that, in agreement with electronegativity differences, it appears at lower binding energy than would be expected for either of these species. In order to accurately fit the Ti-silicide related peak, two components are required indicating the presence of both TiSi and $TiSi_2$[16][17]. The binding energy positions of the Ti-silicide phases are in agreement with other works, however it is difficult to identify the correct phase with certainty when working with films with a thickness of just 1 nm. For such thin films, we expect a 3 Ti + $SiO_2$ -> TiSi + 2 TiO reaction upon deposition, and indeed we primarily see TiSi. However, the Ti remains predominantly metallic in profile and as such it seems that oxygen is being released rather than binding to Ti. Further consumption of silicon from the $SiO_2$ at higher temperatures appears to drive a 3 Ti + 2 $SiO_2$ -> $TiSi_2$ + 2 $TiO_2$ reaction as discussed below. In all cases, fitting peak parameters were kept constant throughout the series of experimental steps.

Upon low temperature thermal annealing at 150$^{o}$C a significant increase in both of the silicide components is observed, indicating further growth of Ti-silicide. The corresponding Ti 3p peak shows a small amount of oxidation of the deposited Ti following the anneal. A further anneal to 300$^{o}$C causes the growth of more Ti-silicide, which is more pronounced for the $TiSi_2$ at higher binding energy.

Notably, the Ti metal appears to become more oxidized following the higher temperature anneal. However, the formation of Ti-silicate can be ruled out, as this peak would be expected at approximately 102.2 eV in the Si 2p spectrum. At 500$^{o}$C, there is evidence for significant interactions at the Ti-$SiO_2$ interface. A peak emerges at 99.1 eV which indicates that $Si^0$ is being released during these interactions. Furthermore, there is growth of $TiSi_2$ with a simultaneous reduction in the TiSi component. The Ti 3p spectrum following 500$^{o}$C anneal indicates further oxidation of the titanium. The oxidation of Ti and presence of Ti-silicide in the Si 2p spectrum indicates that both silicide and oxide are present throughout the sequence

of anneals. The reduction in the $SiO_2$ peak during the experiment can be attributed to oxygen being transferred from Si to Ti.

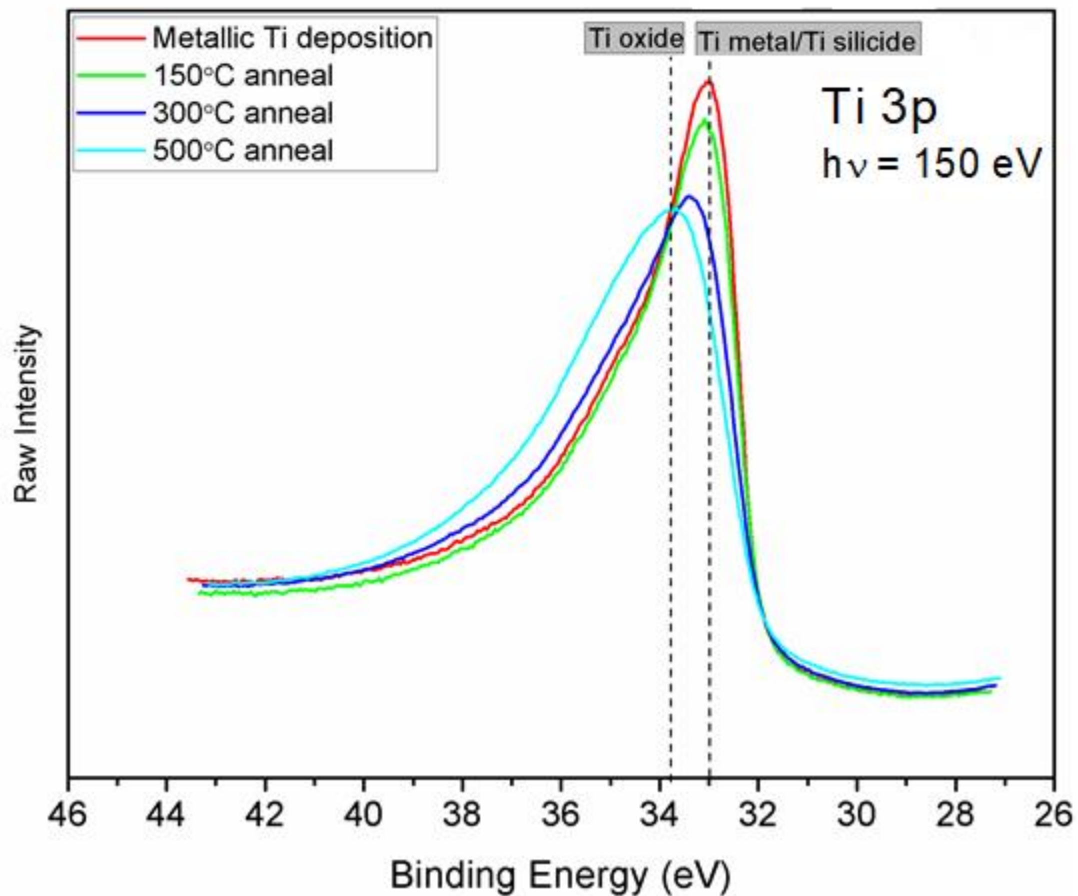


Figure 5.2: Ti 3p spectra upon Ti deposition 5nm $SiO_2$ and various anneals

In order to confirm that the Si 2p peak component at 99.1 eV was indeed $Si^0$, the Ti deposition and sequence of anneals was repeated on a native silicon oxide sample. Exposure of pristine silicon to ambient atmosphere results in the growth of 0.5-1 nm of oxide on the surface, which is typically a mixed phase with the 1+ to 4+ oxidation states all present. However, the predominant oxidation state is typically 4+ corresponding to stoichiometric $SiO_2$. This thin oxide layer allows for a bulk silicon substrate signal to be detected using a photon energy of 150 eV which has a high surface sensitive.

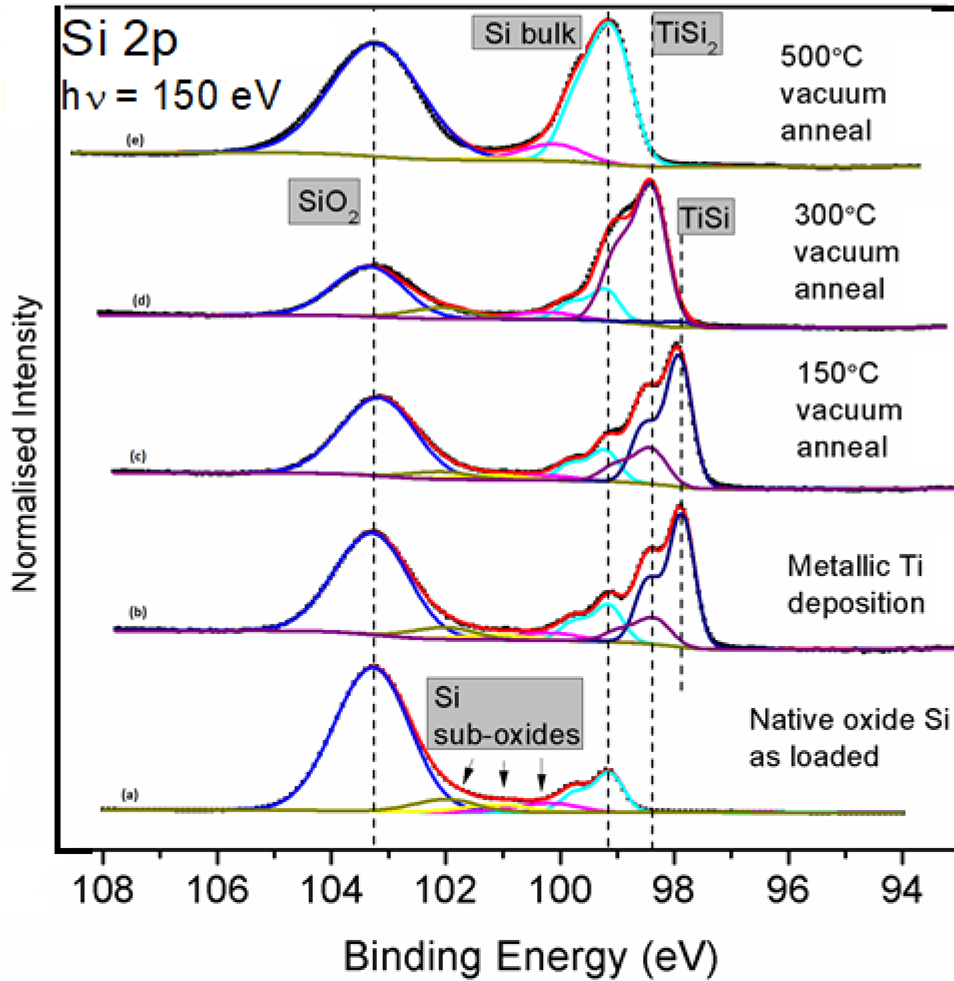


Figure 5.3: Si 2p spectra of native $SiO_2$ upon Ti deposition and anneals

Figure 5.3 shows the silicon 2p spectra for this measurement sequence. The peak at 99.1 eV binding energy is attributed to $Si^0$ in the as-received spectrum. The sub-oxides are also more pronounced in the fit than was the case for the thermally grown $SiO_2$ substrate. Upon further high temperature anneal (500°C), some of the metallic Ti was degassed from the substrate. Hence the buried substrate was oxidized by the oxygen released. The fitting parameters for the native oxide sample tabulated below:

| Peak position (eV) | Gaussian width (eV) |
|---:|---:|
| 104.0 | 1.30 |
| 101.0 | 1.00 |
| 100.0 | 1.00 |
| 99.3 | 0.54 |
| 98.5 | 0.62 |
| 98.0 | 0.50 |

Table 5.2: Fitting parameter used for curve fitting Si 2p of native oxide sample

Upon titanium deposition, we see metallic titanium in the Ti 3p spectrum (fig 5.4) which again cannot be distinguished from Ti-silicide. The deposition results in the formation of Ti-silicide as evidenced in the Si 2p spectrum after deposition in fig 5.3. Again, two silicide components are observed, distinct from that of bulk silicon which gives further confirmation of the attribution of peaks to Ti-silicide in figure 5.1. Low temperature annealing at 150°C causes the growth of both silicide components and very slight oxidation of the titanium. The ratio of the areas of the $Si^0$ to $SiO_2$ peak before and after titanium deposition indicate consumption of the native oxide upon deposition. The consumed material provides silicon for Ti-silicide formation and oxygen which partially oxidises some of the titanium.

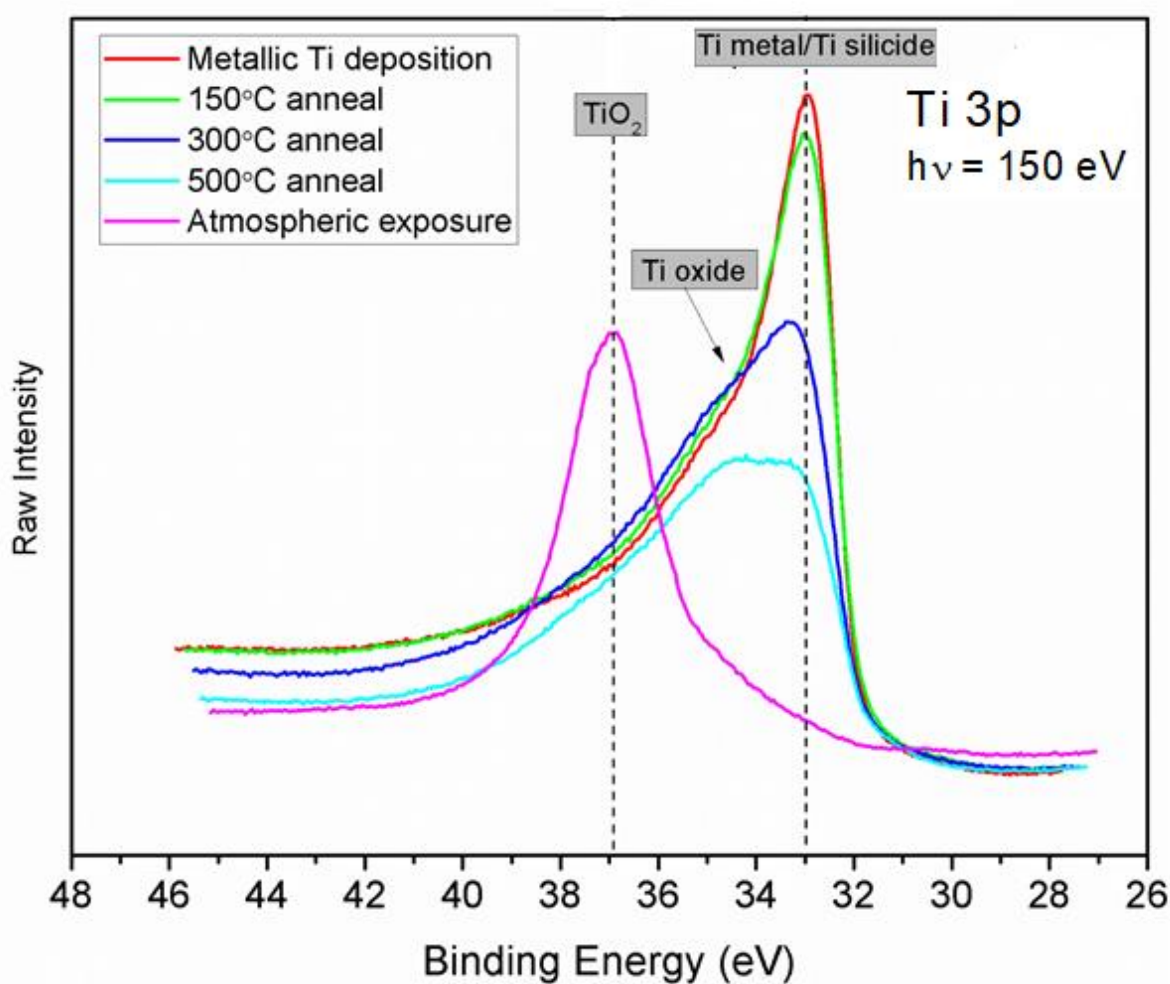


Figure 5.4: Ti 3p spectra upon Ti deposition on native $SiO_2$, anneals and atmospheric exposure

Upon 300°C anneal we see complete conversion of the TiSi to $TiSi_2$ and further consumption of the $SiO_2$. The Ti 3p spectrum shows a move to a higher oxidation state, however there is evidence for significant thinning of titanium, shown by a reduction in peak area. A further 500°C anneal sees the complete conversion of Ti-silicide to $Si^0$, and further loss of titanium metal within the Ti 3p. Atmospheric exposure of the film shows the complete conversion of any remaining titanium to $TiO_2$, while the Si 2p spectrum following exposure resembles that of the thermally grown $SiO_2$ in figure 5.1.

In order to be considered for future integration in advanced high-volume processes, any potential barrier material needs to display compatibility with low-k dielectrics and associated back-end processing temperatures. In order to qualify the potential of titanium-based barriers, the same experiment was performed on a low-k carbon-containing spin-on-glass. The Si 2p spectrum for the as-received substrate (figure 5.5) shows a profile similar to that of 5.4 nm $SiO_2$ sample. However, fitting of the 4+ component requires a Gaussian peak width of 1.6 eV for the SoG as compared with 1.4 eV for the $SiO_2$. Furthermore, we see a larger component from suboxides in the SoG. Upon deposition and 150°C anneal, we again see the formation of Ti-silicide with the larger component attributed to TiSi, however $TiSi_2$ appears to grow more rapidly at low temperature on SoG. We also see significant broadening of the Si 2p oxide peak due to the emergence of a feature at 102 eV, and also the presence of $Si^0$.

| **Peak position (eV)** | **Gaussian width (eV)** |
| --- | --- |
| 103.1 | 1.60 |
| 101.5 | 1.00 |
| 100.0 | 1.00 |
| 98.0 | 0.55 |
| 98.5 | 0.90 |

Table 5.3: Fitting parameters used in Si 2p spectra of SoG sample curve fitting

Following a 300°C anneal the conversion of TiSi to $TiSi_2$ as seen on previous substrates is evident once again. We also see growth of the $Si^0$ peak and that at 102 eV which we attribute to the formation of $TiSiO_4$. This peak component is present even on Ti deposition

indicating that high temperature isn't required to form Ti-silicate on low-k substrates. A final 500°C anneal causes a dramatic change in the Si 2p peak profile with the complete decomposition of both silicide phases and the concurrent conversion of the remaining silicon to a mix of titanium oxide and silicate.

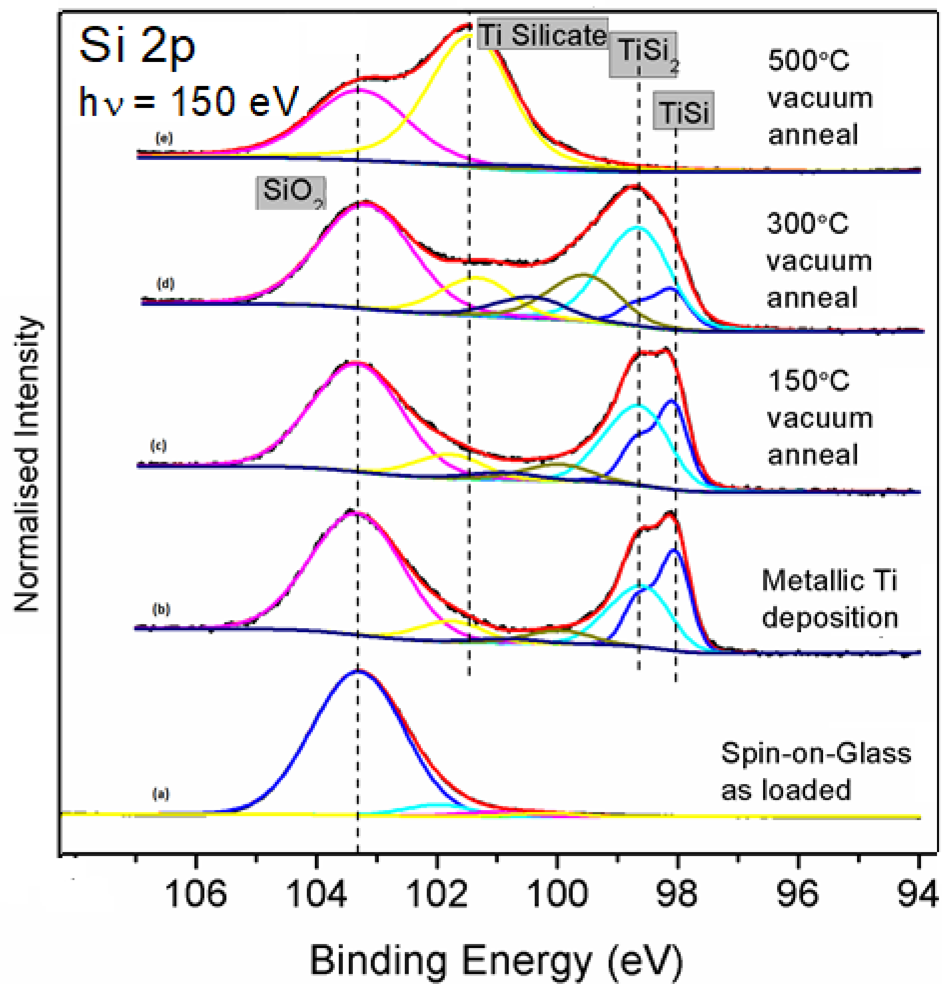


Figure 5.5: Si 2p spectra of SoG upon Ti deposition and anneals

Figure 5.6 shows the Ti 3p spectra for the titanium deposited on SoG. Notably the area of the titanium peak is constant during the experiment and also appears to oxidise far less than for titanium deposited on native oxide and thermally grown $SiO_2$. The major difference between the SoG substrate and those considered previously is the incorporation of 16% carbon in the dielectric. In order to investigate the degree to which the carbon affects the

behavior of the material system, the C 1s spectrum for each experimental step was investigated, and the spectra are shown in figure 5.7.

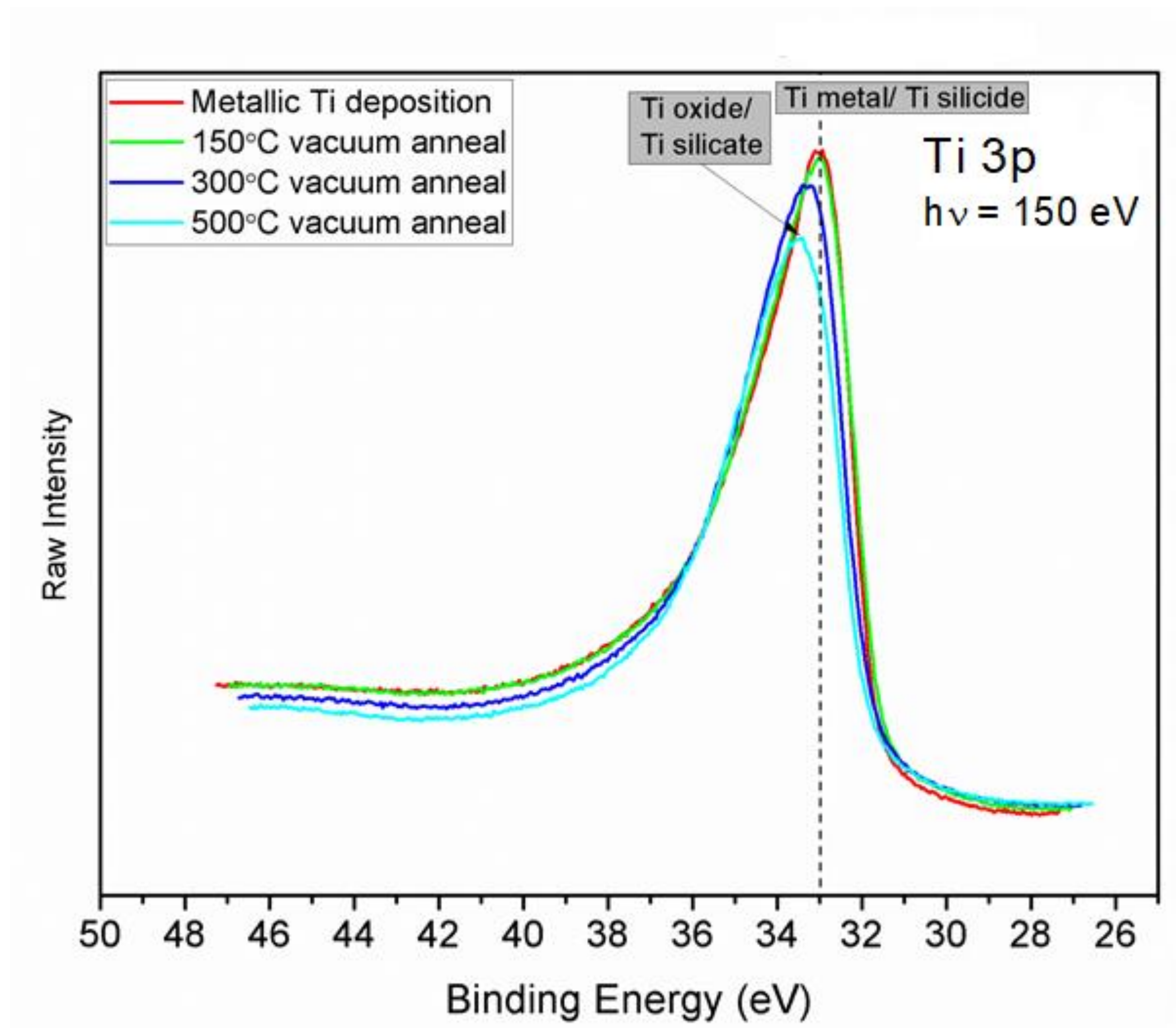


Figure 5.6: Figure 4: Ti 3p spectra upon Ti deposition on SoG substrate and anneals

The binding energy positions of carbon in low-k dielectrics and adventitious carbon are very similar and as such a detailed analysis of the chemical state of the carbon in the as-received SoG proves difficult. The spectrum of the as-loaded sample is typical of that for low-k materials[18]. Upon titanium deposition the spectrum changes significantly, with a binding energy shift to 281.7 eV which is consistent with carbon in a metal-carbide environment. In this case the data can be interpreted as the almost complete incorporation of the carbon within the sampling depth into Ti-carbide. Anneals at 150$^{o}$C and 300$^{o}$C result in a slight

increase in the Ti-carbide signal anneals. As seen from figure 77, within the Ti 3p peak profile it is not possible to distinguish between titanium metal, silicide, and carbide in agreement with electronegativity differences between the elements. However, the consistency of the Ti 3p peak profile on anneal when compared with substrates without carbon is strong evidence of Ti-carbide.

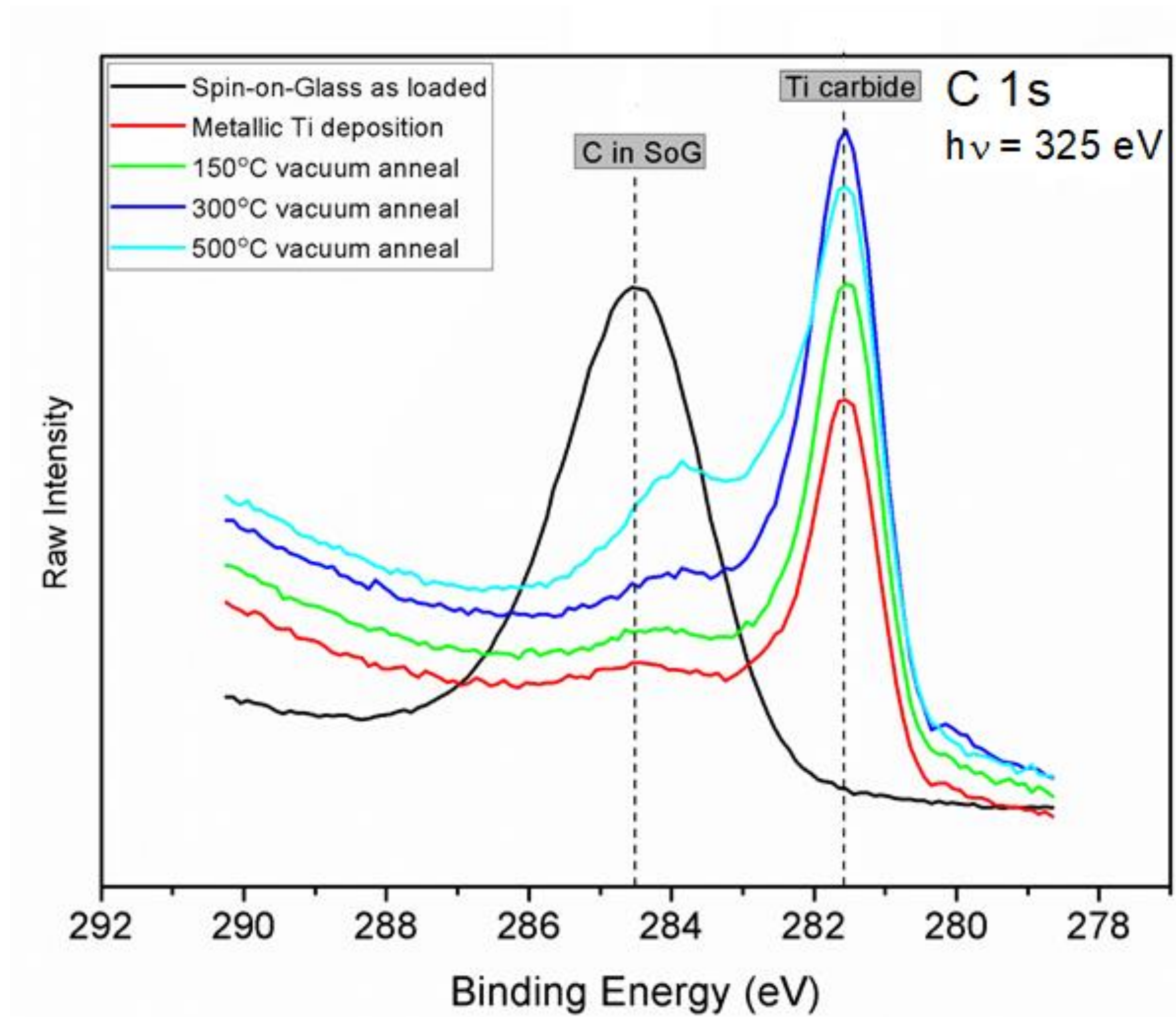


Figure 5.7: C 1s spectra of SoG substrate upon Ti deposition and anneals

At 500°C we see the slight decomposition of the Ti-carbide as evidenced by the reduction at 281.7 eV. The carbon released in this process goes on to form C-C bonds and we see a corresponding increase in signal at 284.5 eV. Upon its release from the Ti-carbide compound, the titanium forms Ti-silicate consistent with figure 5.5.

## 5.3 HAXPES and XANES studies of 20% CoTi Alloy:

Cobalt tends to form islands upon deposition on a $SiO_2$ substrate. Hence a depositing a seed layer of Co through an ALD process is less efficient compared to depositing a different metal as seed layer and adhesion liner. In this work, an alloy of CoTi with 20% Ti metal is analysed for uniformity and the interface chemistry with the $SiO_2$ substrate for future integration into BEOL interconnects.

CoTi alloy targets (4-inch targets) are manufactured by Testbourne Ltd, UK. The alloys were then deposited on 20 nm thermal $SiO_2$ through sputtering technique. As the alloy is to be integrated into the large-scale production process in the manufacturing industries. A 10 nm thin layer of the alloy was deposited and characterized using a range of spectroscopic techniques (XPS, HAXPES and XAS).

HAXPES and XAS spectrum were obtained at SOLEIL synchrotron facility, Paris. The pressure maintained during the data acquisition is ultra-high vacuum ($5*10^{-9}$ mbar) and photon energy used for HAXPES measurements was 6900 eV. The pass energy and energy resolution were 100 eV and 100 meV, respectively, while the spatial resolution was 110 µm. All XPS and HAXPES curve fitting analysis presented in this study was performed using AAnalyzer curve fitting software program version 1.20.

### 5.3.1 XPS and HAXPES Analysis:

Initial XPS measurements are carried out and chemical composition calculations were undertaken for the 10nm CoTi sample deposited on 20nm thermal $SiO_2$ substrate. Fig 5.8 show survey spectrum of CoTi before and after annealing. The major peaks observed are Co 2p (780 eV), O 1s (530 eV), Ti 2p (458 eV), and C 1s (284 eV)[19]. The peaks corresponding to Co 3s and Co 3p are also observed at 103 eV and 62 eV respectively.

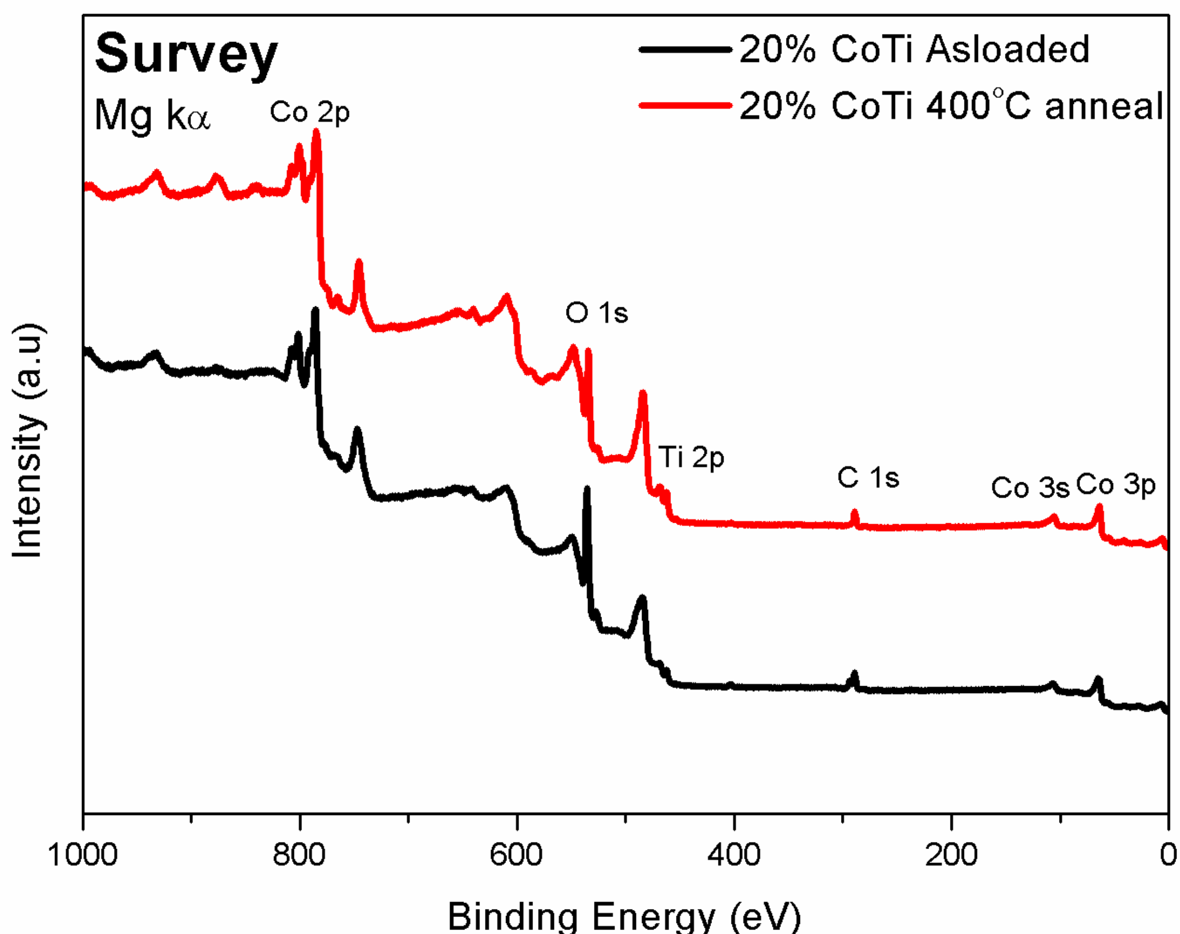


Figure 5.8: XPS spectra of CoTi alloy film on 20 nm thermal $SiO_2$ as loaded and 400°C anneal showing decrease in peak intensity of O 1s while increase in Ti 2p as a result of metal segregation

The Co:Ti compositional ratio was found to be 83:17 in the as loaded sample which is close to the expected 80:20 concentration upon deposition through sputtering from the CoTi target. The ratio changes to 2:1 upon annealing to 300°C. The change in concentration of the Ti metal is attributed to the segregation of the Ti on annealing at the surface as is the principle of self-forming barrier alloys. The ratio of the Co:Ti doesn't change on further high temperature anneals as is displayed in the data in Table 5.1.

The total chemical composition calculations shown in table 5.2 show no Si 2p signal indicating that the films are thicker than the sampling depth of the traditional XPS measurements. High concentration of the carbon is seen as the deposition is carried out at high vacuum and exposed to the atmosphere before loading inside the analysis chamber.

| | Co | Ti |
|---|---|---|
| CoTi as received | 83 | 17 |
| CoTi 300°C | 67 | 33 |
| CoTi 400°C | 67 | 33 |

Table 5.4: Ratio of Co and Ti in CoTi sample before and after annealing

There is a strong O 1s signal seen in the as received sample which is attributed to the oxidation of the metal surface. The decrease in the O1s intensity after the anneal can be attributed to the reduction of cobalt oxide to metallic cobalt as well as the removal of C-O bonds while Ti tends to form more oxide by the released oxygen. Even after 400°C anneal, C1s signal is observed indicating the presence of carbon throughout the film possibly incorporated during the deposition process itself.

| | C 1s | O 1s | Co 2p | Ti 2p |
|---|---|---|---|---|
| CoTi as received | 39 | 42 | 15 | 3 |
| 300°C Anneal | 26 | 28 | 31 | 15 |
| 400°C Anneal | 20 | 20 | 40 | 20 |

Table 5.5: XPS Chemical composition of CoTi sample before and after various anneals

HAXPES measurements were carried out on similar samples and multiple spots were analysed to study the uniformity of the chemical composition within the HAXPES sampling depth which is greater than the 10 nm thickness of the deposited film. There was little to no difference was observed between the survey spectra of multiple spots before and after the anneal, showing that the deposition of the alloy sample is uniform across the wafer. The survey spectra shown in fig 5.9 display a strong Co 2p and Co 2s signal indicating the presence of the metal in the sample. The other peaks observed correspond Co 3p, Ti 2p, Si 1s and C 1s. The Ti 2p peak is observed upon annealed samples, showing the segregation of Ti from the alloy. The strong Si 1s peak around 1840 eV[20] shows that the sampling depth of HAXPES is more than 30 nm. Since the sensitivity of Co 2p peak is high, the multiple components in Si 1s

peak is not observed in survey spectra and peaks corresponding to both oxide and bulk Si is observed from the narrow region scan shown in fig 5.12. The increase in the peak intensity between the as received sample and 300C annealed sample show that upon annealing most of the surface contamination is removed.

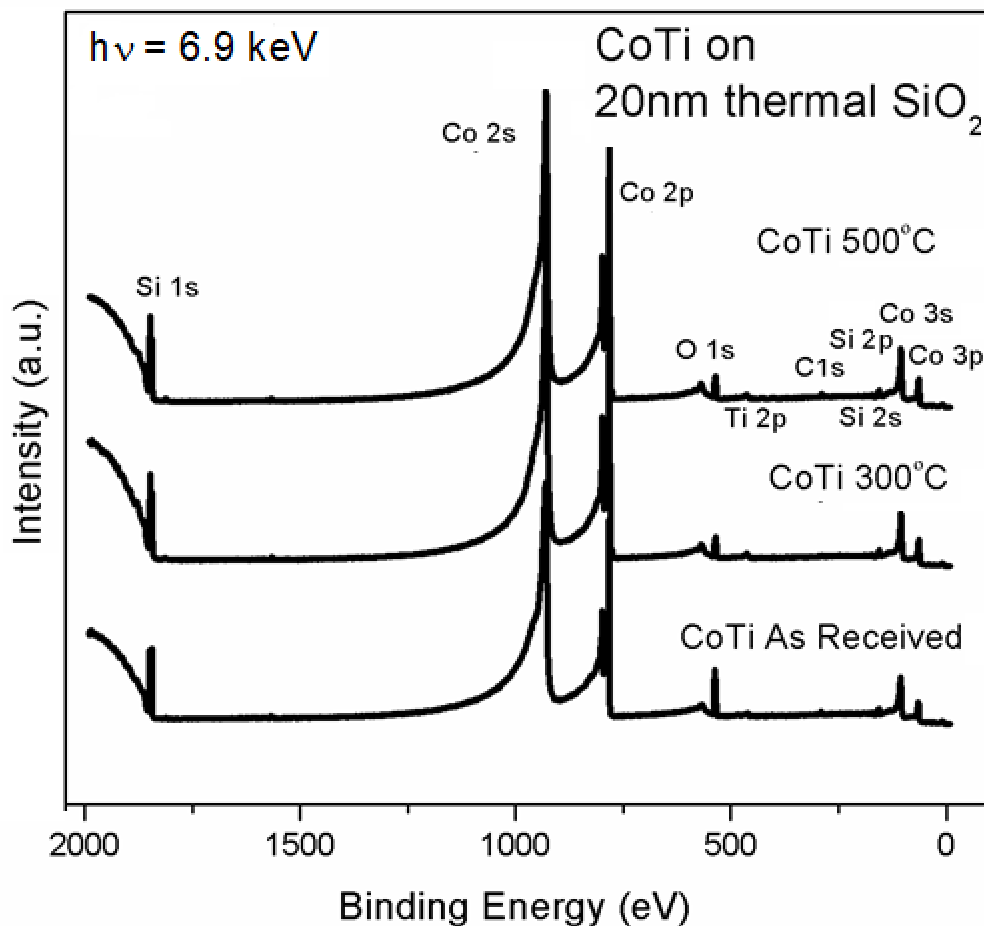


Figure 5.9: HAXPES survey spectra of CoTi on 20nm $SiO_2$ as received and annealed

Co 2p spectrum shown in fig 5.10 indicate the presence of strong metallic cobalt signal at Co (0) oxidation state at 778 eV [21]. There is a shoulder peak corresponding to the +2-oxidation state observed at 780.6 eV [22] and can be attributed to the formation of cobalt carbonate. Although the XPS spectra shows a strong +2 oxidation state peak, in the HAXPES spectra the metallic peak dominates, showing that the carbonate or oxide is present at the surface of the sample while bulk of the film is predominantly metallic.

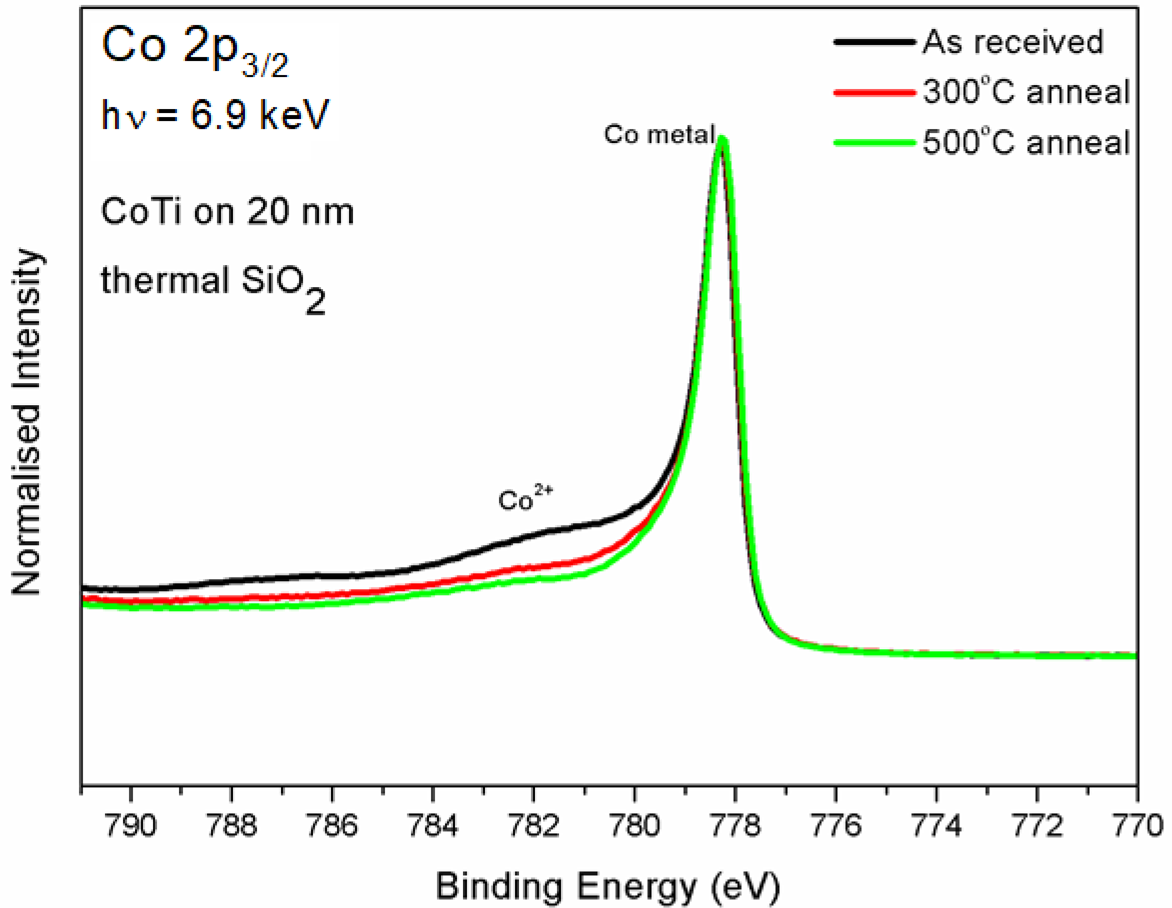


Figure 5.10: HAXPES Co 2p spectra of CoTi on 20nm $SiO_2$ as received and annealed

Upon 300°C annealing, +2 oxidation peak reduces to form metallic cobalt and on 500°C anneal, little evidence of cobalt +2 oxidation state is seen indicating that the cobalt present in the film is completely metallic after the high temperature annealing as is required for the interconnect metal.

Ti 1s spectra in Figure 5.11 show two different peak components, a broad peak at 4973 eV and a narrow peak component at 4969.5 eV. The peak at 4969.5 eV can be attributed to the presence of metallic component while the peak at 4969 eV is seen from the oxidised Ti[23]. The peak position is 3.5 eV from the metallic component and can be attributed to $Ti^{4+}$ oxidation state found in $TIO_2$. Absence of peaks between 4965 eV and 4970 eV indicate that there are no sub-oxides present in the as received sample.

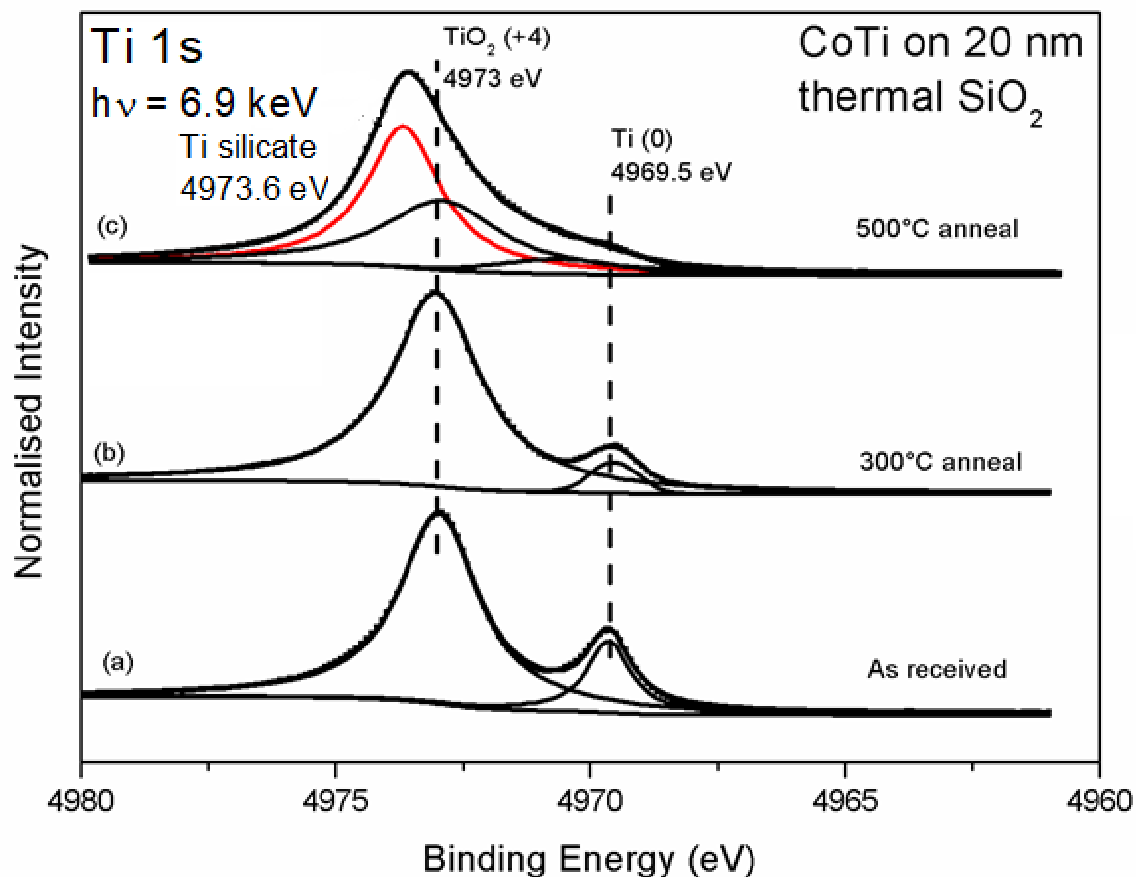


Figure 5.11: HAXPES Ti 1s spectra of CoTi on 20nm $SiO_2$ (a)as received with Single sate $TiO_2$ and metallic Ti (b) 300°C anneal show decrease in metallic Ti signal and (c) 500°C annealed showing formation of Ti silicate at high temperature

The 300°C annealed sample show less metal peak area compared to the as received sample indicating the metal being oxidised after the anneal. As in as-received sample spectra, there are no sub-oxide states present after the 300°C anneal. On further high-temperature anneal, the metallic component decreases further, but there is evidence of multiple component peaks present indicating that other oxidation states of Ti are present. Among them, a component peak with a shift of 0.6 eV towards high binding energy in the $Ti^{4+}$ (4973.6 eV) peak component can be attributed to the formation of titanium silicate at the interface between the alloy and the $SiO_2$ substrate. The curve fitting parameters are tabulated below in table 5.6.

| Peak position (eV) | Gaussian width (eV) |
|---|---|
| 4973.6 | 1.1 |
| 4973.0 | 1.3 |
| 4969.5 | 0.9 |

Table 5.6: Curve fitting parameters of Ti 1s for $TiO_2$ and Ti silicate peak component

Si 1s spectra shown in fig 5.12, show both bulk Si component at 1839 eV as well as $SiO_2$ peak component at 1843.8 eV[20]. This shows that sampling depth is more than 30 nm and the interface between the alloy and the $SiO_2$ substrate can be studied in detail. Upon annealing, a peak at 1842.2 eV is observed which on further annealing grows[24]. The absence of oxide component in Co 2p spectra shown in fig 5.10 indicate the possibility of formation of titanium silicate on annealing.

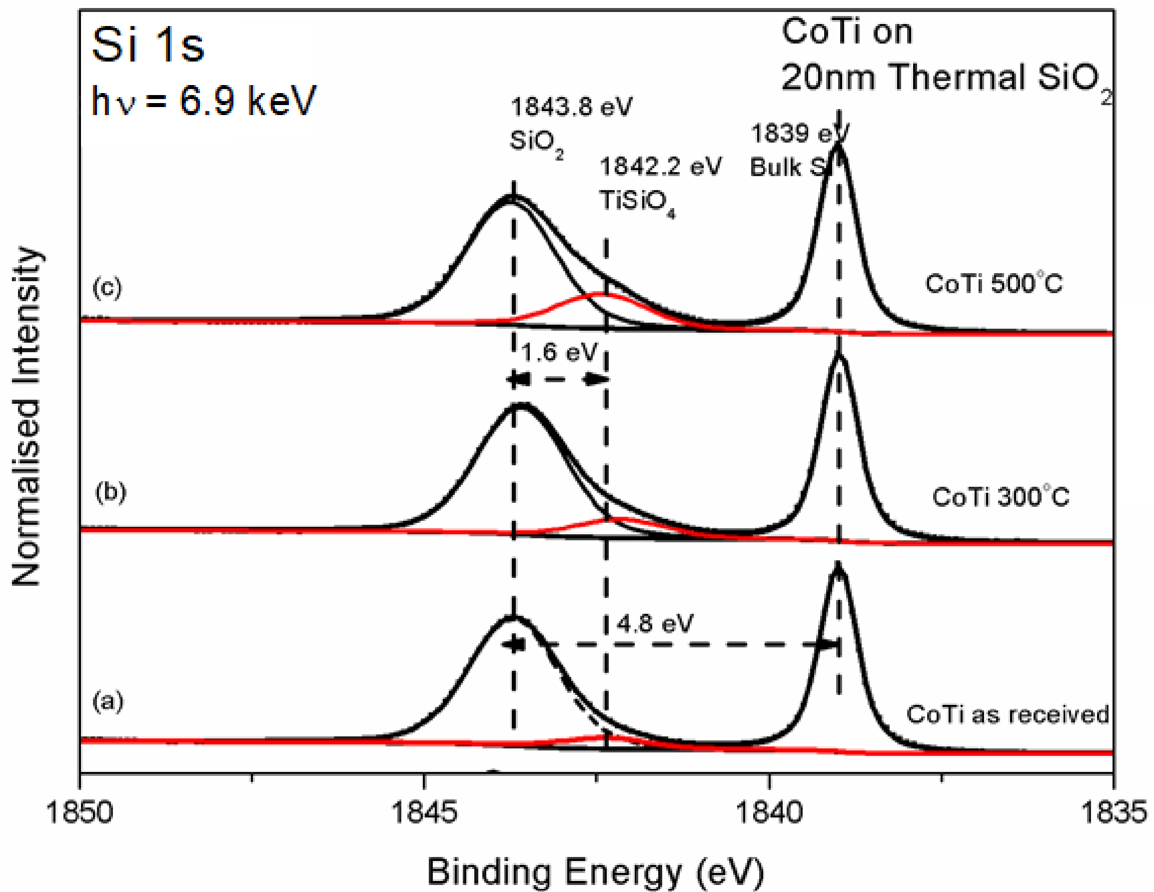


Figure 5.12: HAXPES Si 1s spectra of CoTi on 20 nm $SiO_2$ (a)as received showing $SiO_2$ and bulk Si along with sub-oxide(b) 300°C anneal show formation of Ti silicate and (c) 500°C annealed showing evolution of Ti silicate on high temperature anneals

| Peak position (eV) | Gaussian width (eV) |
|---|---|
| 1843.8 | 1.4 |
| 1842.2 | 1.2 |
| 1839.0 | 0.7 |

Table 5.7: Curve fitting parameters of Si 1s spectra of CoTi sample

The O 1s spectra in fig 5.13 show multiple peaks for the as received sample. The peak at 532.7 eV corresponds to the substrate $SiO_2$ while the peak at 529.6 eV corresponds to titanium dioxide[25]. The peaks at 530.3 eV and 531.4 eV can be attributed to the C-O bonds

and Co carbonate[22] respectively. Upon annealing, the strong peak corresponding to cobalt carbonate bond is attendunted and hence the peak at 531.4 eV is not observed while a peak at 530.6 eV grows. The peaks observed between $TiO_2$ and substrate peak at 532.7 eV can be attributed to the growth of titanium silicate[26]. A corresponding decrease in the substrate is also observed as the $SiO_2$ at the alloy interface is consumed to form titanium silicate.

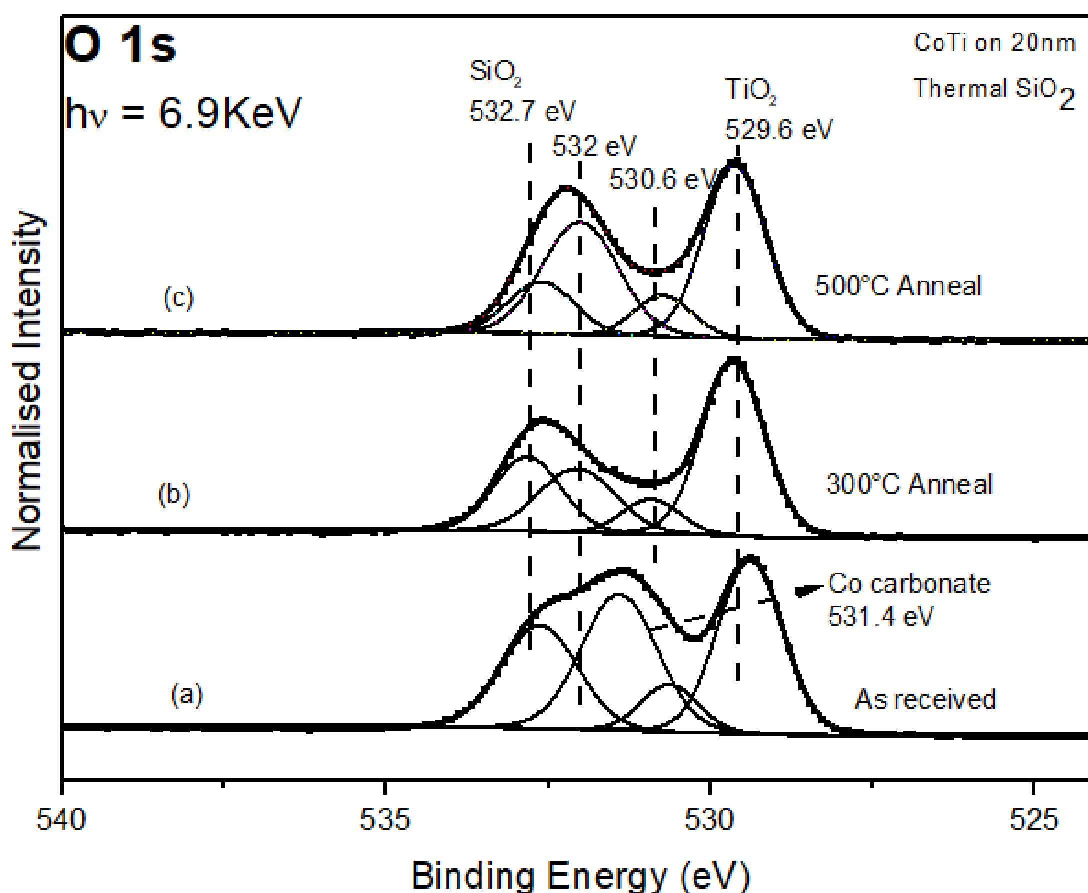


Figure 5.13: HAXPES O 1s spectra of CoTi on 20 nm $SiO_2$ (a)as received showing large surface contamination(b) 300°C anneal show formation of Ti silicate and (c) 500°C annealed showing evolution of Ti silicate on high temperature anneals

| Peak position (eV) | Gaussian width (eV) |
|---|---|
| 532.7 | 1.1 |
| 532.0 | 1.0 |
| 530.6 | 1.0 |
| 529.6 | 0.7 |

Table 5.8: O 1s fitting parameters of CoTi alloy sample before and after anneal

The C 1s spectra acquired at a photon energy of 6.9 keV for this experiment are shown in fig 5.14. Multiple peak components are observed between 285 eV and 290 eV with a strong

peak at 285 eV corresponding to C-C[19]. The peak at 289.3 eV corresponding to carbonate ($CO_3^{2-}$) can be observed in the as received sample which is reduced on anneal. Similarly, the intensity of the C=O related peak at 288 eV is also reduced on anneal. Although, there is free Ti and Co metal is observed from the Co 2p and Ti 1s spectra, there is no peak observed at 282 eV indicating the absence of metal carbide[27]. Even after high temperature anneal, there is still a carbon peak present indicating the presence of carbon - based contamination in the alloy film or at the interface of the substrate and alloy.

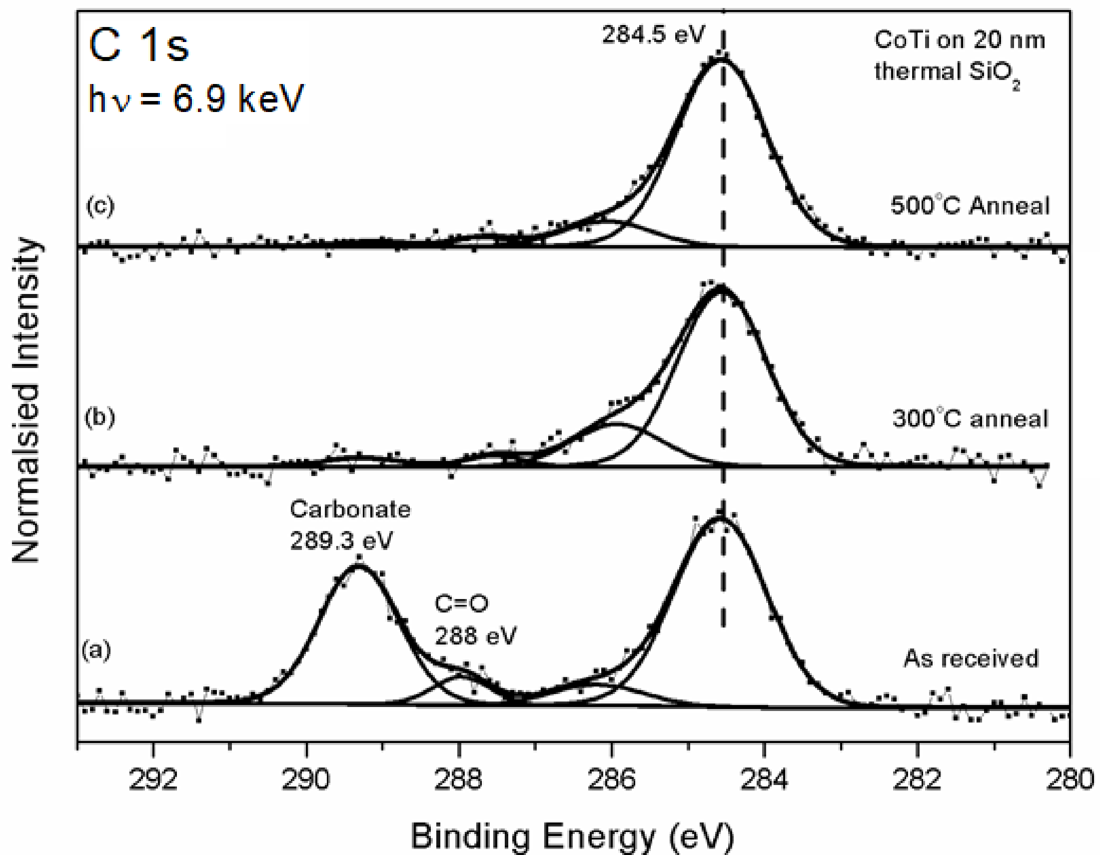


Figure 5.14: HAXPES C 1s spectra of CoTi on 20 nm $SiO_2$ (a)as received sample showing evidence of metal carbonate (b) 300ºC anneal and (c)500ºC show no metal carbonate signal while a large carbon content is present

| Peak position (eV) | Gaussian width (eV) |
| --- | --- |
| 284.5 | 1.4 |
| 286.7 | 1.1 |
| 288.0 | 1.1 |
| 289.3 | 0.7 |

Table 5.9: Curve fit parameters for C 1s spectra of CoTi sample

### 5.3.1 XANES Analysis:

Fig 5.15 shows the Co-K edge XANES spectra of the CoTi alloy sample as received and following the thermal anneals. Initial measurements of the as received spectra show a strong absorption edge around 7710 eV marked as A. The absorption can be attributed to binding energy of Co 1s core level for Co (0) oxidation state and therefore can be attributed to the metallic Co present in the sample. There is strong rising edge observed between 7717 eV and 7725 eV (region B). In order to observe the fine splitting in the region B, a 1$^{st}$ derivative of the XANES spectra is carried out which is shown in fig 5.15(b). The peaks observed don't coincide with the values reported for mixed state Co oxide ($Co_3O_4$) or Co +2 oxide (CoO)[28]. Also, from the HAXPES results shown above there is a strong presence of cobalt carbonate in the as received sample. Hence the multiple peaks observed between 7717 eV and 7725 eV can be attributed to the cobalt carbonate in +2 oxidation state ($CoCO_3$). This confirms the presence of metal as well as strong surface cobalt carbonate as observed in the XPS and HAXPES spectra.

Upon annealing, the peaks between 7717 to 7725 decreases, while the absorption edge at 7710 eV and corresponding 1$^{st}$ derivative peak increases with each anneal. This fact further confirms the HAXPES Co 2p spectra shown in fig 5.10 which indicate the presence of Co metal and absence of carbonate further confirms that the oxygen observed in the metal oxide state corresponds to titanium oxides.

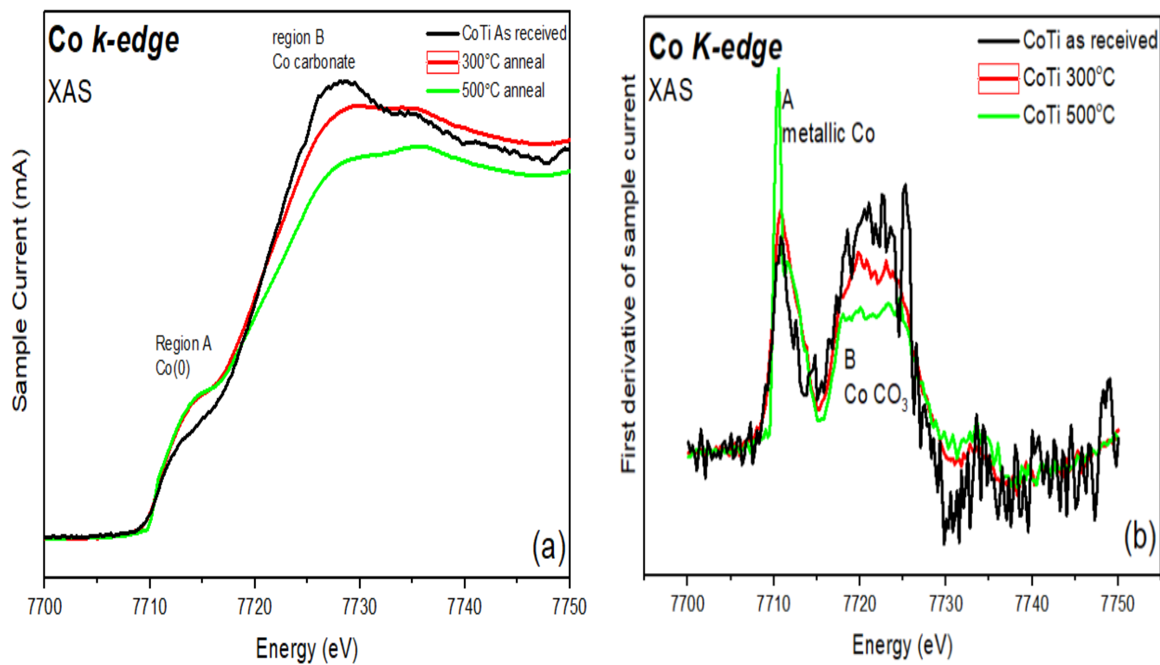


Figure 5.15: XAS spectra of CoTi (a) normalised Co K-edge before and after annealing (b) first derivative of Co K-edge before and after annealing

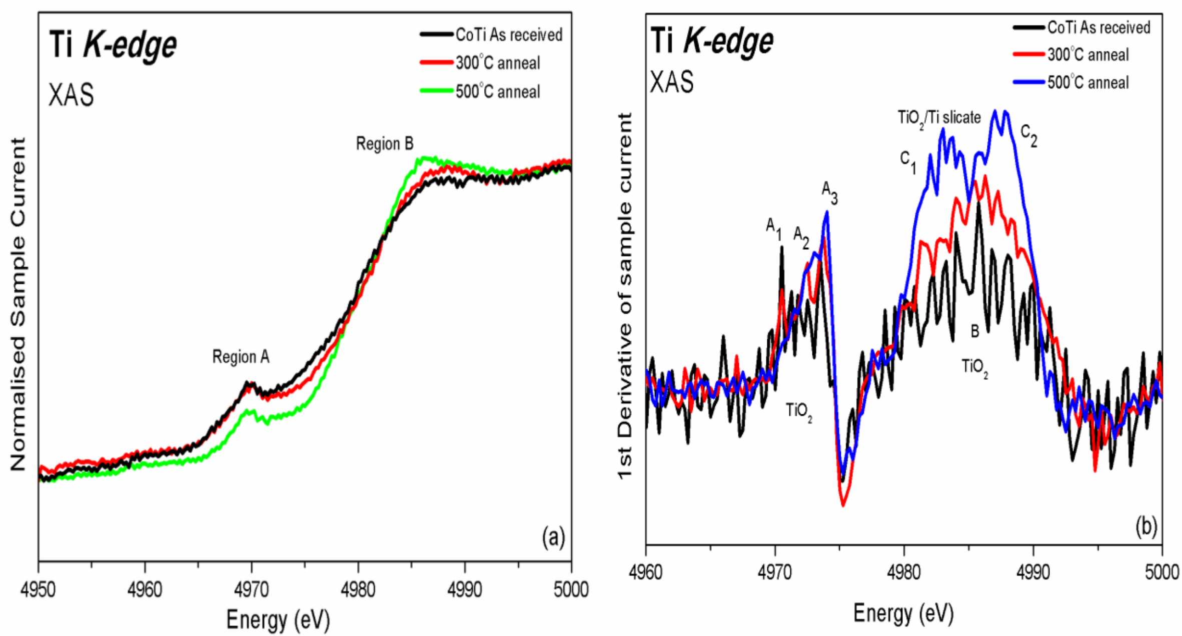


Figure 5.16: XAS spectra of CoTi (a) normalised Ti K-edge before and after annealing (b) first derivative of Ti K-edge before and after annealing

The Titanium K-edge XANES spectra are shown in fig 5.16. Two distinct peaks can be observed: one at 4970 eV corresponding to the pre-edge and other at 4985 eV. The characteristic pre-edge peaks corresponding to the $TiO_2$ [29] are not clearly seen in the as received XAS shown in fig 5.16(a) although XPS and HAXPES spectra show strong $TiO_2$ peaks. Hence a first derivative of the Ti K-edge is shown in fig 5.16(b). The region A can be seen with 3 peaks in the as received as well as annealed sample spectra can be attributed to $TiO_2$. The region B corresponds to absorption edge of $TiO_2$ around 4985 eV. The as received and 300°C annealed spectra looks similar while an extra peak is observed in the region C after the 500°C anneal. The growth of the second peak $C_2$ can be attributed to the formation of the titanium silicate as can be seen from the HAXPES Ti 1s spectra and corresponding Si 1s spectra.

## 5.4 Conclusion

In this work, a synchrotron radiation photoemission study of the interaction of metallic titanium with low-k spin-on-glass was presented in detail. When deposited on thermally grown $SiO_2$, two phases of titanium silicide form upon deposition with TiSi formed upon deposition, which converts to $TiSi_2$ with thermal anneal. The presence of carbon in the low-k material results in the formation of Ti-carbide upon deposition and the complete conversion of Ti-silicide to Ti-silicate upon annealing at 500$^{o}$C.

Additionally, a CoTi self-forming forming barrier alloy was analysed as an alternative interconnect adhesion liner application using various photoelectron spectroscopy techniques. The XPS and HAXPES results indicate the presence of Co metal with surface Co carbonate while Ti metal and $TiO_2$ was also observed. Upon annealing, pure Co metal was observed while the oxygen released oxidises the Ti metal. An interfacial layer of titanium silicate grows on high temperature anneal. XAS results also agree with the removal of Co carbonate resulting in the formation of more Co metal upon annealing while Ti is oxidised. Following the synchrotron studies of Ti on $SIO_2$ and SoG low-κ and CoTi self-forming alloy on $SiO_2$, it can be concluded that CoTi is a good candidate for alternate interconnect/barrier in the future

generation of back-end-of-the-line interconnects while SoG is a good candidate for low-κ dielectric that can be integrated with CoTi self-forming barrier/interconnect stack.

# References


[1] J.M. Roberts, A.P. Kaushik, J.S. Clarke, Resistivity of sub-30 nm copper lines, in: 2015 IEEE Int. Interconnect Technol. Conf. 2015 IEEE Mater. Adv. Met. Conf. IITC/MAM 2015, 2015: pp. 341–343. doi:10.1109/IITC-MAM.2015.7325595.

[2] Y.K. Siew, N. Jourdan, I. Ciofi, K. Croes, C.J. Wilson, B.J. Tang, S. Demuynck, Z. Wu, H. Ai, D. Cellier, A. Cockburn, J. Bommels, Z. Tokei, Cu Wire resistance improvement using Mn-based Self-Formed Barriers, in: 2014 IEEE Int. Interconnect Technol. Conf. / Adv. Met. Conf. IITC/AMC 2014, 2014: pp. 311–314. doi:10.1109/IITC.2014.6831895.

[3] C. Adelmann, L.G. Wen, A.P. Peter, Y.K. Siew, K. Croes, J. Swerts, M. Popovici, K. Sankaran, G. Pourtois, S. Van Elshocht, J. Bommels, Z. Tokei, Alternative metals for advanced interconnects, in: 2014 IEEE Int. Interconnect Technol. Conf. / Adv. Met. Conf. IITC/AMC 2014, 2014: pp. 173–176. doi:10.1109/IITC.2014.6831863.

[4] I. Asselberghs, M. Politou, B. Soree, S. Sayan, D. Lin, P. Pashaei, C. Huyghebaert, P. Raghavan, I. Radu, Z. Tokei, Graphene wires as alternative interconnects, in: 2015 IEEE Int. Interconnect Technol. Conf. 2015 IEEE Mater. Adv. Met. Conf. IITC/MAM 2015, 2015: pp. 317–319. doi:10.1109/IITC-MAM.2015.7325590.

[5] M.H. Van Der Veen, K. Vandersmissen, D. Dictus, S. Demuynck, R. Liu, X. Bin, P. Nalla, A. Lesniewska, L. Hall, K. Croes, L. Zhao, J. Bömmels, A. Kolics, Z. Tökei, Cobalt bottom-up contact and via prefill enabling advanced logic and DRAM technologies, in: 2015 IEEE Int. Interconnect Technol. Conf. 2015 IEEE Mater. Adv. Met. Conf. IITC/MAM 2015, 2015: pp. 25–27. doi:10.1109/IITC-MAM.2015.7325605.

[6] J. Kelly, J.H.C. Chen, H. Huang, C.K. Hu, E. Liniger, R. Patlolla, B. Peethala, P. Adusumilli, H. Shobha, T. Nogami, T. Spooner, E. Huang, D. Edelstein, D. Canaperi, V. Kamineni, F. Mont, S. Siddiqui, Experimental study of nanoscale Co damascene BEOL interconnect structures, in: 2016 IEEE Int. Interconnect Technol. Conf. / Adv. Met.

Conf. IITC/AMC 2016, 2016: pp. 40–42. doi:10.1109/IITC-AMC.2016.7507673.

[7] M. Hosseini, J. Koike, Amorphous $CoTi_x$ as a liner/diffusion barrier material for advanced copper metallization, J. Alloys Compd. 721 (2017) 134–142. doi:10.1016/j.jallcom.2017.05.335.

[8] Y.H. Su, J.N. Shih, Y.S. Wang, W.H. Tseng, W.H. Liao, C.Y. Hung, W.H. Lee, Y.L. Wang, CoW alloy as multi-function diffusion barrier material for next-generation Cu metallization, in: 4th Int. Symp. Next-Generation Electron. IEEE ISNE 2015, 2015. doi:10.1109/ISNE.2015.7132035.

[9] M. He, X. Zhang, T. Nogami, X. Lin, J. Kelly, H. Kim, T. Spooner, D. Edelstein, L. Zhao, Mechanism of Co Liner as Enhancement Layer for Cu Interconnect Gap-Fill, J. Electrochem. Soc. 160 (2013) D3040–D3044. doi:10.1149/2.009312jes.

[10] W.F. Wu, K.C. Tsai, C.G. Chao, J.C. Chen, K.L. Ou, Novel multilayered Ti/TiN diffusion barrier for Al metallization, J. Electron. Mater. 34 (2005) 1150–1156. doi:10.1007/s11664-005-0244-9.

[11] M. Iwami, A. Hiraki, Low-temperature ti-silicide forming reaction in very thin ti-sio2/si(111) contact systems, Jpn. J. Appl. Phys. 24 (1985) 530–536. doi:10.1143/JJAP.24.530.

[12] R.J.O.M. Hoofman, G.J.A.M. Verheijden, J. Michelon, F. Iacopi, Y. Travaly, M.R. Baklanov, Z. T??kei, G.P. Beyer, Challenges in the implementation of low-k dielectrics in the back-end of line, Microelectron. Eng. 80 (2005) 337–344. doi:10.1016/j.mee.2005.04.088.

[13] K. Maex, M.R. Baklanov, D. Shamiryan, F. Iacopi, S.H. Brongersma, Z.S. Yanovitskaya, Low dielectric constant materials for microelectronics, J. Appl. Phys. 93 (2003) 8793–8841. doi:10.1063/1.1567460.

[14] M. Hosseini, D. Ando, Y. Sutou, J. Koike, Co and CoTixfor contact plug and barrier layer in integrated circuits, Microelectron. Eng. 189 (2018) 78–84. doi:10.1016/j.mee.2017.12.017.

[15] A.T. Kohl, Low k, Porous Methyl Silsesquioxane and Spin-On-Glass, Electrochem. Solid-State Lett. 2 (1999) 77. doi:10.1149/1.1390740.

[16] D.K. Sarkar, E. Desbiens, M.A. El Khakani, High-k titanium silicate dielectric thin films grown by pulsed-laser deposition, Appl. Phys. Lett. 80 (2002) 294–296. doi:10.1063/1.1435072.

[17] D. Levy, J.P. Ponpon, A. Grob, J.J. Grob, R. Stuck, Rapid thermal annealing and titanium silicide formation, Appl. Phys. A Solids Surfaces. 38 (1985) 23–29. doi:10.1007/BF00618722.

[18] P. Casey, J. Bogan, G. Hughes, Photoemission study of carbon depletion from ultralow-carbon doped oxide surfaces during the growth of Mn silicate barrier layers, J. Appl. Phys. 110 (2011) 124512. doi:10.1063/1.3669998.

[19] K.D. Moulder, J. F., Stickle, W. F., Sobol, P. E. & Bomben, Handbook of X-ray Photoelectron Spectroscopy, (1995).

[20] C. Caspers, A. Gloskovskii, M. Gorgoi, C. Besson, M. Luysberg, K.Z. Rushchanskii, M. Ležaić, C.S. Fadley, W. Drube, M. Müller, Interface Engineering to Create a Strong Spin Filter Contact to Silicon, Sci. Rep. 6 (2016). doi:10.1038/srep22912.

[21] M.C. Biesinger, B.P. Payne, A.P. Grosvenor, L.W.M. Lau, A.R. Gerson, R.S.C. Smart, Resolving surface chemical states in XPS analysis of first row transition metals, oxides and hydroxides: Cr, Mn, Fe, Co and Ni, Appl. Surf. Sci. 257 (2011) 2717–2730.

[22] S. Jiang, W. Cheng, J. He, J. Huang, Q. Liu, Y. Jiang, S. Wei, XAFS study on the impact of local structure on electrochemical performance for $Co_3O_4$ nanowire arrays, J. Phys. Conf. Ser. 712 (2016) 012115. doi:10.1088/1742-6596/712/1/012115.

[23] P. Risterucci, O. Renault, C. Zborowski, D. Bertrand, A. Torres, J.P. Rueff, D. Ceolin, G. Grenet, S. Tougaard, Effective inelastic scattering cross-sections for background analysis in HAXPES of deeply buried layers, Appl. Surf. Sci. 402 (2017) 78–85. doi:10.1016/j.apsusc.2017.01.046.

[24] M. Gorgoi, N. Mårtensson, S. Svensson, HAXPES studies of solid materials for applications in energy and information technology using the HIKE facility at HZB-BESSY II, J. Electron Spectros. Relat. Phenomena. 200 (2015) 40–48. doi:10.1016/j.elspec.2015.05.005.

[25] A. Pipi, G. Byzynski, L. Ruotolo, Photocatalytic activity and RNO dye degradation of

nitrogen-doped TiO<inf>2</inf>prepared by ionothermal synthesis, Mater. Res. 20 (2017) 628–638. doi:10.1590/1980-5373-MR-2016-0837.

[26] A.Y. Stakheev, E.S. Shpiro, J. Apijok, XPS and XAES study of titania-silica mixed oxide system, J. Phys. Chem. 97 (1993) 5668–5672. doi:10.1021/j100123a034.

[27] L. Zhang, R. V. Koka, A study on the oxidation and carbon diffusion of TiC in alumina-titanium carbide ceramics using XPS and Raman spectroscopy, Mater. Chem. Phys. 57 (1998) 23–32. doi:10.1016/S0254-0584(98)00187-4.

[28] A. Moen, D.G. Nicholson, M. Rønning, G.M. Lamble, J.F. Lee, H. Emerich, X-Ray absorption spectroscopic study at the cobalt K-edge on the calcination and reduction of the microporous cobalt silicoaluminophosphate catalyst CoSAPO-34, J. Chem. Soc. - Faraday Trans. 93 (1997) 4071–4077. doi:10.1039/a704488g.

[29] J. Chaboy, N. Nakajima, Y. Tezuka, Ab initio x-ray absorption near-edge structure study of Ti K-edge in rutile, J. Phys. Condens. Matter. 19 (2007). doi:10.1088/0953-8984/19/26/266206.

# 6. Conclusions and Future work

## 6.1 Conclusions

In this study, the possibility of using self-forming alloys and nitrogen - based barrier stack as a possible replacement for the existing Ta/TaN[1] barrier stack in the future interconnect nodes were studies. The possibility of using low-κ $SiO_2$ based dielectrics[2] and Co as a replacement for Cu as an interconnect metal[3] were also analysed. XPS and HAXPES photoelectron studies were the main techniques used to characterize the thin films. Other techniques such as SIMS and XANES were also used to characterize the films to confirm that the results obtained from the photoelectron studies. Electrical characterization through four-point probe and CV analysis of MOS structures were carried out to test the possibility of using self-forming Cu-based alloys in the device integration.

### 6.1.1 Nitrogen based Mn barrier layer for Cu interconnects

In chapter III, the nitrogen incorporated Mn films were analysed for the possibility of replacing Ta/TaN barrier stack, by forming manganese silicate at the interface and the nitrogen in the film improving the adhesion of the copper films. From previous works, it was found that formation of manganese silicate at the interface of $SiO_2$ and manganese film was effective in stopping copper diffusion[4]. The films were analysed using XPS and found to be forming manganese oxide films with the evidence of nitrogen incorporated throughout the film. Nitrogen incorporated films were found to form manganese silicate upon deposition conditions and were observed the formation of manganese silicate grows on annealing.

To compare the effects of adhesion, a similarly deposited metallic manganese films were analysed with XPS. AFM technique was used to analyze the surface morphology of the films. While the nitrogen incorporated films show uniform surface, the metallic films were

found to have individual islands and the corresponding roughness is high compared to that of the nitrogen incorporated films. This shows that even though stoichiometric MnN was not obtained by CVD process, the presence of even a low concentration of nitrogen in the Mn films influences the homogenous nature of the sample surface. Copper was deposited on both manganese metal film and the nitrogen incorporated films using thermal evaporation technique at high vacuum. Adhesion tape test were carried out on both films and analysed using optical microscope before and after the tape test and results indicate that presence of nitrogen improves the adhesion of copper while the copper deposited on the bare substrate and the Mn metal films without nitrogen were delaminated.

### 6.1.2 Self-forming Mn/Ti based copper alloy systems

In chapter IV, the material and electrical characterization of copper alloys systems of CuMn and CuTi with concentration of 20% by weight was presented. Although the previous studies on CuMn alloy samples show the formation of diffusion barrier at low concentration of Mn and Ti[5], the low concentration alloys (5%) of CuMn and CuTi were found to delaminate at the annealing conditions employed in the fabrication processes. So, a higher concentration alloys had been deposited under industrial conditions and were characterized using photoelectron studies (XPS and HAXPES), SIMS, four-point probe measurements and CV electrical studies.

Both CuMn and CuTi alloys found to be oxidised in the as received samples. No substrate was observed in the traditional XPS measurements and chemical composition calculations show nominal metal concentrations. On annealing, the alloying metal segregates at the interface.

To study the interface, HAXPES measurements were carried out. The as received samples showed sputter damage at the interface and carbon contamination along with the bulk Si signal indicating that the HAXPES results were obtained from a depth at least 30nm. The as received samples show free metallic Mn/Ti in the respective samples. There was no evidence of metal carbide even though there is strong carbon signal[6] which shows that the

free metal is present in the bulk of the alloy film while the carbon contamination was at the surface.

The annealed samples show clear interface layer of silicate formation in both alloy systems. No copper oxide signal was observed and there was no free alloying metal (Mn/Ti) after the anneal. Although there was a decrease in carbon signal, there was some carbon signal observed even after the high temperature anneal. The Si 1s signal show clear interface layer of metal silicate after the anneal, which can be further confirmed by O 1s spectra of the after anneal sample.

The results were further confirmed by the SIMS plots of before and after annealing samples. There was pure Cu observed with no alloying metal and substrate – alloy interface layer of metal silicate after the anneal. While the as received sample show homogenous distribution of metal throughout the alloy, the metal segregation is clearly observed in the after annealing sample.

Electrical characterization was carried out on as received and annealed samples. The four-point probe resistivity measurements of the alloy and Cu samples were measured for the as received samples and various annealing steps. The resistivity decreased upon each step of annealing and the on high temperature anneals, the resistivity approaches to that of the copper film. This can be attributed to the segregation of metals and formation of pure Cu from the alloy.

CV measurements of the samples before and after annealing show that there was strong hysteresis in the both CuMn and CuTi samples due to presence of sputter damage and interface charges. The annealing steps remove the sputter damage and most of the interface charges were removed. Though the flat band voltage was observed at 0 and absence of interface charges in the CuTi samples, the total capacitance was high compared to that of the ideal capacitance for the 20 nm $SiO_2$ dielectric. While the capacitance of the CuMn was low compared to CuTi sample, there was still a small amount of interface charges present and correspondingly, the flat band voltage is shifted away from 0.

### 6.1.3 Synchrotron radiation study of metallic Titanium deposited on low-κ dielectrics:

In chapter V, the possibility of integrating low-κ dielectric with the possibility of using Ti as a probable adhesion liner in the metallic Co future interconnect system. For successful integration, the interface of ultra-thin Ti with low-κ dielectric has to be studied. A synchrotron radiation study of the interaction of metallic titanium with low-k spin-on-glass was carried out to understand the chemical interactions of metallic Ti and low-κ dielctric. When deposited on thermally grown $SiO_2$, two phases of titanium silicide form upon deposition with primarily TiSi formed upon deposition, which converts to $TiSi_2$ with thermal anneal. The presence of carbon in the low-k material results in the formation of Ti-carbide upon deposition and the complete conversion of Ti-silicide to Ti-silicate upon annealing at 500$^{o}$C.

### 6.1.4 HAXPES and XAS studies of CoTi self-forming alloy:

As Co is one of the metals in study for the future interconnect metal, a 10 nm self-forming alloy of 20% CoTi deposited through sputtering technique was analyzed using photoelectron spectroscopy techniques. The as received samples through initial XPS measurements show 83:17 ratio of the alloy and found to be uniform in multiple spots of the sample showing that the deposition process is uniform throughout the wafer. The as received sample doesn't show any Si 2p signal in the conventional XPS, indicating that the films are thicker than the sampling depth of XPS. On anneal, the Co metal was reduced from CoO and $CoCO_3$ and more metallic signal was observed. While the Co:Ti ratio was 83:17 in the as received sample, it increased to 30:70 in the annealed sample indicating that there is strong segregation of Ti metal at the surface which is in accordance with the self-forming barrier principle.

HAXPES results further confirm the presence of Co metal and surface oxide/carbonate and on high temperature anneals, only pure CO metal was observed. The as received sample showed a strong carbon contamination which reduces on anneal. The presence of bulk Si

signal in the HAXPES Si 1s spectra show that the sampling depth is more than 30 nm. Ti 1s spectra showed strong TI oxide signal in the as received signal along with a metallic peak.

After annealing, while the sputter damage observed in Si 1s spectra is removed, there was a growth in peak corresponding to metallic silicate. As there were no cobalt-based oxides were observed in Co 2p spectrum, the silicate can be attribute to Ti silicate. While the Ti 1s spectra showed no metallic signal after the high temperature annealing, multiple peaks were observed near Ti +4 oxidation state and can be attributed to formation of Ti silicate.

XAS measurements of the as received and annealed CoTi samples agree with the results obtained from HAXPES and XPS. It confirms the presence of Co oxide/carbonate in the as received sample which is removed on anneal and more metallic Co is observed. Similarly, Ti oxide was observed in the as received sample and on annealing, a second peak grows which can be attributed to the presence of Ti silicate.

## 6.2 Future Work:

Although, it was found that formation of stoichiometric formation of MnN was difficult from our studies, presence of even small concentration of nitrogen helped in the homogeneity of the Mn thin film and helped in improving the adhesion. Additionally, previous generation of barrier layer for the interconnects included the nitrogen-based metal[7] as a part of the barrier stack. One of the possible future studies is to deposit and characterize ultra-thin nitrogen-based Mn films and subsequent device fabrication and compare the RC time delay of the current generation of barrier layer systems.

In depth analysis of CuMn and CuTi has been done and although the results were favorable for integration into the interconnect stack, actual device fabrication studies had to be done to study the efficiency of the alloy films as self-forming barriers. As presence of nitrogen improves the capability of the Ti and Mn based films as a diffusion barrier material, incorporating nitrogen into the alloy films and subsequent studies of the resulting thin films is a strong possibility for future studies.

Material characterization of CoTi films has been carried out as a possible seed layer and adhesion liner for future interconnects. Detailed electrical characterization has to be carried out in order to observe the efficiency of the CoTi films as a replacement for the copper-based interconnect system. By comparing the RC time delay due to the Co based devices and Cu based devices fabricated in similar conditions, the possibility of using Co based interconnect system in the future generation of ICs can be determined.

# References


[1] T.O. Hiroyuki Shimada, Ichiro Ohshima, Takeo Ushiki Shigetoshi Sugawa, Tantalum Nitride Metal Gate FD-SOI CMOS FETs, IEEE Trans. Electron Devices. 48 (2001) 1619–1626.

[2] D. Shamiryan, T. Abell, F. Iacopi, K. Maex, Low-k dielectric materials, Mater. Today. 7 (2004) 34–39. doi:10.1016/S1369-7021(03)00052-X.

[3] M. Hosseini, J. Koike, Y. Sutou, L. Zhao, S. Lai, R. Arghavani, Amorphous Co-Ti alloy as a single layer barrier for Co local interconnect structure, in: 2016 IEEE Int. Interconnect Technol. Conf. / Adv. Met. Conf. IITC/AMC 2016, 2016: pp. 162–164. doi:10.1109/IITC-AMC.2016.7507718.

[4] C. Byrne, B. Brennan, A.P. McCoy, J. Bogan, A. Brady, G. Hughes, In Situ XPS Chemical Analysis of MnSiO3 Copper Diffusion Barrier Layer Formation and Simultaneous Fabrication of Metal Oxide Semiconductor Electrical Test MOS Structures, ACS Appl. Mater. Interfaces. 8 (2016) 2470–2477. doi:10.1021/acsami.5b08044.

[5] M. Franz, R. Ecke, C. Kaufmann, J. Kriz, S.E. Schulz, Investigation of barrier formation and stability of self-forming barriers with CuMn, CuTi and CuZr alloys, 2015 IEEE Int. Interconnect Technol. Conf. 2015 IEEE Mater. Adv. Met. Conf. IITC/MAM 2015. 156 (2015) 95–97. doi:10.1109/IITC-MAM.2015.7325640.

[6] P. Casey, J. Bogan, G. Hughes, Photoemission study of carbon depletion from ultralow-carbon doped oxide surfaces during the growth of Mn silicate barrier layers, J. Appl. Phys. 110 (2011) 124512. doi:10.1063/1.3669998.

[7] K. Holloway, P.M. Fryer, C. Cabral, J.M.E. Harper, P.J. Bailey, K.H. Kelleher, Tantalum as a diffusion barrier between copper and silicon: Failure mechanism and effect of nitrogen additions, J. Appl. Phys. 71 (1992) 5433–5444. doi:10.1063/1.350566.